https://journals.vsu.ru/kcmf/about

ISSN 1606-867X
eISSN 2687-0711

Конденсированные среды и межфазные границы

РЕЦЕНЗИРУЕМЫЙ НАУЧНЫЙ ЖУРНАЛ

Condensed Matter and Interphases

PEER-REVIEWED SCIENTIFIC JOURNAL

Том / Vol. 25, № / No. 4
2023

Condensed Matter and Interphases
Kondensirovannye sredy i mezhfaznye granitsy

Peer-reviewed scientific journal
Published since January 1999
Periodicity: Quarterly
Volume 25, No. 4, 2023

Full-text version is available in the Russian language on the website: https://journals.vsu.ru/kcmf

Condensed Matter and Interphases (Kondensirovannye Sredy i Mezhfaznye Granitsy) publishes articles in Russian and English dedicated to key issues of condensed matter and physicochemical processes at interfaces and in volumes.

The mission of the journal is to provide open access to the results of original research (theoretical and experimental) at the intersection of contemporary condensed matter physics and chemistry, material science and nanoindustry, solid state chemistry, inorganic chemistry, and physical chemistry, and to share scientific data in the **following sections**: atomic, electron, and cluster structure of solids, liquids, and interphase boundaries; phase equilibria and defect formation processes; structure and physical and chemical properties of interphases; laser thermochemistry and photostimulated processes on solid surfaces; physics and chemistry of surface, thin films and heterostructures; kinetics and mechanism of formation of film structures; electrophysical processes in interphase boundaries; chemistry of surface phenomena in sorbents; devices and new research methods.

The journal accepts for publication: reviews, original articles, short communications by leading Russian scientists, foreign researchers, lecturers, postgraduate and undergraduate students.

FOUNDER AND PUBLISHER:
Voronezh State University

The journal is registered by the Russian Federal Service for Supervision of Communications, Information Technology and Mass Media, Certificate of Registration ПИ № ФС77-78771 date 20.07.2020

The journal is included in the List of peer reviewed scientific journals published by the Higher Attestation Commission in which major research results from the dissertations of Candidates of Sciences (PhD) and Doctor of Science (DSc) degrees are to be published. Scientific specialties of dissertations and their respective branches of science are as follows: 1.4.1. – Inorganic Chemistry (Chemical sciences); 1.4.4. – Physical Chemistry (Chemical sciences); 1.4.6. – Electrochemistry (Chemical sciences); 1.4.15. – Solid State Chemistry (Chemical sciences); 1.3.8. – Condensed Matter Physics (Physical sciences).

The journal is indexed and archived in: Russian Scientific Index Citations, Scopus, Chemical Abstract, EBSCO, DOAJ, CrossRef

Editorial Board and Publisher Office:
1 Universitetskaya pl., Voronezh 394018
Phone: +7 (432) 2208445
https://journals.vsu.ru/kcmf
E-mail: kcmf@main.vsu.ru

When reprinting the materials, a reference to the Condensed Matter and Interphases must be cited

The journal's materials are available under the Creative Commons "Attribution" 4.0 Global License

© Voronezh State University, 2023

EDITOR-IN-CHIEF:
Victor N. Semenov, Dr. Sci. (Chem.), Full Professor, Voronezh State University, (Voronezh, Russian Federation)

VICE EDITORS-IN-CHIEF:
Evelina P. Domashevskaya, Dr. Sci. (Phys.–Math.), Full Professor, Voronezh State University, (Voronezh, Russian Federation)
Polina M.Volovitch, Ph.D. (Chem.), Associate Professor, Institut de Recherche de Chimie (Paris, France)

EDITORIAL BOARD:
Nikolay N. Afonin, Dr. Sci. (Chem.), Voronezh State Pedagogical University (Voronezh, Russian Federation)
Vera I. Vasil'eva, Dr. Sci. (Chem.), Full Professor, Voronezh State University, (Voronezh, Russian Federation)
Aleksandr V. Vvedenskii, Dr. Sci. (Chem.), Full Professor, Voronezh State University, (Voronezh, Russian Federation)
Victor V. Gusarov, Dr. Sci. (Chem.), Associate Member of the RAS, Ioffe Physical-Technical Institute RAS (St. Petersburg, Russian Federation)
Vladimir E. Guterman, Dr. Sci. (Chem.), Full Professor, Southern Federal University (Rostov-on-Don, Russian Federation)
Boris M. Darinskii, Dr. Sci. (Phys.–Math.), Full Professor, Voronezh State University, (Voronezh, Russian Federation)
Vladimir P. Zlomanov, Dr. Sci. (Chem.), Full Professor, Moscow State University, (Moscow, Russian Federation)
Valentin M. Ievlev, Dr. Sci. (Phys.–Math.), Full Member of the RAS, Moscow State University, (Moscow, Russian Federation)
Aleksandr D. Izotov, Dr. Sci. (Chem.), Associate Member of the RAS, Kurnakov Institute of General and Inorganic Chemistry RAS (Moscow, Russian Federation)
Oleg A. Kozaderov, Dr. Sci. (Chem.), Associate Professor, Voronezh State University, (Voronezh, Russian Federation)
Andrey I. Marshakov, Dr. Sci. (Chem.), Full Professor, Frumkin Institute of Physical Chemistry and Electrochemistry RAS (Moscow, Russian Federation)
Irina Ya. Mittova, Dr. Sci. (Chem.), Full Professor, Voronezh State University, (Voronezh, Russian Federation)
Victor V. Nikonenko, Dr. Sci. (Chem.), Full Professor, Kuban State University (Krasnodar, Russian Federation)
Oleg V. Ovchinnikov, Dr. Sci. (Phys.–Math.), Full Professor, Voronezh State University, (Voronezh, Russian Federation)
Sergey N. Saltykov, Dr. Sci. (Chem.), Associate Professor, Novolipetsk Steel (Lipetsk, Russian Federation)
Vladimir F. Selemenev, Dr. Sci. (Chem.), Full Professor, Voronezh State University, (Voronezh, Russian Federation)
Vladimir A. Terekhov, Dr. Sci. (Phys.–Math.), Full Professor, Voronezh State University, (Voronezh, Russian Federation)
Evgeny A. Tutov, Dr. Sci. (Chem.), Associate Professor, Voronezh State Technical University (Voronezh, Russian Federation)
Pavel P. Fedorov, Dr. Sci. (Chem.), Full Professor, Prokhorov General Physics Institute RAS (Moscow, Russian Federation)
Vitaly A. Khonik, Dr. Sci. (Phys.–Math.), Full Professor, Voronezh State Pedagogical University (Voronezh, Russian Federation)
Vladimir A. Shaposhnik, Dr. Sci. (Chem.), Full Professor, Voronezh State University (Voronezh, Russian Federation)
Andrey B. Yaroslavtsev, Dr. Sci. (Chem.), Full Member of the RAS, Kurnakov Institute of General and Inorganic Chemistry RAS (Moscow, Russian Federation)

INTERNATIONAL MEMBERS OF THE EDITORIAL BOARD:
Mahammad Babanly, Dr. Sci. (Chem.), Associate Member of the ANAS, Institute of Catalysis and Inorganic Chemistry ANAS (Baku, Azerbaijan)
Tiziano Bellezze, Dr. Sci. (Chem.), Marche Polytechnic University (Ancona, Italy)
Mane Rahul Maruti, Ph.D. (Chem.), Shivaji University (Kolhapur, India)
Nguyen Anh Tien, Ph.D. (Chem.), Associate Professor, University of Pedagogy (Ho Chi Minh City, Vietnam)
Vladimir V. Pankov, Dr. Sci. (Chem.), Full Professor, Belarusian State University (Minsk, Belarus)
Fritz Scholz, Dr. Sci., Professor, Institut für Biochemie Analytische Chemie und Umweltchemie (Greifswald, Germany)
Mathias S. Wickleder, Dr. Sci., Professor, University of Cologne (Koln, Germany)
Vladimir Sivakov, Dr. rer. nat., Leibniz Institute of Photonic Technology (Jena, Germany)

EXECUTIVE SECRETARY:
Vera A. Logacheva, Cand. Sci. (Chem.), Voronezh State University, (Voronezh, Russian Federation)

ISSN 1606-867X (Print)
ISSN 2687-0711 (Online)
Конденсированные среды и межфазные границы / Condensed Matter and Interphases. 2023, 25(4)

CONTENTS

Kukushkin S. A.
Special Issue. New materials for micro-, nano-, and optoelectronics: properties, structure, and growth mechanisms 479

Review

Baranov S. A.
Surface energy in microwires. Review 484

Original articles

Zakharov A. Yu., ZakharovM. A.
Relativistic model of interatomic interactions in condensed systems 494

Krasnitckii S. A., Smirnov A. M.
Pair interaction of intersecting dilatation and disclination defects 505

Bessolov V. N., Konenkova E. V., Orlova T. A., Rodin S. N.
Semi-polar GaN(11-22) on nano-structured Si(113): a structure for reducing thermal stresses 514

Gridchin V. O., Reznik R. R., Kotlyar K. P., Kirilenko D. A., Dragunova A. S., Kryzhanovskaya N. V., Cirlin G. E.
Structural and optical properties of composition-graded InGaN nanowires 520

Reznik R. R., Gridchin V. O., Kotlyar K. P., Neplokh V. V., Osipov A. V., Kukushkin S. A., Saket O., Tchernycheva M., Cirlin G. E.
Confirmation of spontaneous doping of GaN nanowires grown on vicinal SiC/Si substrate by electron beam induced current mapping 526

Semenov A. N., Nechaev D. M., Troshkov S. I., Berezina D. S., Abbas A. S., Jmerik V. N.
GaN micro- and nanostructures selectively grown on profiled sapphire substrates using PA-MBE without lithography 532

Butenko P. N., Timashov R. B., Stepanov A. I., Pechnikov A. I., Chikiryaka A. V., Guzilova L. I., Stepanov S. I., Nikolaev
Fabrication of a-Ga_2O_3:Sn/a-Cr_2O_3/a-Al_2O_3 heterostructure by mist CVD and HVPE 542

Kaminskii V. V., Kalganov D. A., Panov D. I., Spiridonov V. A., Ivanov A. Yu., Rozaeva M. V., Bauman D. A., Romanov A. E.
A study of gallium oxide by using the piezoelectric composite oscillator technique at a frequency of 100 kHz 548

Osipov A. V., Sharofidinov Sh. Sh., Kremleva A. V., Smirnov A. M., Osipova E. V., Kandakov A. V., Kukushkin S. A.
Phase transformations during the annealing of Ga_2O_3 films 557

Pronin I. P., Kaptelov E. Yu., Gushchina E. V., Senkevich S. V., Pronin V. P., Ryzhov I. V., Ugolkov V. L., Sergeeva O. N.
Crystallization features and physical properties of the thin-film heterostructure of lead zirconate titanate – lead oxide 564

Staritsyn M. V.
Anomalous electron channeling in PZT thin films 572

Baranov S. A.
Natural ferromagnetic resonance in microwires and its applications. Brief review 581

Manyakin M. D., Kurganskii S. I.
Electronic structure of germanium dioxide with rutile structure according to ab initio computer simulation data 587

Plyusnin N. I.
Solid wetting layer, interphase formation, and thin-film nanomaterials. Brief review 594

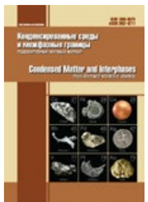

ISSN 1606-867X (Print)
ISSN 2687-0711 (Online)
Condensed Matter and Interphases
Kondensirovannye Sredy i Mezhfaznye Granitsy
https://journals.vsu.ru/kcmf/

Special Issue

New materials for micro-, nano-, and optoelectronics: properties, structure, and growth mechanisms

Sergey A. Kukushkin✉
Website: http://www.ipme.ru/ipme/labs/phase/kukushkin.html

Institute for Problems in Mechanical Engineering of the Russian Academy of Sciences
Bol'shoy Prospekt Vasil'yevskogo Ostrova, Saint Petersburg 199178, Russian Federation

The editorial board of the journal Condensed Matter and Interphases is pleased to present a special issue dedicated to studying the fundamental and applied aspects of the synthesis and properties of new materials used for a wide range of purposes. The issue includes theoretical and review articles, as well as empirical studies that should be interesting for theorists, experimental scientists and technologists.

Currently, the majority of electronic devices are based on silicon. Silicon remains a fundamental material in the electronics industry. However, modern life requires an ever-increasing variety of devices that cannot be produced using only silicon for several reasons. First, silicon, as a semiconductor material, does not exhibit the desired physical properties. Second, it is only suitable for a certain range of devices, for example, silicon has an indirect bandgap, so it cannot be used to produce LEDs, lasers, etc. Moreover, silicon is not resistant to radioactive radiation, therefore, devices based on it cannot operate stably in high-radiation environments, such as outer space and nuclear power plants. In addition, devices produced using silicon cannot operate at high temperatures, and therefore require cooling. Silicon has also several other unavoidable disadvantages.

Modern life and the market require the creation of LEDs, semiconductor lasers, high electron mobility transistors (HEMT), gas control sensors and transmitters, microwave devices, next-generation pyro- and piezo sensors, optical switches, devices that emit and receive terahertz radiation, etc. Nowadays, there is also an urgent need for LEDs that emit hard ultraviolet radiation as well as ultraviolet radiation sensors.

For this reason we are currently focusing on the search for materials that can at least partially replace silicon. Such semiconductor materials include wide bandgap semiconductors: silicon carbide (SiC), gallium nitride (GaN), aluminium nitride (AlN), gallium oxide (Ga_2O_3), their solid solutions, and a number of other materials. These semiconductors have excellent electrical characteristics and can ensure the operation of electronic and optoelectronic devices at elevated temperatures and under high radiation. Semiconductor materials, such as SiC, AlN, GaN, and Ga_2O_3, have wide bandgap. For example, gallium oxide is a new promising wide bandgap semiconductor with a bandgap $E_g \approx 4.9$ eV. This material has several physical properties that make it competitive with silicon carbide and III-nitrides. First of all, it is transparent in the UV spectrum and has a high breakdown voltage (8 MV/cm). In addition, Ga_2O_3 can be doped quite easily, which makes it possible to obtain highly conductive layers of this material. Zinc oxide (ZnO) is also a promising semiconductor owing to its potential use in thin-film transistors, LEDs, lasers, and photodetectors. It is a direct-bandgap semiconductor with a bandgap of 3.4 eV.

✉ Sergey A. Kukushkin, e-mail: sergey.a.kukushkin@gmail.com
© Kukushkin S. A., 2023

The content is available under Creative Commons Attribution 4.0 License.

Ferroelectric materials are also of particular interest to researchers. They are widely used in high-speed elements for static and dynamic memory, microelectromechanical systems (MEMS), infrared technology (IR), microwave electronics, piezoelectronics, and other modern high-tech devices. The main ferroelectric materials used in most chips and devices are solid solutions of lead zirconium titanate $Pb(Ti,Zr)O_3$.

In recent years, progress has been made in research on the growth and application of nanowhiskers of various compounds. Such structures have cross-sectional dimensions of 10-100 nm, and their length exceeds their diameter by an order of magnitude or more. Semiconductor nanowhiskers are promising for applications in microelectronics and optoelectronics, as well as in many other fields, such as cantilevers for probe microscopes, gas analyzers, etc. These nanowhiskers can be used to design field-effect transistors, photovoltaic cells, light-emitting elements, and other functional nanodevices.

Undoubtedly, diamond is one of the most promising materials for electronic devices, as it has a combination of the most important physical parameters. The electron mobility in diamond is about 2200 $cm^2/V·c$, and the breakdown field reaches 107 V/cm. Diamond is chemically stable and insoluble in hydrofluoric, hydrochloric, sulfuric, and nitric acids. Diamond has the highest thermal conductivity of all known materials, about 22 W/cm·K at room temperature. Therefore, diamond can be a "perfect" heat-dissipating dielectric substrate. It is transparent over a wide spectral range (from ultraviolet to radio waves), has high hardness (81–100 GPa), and high sound velocity (18 km/s). Owing to these unique properties, diamond is promising for use as a heat sink in electronic devices. Diamond could also be widely used in the manufacture of high-power gyrotron and laser windows, as well as in the manufacture of various types of surface acoustic wave filters operating in the GHz range, and ionizing radiation detectors.

Graphene is expected to be a serious competitor to silicon for use in electronics in the future. It is most likely that graphene will be used in transistors to replace current metal electrodes, as the contact layer thickness in graphene is only 0.34 nm. However, to date, graphene-based devices are still a distant prospect. Indeed, it is not yet possible to grow graphene wafers of a large size, and it is very difficult to control the conductivity of the graphene layers. In particular, the methods for producing semiconductors from graphene are still underdeveloped. Graphene is primarily used only as a conductor or insulator.

Boron nitride (BN) is another new, little-studied material. Thin, one-atom-thick layers of BN could be used in flexible electronics together with graphene. BN is an insulator with an energy bandgap of about 6 eV, whereas graphene exhibits metalloid properties. However, research on this material is still in its infancy.

For spintronic applications, various composite structures based on semiconductor and magnetic materials are of interest.

The issue includes fifteen articles focusing on the main development areas of modern materials science. Presented below is a brief overview of these articles.

The first article in this issue [1] reviews the theoretical approaches to the calculation of interfacial and surface energies of nanoparticles of various geometries depending on the particle size. It is well-known that the kinetics of the formation of nanoparticles largely depends on their interfacial energies. This is especially evident in nanoparticles, the radii of which are in the single digits of nanometers. The article [1] focuses on this problem.

Of particular interest is also the second article [2]. It presents a new unusual approach to the description of the structures of solids and their properties. The authors suggest a new approach to the foundation of thermodynamics and statistical mechanics. They argue that classical statistical mechanics does not take into account the finiteness of the speed of interaction between particles (atoms, molecules, etc.), i.e. classical statistical mechanics is essentially a non-relativistic theory. The authors of the article [2] suggest a new theory of interaction between particle ensembles and fields based on a relativistic approach. With non-relativistic approximation, interactions between atoms are instantaneous. Therefore, an atom and the instantaneous field created by it are a single entity with a finite number of degrees of freedom. With relativistic theory, every motion of an atom

(the source of the field) leads to the evolution of its field, the propagation velocity of which does not exceed the speed of light. Therefore, the evolution of the system of interacting atoms includes both the dynamics of particles and the dynamics of the relativistic field created by the atoms.

The next article [3] studies the elastic interaction between overlap defects of dilatation and disclination types in the approximation of the linear isotropic medium. The authors calculated the dependence of the interaction energies of such defects on the angle between them. This article is of interest for researchers focusing on the synthesis of new materials due to the fact that a combination of defects, in particular point defects, can both increase and decrease the elastic energy in nanomaterials.

The rest of the articles in the issue present the results of experimental studies. They can be divided into three groups. Articles in the first group [4-7] consider the growth of thin films and nanostructures based on gallium nitride compounds. Article [4] reports the growth of semi-polar GaN (11-22) layers using epitaxy from metal organic compounds on a nanostructured NP-Si (113) substrate. Optoelectronics devices are currently produced based on gallium nitride structures grown in a direction parallel to the c-axis of a hexagonal GaN crystal (polar structures). However, the use of polar structures for the creation of quantum size (QW) III-nitride based optoelectronic devices result in the Stark effect. It is caused by strong piezoelectric polarization in polar structures. The fact that there is no piezoelectric polarization in semi-polar structures presents new opportunities for the creation of new generation devices based on semi-polar (Al, Ga, In)N structures. This explains the significance of the study presented in the article. Articles [5, 6] focus on the growth of filamentary nanostructures InGaN and GaN. Article [5] demonstrates for the first time that composition-graded $In_xGa_{1-x}N$ nanowires with x from 40 to 60% can be grown using plasma-assisted molecular beam epitaxy. The authors determined that the samples demonstrate photoluminescence properties at room temperature with a maximum at about 890 nm. This means that the material can be used to create sources of near IR radiation. Article [6] is devoted to the confirmation of spontaneous doping of GaN nanowires grown on vicinal SiC/Si hybrid substrates. Singular Si facets did not demonstrate the same effect. Article [7] presents a detailed experimental analysis of the formation and growth of ordered arrays of nanocolumns of GaN microcrystals by means of plasma-assisted molecular beam epitaxy on profiled sapphire substrates. The authors demonstrated that there is a significant difference between the growth mechanisms of nanocolumns of GaN microcrystals under nitrogen enriched conditions and metal (Ga) enriched conditions. The article presents a detailed analysis of the processes which determine the kinetics of the growth of III-N nanocolumns by means of plasma-assisted molecular beam epitaxy on profiled sapphire substrates.

The next three articles [8–10] are dedicated to the growth of single crystals and films of a semiconductor compound Ga_2O_3. Gallium oxide is a wide bandgap semiconductor with a bandgap of $Eg \approx 4.9$ eV. This material has a number of physical properties which make it quite competitive with III-nitrides. First of all, it is transparent in the UV spectrum and has a high breakdown voltage (8 MV/cm). The articles included in the issue demonstrate that the area is of current importance and is actively developing. Thus, article [8] demonstrates the possibility to produce the heterostructure based on Ga_2O_3. Article [9] presents the results of the study of the mechanical properties and defect structure of single crystals of the Ga_2O_3, β-phase grown from a melt using the Stepanov technique. Article [10] presents a new technique for obtaining the three main crystalline phases of Ga_2O_3, namely the α-phase, the ε-phase, and the β-phase by means of chloride-hydride epitaxy. The experimental study described in the article determined the conditions for phase transformations from one Ga_2O_3 polytype to another.

It is well-known that ferroelectric materials are of great importance for modern technologies. Thus, thin films of lead zirconate titanate ($Pb(Zr,Ti)O_3$ or PZT), the composition of which corresponds to the morphotropic phase boundary region, are characterized by abnormally high electromechanical and piezoelectric coefficients

and are currently the most common materials used in microelectronics, electro-optics, and microelectromechanics (MEMS). PZT films are used in IR detectors and microwave electronics, as well as static and dynamic memory elements. The issue of the journal includes two articles which focus on the crystallization features of the thin-film heterostructure PZT-PbO_{1+x} [11, 12]. Article [11] shows that the annealing of amorphous PZT films and crystallization of the intermediate pyrochlore phase are accompanied by additional oxidation of the structure resulting in the formation of lead orthoplumbate and lead dioxide, which results in the formation of the perovskite phase. Article [12] describes a new phenomenon occurring in thin PZT films, anomalous electron channeling. This means that the electrons from a scanning electron microscope can penetrate along the planes of the crystal. The phenomenon is explained by the structural features of the crystallographic structure of PZT films.

Out of the last three articles in the issue [13–15] two articles are brief reviews [13, 15]. Article [13] reviews the use of cast glass-coated amorphous micro- and nanowires for the reinforcement of glass aimed at enhancing its mechanical strength. The article presents approaches to the creation of protection screens that can resist mechanical load as well as electromagnetic pulses of various nature. The article proposes ideas related to the technology of production of cast glass-coated amorphous micro- and nanowires.

Article [14] presents a theoretical study of the electronic structure of the tetragonal crystalline modification of germanium dioxide by means of a linearized augmented plane wave method. Germanium dioxide is a wide bandgap semiconductor used in optoelectronics, solar energy, and catalysis. Normally, germanium dioxide exists in two stable crystalline modifications: a hexagonal (quartz structure) and a tetragonal (rutile structure). The results obtained in [14] can be used to analyze experimentally studied specimens of the Ge–O system.

The last article [15] reviews several issues related to the growth of transition metal silicides on a silicon substrate. The review presents a classification of solid phases of metal silicides formed on a silicon substrate. Particular attention is paid to the formation of wetting layers stabilized by a Si substrate. Some of their optical, electrical, and magnetic properties are described. The article points out that wetting layers play an important role in the formation of bulk phases, epitaxial nanofilms, and multilayer nanostructures.

A brief review of the articles demonstrates that the current issue of the journal covers practically all the main areas of modern semiconductor materials studies.

The editorial board is grateful to the authors for the submitted articles and their eagerness to share their latest advances in the field with the scientific community.

References

1. Baranov S. A. Surface energy in microwires. Review. *Condensed Matter and Interphases*. 2023;25(4): 484–493. https://doi.org/10.17308/kcmf.2023.25/11470

2. Zakharov A. Yu., Zakharov M. A. Relativistic model of interatomic interactions in condensed systems. *Condensed Matter and Interphases*. 2023;25(4): 494–504. https://doi.org/10.17308/kcmf.2023.25/11480

3. Krasnitckii S. A., Smirnov A. M. Pair interaction of intersecting dilatation and disclination defects. *Condensed Matter and Interphases*. 2023;25(4): 505–513. https://doi.org/10.17308/kcmf.2023.25/11473

4. Bessolov V. N., Konenkova E. V., Orlova T. A., Rodin S. N. Semi-polar GaN(11-22) on nanostructured Si(113): structure for reducing thermal stresses. *Condensed Matter and Interphases*. 2023;25(1): 514–519. https://doi.org/10.17308/kcmf.2023.25/11477

5. Gridchin V. O., Reznik R. R., Kotlyar K. P., Kirilenko D. A., Dragunova A. S., Kryzhanoskaya N. V., Cirlin G. E. Structural and optical properties of composition-graded InGaN nanowires. *Condensed Matter and Interphases*. 20223;25(4): 520–525. https://doi.org10.17308/kcmf.2023.25/11475

6. Reznik R. R., Gridchin V. O., Kotlyar K. P., Neploh V. V., Osipov A. V., Kukushkin S. A., Saket O., Tchernycheva M., Cirlin G. E. Confirmation of spontaneous doping of GaN nanowires grown on vicinal SiC/Si substrate by electron beam induced current mapping. *Condensed Matter and Interphases*. 20223;25(4): 526–531. https://doi.org/10.17308/kcmf.2023.25/11474

7. Semenov A. N., Nechaev D. M., Troshkov S. I, Berezina D. S., Abbas A. S., Jmerik V. N. Micro- and nanostructures of GaN selectively grown on patterned sapphire substrates by PA-MBE without lithography techniques. *Condensed Matter and Interphases*. 2023;25(4): 532–541. https://doi.org/10.17308/kcmf.2023.25/11482

8. Butenko P. N., Timashov R. B., Stepanov A. I., Pechnikov A. I., Chikiryaka A. V., Guzilova L. I., Stepanov S. I., Nikolaev V. I. Fabrication of α-Ga_2O_3:Sn/α-Cr_2O_3/α-Al_2O_3 heterostructure by mist CVD and HVPE. *Condensed Matter and Interphases*. 2023;25(4): 542–547 https://doi.org/10.17308/kcmf.2023.25/11476

9. Kaminskii V. V., Kalganov D. A., Panov D. I., Spiridonov V. A., Ivanov A. I., Rozaeva M. V., Bauman D. A., Romanov A. E. A study of gallium oxide by using the piezoelectric composite oscillator technique at a frequency of 100 kHz. *Condensed Matter and Interphases*. 20223;25(1): 548–556. https://doi.org/10.17308/kcmf.2023.25/11484

10. Osipov A. V., Sharofidinov Sh. Sh., Kremleva A. V., Smirnov A. M., Osipova E. V., Kandakov A. V., Kukushkin S. A. Phase transformations during the annealing of Ga_2O_3 films. *Condensed Matter and Interphases*. 20223;25(4): 557–563. https://doi.org/10.17308/kcmf.2023.25/11479

11. Pronin I. P., Kaptelov E. Yu., Gushchina E. V., Senkevich S. V., Pronin V. P., Pyzhov I. V., Ugolkov V. L., Sergeeva O. N. Crystallization features and physical properties of the thin-film heterostructure of lead zirconate titanate – lead oxide. *Condensed Matter and Interphases*. 2023;25(4): 564–571. https://doi.org/10.17308/kcmf.2023.25/11483

12. Staritsyn M. V. Anomalous electron channeling in thin films of PZT. *Condensed Matter and Interphases*. 2023;25(1): 572–580. https://doi.org/10.17308/kcmf.2023.25/11481

13. Baranov S. A. Natural ferromagnetic resonance in microwire and its application. Brief review. *Condensed Matter and Interphases*. 2023;25(4): 581–586. https://doi.org/10.17308/kcmf.2023.25/11472

14. Manyakin M. D., Kurganskii S. I. Electronic structure of germanium dioxide with rutile structure according to ab initio computer simulation data. *Condensed Matter and Interphases*. 2023;25(4): 587–593. https://doi.org/10.17308/kcmf.2023.25/11478

15. Plyusnin N. I. Solid wetting layer, interphase formation, and thin-film nanomaterials. Brief review. *Condensed Matter and Interphases*. 2023;25(4): 594–604. https://doi.org/10.17308/kcmf.2023.25/11471

Information about the authors

Sergey A. Kukushkin, Dr. Sci. (Phys.–Math.), Professor, Head of the Laboratory of Structural and Phase Transitions in Condensed Matter, Chief Researcher, Institute for Problems in Mechanical Engineering of the Russian Academy of Sciences (IPME RAS) (Saint-Petersburg, Russian Federation).

https://orcid.org/0000-0002-2973-8645

sergey.a.kukushkin@gmail.com

Translated by Yulia Dymant

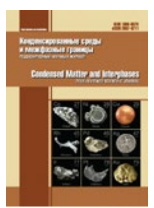

ISSN 1606-867X (Print)
ISSN 2687-0711 (Online)

Condensed Matter and Interphases
Kondensirovannye Sredy i Mezhfaznye Granitsy
https://journals.vsu.ru/kcmf/

Review

Review article
https://doi.org/10.17308/kcmf.2023.25/11470

Surface energy in microwires. Review

S. A. Baranov[1,2]✉

[1]*Moldova State University, Institute of Applied Physics,*
5 Academiei st., Chisinau MD-2028, Republic of Moldova

[2]*Shevchenko Pridnestrov'e State University,*
128 25- Oktyabrya st., Tiraspol 33000, Pridnestrov'e, Republic of Moldova

Abstract

The research involves using an analytical solution of the Gibbs–Tolman–Koenig–Buff equation to calculate the microwire surface tension. The classical theory of nucleation and the statistical theory of density were used to determine dependencies for the surface energy of a cylindrical particle. It was shown that within the linear theory, both approaches produce similar results. However, within the nonlinear theory, the results may differ. The article presents an analysis of the analytical solutions of equations for a cylindrical surface within the van der Waals linear and nonlinear theories.

Keywords: Gibbs–Tolman–Koenig–Buff theory, Tolman length, Van der Waals theory, Surface energy, Cylindrical surface

Funding: The study was supported by the Moldovan National Project and the project of Shevchenko Transnistria State University.

For citation: Baranov S. A. Surface energy in microwires. Review. *Condensed Matter and Interphases*. 2023;25(4): 484–493. https://doi.org/10.17308/kcmf.2023.25/11470

Для цитирования: Баранов С. А. Поверхностная энергия в микропроводах. Обзор. *Конденсированные среды и межфазные границы*. 2023;25(4): 484–493. https://doi.org/10.17308/kcmf.2023.25/11470

✉ Serghei A. Baranov, e-mail: sabaranov07@mail.ru
© Baranov S. A., 2023

The content is available under Creative Commons Attribution 4.0 License.

1. Introduction

The study of the nanoscale effects of solid nanoparticles is extremely important due to the rapid development of nanotechnologies [1–3]. A number of monographs [1–9] (not limited to these papers) have been dedicated to problems associated with the description of surface effects. However, these issues are extremely complex and have not yet been completely solved even for the simplest of models. Therefore, it appears to be interesting to consider some of the problems if only for simple geometric surfaces, for example, for a cylindrical surface [11–16].

Elongated nanoparticles (this pare discusses solid nanoparticles), which can be nanowires or nanowhiskers (hereinafter NWs), are often used in micro- and nanoelectronics. Such materials often have unique electrical, magnetic, optical, and other properties, which makes it possible to use NWs in modern devices (see, for example, [1–3] and the literature cited therein).

Obtaining NWs is technologically challenging. However, this task can be facilitated by using appropriate theoretical models which enable the most basic mathematical modeling of technological processes. The scope of this article does not include a detailed discussion of the technological challenges associated with obtaining filamentary nanoobjects. However, it is worth mentioning that at present they can be produced using a wide range of materials. For example, the list of technologies that we provide below can be easily expanded. For instance, the following technologies are used to grow NWs: gas-phase epitaxy, chemical and electrochemical deposition, molecular beam epitaxy, magnetron deposition method, laser ablation, etc. Recently, nanowires have also been produced by the Taylor–Ulitovsky method (see, for example, [3]). Among the most suitable methods of theoretical modeling which allow understanding the kinetics and details of NWs growth are various types of dynamic modeling. Modeling does not only allow obtaining information about the kinetics of the process, but also allows calculating the morphology of the growth surface. It also allows taking into account the spatio-temporal fluctuations that are significant for the kinetics of the studied process. We are not going to discuss the results of these studies in detail; however, we would like to note that these results tend to be contradictory and differ depending on the group of researchers. In addition, they are not well-founded for large systems and the real calculations are always limited by the upper limit to the number of particles in the system associated with a reasonable counting time. This is the main source of contradictions in the modeling results. To be more precise, for example, some authors get negative values for the limit value of the Tolman parameter, while others predict positive values for the same parameter within similar systems. Therefore, it is undoubtedly of interest to somehow systematize the previously obtained (more verified) results substantiated within the framework of the general approaches of thermodynamics and the simplest models of statistical physics (see, for example, [1, 2]). The content of these results, as will be shown below, allows establishing some general regularities, which can become the starting point for any model calculations.

Therefore, the purpose of this work is to combine the most general results describing nanonucleation and its main thermodynamic parameters, for example, surface energy and its corresponding surface tension, etc., with general thermodynamic results if only for the simplest case of NW. To achieve this goal, we conducted a detailed analysis of the results which we had obtained earlier, defined the main tasks to be performed as a result of this analysis, and presented a number of new results.

2. Thermodynamic approach to a cylindrical particle

We considered an isolated system consisting of two three-dimensional phases with different densities and interfaces between them. In this section, we use the results of the monograph [9].

The initial equation is the Gibbs adsorption equation.

$$d\sigma = -\Gamma d\mu , \tag{1}$$

where Γ is adsorption and μ is chemical potential. To build a thermodynamic model, equation (1) is extended as follows:

$$d\sigma = -\frac{\Gamma}{\Delta\rho} d(\Delta p) = -\delta\left(2 + \frac{\delta}{R}\right) d(\Delta p),$$
$$\mu = \frac{\Delta p}{\Delta\rho},\ \Gamma = \frac{\Delta V}{\omega}\Delta\rho, \tag{2}$$

where $\Delta\rho$ is the difference in the densities of the coexisting phases, δ is the thickness of the transition layer (Tolman length), and ΔV is the volume of the interfacial transition layer with a thickness of δ.

The combination of the formulas produces the following differential equation:

$$\frac{d\ln\sigma}{d\ln R} = \frac{\frac{2\delta}{R} + \left(\frac{\delta}{R}\right)^2}{2 + \frac{2\delta}{R} + \left(\frac{\delta}{R}\right)^2}. \tag{3}$$

Equation (3) is analogous to the well-known Gibbs–Tolman–Koenig–Buff equation (see [3–9]) for a cylindrical surface.

To solve equation (3), the dimensionless variable R/δ is introduced. As a result,

$$\ln\frac{\sigma}{\sigma^{(\infty)}} = -\int_{R/\delta}^{\infty}\left(\frac{2x+1}{2x^3 + 2x^2 + x}\right)dx. \tag{4}$$

The integral in (4) is found by integrating rational functions (i.e. by expanding the integral function into partial fractions [9]). The final result can be represented as [9] (see Fig. 1):

$$\sigma = \frac{\sigma^{(\infty)} R}{\delta}\sqrt{\frac{2}{2\left(\frac{R}{\delta}\right)^2 + 2\frac{R}{\delta} + 1}}\exp\left(-\mathrm{arctg}\left(\frac{1}{1 + 2\frac{R}{\delta}}\right)\right). \tag{5}$$

When $R \gg \delta$, (5) is transformed into a well-known analogue of the Tolman formula:

$$\sigma = \frac{\sigma^{(\infty)}}{1 + \frac{\delta}{R}}, \tag{6}$$

where Tolman parameter δ must have the same sign with the radius of curvature R of the surface (i.e. $\delta > 0$).

The monograph [9] (assuming that Eulerian curvature is small) offers a more general formula for the surface tension of an arbitrarily curved surface as a function of the two main radii of curvature.

When $R \ll \delta$:

$$\sigma / \sigma^{(\infty)} \sim 0.645(R/\delta)$$

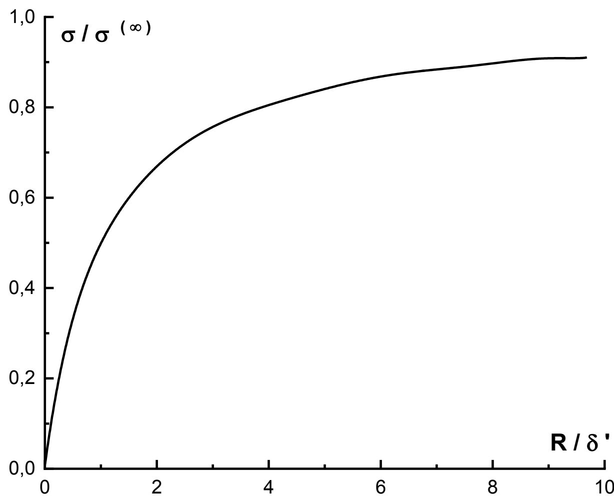

Fig. 1. Functions graphs of solution (5) (see [9])

from (5) follows Rusanov's formula [6, 9] for a cylindrical particle.

3. Linear Theory

First, we will consider the linear theory proposed in [9], which will help us when choosing the van der Waals equation. As the resulting function, we accept the value proportional to the volume density of the fragments of the $n(x)$ particles which the cylindrical particle consists of. This allows obtaining in the linear approximation a simple equation, which, importantly, can be solved analytically [9]:

$$n'' + \frac{n'}{r} - \frac{1}{\delta^2}(n-1) = 0, \tag{7}$$

where r is the coordinate of the radius of the nanocylinder. In our equation, the value of the volume density of the particles $n(0)$ in the center per unit was pre-normalized, which is not important but will be very convenient for our purposes later on.

The function $n(x)$ (the dimensionless variable: $x = r/\delta$ is introduced) is proportional to the volume density function, which we designate as $N(x)$ (see below).

A particular physical solution (7) is used, which has the form of [9]:

$$n(x) = cK_0(x), \tag{8}$$

where $K_0(x)$ is a modified Bessel function.

Now, we find the real physical quantity called the normalized function of the volume density of

particles $N(r/\delta)$. For it, the boundary conditions can be described as:

$$\begin{aligned} &N(r/\delta) \to n(0) \equiv n(R) = 1, \\ &N(+\infty) \to n(+\infty) = 0. \end{aligned} \quad (9)$$

Using solution (8) and conditions (9), we get:

$$N(r/\delta) = \begin{cases} 1, \; r \le R, \\ \dfrac{K_0(r/\delta)}{K_0(R/\delta)}, \; r > R, \end{cases} \quad (10)$$

which is shown schematically in Fig. 2.

Using (10) in [9], we derive the equation:

$$\frac{d\ln\sigma}{d\ln x} = \frac{1}{x\{K_0(x)/K_1(x_0)\}+1}. \quad (11)$$

If $x >> 1$:

$$\frac{K_0(x)}{K_1(x_0)} \to 1,$$

As a result,

$$\frac{d\ln\sigma}{d\ln x} = \frac{1}{x+1},$$

where follows the Tolman formula (6).

When $x << 1$:

$$\frac{K_0(x)}{K_1(x)} \approx x\ln\frac{2}{\gamma x},$$

where $\gamma = 1.781$, and

$$\frac{d\ln\sigma}{d\ln x} = \frac{1}{x\ln\frac{2}{\gamma x}+1}.$$

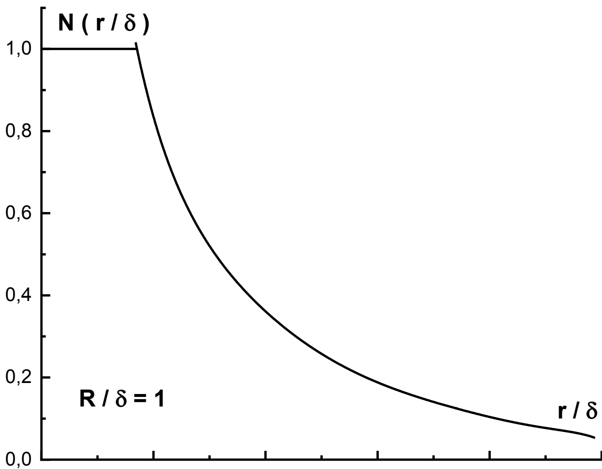

Fig. 2. Volume density function, $N(r/\delta)$ (10)

As follows from the graph (Fig. 2), it can be assumed that the emerging nanocylinder reaches thermodynamically equilibrium dimensions $R \sim \delta$ (with a relative volume density of its constituent fragments equal to one). This equilibrium dimension $\sim \delta$ in the Cahn–Hilliard–Hillert theory was defined in [7, 10–15]. Around the equilibrium dimension $R \sim \delta$, there is an "atmosphere" of the volume density of the nanoparticle components (or discharged nanoparticle fragments), $N(r/\delta)$, which asymptotically approaches zero only within the $r/\delta \to \infty$ limit, since in this case the forces are not short-range.

This modeling result physically meant that the equilibrium nanocylinder (solid phase) was surrounded by an infinite "atmosphere" of its fragments. Therefore, the thermodynamic growth of cylindrical nanoparticles beyond their equilibrium dimensions in the presented approximation is not limited. This result is in line with the classical theory of nucleation (CTN).

The section above showed that to describe the dependence of surface tension on the Tolman parameter δ, a differential equation was used, which was the Gibbs-Tolman-Koenig-Buff equation (GTKB). It is obvious that the linear theory presented here based on the linear dependence of the density on the coordinate (equation (7)), is in line with the GTKB theory [9] and, accordingly, with the classical theory of nucleation.

4. Nonlinear theory

Let us move on to the nonlinear analogue of the differential equation (7). Let us introduce an interaction space D relevant for nanonucleation (correlation radius).

Since we do not know the differential equation, we have the right to propose a simplest model that within the boundaries coincides with the model used for the linear theory (a correspondence between the linear theory and CTN).

Then, based on the previous equation (7), the nonlinear equation could be modeled as follows:

$$n_1'' + \frac{1}{r}n_1' + \frac{1}{\delta_1^2}\exp\{-n_1\} = 0, \quad (12)$$

where $n_1(r)$ is a function similar to the function $n(r)$ but for a nonlinear equation.

Choosing the function in the form of $\frac{1}{\delta_1^2}\exp\{-n_1\}$ is undoubtedly an arbitrary decision when modeling an unknown functional. However, if we expand the exponent $\frac{1}{\delta_1^2}\exp\{-n_1\}$, we can obtain equation (7).

On the other hand, in our opinion, the function $\frac{1}{\delta_1^2}\exp\{-n_1\}$ models the short-range force of the interaction between fragments which occurs in the model of N-dimensional fractal cluster [12].

The physical solution (taking into account the normalization) is presented as:

$$n_1 = 2\ln[1 - X_1^2], \tag{13}$$

where (see below):

$$X_1 = r/(2\sqrt{2}\delta_1). \tag{14}$$

It should be noted that we chose a solution that satisfied the following conditions:

$$n_1(0) = n_1'(0) = 0$$

A correspondence between the radius D and the Tolman parameter δ_1 is introduced through the normalization integral:

$$\int_0^\infty \frac{2\pi r dr}{1 + (r^2)/(8\delta_1^2)} = 8\pi\delta_1^2 = \pi D^2, \tag{15}$$

from which it was derived that

$$D = 2\sqrt{2}\delta_1. \tag{16}$$

This means that the radius D and the Tolman length are related by the relation (16) presented here. The coupling coefficient for these values is of a model character, however, we can state that by an order of magnitude $D \sim \delta_1$.

As a result, the function of the volume density of particles can be represented as:

$$N = 1 + 2\ln[1 - X_1^2]. \tag{17}$$

It should be noted that there is no analytical correspondence between solutions (10) and (17). As evidence, we provide a graph for solution (17), which is shown in Fig. 3.

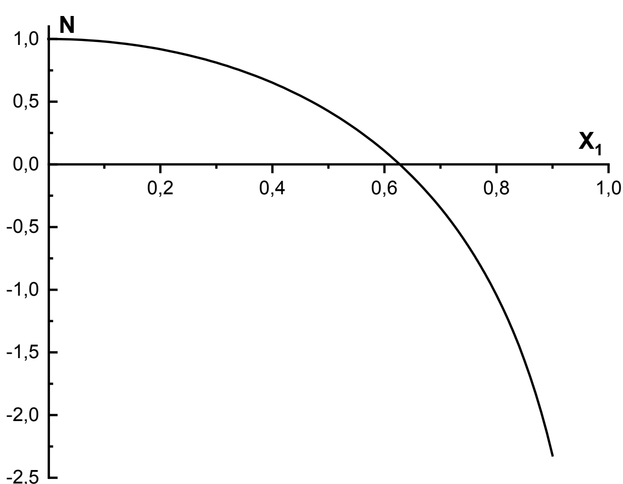

Fig. 3. Plot of function (17) obtained from solution of Eq. (13). Only the solution for N, when this function is greater or equal to zero, has a physical sense

The difference between solutions of the linear and nonlinear equations (Fig. 2 and 3) is fundamental. In the first case, as we have already noted, the thermodynamic growth of cylindrical nanoparticles beyond their equilibrium dimensions ($R \sim \delta$) is not limited. This result is in line with the classical theory of nucleation (CTN). In the case of the nonlinear equation (equation (12)), the growth of the nucleus is ultimately limited, which will be discussed below.

5. Surface energy for nanowires

If the droplet sizes are comparable with the Tolman length, there is a problem associated with an additive calculation of surface energy from the volume part of the energy. It is possible that in some cases negative Tolman lengths are due to inappropriate approaches used to solve this problem.

An alternative method is to use the model density profile in the van der Waals theory (see, for example, [16]). This theory was also proposed in a generalized form by L. D. Landau to describe phase transitions. It should be noted that all these theories became the theoretical foundation for a series of works by Cahn and Hilliard. Below we use a version of the theory similar to the theory of V. L. Ginzburg, L. D. Landau, and A. A. Abrikosov.

We consider a particular case of applying these theories, when the nucleus of the condensed phase is shaped as a long cylinder. We used a cylindrical coordinate system, for which the characteristic spin function [16] is represented by the angle function $\theta(\rho)$ relative to the cylinder axis z. The physical interpretation of the spin

function differs from the interpretation of the concentration density, but in the style of the Landau's theory it can be assumed that these quantities are both order parameters. In our case, this order parameter characterizes the energy state (of the atom) in the nanoparticle as a function of the radius of the base of the cylinder. The free energy in this model can have the following form [16]:

$$H_{g,c} = \frac{A}{2}\left[\theta'^2 + \frac{\sin^2\theta}{r^2}\right], \tag{18}$$

where $\theta(r)$ is the angle between the cylinder axis and the magnetization vector and r is the radial coordinate. Thus, unlike the previous three-dimensional problem, this time we considered a two-dimensional problem. The solution of the three-dimensional problem is reduced to numerical methods and this problem will be dealt with in another paper.

The model kinetic energy in (18) is a classical analogue of the exchange energy in the Heisenberg model for the two-dimensional space in a continuous approximation, which corresponds in our case to the infinite cylinder model. It can be assumed that the kinetic energy in (18) coincides in form with the kinetic energy of a quasiparticle (in cylindrical coordinates). This fact is not accidental and is due to the fact that the studied model allows accurate analytical solutions in the form of quasiparticles, nonlinear waves known as instantons (or skyrmions [16]). It should also be noted that in our case these quasiparticles are topological compositions rather than dynamic particles. Therefore, in our case the virtual kinetic energy of the topological instanton is meant by the kinetic energy.

The theory considered below is scale invariant, which allows us to introduce a relative coordinate:

$$\rho = \frac{r}{R_c}, \tag{19}$$

where R_c is the equilibrium radius of the droplet. Now, let us consider the topological space as the initial droplet. Then, there is a condition of $0 \leqslant \rho \leqslant 1$. The proposed continuum model of energy (18) appears to be a Heisenberg model in which the interacting spins act as energy states of the particles associated with the constant exchange interaction A (with the dimension for the exchange energy [J/m]).

Using (18), it is simple to derive the Euler-Lagrange equation:

$$\theta''(\rho) + \frac{\theta'(\rho)}{\rho} - \frac{\sin\theta\cos\theta}{\rho^2} = 0. \tag{20}$$

For simplicity, it is sufficient to only use a particular solution of this equation describing the nucleation process under simple boundary conditions:

$$\theta(\rho) = \begin{cases} \pi, \ \rho = 0, \\ \dfrac{\pi}{2}, \ \rho = 1. \end{cases} \tag{21}$$

The solutions of equations (20) and (21) look simple:

$$\tan\left(\frac{\theta}{2}\right) = \frac{1}{\rho}, \tag{22}$$

which is convenient for further analysis.

Let us introduce the model surface energy to obtain the Euler-Lagrange equations for the scale invariant theory:

$$\theta_a''(\rho) + \frac{\theta_a'(\rho)}{\rho} - \frac{a^2\sin\theta_a\cos\theta_a}{\rho^2} = 0, \tag{23}$$

where a^2 is the ratio of anisotropy energy to exchange interaction constant A. Parameter a^2 was determined in [16]:

$$a^2 = \frac{B}{A} + 1, \tag{24}$$

The definition of the anisotropy function was also given there:

$$\frac{B\sin^2\theta_a}{2\rho^2}, \tag{25}$$

where B is a positive energy quantity, the dimension of which coincides with A.

For agreement with the previous solution, we assume that there is no anisotropy in (23) when $B = 0$, and when $B > 0$, it is present. The solution of equation (8) is as follows:

$$\tan\left(\frac{\theta_a}{2}\right) = \frac{1}{\rho^a}. \tag{26}$$

It should be noted that solutions (22) and (26) join analytically, therefore, the indices are further

omitted. Let us consider one general solution (26). This solution is shown schematically in Fig. 4.

It is easy to show that the function θ(ρ) when $a = 1$ and $0 < \rho \leqslant 1$ has no inflection point. This point only appears when $a > 1$. This means that the surface layer in our model can only exist at $a > 1$. In this case, a certain volume whose energy is the surface energy of the cylindrical particle can be chosen as the surface layer. For definiteness, let us suppose, for example, that the surface layer begins to clearly manifest itself when $a > 4$. Thus, we assume that at $a = 1$, there is no anisotropy in the system, and the Tolman length actually coincides with the droplet size. If $a \gg 1$, within the proposed model, the specific anisotropy exceeds the exchange interaction, and in relation to the droplet there appears a parameter (Tolman length) that characterizes the dimension of the interfacial region. The case of $a < 1$ corresponds to the negative surface energy (in Fig. 4 this case is shown for $a = 0.5$) and is not considered in detail in this article since it is associated with the instability of the condensed phase.

The change in the free energy from the center of the particle to its surface can be estimated. This estimation allows the physical interpretation of the introduced model parameters and their comparison with the conventional energy characteristics that are used to describe the nucleation process.

Let us first consider the layer-by-layer change in the free energy of a cylindrical droplet. We will use again the formula for the energy that we used to derive the equation of motion. It is as follows: $E(\rho) = T + U$. Considering solution (26), we find that the kinetic energy is equal to the potential energy: $T = U$. This important result for the closed dynamic system is associated with the virial theorem for the finite motion, and in our case can be used to check if our approach to problem solution was correct. For total energy, we have:

$$E(\rho) = T + U = 4A\left(\frac{a}{\rho}\right)^2 \frac{\rho^{2a}}{(1+\rho^{2a})^2}. \qquad (27)$$

It follows from (27) that for $a = 1$ and $\rho \to 1$, the equality $E(\rho) = A$ is satisfied. When $B > 0$, the cylinder surface energy tends to $Aa^2 \sim B$ and the higher the B value, the higher the limit. Therefore, just this parameter B can be associated with the parameter of specific thermodynamic surface

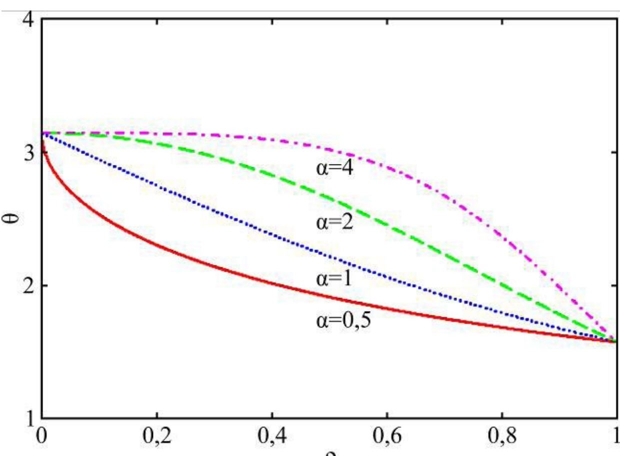

Fig. 4. Diagrams of solution (26) at different values of parameter *a*

energy used in thermodynamic theories provided that these energies have different dimensions.

A sharp increase in free energy (see Fig. 5) depending on parameter a is associated with the phase transition that occurs in the system in the event of an infinitesimal anisotropy. To find the total energy of the particle assigned to the cylinder length unit, it is necessary to take the integral of $E(\rho)$ over the cylinder volume. Let us start with a qualitative analysis of the model. It should be noted that for the particular case of $a = 1$ and $B = 0$, this integral must be equal to A (up to factor). Then, there is no other energy in the system; A is the only internal model energy

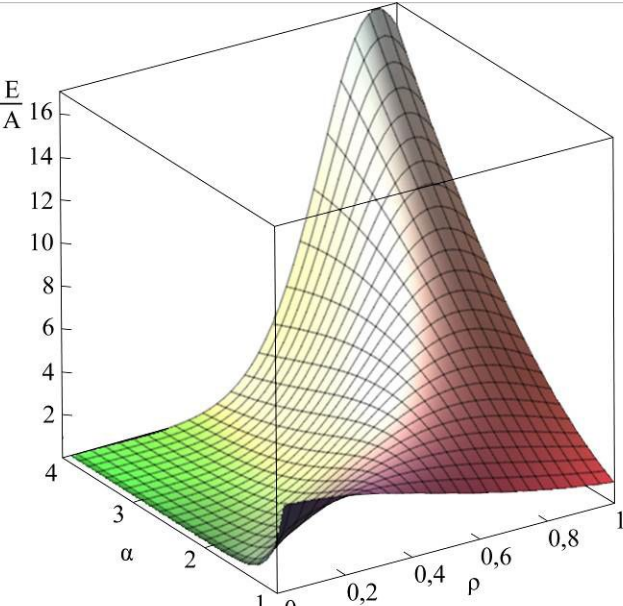

Fig. 5. Three-dimensional dependence of energy on parameters *a* and ρ

of the system. In another limiting case, a high value of a is sufficient for the total energy to tend to anisotropy energy B. In the general case, the total specific energy (for the cylinder length unit) will be as follows:

$$W = 2\pi\int_0^1 E(\rho)\rho d\rho = 8\pi a^2 A\int_0^1 \frac{\rho^{2a-1}d\rho}{(1+\rho^{2a})^2} = 2\pi aA. \quad (28)$$

According to the Cahn–Hilliard theory, the energy of the activation barrier is proportional to the geometric average of two energy parameters: $E_c \sim \sqrt{AB}$. Unlike the proposed theory, the Cahn–Hilliard theory is not scale invariant, and the quantity of B has a dimension of J/m^3. In our case, the integral formula derived from (28) for the activation energy has the same form, which indicates that these theories coincide when calculating the average activation energy (in the volume unit). Therefore, it can be concluded that the proposed theory qualitatively coincides with the Cahn–Hilliard theory.

6. Conclusions

A decrease in the size of the condensed phase leads to an increase in the relative proportion of surface atoms. As a result, the influence of the interfaces increases. What is more, the size dependence of the surface tension is due to the Tolman length, i.e. the thickness of the interfacial (transition) layer. This is especially evident in nanoparticles, the radius of which is ones to tens of nanometers.

The final section of the article provided the results related to the van der Waals gradient theory, which can be summarized as follows. If only one form of energy is present during the formation of a nanoparticle, which acts as exchange interaction A, it is not correct to separate additive energies of the system into the surface energy and the energy of the nanoparticle volume within the framework of the proposed model. However, in this case, it would be possible to introduce the average energy of the entire nanoparticle and to derive Rusanov's linear formula for surface energy based on geometric considerations. Typically, Rusanov's formula is assumed to be universally applicable. This fact is not confirmed when our model is complicated by anisotropy energy.

The concept of anisotropy energy, which is introduced into the theory in the form of the proposed model as a modified Rapini potential, leads to the emergence of surface energy. It should be noted that the conventional Rapini potential has no multiplier of the form of $1/\rho^2$ [16]. The anisotropy energy can become the energy of a double electric layer (in electrochemistry). However, in the case of the formation of extremely small equilibrium particles with differentiated surface energy, the electric capacity of the nanosystem where this nanoparticle is formed should be increased. Thus, it can be assumed that the nanonucleation process can be efficiently controlled.

The main result of all parts of the work can be considered obtaining a profile of surface energy from the thermodynamic parameters of the system, which allows expanding to a certain extent the understanding of capillary phenomena in nanosystems.

The question of the Tolman length, which determines the dimensional effect of the surface tension and the scope of the theory, requires separate consideration. According to the thermodynamic definition, the Tolmen length is numerically equal to the distance between the equimolecular surface and the tension surface [4, 5]:

$$\delta = z_e - z_s, \quad (29)$$

where z_e and z_s are the positions of the equimolecular surface and the tension surface on the same half-axis. The equimolecular surface corresponds to the condition $\Gamma = 0$. The dividing surface, for which the Laplace equation is valid, is the tension surface. The tension surface is generally taken as a true dividing surface.

The equimolecular surface and the tension surface are always located inside the interfacial transition layer, so the thickness of this layer can be taken as the maximum value of the Tolman length δ. For larger droplets, the Tolman length can be considered to be a constant value related to a flat surface. By definition, the Tolman length for a flat dividing surface is:

$$\delta = \frac{\Gamma}{\Delta n}, \ \Delta n = n_1 - n_2, \quad (30)$$

where $n_{1,2}$ are volume densities of coexisting phases in equilibrium. There is contradictory information about numerical values and even the sign of the Tolman length. It follows from (30)

that the sign of δ depends on the sign of Gibbs adsorption on the tension surface. You can determine the sign of the Tolman length if you use the well-known formula for the density distribution profile in the flat interfacial region:

$$n(z) = \frac{n_1 + n_2}{2} - \frac{\Delta n}{2} \operatorname{th}\left(\frac{z}{z_0}\right), \ \Delta n > 0, \quad (31)$$

where z is the coordinate; z_0 is the parameter characterizing the slope of the density distribution profile. Formula (31) specifies a density distribution profile symmetrical relative to the point $z = 0$. The denser and less dense phases are located on the positive and negative semi-axes. For adsorption, we have:

$$\Gamma = \int_{z_i}^{\infty} [n(z) - n_1] dz + \int_{-\infty}^{z_i} [n(z) - n_2] dz, \quad (32)$$

where z_i specifies the position of the arbitrary dividing surface. The integration of (32) with (31) gives:

$$\Gamma = z_i \Delta n. \quad (33)$$

For equimolecular surface and tension surface:

$z_i = 0$ and $z_i = z_s$,

therefore, from (30) and (32) for the Tolman length, we find:

$$\delta = z_s, \quad (34)$$

where z_s is counted from the origin, i.e. from the middle of the profile. Formula (34) allows us to conclude that the sign of the Tolman length depends on the location of the tension surface. If the tension surface is near the dense phase (which, in our opinion, is the most natural), the Tolman length will be positive. Shifting the tension surface to a less dense phase relative to the equimolecular surface changes the sign of δ to negative.

It should be noted that for certain thermodynamic systems the Tolman parameter can be considered negative, however, this case is not considered in this study.

For a small droplet with radius r, the stability condition has the form $(\partial\sigma / \partial r)_{T,p} > 0$. It follows that the function σ(r) must be increasing and the droplet must meet the condition δ > 0.

Conflict of interests

The author declares that they has no known competing financial interests or personal relationships that could have influenced the work reported in this paper.

References

1. Dubrovskii V. G. Nucleation theory and growth of nanostructures. In: *Nucleation Theory and Growth of Nanostructures*. Berlin Heidelberg: Springer-Verlag; 2014. pp. 1–73. https://doi.org/10.1007/978-3-642-39660-1_1
2. Vosel S. V., Onischuk A. A., Purtov P. A., Tolstikova T. G. Classical nucleation theory: account of dependence of the surface tension on curvature and translation-rotation correction factor. In: *Aerosols Handbook. Measurement, Dosimetry, and Health Effects*. L. S. Ruser and Naomi H. Harley (Eds.). London, New-York, Washington: CRC Press Boca Raton; 2012. pp. 503–528. https://doi.org/10.1201/b12668-24
3. Baranov S. A. *An engineering review about microwire.* Lambert, Academic publishing; 2017. 42 p.
4. Ono S., Kondo S. *Molecular theory of surface tesion in liquids*. Berlin: Springler – Verlag; 1960. 280 p.
5. Rowlinson J. S., Widom B. *Molecular theory of capillarity*. Oxford: Clarendon Press; 1982. 380 p.
6. Rusanov A. I. *Lectures on the thermodynamics of surfaces**. St. Petersburg: Lan Publ.; 2013. 240 p. (In Russ.)
7. Roldugin V. I. *Physical chemistry of surfaces**. Dolgoprudny: Intelligence Publ.; 2008. 568 p. (In Russ.)
8. Magomedov M. N. *Study of interatomic interaction, formation of vacancies and self-diffusion in crystals**. Moscow: Fizmat. Lit. Publ., 2010. 544 p. (In Russ.)
9. Rekhviashvili S. Sh. *Dimensional phenomena in condensed matter physics and nanotechnology**. Nalchik; 2014. 250 p. (In Russ.)
10. Baranov S. A. Surface energy of micro- and nanowire. *Annals of Advances in Chemistry*. 2023;7(1): 025–030. https://doi.org/10.29328/journal.aac.1001039
11. Baranov S. A. Surface energy for nanowire. *Annals of Mathematics and Physics*. 2022;5(2): 81–86. https://doi.org/10.17352/amp.000043
12. Baranov S. A., Dikusar A. I. Kinetics of electrochemical nanonucleation upon induced codeposition of iron-group metals with refractory metals (W, Mo, Re). *Surface Engineering and Applied Electrochemistry*. 2022;58 (5): 429–439. https://doi.org/10.3103/s1068375522050027
13. Baranov S. A. Non-classical cluster formation in minerology. *Aspects in Mining & Mineral Science*. 2022;10(2): 1128–1130. https://doi.org/10.31031/amms.2022.10.000732

14. Baranov S. A. Surface energy and production micro-and nanowire. *Journal of Nanosciences Research &Reports*. 2022;4(4): 1–4. https://doi.org/10.47363/jnsrr/2022(4)142

15. Baranov S. A. The surface tension problem for micro- and nanowire. *Moldavian Journal of the Physical Sciences.ю* 2022;21(1): 78–85. https://doi.org/10.53081/mjps.2022.21-1.08

16. Baranov S. A., Rekhviashvili S. Sh., Sokurov A. A. Some problems of simulation of the thermodynamic properties of droplets. *Surface Engineering and Applied Electrochemistry*. 2019;55(3): 286 -293. https://doi.org/10.3103/s1068375519030025

* *Translated by author of the article*

Information about the authors

Serghei A. Baranov, Dr. Sci. (Phys.–Math.), Senior Researcher of the Moldova State University, Institute of Applied Physics, Laboratory of Electrical and Electrochemical Treatment of Materials (Chisinau, Republic of Moldova); Associate Professor of the Shevchenko Pridnestrov'e State University (Tiraspol, Pridnestrov'e, Republic of Moldova).

sabaranov07@mail.ru

Received 20.09.2023; approved after reviewing 25.09.2023; accepted for publication 16.10.2023; published online 25.12.2023.

Translated by Irina Charychanskaya

ISSN 1606-867X (Print)
ISSN 2687-0711 (Online)
Condensed Matter and Interphases
Kondensirovannye Sredy i Mezhfaznye Granitsy
https://journals.vsu.ru/kcmf/

Original articles

Research article
https://doi.org/10.17308/kcmf.2023.25/11480

Relativistic model of interatomic interactions in condensed systems

A. Yu. Zakharov[1]✉, M. A. Zakharov[1]

*[1]Yaroslav-the-Wise Novgorod State University,
41, ul. Bolshaya Saint Petersburgskaya, Veliky Novgorod 173003, Russian Federation*

Abstract

A method was proposed to describe the dynamics of systems of interacting atoms in terms of an auxiliary field. The field is equivalent to the specified interatomic potentials at rest, and represents the classical relativistic field under dynamic conditions. It was determined that for central interatomic potentials, allowing for the Fourier transform, the auxiliary field is a superposition of elementary fields satisfying the Klein-Gordon-Fock equation with complex mass parameters.

Keywords: Interatomic potentials, Classical relativistic dynamics, Retarded interactions, Irreversibility phenomenon, Klein-Gordon-Fock equation

For citation: Zakharov A. Yu., Zakharov M. A. Relativistic model of interatomic interactions in condensed systems. *Condensed Matter and Interphases*. 2023;25(4): 494–504. https://doi.org/10.17308/kcmf.2023.25/11480

Для цитирования: Захаров А. Ю., Захаров М. А. Релятивистская модель межатомных взаимодействий в конденсированных системах. *Конденсированные среды и межфазные границы*. 2023;25(4): 494–504. https://doi.org/10.17308/kcmf.2023.25/11480

✉ Anatoly Yu. Zakharov, e-mail: anatoly.zakharov@novsu.ru

© Zakharov A. Yu., Zakharov M. A., 2023

The content is available under Creative Commons Attribution 4.0 License.

1. Introduction

Nowadays, the modeling of both thermodynamic and kinetic properties of condensed systems is performed mainly in terms of nonrelativistic approximation. The smallness of the velocities of atomic particles compared to the speed of light serves as some basis for neglecting the relativistic effect of interactions retardation. In this framework, the system of interacting atoms is characterized by a Hamiltonian, which gives a principal (but still far from real) possibility to calculate the partition function or the generating functional of the system in terms of the Gibbs approach, or to solve the hierarchy of equations for equilibrium or nonequilibrium distribution functions in terms of the BBGKY (Bogoliubov-Born-Green-Kirkwood-Yvon) approach. However, the exact solutions in each of these options for any "realistic" interatomic potentials are still unknown. There are no a priori estimates of the errors of the approximations used.

However, the issue of modeling condensed systems is not limited to solving problems within the framework of statistical mechanics. This is because the microscopic foundation of thermodynamics within the framework of statistical mechanics, which combines Newtonian classical mechanics (in Hamiltonian form) with the concept of probability, is not a comprehensive and flawless option, and is not the only possible solution. Besides, there are no solutions of many fundamental issues within the framework of statistical mechanics.

1. The zeroth law of thermodynamics (stating the existence of a state of thermodynamic equilibrium in macroscopic systems) has not been explained within the framework of statistical mechanics, but is a postulate in the same way as in phenomenological thermodynamics [1].

2. Classical mechanics itself is in clear contradiction with thermodynamics, so a microscopic foundation of thermodynamics requires going beyond Newtonian classical mechanics. In the late 19th – early 20th century, the concept of probability was expected to solve this issue (Maxwell, Boltzmann, Gibbs, Einstein, Smoluchowski, P. and T. Ehrenfest, …). However, in 1909, a discussion paper by Ritz and Einstein was published [2], in which Ritz argued that the cause of irreversibility was due to the (relativistic) effect of retarded interactions, and Einstein argued that probability was the only cause of irreversibility. Finally, in 1956, Kac proposed an exactly solvable mechanical model, the Kac ring model [3]. He found an exact solution of this model, which is deterministic, reversible, and does not show any features of thermodynamic behavior. The same study showed that introducing a very plausible probabilistic adjustment into the model leads to the thermodynamic behavior of the system and to the phenomenon of irreversibility. Thus, the reason for the thermodynamic behavior of the ring model is not only beyond classical mechanics, but also contradicts it. Therefore, combining mutually exclusive Newtonian deterministic mechanics and the concept of probability does not seem convincing.

3. In the following years, many papers have been published, providing substantial arguments in favor of Ritz's hypothesis [2]. Papers [4–7] studied two-body problems with retarded interactions between the bodies and determined that the systems irreversibly transfer to the state of rest within $t \to \infty$. In paper [8], the dynamics of a two-particle harmonic oscillator with retarded interaction between particles was studied. It was determined that there always are nonstationary (both growing and damped) free oscillations in this system. Paper [9] studied the dynamics of a one-dimensional chain of atoms with retarded interactions. It was determined that stationary free oscillations in this system are impossible, i.e., the irremovable relativistic retardation of interactions between atoms completely destroys the classical non-relativistic dynamical picture of Born. Besides, the paper described a microscopic dynamical (i.e. free from probability) mechanism of reaching thermodynamic equilibrium in crystals.

4. The Kolmogorov probability theory is based on the theory of measure and is not a unique model, but only one of many non-equivalent probability models [10]. Probability measures in phase space (microcanonical, canonical, and grand canonical ensembles), axiomatically introduced by Gibbs, are also non-unique. In particular, even the Gibbs principle of equal a priori probabilities in the microcanonical distribution is a postulate. Its application does

not lead to an unambiguous result due to the peculiarities of the measures distribution in multidimensional (infinite-dimensional at the limit) spaces [11, 12] (in this case it refers to measures in the phase space of the system).

Thus, nonrelativistic statistical mechanics is based on two not quite consistent concepts: Newtonian classical mechanics (in Hamiltonian form) and the concept of probability. These concepts can be coordinated only when there is an external stochasticization mechanism. The hypothesis of molecular chaos of Boltzmann, the principle of weakening of correlations of Bogoliubov, separate consideration of long-range and short-range parts of interparticle potentials (Boltzmann–Vlasov, Vlasov–Maxwell equations, etc.) can be used to simulate such a mechanism in terms of kinetic theory, but there is no direct evidence for choosing any of these options.

At the same time, in the framework of relativistic dynamics there are indications of thermodynamic behavior even in few–body systems without the application of the concept of probability. Therefore, the modeling of relativistic dynamics of particle systems is a promising direction.

The aim of this study was to develop a classical relativistic kinetic theory of systems of interacting particles (atoms).

It solved the following specific tasks.

1. The field form of relativistic dynamics of the system of interacting atoms was developed.

2. It was determined that the interatomic central potentials of general form admit a decomposition by Klein-Gordon-Fock static potentials with complex mass parameters.

3. We developed an unambiguous procedure for the transition from the classical nonrelativistic model of interatomic interactions to the relativistic auxiliary field providing the interaction between atoms.

4. The qualitative properties of solutions of the relativistic auxiliary field dynamics equations were analyzed.

2. Field form of interatomic interactions and substantiation of the auxiliary field concept

Let us consider a model of a condensed system consisting of neutral particles (atoms), which in the nonrelativistic approximation is characterized by a scalar two-particle central interatomic potential of a general form $v(r)$, which can be represented by a Fourier integral:

$$v(r) = \int \frac{d\mathbf{k}}{(2\pi)^3} \tilde{v}(k^2) e^{i\mathbf{kr}}, \quad (1)$$

where

$$\tilde{v}(k^2) = \int d\mathbf{r} v(r) e^{-i\mathbf{kr}}. \quad (2)$$

This potential is a starting point for the transition from static interatomic potentials to an auxiliary relativistic dynamical field, which is equivalent to interatomic potentials only under static conditions.

Currently, quite a lot of model interatomic potentials are known [13–15], but only a small part of them is used in studies based on the molecular dynamics method [16–18].

Under the nonrelativistic approximation, interactions between atoms are instantaneous. Therefore, an atom and the instantaneous field created by it are a single entity with a finite number of degrees of freedom. In the relativistic theory, every motion of an atom (the source of the field) leads to the evolution of its field, the propagation velocity of which does not exceed the speed of light. Therefore, the evolution of the system of interacting atoms includes both the dynamics of particles and the dynamics of the relativistic field created by the atoms.

Thus, the nonrelativistic approximation in the dynamics of interacting atoms is characterized by taking into account a finite number of degrees of freedom of the atoms and neglecting an infinite set of degrees of freedom of the accompanying field.

2.1. Relativization in physics

The long and complicated process of “relativization” of all branches of physics from classical mechanics to thermodynamics began soon after the introduction of the theory of relativity. The first works on the relativistic generalization of the kinetic theory of ideal gases were published by Planck [19] and Jüttner [20, 21]. Synge [22] constructed the relativistic gas dynamics for an ideal gas. Later, numerous vigorous attempts have been made to formulate relativistic thermodynamics [23–25], relativistic statistical mechanics, and kinetics [26–34].

However, so far it has not been possible to develop a unified approach to the development of relativistic thermodynamics, relativistic statistical mechanics, and relativistic kinetic theory of systems consisting of interacting particles [35]. The main difficulty is to find a covariant form of accounting interactions between particles, since the relativistic theory does not include the concept of potential energy of interparticle interactions [36–38]. Therefore, only the model of contact interaction between particles was developed for the relativistic kinetic theory: the interaction occurs only at the points of intersection of their world lines [39–41]. The scope of applicability of this model is limited to the case of extremely short-range interactions between particles, which is obviously insufficient for applications in terms of the theory of condensed systems.

In the relativistic theory, atoms interact via the field, so the system of interacting particles actually consists of two subsystems: the particles and the field. The interaction between atoms is of electromagnetic origin, but the model (1) is sufficient to describe the dynamics of the system of interacting atoms, without detailing the origin of interatomic interactions.

2.2. Equations for static fields

We assumed that the Fourier transform (2) of the interatomic potential (1) had no singularities on the semi-axis $k^2>0$ of the complex plane k^2. Following [42], the equation for the static potential $v(r)$, generated by a particle located at the origin $\boldsymbol{r}=0$, was:

$$f(\Delta)\{v(\mathbf{r})\}=\int\frac{d\mathbf{k}}{(2\pi)^3}f(-k^2)\tilde{v}(k^2)e^{-i\mathbf{kr}}=-4\pi\delta(\mathbf{r}), \quad (3)$$

where $f(\Delta)$ is the required function of the Laplace operator Δ.

Using the Fourier transform, we found:

$$f(-k^2)=-\frac{4\pi}{\tilde{v}(k^2)}. \quad (4)$$

This relation connects the Fourier transform of the static potential $\tilde{v}(k^2)$ with the differential equation (3) describing the corresponding static field.

In particular:

• The Fourier-transform of the Coulomb potential $\tilde{v}_1(k^2)=\frac{4\pi}{k^2}$ corresponds to the Poisson equation:

$$\Delta\varphi(\mathbf{r})=-4\pi\delta(\mathbf{r}), \quad (5)$$

• The Fourier transform of the Yukawa potential $\tilde{v}_1(k^2)=\frac{4\pi}{k^2}$ corresponds to the static Klein–Gordon–Fock equation (or the Debye–Hьckel equation [43]):

$$(\Delta-\mu^2)\varphi(\mathbf{r})=-4\pi\delta(\mathbf{r}). \quad (6)$$

Thus, the static interatomic potential $v(r)$, which can be represented as a Fourier integral (1), corresponds to the static field $\varphi(\mathbf{r})$, which satisfies the linear equation:

$$(\tilde{v}(-\Delta))^{-1}\varphi(\mathbf{r})=\rho(\mathbf{r}), \quad (7)$$

where $\rho(\boldsymbol{r})$ is the field source density.

The general solution of this equation is the sum of the general solution of the corresponding homogeneous equation:

$$(\tilde{v}(-\Delta))^{-1}\varphi(\mathbf{r})=0 \quad (8)$$

and any particular solution of equation (7).

2.3. Qualitative analysis of solutions of the homogeneous static field equation

According to equation (8), the eigenvalue of the operator $(\tilde{v}(-\Delta))^{-1}$ is zero. Taking into account the relation (4), this means that the function $(\tilde{v}(k^2))^{-1}$ equals zero at the corresponding value of k^2:

$$\frac{1}{\tilde{v}(k^2)}=0. \quad (9)$$

We will consider this condition as an equation with respect to k.

Since the function $\tilde{v}(k^2)$ at all real values of k is real and has no singularities, the imaginary parts of all roots of equation (9) must not equal zero:

$$k_s=\alpha_s+i\beta_s\Rightarrow k_s^2=(\alpha_s^2-\beta_s^2)+2i\alpha_s\beta_s,\ \beta_s\neq0. \quad (10)$$

In particular, k_s can be purely imaginary (at $\alpha_s=0$), as it takes place for the Yukawa potential.

We introduced the notation:

$$\mu_s^2 = -k_s^2 \quad (11)$$

and transformed equation (9) into:

$$\frac{1}{\tilde{v}(k^2)} = \left(\prod_s \left[k^2 + \mu_s^2\right]^{\gamma_s}\right) F(k^2) = 0, \quad (12)$$

where $F(k^2)$ is a certain function with no zeros, γ_s is the multiplicity of the root μ_s^2.

As $k^2 = -\Delta$ and all the operators:

$$\hat{L}_s = \left[\Delta - \mu_s^2\right]^{\gamma_s}, \quad \hat{L} = \prod_s \left[\Delta - \mu_s^2\right]^{\gamma_s}, \quad F(-\Delta) \quad (13)$$

commute, equation (8) is equivalent to the family of equations:

$$\left(\Delta - \mu_s^2\right)^{\gamma_s} \varphi_s(\mathbf{r}) = 0. \quad (14)$$

To avoid unnecessary complexity, we restrict ourselves to considering the case when the multiplicity of all the roots of equation (9) is equal to 1, $\gamma_s = 1$:

$$\left(\Delta - \mu_s^2\right)\varphi_s(\mathbf{r}) = 0. \quad (15)$$

The form of this equation resembles the problem of mathematical physics on the eigenvalues μ_s^2 of the Laplace operator, which can be obtained from the boundary conditions imposed on the function $\varphi_s(\mathbf{r})$. However, this similarity is only apparent. In this case, μ_s^2 are not derived from the boundary conditions for the functions $\varphi_s(\mathbf{r})$, but are solutions of equation (9).

In the particular case when $\tilde{v}(k^2)$ is a rational algebraic function, the set of operators $\hat{L}_s$ is finite ($s = 1, 2, \ldots, M$). Otherwise, this set may be infinite.

It should be noted that each of the functions $\varphi_s(\mathbf{r})$ satisfying equation (14), as well as all linear combinations of these functions equal zero upon the application of the operator $\hat{L}$. The general solution of equation (8) is a linear combination of the general solutions of equations (14) with arbitrary coefficients:

$$\varphi(\mathbf{r}) = \sum_s C_s \varphi_s(\mathbf{r}). \quad (16)$$

Thus, the free auxiliary static field $\varphi(r)$, equivalent to the instantaneous central interatomic potential, can be represented as a superposition of **elementary fields** $\varphi_s(r)$ satisfying equation (14).

As an example, let us briefly analyze possible variants of **static elementary potentials** depending on the complex parameter μ_s and satisfying equation (14). In this case we will not omit the solutions to this equation, which at first glance may seem "non-physical".

In the case of central (i.e., spherically symmetric) potentials, the general solution of equation (14) is as follows:

$$\varphi_s(r) = \frac{1}{r}\left(A_s e^{\mu_s r} + B_s e^{-\mu_s r}\right), \quad (17)$$

where

$$\mu_s = ik_s = -\beta_s + i\alpha_s, \quad r = |\mathbf{r}|, \quad (18)$$

and α_s and β_s are determined by formula (10).

At $\alpha_s = 0$, the potential $\varphi_s(\mathbf{r})$ is a linear combination of two terms, $\frac{e^{-\beta_s r}}{r}$ and $\frac{e^{\beta_s r}}{r}$. One of them tends to zero at $r \to \infty$ (Yukawa potential), and the second increases infinitely in absolute value and may seem "unphysical". However, there is a precedent for an interparticle potential that does not tend to zero at $r \to \infty$ and provides quark confinement in terms of quantum chromodynamics [44, 45].

In a more general case $\alpha_s \neq 0$, the elementary potentials $\varphi_s(r)$ are complex-valued functions of the coordinate r, depending on the complex parameters μ_s. In this case, the total potential (16), a linear combination of elementary potentials, is a real-valued function. In particular, if the number of complex elementary potentials is two, then the parameters μ_1, μ_2 are mutually conjugate:

$$\mu_2 = \mu_1^*, \quad (19)$$

and the total real static potential is as follows:

$$\varphi(r) = \frac{1}{r}\left\{\begin{aligned} & e^{-ar}\left[A\cos(br) + B\sin(br)\right] + \\ & + e^{ar}\left[C\cos(br) + D\sin(br)\right] \end{aligned}\right\}, \quad (20)$$

where $a = \operatorname{Re}\mu_1, b = \operatorname{Im}\mu_1$, and A, B, C, D are arbitrary real constants. This potential is a linear combination of sinusoidal functions of r. Their amplitudes change exponentially.

Note that the statistical thermodynamics of systems involving model potentials as in (20) and decreasing oscillation amplitudes was studied in [46, 47]. However, statistical thermodynamics of systems with model potentials, the oscillation amplitudes of which increase at $r \to \infty$, does not exist due to the divergence of configuration integrals. But this circumstance is not an obstacle

to studying the dynamics of systems with such model potentials.

2.4. Equations for dynamical fields

In terms of the nonrelativistic theory, the static field is closely related to the particles generating it and does not constitute separate degrees of freedom. The situation changes radically in terms of the theory of relativity: the dynamical field, generated by the particles and described by the relativistic equations of motion, comes into play.

The transition from static field equations to dynamic equations for electromagnetism was carried out by L. Lorenz and Riemann [48,49] in 1867 long before the theory of relativity appeared. The result was to replace the Laplace operator Δ in the Laplace and Poisson equations by the D'Alembert operator $\Box$:

$$\Delta = \frac{\partial^2}{\partial x^2} + \frac{\partial^2}{\partial y^2} + \frac{\partial^2}{\partial z^2} \Rightarrow \Rightarrow \Box = \frac{\partial^2}{\partial x^2} + \frac{\partial^2}{\partial y^2} + \frac{\partial^2}{\partial z^2} - \frac{1}{c^2}\frac{\partial^2}{\partial t^2}. \quad (21)$$

Thus, after the Lorenz-Riemann transformation (21), the field becomes a component of the system of interacting particles. The consequences of this transformation are as follows.

1. The system consists of two subsystems, one of which is the particles and the other is the dynamic field produced by these particles.

2. Neither the direct action of atoms on each other nor the direct action of the field on itself (self-action) exist.

3. The only type of interactions that exists in a system is the interaction between atoms and the field. A well-known example of such type of theories is classical electrodynamics.

4. The set of degrees of freedom of the system of "particles + field which provides interaction between particles" is infinite even when the number of particles is finite. As a result, the system of interacting particles is no longer a dynamical system with a finite number of degrees of freedom. Setting initial conditions only for particles is not sufficient for the unique solvability of the Cauchy problem for particles.

5. The dynamics of a system of interacting particles within the field framework depends not only on the equations of particle motion and field evolution, but also on the boundary conditions for the field.

6. In the microscopic foundation of thermodynamics on the basis of the nonrelativistic theory with instantaneous interatomic interactions within the framework of Gibbs statistical mechanics, a finite number of degrees of freedom is taken into account. An infinite (continual) set of field degrees of freedom of the system as a whole is ignored.

7. The existence of a field, as a mediator of interactions between particles, leads to both a radical change in the physical picture of the dynamics of a system of particles and to the development of an appropriate mathematical apparatus. In relativistic field dynamics, there are no Liouville equation, Poincaré recurrence theorem, and integral invariants. These theorems of analytical mechanics play a key role in the microscopic justification of thermodynamics in Gibbs statistical mechanics but have no place in relativistic field dynamics.

3. Green's functions of elementary fields and multiplicity of interaction retardations

The Green function of the Klein-Gordon operator $\hat{L}_s = \Box - \mu_s^2$ defined by the equation:

$$\left(\Box - \mu_s^2\right) G_s\left(\mathbf{r}-\mathbf{r}', t-t'\right) = -\delta\left(\mathbf{r}-\mathbf{r}'\right)\delta\left(t-t'\right) \quad (22)$$

and has the known form [50]:

$$G_s\left(\mathbf{r}-\mathbf{r}', t-t'\right) = \frac{\delta\left(t-t'-\frac{|\mathbf{r}-\mathbf{r}'|}{c}\right)}{4\pi|\mathbf{r}-\mathbf{r}'|} - \theta\left(t-t'-\frac{|\mathbf{r}-\mathbf{r}'|}{c}\right) c\mu_s \frac{J_1\left(\mu_s\sqrt{c^2\left(t-t'\right)^2 - |\mathbf{r}-\mathbf{r}'|^2}\right)}{4\pi\sqrt{c^2\left(t-t'\right)^2 - |\mathbf{r}-\mathbf{r}'|^2}}, \quad (23)$$

where $\theta(t)$ is the Heaviside step function and $J_1(x)$ is the Bessel function.

This implies the retarded potential of the Klein–Gordon field [50]:

$$\varphi_s(\mathbf{r}, t) = \int d\mathbf{r}' \left[\frac{\rho\left(\mathbf{r}', t-\frac{|\mathbf{r}-\mathbf{r}'|}{c}\right)}{4\pi|\mathbf{r}-\mathbf{r}'|} - \mu_s \int_0^\infty \rho\left(\mathbf{r}', t-\frac{1}{c}\sqrt{\xi^2 + |\mathbf{r}-\mathbf{r}'|^2}\right) \frac{J_1\left(\mu_s\xi\right)}{4\pi\sqrt{\xi^2 + |\mathbf{r}-\mathbf{r}'|^2}} d\xi\right], \quad (24)$$

where

$$\rho(\mathbf{r},t)=\sum_a \delta(\mathbf{r}-\mathbf{r}_a(t)) \qquad (25)$$

is the instantaneous microscopic density of the number of particles (atoms).

1. The first summand in the right part of formula (24) contains the uniquely defined retardation τ_1 between the points $\mathbf{r}$ and $\mathbf{r}'$, corresponding to the waves travels at the speed of light c:

$$\tau_1=\frac{|\mathbf{r}-\mathbf{r}'|}{c}. \qquad (26)$$

2. The second summand of the same formula contains an infinite set of retardations $\tau_2(\xi)$ between the same points $\mathbf{r}$ and $\mathbf{r}'$, depending not only on the distance between the points but also on the parameter ξ:

$$\tau_2(\xi)=\frac{\sqrt{\xi^2+|\mathbf{r}-\mathbf{r}'|^2}}{c}\geq\tau_1, \quad (0\leq\xi<\infty), \qquad (27)$$

depending on the continuous parameter ξ and corresponding to Klein–Gordon waves travels propagating at speeds between 0 and c. Note that the retardation $\tau_2(\xi)$ can take arbitrarily large values. This means that no matter how distant the past of the system has a direct impact on its evolution at the current moment in time.

Note that the value $\sqrt{\xi^2+|\mathbf{r}-\mathbf{r}'|^2}$ can be formally mathematically interpreted as a distance in four-dimensional space x,y,z,ξ with a metric $d_2=\sqrt{x^2+y^2+z^2+\xi^2}$, where the propagation velocity of the Klein–Gordon field is equal to the speed of light c. Consequently, the projection of the velocity from the four-dimensional space x,y,z,ξ to the three-dimensional subspace x,y,z can take any values from 0 to c.

Thus, the relation between the evolution of the relativistic auxiliary field $\varphi(r,t)$ and the dynamics of the system of particles generating this field is non-local both in spatial variables and over time. Therefore, the interaction between the particles carried by the auxiliary field is also non-local.

We considered the contribution of one particle from the group of particles (25) moving according to the law $\mathbf{r}=\mathbf{r}_a(t)$, to the retarded Klein–Gordon potential (24). The microscopic density corresponding to one particle is defined by the expression:

$$\rho_a\left(\mathbf{r}',t-\frac{|\mathbf{r}-\mathbf{r}'|}{c}\right)=\delta\left(\mathbf{r}'-\mathbf{r}_a\left(t-\frac{|\mathbf{r}-\mathbf{r}'|}{c}\right)\right). \qquad (28)$$

The contributed includes two components.

1.

$$\varphi_s^{(1)}(\mathbf{r},t)=\int d\mathbf{r}'\frac{\rho\left(\mathbf{r}',t-\frac{|\mathbf{r}-\mathbf{r}'|}{c}\right)}{4\pi|\mathbf{r}-\mathbf{r}'|}=\frac{1}{4\pi\left(|\mathbf{r}-\mathbf{r}_a(\tau)|-\frac{((\mathbf{r}-\mathbf{r}_a(\tau))\cdot\dot{\mathbf{r}}_a(\tau))}{c}\right)}, \qquad (29)$$

where τ is the variable related to t by a relationship:

$$\tau+\frac{|\mathbf{r}-\mathbf{r}_a(\tau)|}{c}=t. \qquad (30)$$

2.

$$\varphi_s^{(2)}(\mathbf{r},t)=-\mu_s\int d\mathbf{r}'\int_0^\infty\frac{\rho\left(\mathbf{r}',t-\frac{1}{c}\sqrt{\xi^2+|\mathbf{r}-\mathbf{r}'|^2}\right)}{4\pi\sqrt{\xi^2+|\mathbf{r}-\mathbf{r}'|^2}}J_1(\mu_s\xi)d\xi. \qquad (31)$$

Expression (29) for $\varphi_s^{(1)}(\mathbf{r},t)$ is a Lienard–Wiechert retarded potential [50, 51], depending on the position $\mathbf{r}_a(\tau)$ of the a-th particle and its velocity $\dot{\mathbf{r}}_a(\tau)$ at a single moment of time τ, determined by relation (30).

Expression (31) for $\varphi_s^{(2)}(\mathbf{r},t)$ has a noticeably more complicated structure. We changed the order of integration over the variables ξ and $\mathbf{r}'$ in formula (31) and considered the integral over $\mathbf{r}'$:

$$\Psi(\xi,\mathbf{r},t)=\int d\mathbf{r}'\delta\left(\mathbf{r}'-\mathbf{r}_a\left(t-\frac{1}{c}\sqrt{\xi^2+|\mathbf{r}-\mathbf{r}'|^2}\right)\right)\frac{1}{\sqrt{\xi^2+|\mathbf{r}-\mathbf{r}'|^2}}. \qquad (32)$$

To integrate over $\mathbf{r}'$, we multiplied both sides of this relation by $\delta\left(\tau-t+\frac{1}{c}\sqrt{\xi^2+|\mathbf{r}-\mathbf{r}'|^2}\right)$ and integrated over the variable τ. As a result, the left part of this equality remained unchanged, and the right part was transformed to the following form:

$$\Psi(\xi,\mathbf{r},t)=\int d\tau\int d\mathbf{r}'\delta\left(\tau-t+\frac{1}{c}\sqrt{\xi^2+|\mathbf{r}-\mathbf{r}'|^2}\right)\times$$
$$\times\frac{1}{\sqrt{\xi^2+|\mathbf{r}-\mathbf{r}'|^2}}\delta(\mathbf{r}'-\mathbf{r}_a(\tau))= \quad (33)$$
$$=\int d\tau\delta\left(\tau-t+\frac{1}{c}\sqrt{\xi^2+|\mathbf{r}-\mathbf{r}_a(\tau)|^2}\right)\frac{1}{\sqrt{\xi^2+|\mathbf{r}-\mathbf{r}_a(\tau)|^2}}.$$

The last integral has the form:

$$J(\xi,t,\mathbf{r})=\int d\tau\delta(F(\xi,t,\tau,\mathbf{r}))f(\xi,\mathbf{r},\tau), \quad (34)$$

where

$$F(\xi,t,\tau,\mathbf{r})=\tau-t+\frac{1}{c}\sqrt{\xi^2+|\mathbf{r}-\mathbf{r}_a(\tau)|^2}, \quad (35)$$

and

$$f(\xi,\mathbf{r},\tau)=\frac{1}{\sqrt{\xi^2+|\mathbf{r}-\mathbf{r}_a(\tau)|^2}}. \quad (36)$$

Integral (34) is calculated by the known formula:

$$J(\xi,t,\mathbf{r})=\sum_k\frac{f(\xi,\mathbf{r},\tau_k)}{\left|F_\tau'(\xi,t,\tau_k,\mathbf{r})\right|}, \quad (37)$$

where τ_k are the equation roots:

$$F(\xi,t,\tau,\mathbf{r})=\tau-t+\frac{1}{c}\sqrt{\xi^2+|\mathbf{r}-\mathbf{r}_a(\tau)|^2}=0 \quad (38)$$

in relation to τ. To show that this equation has a single root depending on ξ and t, we obtained the partial derivative of the function $F(\xi,t,\tau,\mathbf{r})$ on the variable τ:

$$F_\tau'(\xi,t,\tau,\mathbf{r})=1-\frac{1}{c}\frac{(\mathbf{r}-\mathbf{r}_a(\tau))\dot{\mathbf{r}}_a(\tau)}{\sqrt{\xi^2+|\mathbf{r}-\mathbf{r}_a(\tau)|^2}}. \quad (39)$$

It follows from the inequality:

$$F_\tau'(\xi,t,\tau,\mathbf{r})>0 \quad (40)$$

and the asymptotic behavior of the function $F(\xi,t,\tau,\mathbf{r})$ at $\tau\to\pm\infty$ that the solution of equation (38) in relation to τ exists and is unique:

$$\tau=\tau(\xi,t). \quad (41)$$

Thus, for any values of ξ, there is an unambiguous correspondence between t and τ:

$$t=t(\xi,\tau),\quad \tau=\tau(\xi,t). \quad (42)$$

By substituting (41), (39), (37), and (36) into (33), we obtained:

$$\Psi(\xi,\mathbf{r},t)=$$
$$=\frac{1}{\sqrt{\xi^2+|\mathbf{r}-\mathbf{r}_a(\tau(\xi,t))|^2}-\frac{(\mathbf{r}-\mathbf{r}_a(\tau(\xi,t)))\dot{\mathbf{r}}_a(\tau(\xi,t))}{c}}. \quad (43)$$

As a result, the expression for $\varphi_s^{(2)}(\mathbf{r},t)$ was transformed into:

$$\varphi_s^{(2)}(\mathbf{r},t)=$$
$$=-\frac{\mu_s}{4\pi}\int_0^\infty\frac{J_1(\mu_s\xi)}{\left(\sqrt{\xi^2+|\mathbf{r}-\mathbf{r}_a(\tau(\xi,t))|^2}-\frac{(\mathbf{r}-\mathbf{r}_a(\tau(\xi,t)))\dot{\mathbf{r}}_a(\tau(\xi,t))}{c}\right)}d\xi. \quad (44)$$

Note that using this representation to quantitatively analyze the retarded Klein–Gordon field potential implies knowledge of the function $\tau(\xi,t)$, which is formally defined as a solution of equation (38) with respect to τ. This equation is transcendental, and it is hardly possible to find an exact analytical solution to it for the general case. However, under certain conditions, an approximate solution can be found, which only deviates from the exact solution by an arbitrarily small amount.

There is a fundamental difference between expressions (29) for $\varphi_s^{(1)}(\mathbf{r},t)$ and (44) for $\varphi_s^{(2)}(\mathbf{r},t)$.

1. The potential $\varphi_s^{(1)}(\mathbf{r},t)$ at the point $\mathbf{r}$ at the moment t depends on the instantaneous position $\mathbf{r}_a(\tau)$ and instantaneous velocity $\dot{\mathbf{r}}_a(\tau)$ of the generating particle at the single moment of time τ, determined by condition (30).

2. The potential $\varphi_s^{(2)}(\mathbf{r},t)$ at the point $\mathbf{r}$ at the moment t depends on an infinite series of positions $\mathbf{r}_a(\tau(\xi,t))$ and an infinite series of instantaneous velocities $\dot{\mathbf{r}}_a(\tau(\xi,t)\tau)$ of the generating particle at all moments of time, determined by condition (38) and parameterized by the variable $0\le\xi<\infty$.

In other words, an observer located at the point $\boldsymbol{r}$ at the moment t and using the field $\varphi_s^{(1)}(\mathbf{r},t)$ for observation, sees a point source of this field.

The same observer located at the point $\mathbf{r}$ at the moment t and using the field $\varphi_s^{(2)}(\mathbf{r},t)$ for observation, sees infinitely many sources instead of a point source of this field. These sources fill the whole trajectory of the source from the distant past to the point $\mathbf{r}=\mathbf{r}_a(t-\tau(\xi,t))\big|_{\xi=0}$.

4. Discussion and conclusions

The basic principles underlying this study are as follows.

1. Interatomic interactions have a field character. Therefore, any real system consists of particles and a field created by these particles, transmitting interactions between these particles.

2. In the case of atoms at rest, the interaction between them can be described by interatomic potentials. In the case of moving atoms, their interaction is described by an auxiliary scalar relativistic field.

3. The auxiliary scalar field is a superposition of elementary fields. Each of them is characterized by its own complex mass and satisfies the Klein-Gordon-Fock equation. The parameters of elementary fields are uniquely expressed through the characteristics of static interatomic potentials.

4. By virtue of finiteness of masses of elementary fields, the propagation velocity of Klein-Gordon-Fock fields can take any values smaller than the speed of light. This leads to the fact that the retardation of interactions between particles can reach any large values.

5. The retardation of interactions between particles is a real physical mechanism leading to irreversibility of the dynamics of both many-particle and few-particle systems.

Contribution of the authors

The authors contributed equally to this article.

Conflict of interests

The authors declare that they have no known competing financial interests or personal relationships that could have influenced the work reported in this paper.

References

1. Uhlenbeck G. E., Ford G. W. *Lectures in statistical mechanics*. American Mathematical Society (1963). Providence: AMS; 1963. 171 p.

2. Ritz W., Einstein A. Zum gegenwärtigen Stand des Strahlungsproblems. *Physikalische Zeitschrift*. 1909; 10(9): 323–324.

3. Kac M. Some remarks on the use of probability in classical statistical mechanics. *Bull. de l'Académie Royale de Belgique (Classe des Sciences)*. 1956;42(5): 356–361. https://doi.org/10.3406/barb.1956.68352

4. Synge J. L. The electromagnetic two-body problem. *Proceedings of the Royal Society of London. Series A. Mathematical and Physical Sciences*. 1940;177(968): 118–139. http://dx.doi.org/10.1098/rspa.1940.0114

5. Driver R. D. A two-body problem of classical electrodynamics: the one-dimensional case. *Annals of Physics*. 1963;21(1): 122–142. http://dx.doi.org/10.1016/0003-4916(63)90227-6

6. Hsing D. K. Existence and uniqueness theorem for the one-dimensional backwards two-body problem of electrodynamics. *Physical Review D*. 1977;16(4): 974–982. https://doi.org/10.1103/physrevd.16.974

7. Hoag J. T.; Driver R. D. A delayed-advanced model for the electrodynamics two-body problem. *Nonlinear analysis: Theory, Methods & Applications*. 1990;15(2): 165–184. https://doi.org/10.1016/0362-546x(90)90120-6

8. Zakharov A. Yu. On physical principles and mathematical mechanisms of the phenomenon of irreversibility. *Physica A: Statistical Mechanics and its Applications*. 2019;525: 1289–1295. https://doi.org/10.1016/j.physa.2019.04.047

9. Zakharov A. Y., Zakharov M. A. Microscopic dynamic mechanism of irreversible thermodynamic equilibration of crystals. *Quantum Reports*. 2021;3(4): 724–730. https://doi.org/10.3390/quantum3040045

10. Khrennikov A. Yu. *Interpretations of probability*. Berlin – New York: Walter de Gruyter; 2009. 237 p. https://doi.org/10.1515/9783110213195

11. Borel E. *Introduction géométrique à quelques théories physiques*. Paris: Gauthier-Villars; 1914. 147 p.

12. Levy P. *Specific problems of functional analysis**. Moscow: Nauka Publ., 1967. 511 p. (In Russ.)

13. Rowlinson J. S. C. *A scientific history of intermolecular forces*. Cambridge: Cambridge University Press; 2002. 343 p.

14. Kaplan I. G. *Intermolecular interactions: physical picture, computational methods and model potentials*. Chichester: Wiley; 2006. 375 p. https://doi.org/10.1002/047086334x

15. Stone A. *The theory of intermolecular forces*. Oxford: Oxford University Press; 2013. 352 p. https://doi.org/10.1093/acprof:oso/9780199672394.001.0001

16. *Molecular dynamics method in physical chemistry**. (Ed. Yu. K. Tovbin). Moscow: Nauka Publ., 1996; 169 p. (In Russ.)

17. Kamberaj H. *Molecular dynamics simulations in statistical physics: theory and applications*. Cham: Springer; 2020. 470 p. https://doi.org/10.1007/978-3-030-35702-3

18. Kun Zhou, Bo Liu. *Molecular dynamics simulation: fundamentals and applications*. Amsterdam: Elsevier; 2022. 374 p. https://doi.org/10.1016/b978-0-12-816419-8.00006-4

19. Planck M. Zur Dynamik bewegter Systeme. *Annalen der Physik*. 1908;331(6): 1–34. https://doi.org/10.1002/andp.19083310602

20. Jüttner F. Das Maxwellsche Gesetz der Geschwindigkeitsverteilung in der Relativtheorie. *Annalen der Physik.* 1911;339(5): 856–882. https://doi.org/10.1002/andp.19113390503

21. Jüttner F. Die dynamik eines bewegten Gases in der Relativtheorie. *Annalen der Physik*. 1911;340(6): 145–161. https://doi.org/10.1002/andp.19113400608

22. Synge J. L. *The relativistic gas.* Amsterdam: North-Holland; 1957. 119 p.

23. Tolman R. C. Thermodynamics and relativity. *Bulletin of the American Mathematical Society*. 1933;39(2): 49–74. https://doi.org/10.1090/s0002-9904-1933-05559-3

24. ter Haar D., Wergeland H. Thermodynamics and statistical mechanics in the special theory of relativity. *Physics Reports*. 1971;1(2): 31–54. https://doi.org/10.1016/0370-1573(71)90006-8

25. Nakamura T. K. Three views of a secret in relativistic thermodynamics. *Progress of Theoretical Physics*. 2012;128(3): 463–475. https://doi.org/10.1143/ptp.128.463

26. Chernikov N. A. Derivation of the equations of relativistic hydrodynamics from the relativistic transport equation. *Physics Letters*. 1963;5(2): 115–117. https://doi.org/10.1016/s0375-9601(63)91750-x

27. de Groot S. R., van Leeuwen W. A., van Weert Ch. G. *Relativistic kinetic theory: principles and applications*. Amsterdam: North-Holland; 1980. 433 p.

28. Trump M. A., Schieve W. C. *Classical relativistic many-body dynamics*. Dordrecht: Springer; 1999. 375 p. https://doi.org/10.1007/978-94-015-9303-8

29. Cercignani C., Kremer G. M. *The relativistic Boltzmann equation: theory and applications*. Basel: Birkhдuser; 2002. 394 p. https://doi.org/10.1007/978-3-0348-8165-4

30. Hakim R. *Introduction to relativistic statistical mechanics: classical and quantum*. New Jersey: World Scientific; 2011. 566 p. https://doi.org/10.1142/7881

31. Kuz'menkov L. S. Field form of dynamics and statistics of systems of particles with electromagnetic interaction. *Theoretical and Mathematical Physics.* 1991;86(2): 159–168. https://doi.org/10.1007/bf01016167

32. Liboff R. *Kinetic theory: classical quantum and relativistic descriptions*. New York: Springer; 2003. 587 p.

33. Balescu R., Kotera T. On the covariant formulation of classical relativistic statistical mechanics. *Physica*. 1967;33(3): 558–580. https://doi.org/10.1016/0031-8914(67)90204-2

34. Schieve W. C. Covariant relativistic statistical mechanics of many particles. *Foundations of Physics.* 2005;35(8): 1359–1381. ttps://doi.org/10.1007/s10701-005-6441-9

35. Lusanna L. From relativistic mechanics towards relativistic statistical mechanics. *Entropy*. 2017;19(9): 436. https://doi.org/10.3390/e19090436

36. Currie D. G. Interaction contra classical relativistic Hamiltonian particle mechanics. *Journal of Mathematical Physics.* 1963;4(12): 1470-1488. https://doi.org/10.1063/1.1703928

37. Currie D. G., Jordan T. F., Sudarshan E. C. G. Relativistic invariance and Hamiltonian theories of interacting particles. *Reviews of Modern Physics*. 1963;35(2): 350-375. https://doi.org/10.1103/revmodphys.35.350

38. Leutwyler H. A no-interaction theorem in classical relativistic Hamiltonian particle mechanics. *Nuovo Cimento*. 1965;37(2): 556–567. https://doi.org/10.1007/bf02749856

39. Dirac P. A. M. Forms of relativistic dynamics. *Reviews of Modern Physics*. 1949,21(3): 392–399. https://doi.org/10.1103/revmodphys.21.392

40. van Dam H., Wigner E. P. Classical relativistic mechanics of interacting point particles. *Physical Review*. 1965;138(6B): 1576–1582. https://doi.org/10.1103/physrev.138.b1576

41. van Dam H., Wigner E. P. Instantaneous and asymptotic conservation laws for classical relativistic mechanics of interacting point particles. *Physical Review*. 1966;142(4): 838–843. https://doi.org/10.1103/physrev.142.838

42. Zakharov A. Y., Zubkov V. V. Field-theoretical representation of interactions between particles: classical relativistic probability-free kinetic theory. *Universe*. 2022;8(281): 1–11. http://dx.doi.org/10.3390/universe8050281

43. Debye P., Hückel E. Zur Theorie der Elektrolyte. *Physikalische Zeitschrift*. 1923;24(9): 185–206.

44. Ali A., Kramer G. JETS and QCD: a historical review of the discovery of the quark and gluon jets and its impact on QCD. *The European Physical Journal H*. 2011;36: 245–326. https://doi.org/10.1140/epjh/e2011-10047-1

45. Sazdjian H. The interplay between compact and molecular structures in tetraquarks. *Symmetry*. 2022; 14, 515. https://doi.org/10.3390/sym14030515

46. Loktionov I. K. Application of two-parameter oscillating interaction potentials for specifying the thermophysical properties of simple liquids. *High Temperature*. 2012;50(6): 708–716. https://doi.org/10.1134/S0018151X12050094

47. Loktionov I. K. Studying equilibrium thermophysical properties of simple liquids based on a four-parameter oscillating interaction potential.

High Temperature. 2014;52(3): 390–402. https://doi.org/10.1134/S0018151X14020151

48. Lorenz L. On the identity of the vibrations of light with electrical currents. *The London, Edinburgh, and Dublin Philosophical Magazine and Journal of Science*. 1867;34(230): 287–301. https://doi.org/10.1080/14786446708639882

49. Riemann B. A contribution to electrodynamics. *The London, Edinburgh, and Dublin Philosophical Magazine and Journal of Science*. 1867;34(231): 368–372. https://doi.org/10.1080/14786446708639897

50. Ivanenko D. D.; Sokolov A. A. *The classical theory of fields**. Moscow: GITTL Publ., 1949. 480 p. (In Russ.)

51. Landau L. D., Lifshitz E.M. *The classical theory of fields**. Oxford.: Pergamon Press; 1975. 402 p.

* *Translated by author of the article.*

Information about the authors

Anatoly Yu. Zakharov, Dr. Sci. (Phys.-Math.), Full Professor, Professor at the Department of General and Experimental Physics, Yaroslav-the-Wise Novgorod State University (Veliky Novgorod, Russian Federation)

https://orcid.org/0000-0002-7850-0086

anatoly.zakharov@novsu.ru

Maxim A. Zakharov, Dr. Sci. (Phys.-Math.), Docent, Professor at the Department of Solid State Physics and Microelectronics, Yaroslav-the-Wise Novgorod State University (Veliky Novgorod, Russian Federation)

https://orcid.org/0000-0002-9144-340X

maxim.zakharov@novsu.ru

Received 28.09.2023; approved after reviewing 10.10.2023; accepted for publication 16.10.2023; published online 26.12.2023.

Translated by Anastasiia Ananeva

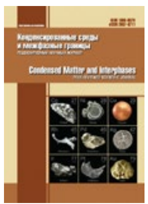

ISSN 1606-867X (Print)
ISSN 2687-0711 (Online)
Condensed Matter and Interphases
Kondensirovannye Sredy i Mezhfaznye Granitsy
https://journals.vsu.ru/kcmf/

Original articles

Research article
https://doi.org/10.17308/kcmf.2023.25/11473

Pair interaction of intersecting dilatation and disclination defects

S. A. Krasnitckii✉[1], A. M. Smirnov[1]

[1]ITMO University,
49 Kronverksky pr., bldg. A, St. Petersburg 197101, Russian Federation

Abstract

An elastic interaction of the intersecting dilatation and disclination defects located in an infinite linear isotropic media is investigated. The eigenstrain approach is employed to obtain the analytical expressions describing the pair interaction between intersecting dilatational lines and intersecting wedge disclinations. It is demonstrated that the interaction energy strongly depends on the intersection angle between the defects. The energy reaches the maximum value if the defect lines are coincided while the energy reaches the minimum value if the defect lines are orthogonal. Besides, it is shown that interaction energy of intersecting wedge disclinations strongly depends on the elastic properties of the media: the less the Poisson ratio, the less the energy. The obtained analytical results seem to be applicable for the theoretical analysis of the residual stress relaxation mechanisms in heterostructures with pentagonal symmetry such as icosahedral particles.

Keywords: Disclination, Dilatation line, Pair interaction

Funding: The study was supported by the Russian Science Foundation, project No 23-72-10014.

For citation: Krasnitckii S. A., Smirnov A. M. Pair interaction of intersecting dilatation and disclination defects. *Condensed Matter and Interphases*. 2023;25(4): 505–513. https://doi.org/10.17308/kcmf.2023.25/11473

Для цитирования: Красницкий С. А., Смирнов А. М. Энергия парного взаимодействия пересекающихся дефектов дилатационного и дисклинационного типа. *Конденсированные среды и межфазные границы*. 2023;25(4): 505–513. https://doi.org/10.17308/kcmf.2023.25/11473

✉ Stanislav A. Krasnitckii, e-mail: krasnitsky@inbox.ru
© Krasnitckii S. A., Smirnov A. M., 2023

The content is available under Creative Commons Attribution 4.0 License.

1. Introduction

Due to the unique functional properties, inhomogeneous nanostructures are widely used in the design of modern electronic devices [1], photonics [2] and plasmonics [3]. The stability of the properties of such nanostructures is mainly determined by crystal defects that arise during the relaxation of mechanical stresses [4–7]. The main mechanisms of stress relaxation include the formation of point defects complexes [8, 9], generation of dislocation [10–17] and disclination [18–20] configurations, nucleation of cracks and various V-shaped defects [21–23], diffusion perturbation of the surface [21, 24].

The processes of stress relaxation in inhomogeneous particles with fifth-order symmetry axes (pentagonal prism, decahedron and icosahedron) are of particular interest [25, 26]. The residual strains and stresses attributed to these particles are caused by five-fold twinning around the fifth-order symmetry axes and can be described within the framework of the disclination concept [27, 28]. According to this concept, pentagonal whiskers and decahedral particles contain one positive wedge disclination with strength 0.128 rad, (the disclination axis coincides with the symmetry axis of the fifth order), while icosahedral particles contain six positive wedge disclinations with strength 0.128 rad, passing through the opposite apexes of the icosahedron and intersecting at its centre. The elastic field of wedge disclination as a strong sink have a significant influence on point defect migration. Therefore, on the initial stages of residual stress relaxation, the formation of atmospheres of impurity atoms and vacancies along the cores of wedge disclinations can be expected. On the following stages of relaxation process the concentration of vacancies (impurity atoms) can reach essential enough supersaturation to condense to pores (second phase nuclei), that was observed experimentally [29, 30] and theoretically described in [32–34].

Thus, an analysis of the initial stages of residual stress relaxation due to the segregation of point defects on the disclination cores in icosahedral particles can be performed through the determination of the interaction energies of the defects under consideration. This study presents analytical expressions for the pair interaction energies of the following defect configurations: intersecting dilatation lines and intersecting wedge disclinations placed in the infinite medium. Despite the fact that the obtained results are valid for the infinite medium assumption, they can be used as a starting point for calculating the energy of the pair interactions of intersecting defects in finite bodies with a free surface in future.

2. Theoretical part

In this section an elastic isotropic medium containing intersecting direct defects, such as dilatation lines and wedge disclinations is considered. The energy of the pair interactions of these defects can be defined as the work spending on the generation of one of the defects in the stress field of another defect [35]:

$$W_{\text{int}}^{I-II} = -\int_V \beta_{ij}^{I} \sigma_{ij}^{II} dV = -\int_V \beta_{ij}^{II} \sigma_{ij}^{I} dV \,, \tag{1}$$

where β_{ij}^{I} and β_{ij}^{II} are components of the plastic distortion tensor of the defects (I) and (II), σ_{ij}^{I} and σ_{ij}^{II} are components of the elastic stress tensor of the defects (I) and (II), induced in the material volume V.

2.1. Energy of the pair interactions of intersecting dilatation lines

Consider the straight dilation lines L_I and L_{II}, intersecting at a point O under the angle α (Fig. 1a). We introduce the Cartesian coordinate systems $Oxyz$ and $Oxy'z'$, associated with lines of defects L_I and L_{II} respectively (axis x is perpendicular to the intersection plane of defects, axes z and z' coinciding with the lines of defects L_I and L_{II}, direction of axes y and y' prescribed by the right-hand rule). The stress field of these defects in an infinite elastic medium is known (see, for example, [36]). The non-zero components of the stress tensor of the dilatation line L_I in the Cartesian coordinate system can be presented in the following way:

$$\sigma_{xx}^{L_I} = -C_0 \xi^2 \frac{x^2 - y^2}{(x^2 + y^2)^2} \,, \tag{2a}$$

$$\sigma_{yy}^{L_I} = -C_0 \xi^2 \frac{y^2 - x^2}{(x^2 + y^2)^2} \,, \tag{2b}$$

$$\sigma_{zz}^{L_I} = -2C_0 H(\xi - x) H(\xi - y) \,, \tag{2c}$$

$$\sigma_{xy}^{L_I} = -C_0 \xi^2 \frac{2xy}{(x^2 + y^2)^2} \,, \tag{2d}$$

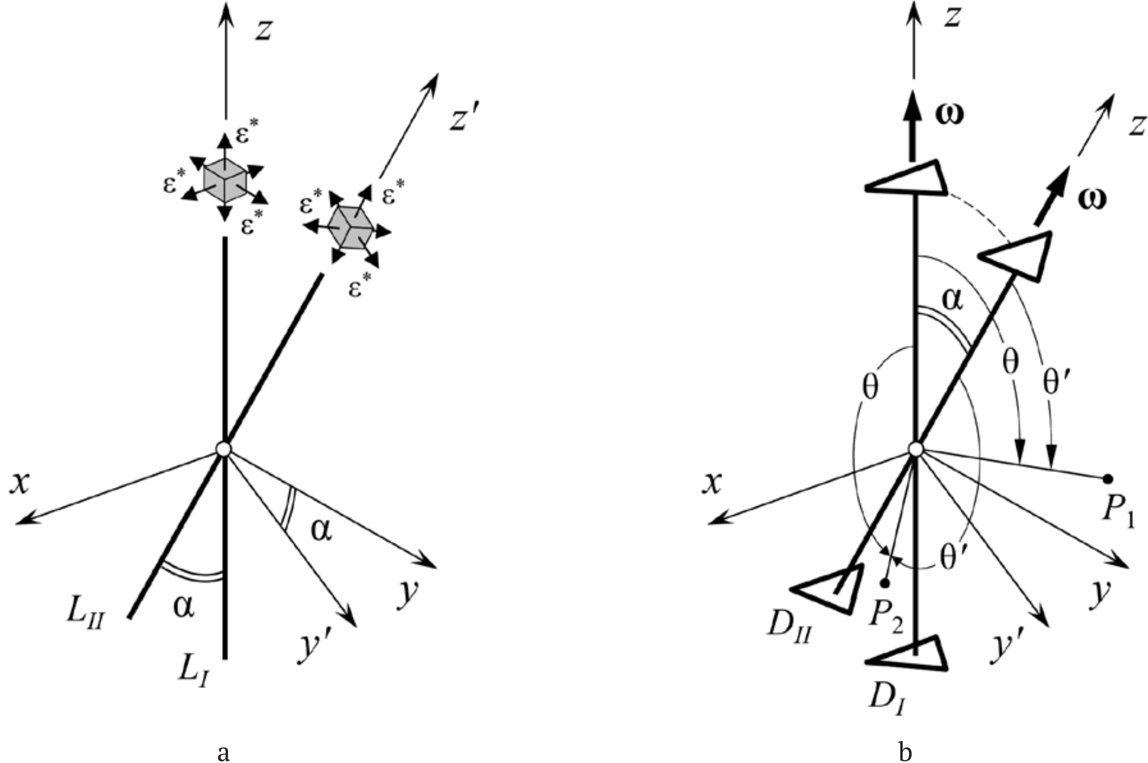

Fig. 1. An elastic model of the defects with an intersection angle α: a) dilatation lines L_I and L_{II} subjected to 3D eigenstrain ε^*; b) wedge disclinations D_I and D_{II} with strength ω. Points P_1 and P_2 belong to areas $S_1 = \{R \geqslant 0, \varphi = \pi/2, \alpha \leqslant \theta \leqslant \pi\}$ and $S_2 = \{R \geqslant 0, \varphi = 3\pi/2, \pi - \alpha \leqslant \theta' \leqslant \pi\}$ respectively

where $C_0 = G\varepsilon^*(1+\nu)/(1-\nu)$, G is a shear modulus; ν is a Poisson ratio; ε^* is a dilatation eigenstrain of the defect; $H(\ldots)$ is a Heaviside function; ξ is a small parameter defining the radius of the core of the dilatation defect line. Expression (2c) for the axial component of the dilatation line stress tensor is a generalized function: the stress equals zero at all points of the medium, except for the points corresponding to the line of the dilatation defect.

The eigenstrain distortion of the dilatation line is characterized by triaxial deformation ε^*, distributed along the lines of defects. According to [36], non-zero components of the eigenstrain distortion of the dilatation line (II) can be expressed as:

$$\beta_{ii}^{L_{II}} = \varepsilon^* s\delta(x)\delta(y'), \quad (3)$$

where $s = \pi\xi^2$, $\delta(\ldots)$ is a one-dimensional Dirac delta function.

To determine the pair interaction specific energy of intersecting dilatation lines L_I and L_{II} we substitute (2) and (3) in the expression (1) for energy:

$$\begin{aligned}\tilde{W}_{\text{int}}^{L_{I-II}} &= -\int_S \beta_{ij}^{L_{II}} \sigma_{ij}^{L_I} dS = \\ &= 4\varepsilon^* sC_0 \iint_{-\infty}^{+\infty} H(\xi - x)H(\xi - y)\delta(x)\delta(y')dxdy = . \quad (4)\\ &= 4\varepsilon^* sC_0 \int_{-\xi}^{\xi}\delta(x)dx \int_{-\xi}^{\xi}\delta(y')dy.\end{aligned}$$

The first integral in (4) is taken by the definition of the Dirac delta function, the second is taken by using a change in variable $y = y'\cos\alpha$. Finally, we obtain:

$$\tilde{W}_{\text{int}}^{L_{I-II}} = 4\varepsilon^* sC_0 |\cos\alpha|. \quad (5)$$

Let us consider the specific case when the defect lines L_I and L_{II} are orthogonal ($\alpha = \pi/2$). In this case, the total interaction energy of defects can be determined using the expression (1), with $y' = z$ we have:

$$\begin{aligned}W_{\text{int}}^{L_{I-II}}\big|_{\alpha=\pi/2} &= \\ &= 4\varepsilon^* sC_0 \iiint_{-\infty}^{+\infty} H(\xi - x)H(\xi - y)\delta(x)\delta(z)dxdydz = \quad (6)\\ &= 4\varepsilon^* sC_0 \int_{-\xi}^{\xi}\delta(x)dx \int_{-\xi}^{\xi}dy \int_{-\infty}^{+\infty}\delta(z)dz.\end{aligned}$$

Finally, we obtain the energy of the pair interaction of dilatational lines intersecting under right angles:

$$W_{\text{int}}^{L_{I-II}}\Big|_{\alpha=\pi/2} = 8\varepsilon^* s\xi C_0. \quad (7)$$

2.2. Energy of the pair interactions of intersecting wedge disclinations

The wedge disclinations D_I and D_{II} with equal moduli of Frank vectors is considered. The disclination axes intersect at the point O under the angle α. The axes of Cartesian coordinate systems $Oxyz$ and $Oxy'z'$ are similar to the previous section (see Fig. 1b).

Elastic stress fields of wedge disclinations in an infinite medium are known (see, for example, [28] and [37]). The non-zero components of the wedge disclination stress tensor in a spherical coordinate system are given below:

$$\sigma_{xx}^{D_I} = C_1\left(\frac{\nu}{1-2\nu} + \frac{y^2}{r^2} + \log r\right), \quad (8a)$$

$$\sigma_{yy}^{D_I} = C_1\left(\frac{\nu}{1-2\nu} + \frac{x^2}{r^2} + \log r\right), \quad (8b)$$

$$\sigma_{zz}^{D_I} = C_1\left(\frac{\nu}{1-2\nu} + 2\nu\log r\right), \quad (8c)$$

$$\sigma_{xy}^{D_I} = -C_1\frac{xy}{r^2}, \quad (8d)$$

where $C_1 = G\omega/[2\pi(1-\nu)]$, ω is a disclination strength; polar radius $r = (x^2+y^2)^{1/2}$. As can be seen from expressions (8), the stress field components of a wedge disclination located in an infinite elastic medium are characterized by logarithmic singularity. This singularity can be eliminated by incorporating self-screening systems, for instance, the disclination dipoles and quadrupoles [38] and the disclinations in finite bodies bounded by cylindrical [38] or spherical [39] surfaces.

The plastic distortion of the wedge disclination D_{II} is defined on the half-plane as $S_{II} = \{x = 0, y' > 0, z'\}$. The non-zero component of the disclination plastic distortion tensor D_{II} is:

$$\beta_{xx}^{D_{II}} = -\omega y'\delta(x)H(S_{II}), \quad (9)$$

where $H(S_{II})$ is the two-dimensional Heaviside function equal to 1 at $x, y \in S_{II}$ and equal to 0 at $x, y \notin S_{II}$.

Taking into account (8) and (9), the energy of the pair interaction of intersecting wedge disclinations D_I and D_{II} can be expressed:

$$W_{\text{int}}^{D_{I-II}} = \omega\iiint_{-\infty}^{+\infty}\sigma_{xx}^{D_I} y'\delta(x)H(S_{II})dxdy'dz' = \omega\int_{-\infty}^{+\infty}\int_{0}^{+\infty}\sigma_{xx}^{D_I}\Big|_{S_{II}} y'dy'dz'. \quad (10)$$

Spherical coordinates (R, φ, θ) and (R, φ', θ') with the origin at the point O are introduced. Polar (colatitude) angles θ and θ′ are measured from the axes by disclination D_I and D_{II} accordingly ($0 \leqslant \theta, \theta' \leqslant$ p). Azimuthal angles φ and φ′ are measured from the axis x ($0 \leqslant \varphi, \varphi' \leqslant 2\pi$). Taking into account the relationship between spherical and Cartesian coordinates: $y' = R\sin\theta'$, $z' = R\cos\theta'$, $dy'dz' = -RdRd\theta'$, we present (10) in the following form:

$$W_{\text{int}}^{D_{I-II}} = -\omega\int_0^A\int_0^\pi\sigma_{xx}^{D_I}\Big|_{S_{II}}\sin\theta' d\theta' R^2 dR, \quad (11)$$

where A – parameter, in the case of an infinite medium $A \to +\infty$.

It is worth noting that in the coordinate system associated with the disclination D_I, the half-plane S_{II} is determined by the sum of regions $S_1 = \{R \geqslant 0, \varphi = \pi/2, \alpha \leqslant \theta \leqslant \pi\}$ and $S_2 = \{R \geqslant 0, \varphi = 3\pi/2, \pi-\alpha \leqslant \theta \leqslant \pi\}$. With respect to the change of variable $\theta' = 2\pi - \alpha - \theta$, $d\theta' = -d\theta$ at $\pi - \alpha \leqslant \theta \leqslant \pi$. And $\theta' = \theta - \alpha$, $d\theta' = d\theta$ at $\alpha \leqslant \theta \leqslant \pi$, we present integral (11) as a sum of integrals over regions S_1 and S_2:

$$W_{\text{int}}^{D_{I-II}} = -\omega\int_0^A\left(\begin{array}{l}\displaystyle\int_{\pi-\alpha}^{\pi}\sigma_{xx}^{D_I}\Big|_{S_1}\sin(\theta+\alpha)d\theta + \\ \displaystyle+\int_{\alpha}^{\pi}\sigma_{xx}^{D_I}\Big|_{S_2}\sin(\theta-\alpha)d\theta\end{array}\right)R^2 dR. \quad (12)$$

Integrals in (12) with regard to (8a) and $x = 0$, $y = R\sin\theta$ can be calculated analytically, for example, using tables of integrals [40]. Here we present the final expression for the interaction energy stored by wedge disclinations D_I and D_{II} in a subregion bounded by the surface of a sphere of radius A:

$$W_{\text{int}}^{I-II} = \omega C_1\frac{A^3}{3}\left[\begin{array}{c}-\dfrac{1-5\nu}{3(1-2\nu)} - \cos\alpha\,\ln\left(\tan\dfrac{\alpha}{2}\right) + \\ +\log(A\sin\alpha)\end{array}\right]. \quad (13)$$

To determine the energy density of the interaction of disclinations D_I and D_{II}, stored in a sphere of radius A, we divide expression (13)

by the volume of the sphere and present it in the following form:

$$w_{\mathrm{int}}^{D_{I-II}} = w_A + w_\alpha \,, \tag{14}$$

where the first term contains a logarithmic singularity of disclination-type defects determining the contribution of the scale factor to the disclination interaction energy:

$$w_A = \frac{\omega C_1}{4\pi} \log A \,, \tag{15}$$

the second term contains the dependence of the interaction energy density of the disclination D_I and D_{II} on the angle between them:

$$w_\alpha = \frac{\omega C_1}{4\pi}\left[\begin{array}{c} -\dfrac{1-5\nu}{3(1-2\nu)} + \cos\alpha \log(1+\cos\alpha) + \\ +(1-\cos\alpha)\log(\sin\alpha) \end{array} \right]. \tag{16}$$

Thus, analytical expressions (14), (15), and (16) were obtained for the interaction energy density of intersecting disclinations in an infinite medium. Equation (15) expresses the dependence of the interaction of energy density on the size of the considered region: the interaction energy density increases according to the logarithmic law if the size of the considered region increases ($w_A \sim \log A$ at $A \to +\infty$). For the case of finite bodies (particles, whiskers, etc.), the expression (15) is modified due to screening effect of the surfaces, and the energy density w_A has a finite value (see, for example, similar calculations for the disclination energy in an elastic sphere [41]). The equation (16) shows the influence of the angle between disclinations α on the energy of pair interactions and it is the main interest of this study.

3. Results and discussion

Let us proceed to the analysis of the obtained expressions (5) and (7) for the energies of the pair interaction of intersecting dilatation lines L_I and L_{II}. The specific interaction energy of defects depending on the angle between them is shown in Fig. 2. Energy of interaction $\tilde{W}_z^{L_{I-II}}$ takes the highest value for angles α = 0, π and equals to the linear elastic energy of one dilatational line with its eigenstrain deformation $2\varepsilon^*$. The specific energy takes the zero value when the lines of defects intersect under right angles (α = π/2). In this specific case, the interaction of defects is determined by the total energy of the system presented in (7). Thus, it can be inferred that the interaction of dilatation lines intersecting under right angles is completely determined by their total eigenstrain deformation at the point of their intersection; the remaining sections do not contribute to the total interaction energy. It is worth noting that the energy of the pair interaction in (7) is equal to doubled elastic energy of a point defect with its triaxial eigenstrain ε^*.

Now turn to the dependences of the interaction energy density of intersecting wedge disclinations. In Fig. 3a the dependences of the normalized energy density w_α on the value of the angle between them α, plotted for different values of the Poisson ratio of the medium ν = 0.1 and 0.3 are shown. According to Fig. 3a it can be seen that the energy densities take the smallest value ($\sim 0.6G\omega^2/(4\pi^2)$ for ν = 0.3) in the case when the disclination axes intersect under right angles. On the contrary, the energy densities take the greatest value ($\sim 1.6G\omega^2/(4\pi^2)$ for ν = 0.3) in the case when the disclination axes coincide (α = 0, π). Here we present analytical formulas for determining the interaction energy density of disclinations intersecting under angles α = π/2 and 0, π, obtained from expression (16):

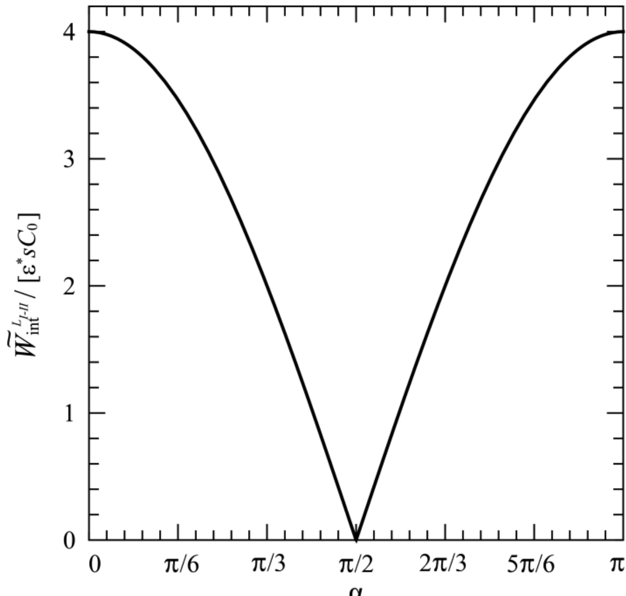

Fig. 2. Specific interaction energy of intersecting dilatational lines in dependence on the angle α. The energy is given in units $\varepsilon^* s C_0$

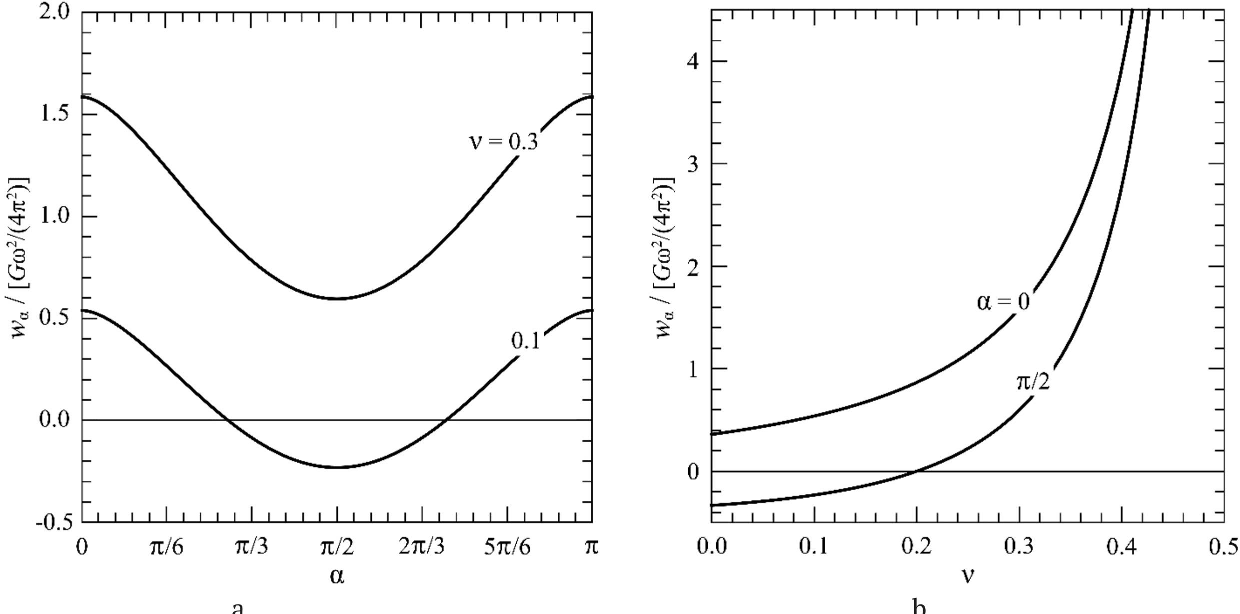

Fig. 3. Dependences of the interaction energy density of intersecting wedge disclinations w_α: a) on the intersection angle α for ν = 0.1 and 0.3; b) on the Poisson ratio ν of the elastic medium for α = 0 and π/2. The energy density is given in units $G\omega^2/(4\pi^2)$

$$w_{\alpha=\pi/2} = \frac{G\omega^2}{4\pi^2(1-\nu)}\left[-\frac{1-5\nu}{3(1-2\nu)}\right], \quad (17)$$

$$w_{\alpha=0,\,\pi} = \frac{G\omega^2}{4\pi^2(1-\nu)}\left[-\frac{1-5\nu}{3(1-2\nu)} + \log 2\right]. \quad (18)$$

Expression (18) can also be used to determine the part of the elastic energy density of a disclination with strength of 2ω independent of R.

In addition, we note that according to Fig. 3a, disclinations located in elastic space with a relatively large Poisson ratio ν has a higher energy density: with increasing ν, the interaction energy density w_α increases. Let us turn to the dependences of the energy density of the interaction of disclinations w_α from the Poisson ratio of the medium ν (0.0 < ν < 0.5), presented in Fig. 3b. In the case when the disclination axes coincide (α = 0 or π), the interaction energy density is positive. On the contrary, in the case when the disclination axes intersect under right angles (α = π/2), the interaction energy density can take negative values. The value of Poisson ratio, at which the energy density changes sign, is determined from expression (17) and equal to 0.2. This means that in media with a relatively low Poisson ratio, a disclination can decay into two intersecting disclinations, subsequently reducing the total energy of the system. Similar phenomenon were observed experimentally for the case of translational decay of a disclination, for example, in decahedral particles containing one wedge positive disclination with a strength of 0.128 rad the decay of the disclination in two ones with parallel axes, was recorded during the growth of particles [42].

4. Conclusions

Thus, the study presents a calculation of the pair interaction energies of two intersecting defects. In the first part of the study, the specific energy of intersecting dilatation lines was determined in dependence on the angle between the lines of defects. It was shown that the energy of the pair interactions of intersecting dilatation lines takes a finite value, completely determined by the fields of defects in the vicinity of the intersection point. In the second part of the study, the interaction energy of intersecting wedge disclinations is found as the sum of two components: the first component contains the logarithmic singularity of the radial coordinate attributed to elastic fields and energies of disclination-type defects, the second term demonstrates the influence of the angle between the disclination axes on their interaction energy. The latter term is discussed in detail in the study. For instance, it was

demonstrated that disclinations intersecting under right angles have less interaction energy then disclinations with coincided axes. In addition, it was shown that the interaction energy of intersecting disclinations strongly depends on the properties of the elastic medium viz the Poisson ratio. For example, the higher Poisson ratio of the media the higher pair interaction energy of disclinations. The interaction energy of intersecting disclinations can take negative values in media with a relatively small Poisson ratio ($\nu < 0.2$). Probably, in the media with relatively small Poisson ratio the disclination could decay in two intersecting disclinations decreasing the total energy. In conclusion, it is worth noting that the obtained analytical relations for the pair interaction energy of intersecting dilatation lines and disclinations are of practical interest for further research, in particular, to employ construction of in theoretical modelling of residual stresses relaxation in icosahedral particles containing 6 intersecting wedge disclinations with a strength of 0.128 rad due to the impurity segregation at the cores of the disclinations.

Contribution of the authors

The authors contributed equally to this article.

Conflict of interests

The authors declare that they have no known competing financial interests or personal relationships that could have influenced the work reported in this paper.

References

1. Martinez A. D., Fioretti A. N., Toberer E. S., Tamboli A. C. Synthesis, structure, and optoelectronic properties of II–IV–V 2 materials. *Journal of Materials Chemistry A*. 2017;5(23): 11418–11435. https://doi.org/10.1039/C7TA00406K

2. Zhou H., Xu J., Liu X., ... Fan T. Bio-inspired photonic materials: Prototypes and structural effect designs for applications in solar energy manipulation. *Advanced Functional Materials*. 2018;28(24): 1705309. https://doi.org/10.1002/adfm.201705309

3. Shao L., Zhuo X., Wang J. Advanced plasmonic materials for dynamic color display. *Advanced Materials*. 2018;30(16): 1704338. https://doi.org/10.1002/adma.201704338

4. Matthews J. W., Blakeslee A. E. Defects in epitaxial multilayers: I. Misfit dislocations. *Journal of Crystal Growth*. 1984;27: 118–125. https://doi.org/10.1016/S0022-0248(74)80055-2

5. Freund L. B., Suresh S. *Thin film materials: stress, defect formation and surface evolution*. Cambridge: Cambridge University Press; 2003. 803 p. https://doi.org/10.1017/CBO9780511754715

6. Gutkin M. Yu., Kolesnikova A. L., Romanov A. E. Nanomechanics of stress relaxation in composite low-dimensional structures. *Encyclopedia of Continuum Mechanics*. 2020: 1778–1799. https://doi.org/10.1007/978-3-662-55771-6_161

7. Smirnov A. M., Kremleva A. V., Ivanov A. Yu., ... Romanov A. E. Stress-strain state and piezoelectric polarization in orthorhombic Ga_2O_3 thin films depending on growth orientation. *Materials and Design*. 2023;226: 111616. https://doi.org/10.1016/j.matdes.2023.111616

8. Kukushkin S. A., Osipov A. V. A new mechanism of elastic energy relaxation in heteroepitaxy of monocrystalline films: Interaction of point defects and dilatation dipoles. *Mechanics of Solids*. 2013;48: 216–227. https://doi.org/10.3103/S0025654413020143

9. Ramdani R., Hounkpati V., Chen J., Ruterana P. Stress relaxation in III-V nitrides: investigation of metallic atoms interaction with the N-vacancy. *Europhysics Letters*. 2022;137(6): 66003. https://doi.org/10.1209/0295-5075/ac6067

10. Gutkin M. Yu., Kolesnikova A. L., Romanov A. E. Misfit dislocations and other defects in thin films. *Materials Science and Engineering: A*. 1993;164(1-2): 433–437. https://doi.org/10.1016/0921-5093(93)90707-L

11. Bobylev S. V., Morozov N. F., Ovid'Ko I. A., Semenov B. N., Sheinerman A. G. Misfit dislocation configurations at interphase boundaries between misoriented crystals in nanoscale film-substrate systems. *Reviews on Advanced Materials Science*. 2012;32(1): 24–33.

12. Gutkin M. Yu., Kolesnikova A. L., Krasnitckii S. A., Romanov A. E., Shalkovskii A. G. Misfit dislocation loops in hollow core-shell nanoparticles. *Scripta Materialia*. 2014;83: 1–4. https://doi.org/10.1016/j.scriptamat.2014.03.005

13. Kukushkin S. A., Osipov A. V., Bessolov V. N., Konenkova E. V., Panteleev V. N. Misfit dislocation locking and rotation during gallium nitride growth on SiC/Si substrates. *Physics of the Solid State*. 2017;59(4): 674–681. https://doi.org/10.1134/S1063783417040114

14. Krasnitckii S. A., Smirnov A. M., Gutkin M. Yu. Axial misfit stress relaxation in core-shell nanowires with polyhedral cores through the nucleation of misfit prismatic dislocation loops. *Journal of Materials Science*. 2020;55: 9198–9210. https://doi.org/10.1007/s10853-020-04401-3

15. Smirnov A. M., Krasnitckii S. A., Gutkin M. Yu. Generation of misfit dislocations in a core-shell

nanowire near the edge of prismatic core. *Acta Materialia*. 2020;186: 494–510. https://doi.org/10.1016/j.actamat.2020.01.018

16. Smirnov A. M., Krasnitckii S. A., Rochas S. S., Gutkin M. Yu. Critical Conditions of Dislocation Generation in Core-Shell Nanowires: A Review. *Reviews on Advanced Materials and Technologies*. 2020;2(3): 19–43. https://doi.org 10.17586/2687-0568-2020-2-3-19-4

17. Smirnov A. M., Young E. C., Bougrov V. E., Speck J. S., Romanov A. E. Stress relaxation in semipolar and nonpolar III-nitride heterostructures by formation of misfit dislocations of various origin. *Journal of Applied Physics*. 2019;126(24): 245104. https://doi.org/10.1063/1.5126195

18. Sheinerman A. G., Gutkin M. Yu. Misfit disclinations and dislocation walls in a two-phase cylindrical composite. *Physica Status Solidi (a)*. 2001;184(2): 485–505. https://doi.org/10.1002/1521-396X(200104)184:2<485::AID-PSSA485>3.0.CO;2-4

19. Kolesnikova A. L., Ovidko I. A., Romanov A. E. Misfit disclination structures in nanocrystalline and polycrystalline films. *Solid State Phenomena*. 2002;87: 265–276. https://doi.org/10.4028/www.scientific.net/SSP.87.265

20. Skiba N. V., Ovid'ko I. A., Sheinerman A. G. Misfit disclination dipoles in nanocrystalline films and coatings. *Physics of the Solid State.* 2009;51(2): 280–285. https://doi.org/10.1134/S1063783409020127

21. Telyatnik R. S., Osipov A. V., Kukushkin S. A. Pore-and delamination-induced mismatch strain relaxation and conditions for the formation of dislocations, cracks, and buckles in the epitaxial AlN (0001)/SiC/Si (111) heterostructure. *Physics of the Solid State*. 5015;57(1): 162–172. https://doi.org/10.1134/S106378341501031X

22. Argunova T. S., Gutkin M. Yu., Mokhov E. N., Kazarova O. P., Lim J. H., Shcheglov M. P. Prevention of AlN crystal from cracking on SiC substrates by evaporation of the substrates. *Physics of the Solid State.* 2015;57(12): 2473–2478. https://doi.org/10.1134/S1063783415120057

23. Kukushkin S. A., Osipov A. V., Rozhavskaya M. M., Myasoedov A. V., Troshkov S. I., Lundin V. V., Sorokin L. M., Tsatsul'nikov A. F. Growth and structure of GaN layers on silicon carbide synthesized on a Si substrate by the substitution of atoms: a model of the formation of V-defects during the growth of GaN. *Physics of the Solid State*. 2015;57(9): 1899–1907. https://doi.org/10.1134/S1063783415090218

24. Schmidt V., McIntyre P. C., Gцsele U. Morphological instability of misfit-strained core-shell nanowires. *Physical Review B*. 2008;77(23): 235302. https://doi.org/10.1103/PhysRevB.77.235302

25. Hofmeister H. Shape variations and anisotropic growth of multiply twinned nanoparticles. *Zeitschrift fьr Kristallographie*. 2009;224(11): 528–538. https://doi.org/10.1524/zkri.2009.1034

26. Ruditskiy A., Peng H. C., Xia Y. Shape-controlled metal nanocrystals for heterogeneous catalysis. *Annual Rview of Chemical and Biomolecular Engineering*. 2016;7: 327–348. https://doi.org/10.1146/annurev-chembioeng-080615-034503

27. Romanov A. E., Kolesnikova A. L. Application of disclination concept to solid structures. *Progress in Materials Science*. 2009;54(6): 740–769. https://doi.org/10.1016/j.pmatsci.2009.03.002

28. Romanov A. E., Kolesnikova A. L. Elasticity boundary-value problems for straight wedge disclinations. A review on methods and results. *Reviews on Advanced Materials and Technologies*. 2021;3(1): 55–95. https://doi.org/10.17586/2687-0568-2021-3-1-55-95

29. Yasnikov I. S., Vikarchuk A. A. Voids in icosahedral small particles of an electrolytic metal. *JETP Letters.* 2006;83(1): 42–45. https://doi.org/10.1134/S0021364006010103

30. Huang J., Yan Y., Li X., Qiao X., Wu X., Li J., Shen R., Yang D., Zhang H. Unexpected Kirkendall effect in twinned icosahedral nanocrystals driven by strain gradient. *Nano Research*. 2020;13: 2641–2649. https://doi.org/10.1007/s12274-020-2903-9

31. Romanov A. E., Polonsky I. A., Gryaznov V. G., Nepijko S. A., Junghanns T., Vitrykhovski N. J. Voids and channels in pentagonal crystals. *Journal of Crystal Growth*. 1993;129(3-4): 691–698. https://doi.org/10.1016/0022-0248(93)90505-Q

32. Gutkin M. Yu., Panpurin, S. N. Spontaneous formation and equilibrium distribution of cylindrical quantum dots in atomically inhomogeneous pentagonal nanowires. *Journal of Macromolecular Science, Part B*. 2013;*52*(12): 1756–1769. https://doi.org/10.1080/00222348.2013.808929

33. Krasnitckii S. A., Gutkin M. Yu., Kolesnikova A. L., Romanov A. E. Formation of a pore as stress relaxation mechanism in decahedral small particles. *Letters on Materials*. 2022;12(2): 137–141. https://doi.org/10.22226/2410-3535-2022-2-137-141

34. Khramov A. S., Krasnitckii S. A., Smirnov A. M., Gutkin M. Yu. The void evolution kinetics driven by residual stress in icosahedral particles. *Materials Physics and Mechanics*. 2022;50(3): 401–409. https://doi.org/10.18149/MPM.5032022_4

35. Mura T. *Micromechanics of defects in solids*. Boston: Martinus Nijhoff Publishers; 1987. 587 p.

36. Kolesnikova A. L., Soroka R. M., Romanov A. E. Defects in the elastic continuum: classification, fields and physical analogies. *Materials Physics and Mechanics.* 2013;17(1): 71–91.

37. De Wit R. Partial disclinations. *Journal of Physics C: Solid State Physics*. 1972;5(5): 529–534. https://doi.org/10.1088/0022-3719/5/5/004

38. Vladimirov V. I., Romanov A. E. *Disclinations in Crystals*. Leningrad: Izdatel'stvo Nauka; 1986. 224p.

39. Kolesnikova A. L., Gutkin M. Yi., Proskura A. V., Morozov N. F., Romanov A. E. Elastic fields of straight wedge disclinations axially piercing bodies with spherical free surfaces. *International Journal of Solids and Structures*. 2016;99: 82–96. https://doi.org/10.1016/j.ijsolstr.2016.06.029

40. Prudnikov A. P., Brychkov I. A., Marichev O. I. *Integrals and series: special functions (Vol. 2)*. Amsterdam: Gordon and Breach Science Publishers; 1998. 740p.

41. Polonsky I. A., Romanov A. E., Gryaznov V. G., Kaprelov A. M. Disclination in an elastic sphere. *Philosophical Magazine A*. 1991;64(2): 281–287. https://doi.org/10.1080/01418619108221185

42. Mayoral A., Barron H., Estrada-Salas R., Vazquez-Duran A., Josй-Yacamбn M. Nanoparticle stability from the nano to the meso interval. *Nanoscale*. 2010;2(3): 335–342. https://doi.org/10.1039/B9NR00287A

Information about the authors

Stanislav A. Krasnitckii, Cand. Sci. (Phys.–Math.), Associate Professor at the Institute of Advanced Data Transfer Systems, ITMO University (St. Petersburg, Russian Federation).

https://orcid.org/0000-0003-4363-8242
krasnitsky@inbox.ru

Andrei M. Smirnov, Cand. Sci. (Phys.–Math.), Associate Professor at the Institute of Advanced Data Transfer Systems, ITMO University (St. Petersburg, Russian Federation).

https://orcid.org/0000-0002-7962-6481
smirnov.mech@gmail.com

Received 21.09.2023; approved after reviewing 28.09.2023; accepted for publication 16.10.2023; published online 25.12.2023.

Translated by Valentina Mittova

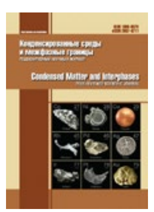

ISSN 1606-867X (Print)
ISSN 2687-0711 (Online)

Condensed Matter and Interphases

Kondensirovannye Sredy i Mezhfaznye Granitsy

https://journals.vsu.ru/kcmf/

Original articles

Research article
https://doi.org/10.17308/kcmf.2023.25/11477

Semi-polar GaN(11-22) on nano-structured Si(113): a structure for reducing thermal stresses

V. N. Bessolov✉**, E. V. Konenkova, T. A. Orlova, S. N. Rodin**

Ioffe Physical-Technical Institute of the Russian Academy of Sciences,
26 Politekhnicheskaya st., St. Petersburg 194021, Russian Federation

Abstract

The article reports the growth of semi-polar GaN(11-22) layers using epitaxy from metal organic compounds on a nano-structured NP-Si(113) substrate. It was shown that upon the emergence of an island layer, elastic deformed structures of GaN(11-22)/NP-Si(113) form a nano-meter compliant silicon layer on a substrate while elastic stresses conditioned by the difference of temperature coefficients of GaN and Si in such a structure decrease.

Keywords: Semi-polar gallium nitride, Nano-structured silicon, Elastic and plastic structure deformation

Acknowledgments: The authors thank V. K. Smirnov for providing nanostructured Si(113) substrates, M. P. Shcheglov, M. E. Kompan for measurements.

***For citation*:** Bessolov V. N., Konenkova E. V., Orlova T. A., Rodin S. N. Semi-polar GaN(11-22) on nanostructured Si(113): structure for reducing thermal stresses. *Condensed Matter and Interphases*. 2023;25(4): 514–519. https://doi.org/10.17308/kcmf.2023.25/11477

Для цитирования: Бессолов В. Н., Коненкова Е. В., Орлова Т. А., Родин С. Н. Полуполярный GaN(11-22) на наноструктурированном Si(113): структура для снижения термических напряжений. *Конденсированные среды и межфазные границы*. 2023;25(4): 514–519. https://doi.org/10.17308/kcmf.2023.25/11477

✉ Vasily N. Bessolov, e-mail: bes@triat.ioffe.ru
© Bessolov V. N., Konenkova E. V., Orlova T. A., Rodin S. N., 2023

The content is available under Creative Commons Attribution 4.0 License.

1. Introduction

Semiconductor materials of wide band III-nitrides (AlN, GaN) have become the most important materials that can be used in emitters and detectors in the visible and ultraviolet spectral range, as well as in powerful electronic devices. AlN and GaN layers are usually grown on sapphire, silicon carbide, or silicon substrates. Silicon substrates are preferable due to their low cost, high availability, and potential integration of gallium nitride and silicon optoelectronics. The main disadvantages of obtaining gallium nitride on a silicon substrate are a high percentage of mismatch of crystal lattices (17%) and differences in the thermal expansion coefficients, which causes tensile stress in a layer when cooled from growth to room temperature. Strong bending and cracking of the GaN layer occurs in flat layers in case their thickness exceeds 1 μm [1]. As far as we know, the thickest GaN layer on a Si substrate was grown without cracks using surface faceting with a thickness of 19 μm and dislocation density of $1.1\cdot10^{7}$ cm^{-2} [2].

Recently, it has been proposed to use structured surfaces of Si(100) substrates, mainly in the form of linear, rectangular, or triangular micron and nano-micron sized ridges, to grow semi-polar layers. When using this technology, the preliminarily masked surface is treated with a chemical etching agent. Due to the anisotropic etching rate for different crystallographic directions, the Si(111) face can be exposed and a GaN(10-11) layer can be grown on a structured Si(100) substrate [3], or a GaN(11-22) layer can be obtained on a structured Si(113) substrate [4]. The use of faces of a structured substrate for the synthesis of semi-polar structures was shown in a number of reviews, for example, in [5, 6].

To obtain a semi-polar orientation layer, the angle between the planes of the emergence face and the substrate surface must be equal to the angle between the GaN “*c*” plane and the target semi-polar plane. The Si(113) substrate is suitable for growing semi-polar GaN(11-22) because the angle between the Si(111) planes and the (113) silicon substrate surface is close to the inclination angles of the semi-polar (11-22) plane to the (0001) plane.

The main problem of epitaxy in case of GaN heteroepitaxy on a silicon substrate is the reduction of elastic energy caused by the mismatch of lattice parameters and differences in thermal expansion coefficients, while dislocation density in the layer must be kept at a low level.

One of the promising technological methods allowing to reduce elastic stresses in the GaN(0001) layer is the use of a “compliant” Si(111) substrate due to the arrangement of pores in the near-surface layer [7].

Heteroepitaxy of a GaN layer on a Si substrate can result in the growth of elastically stressed thick epitaxial layers if the thickness of the substrate is less than the value at which its plastic deformation occurs [8]. Several experiments were conducted related to this area, including the growth of GaN on preliminarily prepared silicon nano-membranes [9] and on Si substrates etched on the reverse side to a thickness of 10 μm. However, due to the difficulties of handling nano-membranes and thin films this approach remains rather complicated for obtaining an effective “compliant” substrate. In our experiments we used a nano-sized structured layer that formed a semi-polar GaN(11-22) layer as an analogue of a “compliant” substrate.

This work is dedicated to the reduction of thermal stresses in semi-polar GaN(11-22) layers upon epitaxy on nano-structured NP-Si(113) substrates.

2. Experimental

Epitaxy of a semi-polar layer occurred on a nano-structured Si(113) substrate which had a formed U-shape (Fig. 1A) structure with a period of 30 nm and height of inclined nano-ridges of 75 nm. The nanomask was formed as a result of a two-stage process described in [11]. AlN and GaN layers on NP-Si(113) substrates were grown by metal organic chemical vapor deposition (MOCVD) on a modified EpiQuip unit with a horizontal reactor similar to [12]. Hydrogen was used as the carrier gas, while ammonia, trimethylgallium, and trimethylaluminum were used as precursors. There were structures of two types that consisted of an AlN buffer layer with a thickness of about 10 nm (Fig. 1b) and, first of all, a GaN island layer (Fig. 1c) and, second, a continuous GaN layer with a thickness of ~1 μm. X-ray diffraction analysis showed that continuous GaN(11-22)/NP-Si(113) structures

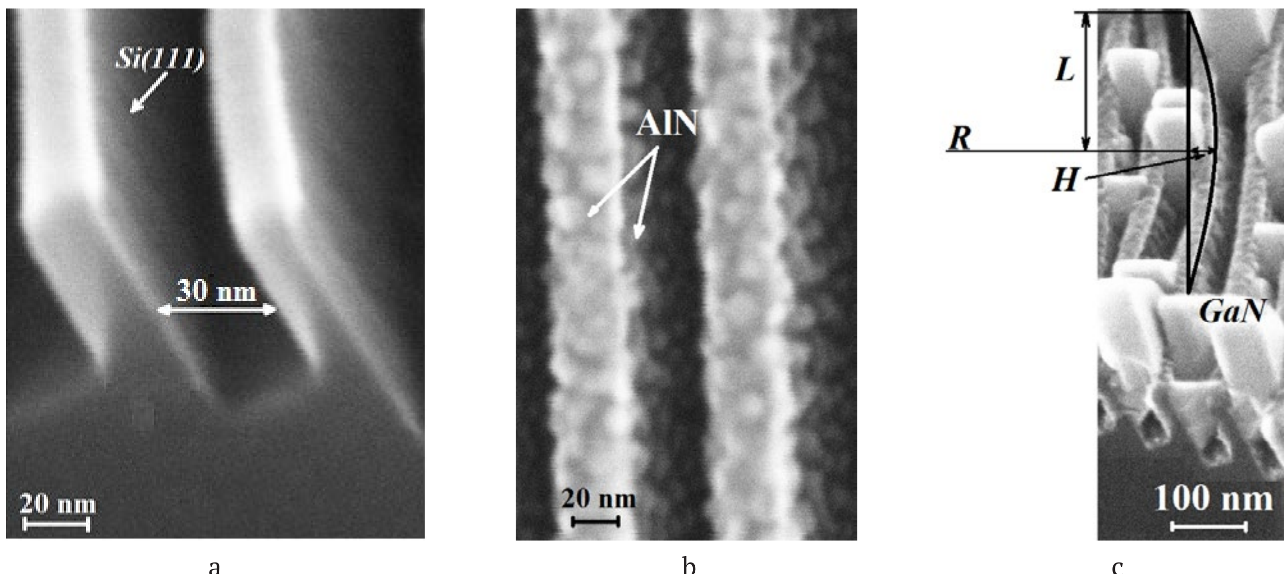

Fig. 1. SEM image of a NP-Si(113) cleavage of substrate (a), substrate covered with a thin layer of AlN (b), and an insular layer of GaN (c)

had the half-width of an X-ray diffraction curve ω_Θ ~ 30 arcmin.

Scanning electron microscopy (SEM) showed that after the growth of the AlN buffer layer, there were no distortions of the surface pattern of the structure (Fig. 1b), and after the synthesis of the island layer, deformations on the surface Si ridges were observed.

To evaluate the elastic stresses of structures with a continuous layer, Raman spectra were measured in the region of the E_2(high) phonon mode. As for GaN(11-22), line E_2(high) = 565.2 cm^{-1}, while, as we know, for an unstrained structure position E_2(high) = 568 cm^{-1}, which indicates the presence of GaN compression deformation. For GaN(11-22) layers, according to $\Delta\omega = K\cdot\sigma$, where K = 4.2 cm^{-1}/GPa we estimated the value of longitudinal elastic stressed which was −0.67 GPa, while the same value for the GaN layer grown on a Si(111) flat substrate was −1.19 GPa [12].

3. Results and discussion

Upon GaN heteroepitaxy on Si(111), the values of elastic stresses that occur due to the mismatch of lattice parameters are significantly greater as compared to the values of thermal stresses. We assumed that there was no plastic deformation in the island layer and, therefore, the behavior of the structured surface, which was determined using an electron microscope, would be identified mainly by the difference in the layer lattice and the substrate constants. Plastic deformation would occur in a continuous 1 µm thick GaN(11-22) layer at the epitaxy temperature, and the elastic stresses measured by Raman scattering would be determined by thermal stresses.

The bending of the ridges on the NP-Si(113) surface in a structure with an island layer clearly indicates the “compliance” of the structured substrate. The arcuate bending of the “ridge” (Fig. 1c) allowed us to evaluate the bending radius of a “compliant” Si layer parallel to the plane of the Si(111) face based on the values H, the height of arc, and L, half-length of the arc horde (Fig. 1c). For this we used the formula $R = \frac{L^2 + H^2}{2H}$. The bend radius of the ridge was about R = 510 nm.

In case of epitaxy of hexagonal GaN on cubic silicon with a thickness of about 400 µm, the critical layer thickness that results in plastic deformation would be small, as even in case of GaN epitaxy on a standard sapphire substrate with a thin AlN buffer layer it is about 29 Å [13]. We assume that this thickness slightly increases for islands, but they have no plastic deformations (Fig. 2a). Elastic stresses in the GaN layer cause a bending moment on the face of the Si(111) substrate, which leads to a curvature in the ridge. Assuming isotropic elastic behavior and spatially

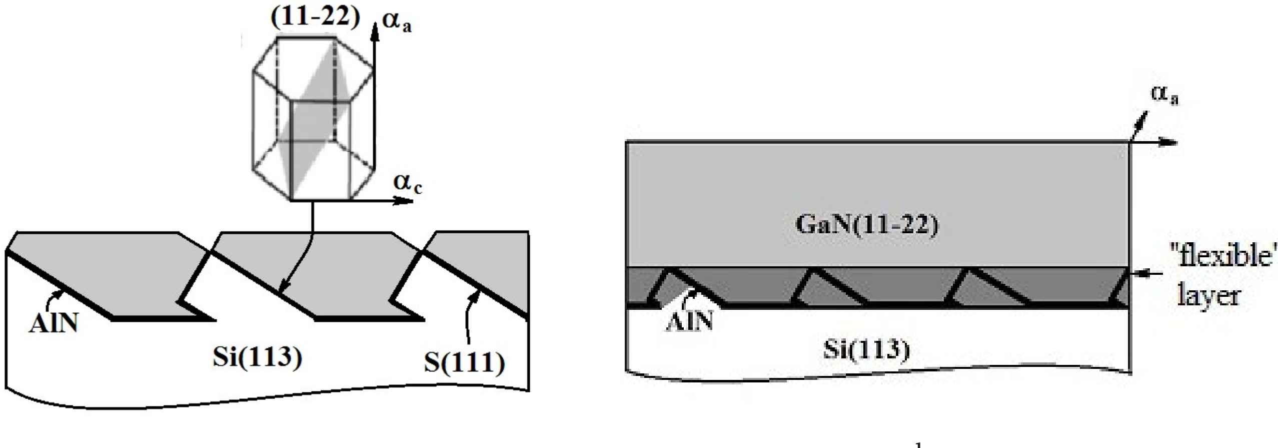

a b

Fig. 2. A schematic representation of the growth of GaN(11-22) layers on a NP-Si(113) substrate: a) insular; b) solid

homogeneous biaxial misfit deformation between the GaN layer and the "compliant" substrate layer, the curvature κ = 1/*R* can be calculated using the expression [14,15]:

$$\frac{1}{R} = 6m\varepsilon_m\left(\frac{h}{h_S}\right)\left(\frac{1+h}{1+mh\left(4+6h+4h^2\right)+m^2h^4}\right), (1),$$

where $m = \frac{M_f}{M_S}, h = \frac{h_f}{h_S} = 1$.

While with ε = 0.17, E_{GaN} = 295 GPa and ν_{GaN} = 0.25, and E_{Si} = 165.5 GPa and ν_{Si} = 0.18, value *R* = about 290 nm, which is approximately twice less than the experimentally estimated value. The difference can be explained by the influence of the mechanical connections of the "compliant" layer with the rest of the substrate on the bending radius.

Upon heteroepitaxy of a continuous GaN layer, the value of the elastic stresses of GaN(11-22)/NP-Si(113) structures emerging during cooling depended on the difference in the thermal expansion coefficients of GaN and Si Δα = αGaN – αSi. The thermal expansion coefficient of an isotropic silicon substrate was $\alpha_{Si} = 3.6\cdot10^{-6}$ K^{-1} [16], while the thermal expansion coefficients for anisotropic semi-polar GaN differed in the direction of the axes: "*a*" – $\alpha^{l}_{GaN(a)}$ – $5.6\cdot10^{-6}$ K^{-1} и "*c*" – $\alpha^{l}_{GaN(c)} = 4.8\cdot10^{-6}$ K^{-1} [17]. Then, according to expression 2 [13], stresses along axes "*a*" and "*c*" would have values σ_a = –0.78 Gpa and σ_c = –0.47 GPa:

$$\sigma_f = \frac{E_{GaN}}{1-\nu_{GaN}} \frac{\Delta\alpha\Delta T}{1+\frac{E_{GaN}(1-\nu_{Si})h_{GaN}}{E_{Si}\left(1-\nu_{GaN}\right)H_{Si}}}, \quad (2)$$

where Δ*T* =1000 °C, *H* = 400 μm, *h* = 1 μm. When estimating stresses for a heterostructure with a continuous layer, a significant role is attributed to, first of all, the degree of correlation between the compliant layer with its bulk part and, second, the possible impact of the faceting of the crystallized layer surface on the value of thermal stresses, similar to [18]. The value of thermal stresses, estimated using expression (2), shows a satisfactorily correspondence to the value of stresses in the structure obtained by Raman spectra. Indeed, according to Raman data, the stress value in a 1 μm thick GaN layer was -0.67 GPa, which corresponded to the effective value of the thermal expansion coefficient for GaN(11-22).

During epitaxy of a semi-polar GaN(11-22) layer on a nano-structured NP-Si(113) substrate in the course of the formation of islands, the compliant near-surface layer was elastically deformed on the nano-structured Si(113) substrate, which formed a compliant layer and reduced the value of thermal deformation of the semi-polar layer (Fig. 2b).

4. Conclusions

Therefore, it was found that at the initial stage of GaN(11-22) epitaxy the nano-structured Si(113) substrate formed a "compliant" layer that

can reduce thermal stresses. This approach can be useful for the technology of structure integration based on GaN-on-Si.

Contribution of the authors

The authors contributed equally to this article.

Conflict of interests

The authors declare that they have no known competing financial interests or personal relationships that could have influenced the work reported in this paper.

References

1. Dadgar A. Sixteen years GaN on Si. *Physica Status Solidi (b)*. 2015;252(5): 1063–1068. https://doi.org/10.1002/pssb.201451656

2. Tanaka A., Choi W., Chen R., Dayeh Sh. A. Si complies with GaN to overcome thermal mismatches for the heteroepitaxy of thick GaN on Si. *Advanced Materials*. 2017;29: 1702557. https://doi.org/10.1002/adma.201702557

3. Tanikawa T., Hikosaka T., Honda Y., Yamaguchi M., Sawaki N. Growth of semi-polar (11-22) GaN on a (113) Si substrate by selective MOVPE. *Physica Status Solidi (c)*. 2008;5: 2966–2968. https://doi.org/10.1002/pssc.200779236

4. Bai J., Yu X., Gong Y., Hou Y. N., Zhang Y., Wang T. Growth and characterization of semi-polar (11-22) GaN on patterned (113) Si substrates. *Semiconductor Science and Technology*. 2015;30: 065012. https://doi.org/10.1088/0268-1242/30/6/065012

5. Li H., Zhang H., Song J., Li P., Nakamura Sh., DenBaars S. P. Toward heteroepitaxially grown semipolar GaN laser diodes under electrically injected continuous-wave mode: From materials to lasers. *Applied Physics Reviews*. 2020;7: 041318. https://doi.org/10.1063/5.0024236

6. Wang T. Topical review: Development of overgrown semi-polar GaN for high efficiency green/yellow emission. *Semiconductor Science Technology*. 2016;31: 93003. https://doi.org/10.1088/0268-1242/31/9/093003

7. Ishikawa H., Shimanaka K., Tokura F., Hayashi Y., Hara Y., Nakanishi M. MOCVD growth of GaN on porous silicon substrates. *Journal of Crystal Growth*. 2008;310: 4900–4903. https://doi.org/10.1016/j.jcrysgro.2008.08.030

8. Lo Y. H. New approach to grow pseudomorphic structures over the critical thickness. *Applied Physics Letters*. 1991;59(18): 2311-2313. https://doi.org/10.1063/1.106053

9. Wang K., Song Y., Zhang Y., Zhang Y., Cheng Z. Quality improvement of GaN epi-layers grown with a strain-releasing scheme on suspended ultrathin Si nanoflm substrate. *Nanoscale Research Letters*. 2022;17(1): 99. https://doi.org/10.1186/s11671-022-03732-1

10. Wang X., Wu A., Chen J., Wu Y., Zhu J., Yang H. Study of GaN growth on ultra-thin Si membranes. *Solid State Electron*. 2008;52(6): 986–989. https://doi.org/10.1016/j.sse.2008.01.026

11. Smirnov V. K., Kibalov D. S., Orlov O. M., Graboshnikov V. V. Technology for nanoperiodic doping of a metal–oxide–semiconductor field-effect transistor channel using a self-forming wave-ordered structure. *Nanotechnology*. 2003;14(7): 709–715. https://doi.org/10.1088/0957-4484/14/7/304

12. Bessolov V. N., Kompan M. E., Konenkova E. V., Rodin S. N. Deformation of semipolar and polar gallium nitride synthesized on a silicon substrate. *Izvestiya Rossiiskoi Akademii Nauk. Seriya Fizicheskaya*. 2022;86(7): 981–984. (In Russ., Abstract in Eng.). https://doi.org/10.31857/S0367676522070109

13. Kim Ch., Robinson I. K., Myoung J., Shim K., Yoo M. C., Kim K. Critical thickness of GaN thin films on sapphire (0001). *Applied Physics Letters*. 1996;69: 2358–2360. https://doi.org/10.1063/1.117524

14. Freund L. B., Floro J. A., Chason E. Extensions of the Stoney formula for substrate curvature to configurations with thin substrates or large deformations. *Applied Physics Letters*. 1999;74: 1987–1989. *https://doi.org/10.1063/1.123722*

15. Krost A., Dadgar A., Strassburger G., Clos R. GaN-based epitaxy on silicon: stress measurements. *Physica Status Solidi (a)*. 2003;200(1): 26–35. https://doi.org/10.1002/pssa.200303428

16. Katona M., Speck J. S., Denbaars S. P. Effect of the nucleation layer on stress during cantilever epitaxy of GaN on Si (111). *Physica Status Solidi (a)*. 2002;194(2): 550–553. https://doi.org/10.1002/1521-396x(200212)194:2<550::aid-pssa550>3.0.co;2-r

17. Wang K., Reeber R.R. Thermal expansion of GaN and AlN. *Materials Research Society Symposia Proceedings*. 1998;482: 863–868. https://doi.org/10.1557/PROC-482-863

18. Tanaka A., Choi W., Chen R., Dayeh Sh. A. Si complies with GaN to overcome thermal mismatches for the heteroepitaxy of thick GaN on Si. *Advanced Materials*. 2017;29(38): 1702557. https://doi.org/10.1002/adma.201702557

Information about the authors

Vasily N. Bessolov, Cand. Sci. (Phys.–Math.), Senior Researcher, Ioffe Physical-Technical Institute of the Russian Academy of Sciences (St. Petersburg, Russian Federation).

https://orcid.org/0000-0001-7863-9494
bes@triat.ioffe.ru

Elena V. Konenkova, Cand. Sci. (Phys.–Math.), Senior Researcher, Ioffe Physical-Technical Institute of the Russian Academy of Sciences (St. Petersburg, Russian Federation).

https://orcid.org/0000-0002-5671-5422
lena@triat.ioffe.ru

Tatiana A. Orlova, Cand. Sci. (Phys.–Math.), Researcher, Ioffe Physical-Technical Institute of the Russian Academy of Sciences (St. Petersburg, Russian Federation).

https://orcid.org/0009-0007-8234-127X
Shikina71@hotmail.com

Sergey N. Rodin, Researcher, Ioffe Physical-Technical Institute of the Russian Academy of Sciences (St. Petersburg, Russian Federation).

https://orcid.org/0000-0003-2236-8642
s_rodin77@mail.ru

Received 14.08.2023; approved after reviewing 28.08.2023; accepted for publication 16.10.2023; published online 26.12.2023.

Translated by Marina Strepetova

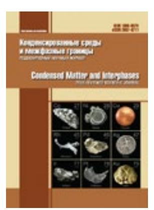

ISSN 1606-867X (Print)
ISSN 2687-0711 (Online)
Condensed Matter and Interphases
Kondensirovannye Sredy i Mezhfaznye Granitsy
https://journals.vsu.ru/kcmf/

Original articles

Research article
https://doi.org10.17308/kcmf.2023.25/11475

Structural and optical properties of composition-graded InGaN nanowires

V. O. Gridchin[1–3]✉, R. R. Reznik[1–4], K. P. Kotlyar[1], D. A. Kirilenko[5], A. S. Dragunova[6], N. V. Kryzhanovskaya[6], G. E. Cirlin[1–5]

*[1]St. Petersburg State University,
7-9 Universitetskaya Embankment, St. Petersburg 199034, Russian Federation*

*[2]Alferov University,
8/3 Khlopina st., St. Petersburg 194021, Russian Federation*

*[3]Institute for Analytical Instrumentation of the Russian Academy of Sciences,
26 Rizhsky st., St. Petersburg 190103, Russian Federation*

*[4]ITMO University,
49 Kronverksky pr., bldg. A, St. Petersburg 197101, Russian Federation*

*[5]Ioffe Institute,
26 Polytechnicheskaya st., St. Petersburg 194021, Russian Federation*

*[6]HSE University,
3/1 A Kantemirovskaya st., St. Petersburg 194100, Russian Federation*

Abstract

At the moment, InGaN ternary compounds are of a great interest for the development of devices for sunlight driven water splitting. However, the synthesis of such materials is hindered by the fact that $In_xGa_{1-x}N$ layers are susceptible to phase decomposition at *x* from 20 to 80%. Nanowires can be a promising solution to this problem. The purpose of our study was to analyze the structural and optical properties of $In_xGa_{1-x}N$ nanowires with a gradient x content being inside the miscibility gap.

$In_xGa_{1-x}N$ nanowires were grown on silicon substrates using plasma-assisted molecular beam epitaxy. The structural properties of nanowires were studied using scanning and transmission electron microscopy. The chemical composition and optical properties of nanowires were analyzed using energy-dispersive microanalysis and photoluminescence spectroscopy.

It was shown for the first time that the composition-graded $In_xGa_{1-x}N$ nanowires with x from 40 to 60% can be grown using plasma-assisted molecular beam epitaxy. The grown samples exhibit photoluminescence at room temperature with a maximum at about 890 nm, which corresponds to an In content of about 62% according to the modified Vegard's rule and the transmission electron microscopy data. The obtained results can be of practical interest for the development of devices for water splitting induced by sunlight or sources of near IR radiation.

Keywords: InGaN, Structural properties, Miscibility gap, Molecular beam epitaxy, Optical properties, Photoluminescence, silicon

Funding: The synthesis of the experimental samples and the optical measurements were conducted with the financial support of the Russian Science Foundation, grant No. 23-79-00012. The study of the morphological properties of the grown samples was conducted with the financial support of the Ministry of Science and Higher Education of the Russian Federation, research project No. 2019-1442 (project reference number FSER-2020-0013). The structural properties of the grown samples were studied with the financial support of St. Petersburg State University, research grant No. 94033852.

✉ Vladislav O. Gridchin, e-mail: gridchinvo@gmail.com

© Gridchin V. O., Reznik R. R., Kotlyar K. P., Kirilenko D. A., Dragunova A. S., Kryzhanovskaya N. V., Cirlin G. E., 2023

The content is available under Creative Commons Attribution 4.0 License.

For citation: Gridchin V. O., Reznik R. R., Kotlyar K. P., Kirilenko D. A., Dragunova A. S., Kryzhanoskaya N. V., Cirlin G. E. Structural and optical properties of composition-graded InGaN nanowires. *Condensed Matter and Interphases*. 20223;25(4): 520–525. https://doi.org10.17308/kcmf.2023.25/11475

Для цитирования: Гридчин В. О., Резник Р. Р., Котляр К. П., Кириленко Д. А., Драгунова А. С., Крыжановская Н. В., Цырлин Г. Э. Структурные и оптические свойства InGaN нитевидных нанокристаллов с градиентным химическим составом. *Конденсированные среды и межфазные границы*. 2023;25(4): 520–525. https://doi.org10.17308/kcmf.2023.25/11475

1. Introduction

One of the main trends in the modern semiconductor industry is the development of devices which can be sources of renewable energy. In particular, devices for sunlight driven water splitting. There are a large number of materials that can be used to make water-splitting photoelectrochemical cells, including $In_xGa_{1-x}N$ ternary compounds, which are currently of great interest (1–6). Such an interest is explained by the fact that the band gap of $In_xGa_{1-x}N$ can be varied practically within the whole solar spectrum (from 0.7 eV for InN to 3.4 eV for GaN) and adjusted to the redox potential of water [1,7]. Moreover, $In_xGa_{1-x}N$ ternary compounds have a high chemical stability and a high catalytic activity [1, 2, 8]. However, the synthesis of such materials is hindered by the fact that $In_xGa_{1-x}N$ compounds are susceptible to phase decomposition, when x is from 20 to 80%, which results in low crystalline and optical quality of the grown structures [9, 10]. Nanowires can be a promising solution to this problem, since nanowires based on ternary compounds are less susceptible to phase decomposition and can be grown with a set chemical composition [11–13]. Besides, nanowires of a high crystalline quality can be grown epitaxially on substrates which differ significantly from the grown material in terms of the parameters of the crystal lattice and temperature coefficient, including on silicon [14, 15]. However, there are very few studies focusing on the growth of $In_xGa_{1-x}N$ nanowires with In within the phase decomposition region on silicon by means of molecular beam epitaxy [16–21].

The purpose of our study was to analyze the structural and optical properties of $In_xGa_{1-x}N$ nanowires with a gradient of x content being inside the miscibility gap.

2. Experimental

Samples were grown on a Riber Compact 12 molecular beam epitaxy setup with a nitrogen plasma source. The experiments were conducted on 2/4 2″ silicon substrates with crystallographic orientation (111). The substrates were put in the growth chamber and annealed at the temperature of 950 °C for 20 minutes for thermal cleaning. Then the growth temperature was reduced to 560 °C (the thermocouple temperature) and the nitrogen plasma source was ignited. The nitrogen plasma power was 400 W. The nitrogen flow rate was 0.4 cm^3/min, which corresponded to the pressure in the growth chamber of $7.4 \cdot 10^{-6}$ Torr. After the pressure in the chamber was stabilized, Ga, In, and Si control valves were opened simultaneously. The beam equivalent pressures of Ga and In flows were $1 \cdot 10^{-7}$ Torr. The temperature of the silicon source was 1350 °C. The samples were doped with silicon so that they could be further used as an anode of the photoelectrochemical cell. The growth time of the samples was 20 hours and 25 minutes.

The morphology and the structural properties of the samples were studied by means of electron microscopy using a Supra 25 scanning electron microscope (Carl Zeiss) and a JEM-2100FTEM transmission electron microscope (Jeol) with an XFlash 6TI30 energy-dispersive microanalysis system (Bruker). The optical properties of the samples were analyzed on a unique setup “Complex optoelectronic unit of the National Research University Higher School of Economics – St. Petersburg” by means of photoluminescence (PL) spectroscopy at room temperature using a He-Cd laser (325 nm) with a power of 6.5 mW. The PL signal from the samples was registered using an Ms5204i monochromator (Sol instruments) and a silicon photodetector.

3. Results and discussion

Fig. 1a-c demonstrate typical SEM images of the grown InGaN nanowires. According to the SEM data, the nanowires were formed in several stages. During the first stage, nanotubes with the length of 560 nm and diameters of ~ 50 nm (Fig. 1c)

were formed near the surface of the substrate. Then, nanowires with diameters from 100 to 200 nm were formed. The fact that the diameter of the nanowires was larger than the diameter of the nanotubes indicates a local increase in the III/V ratio. Since in our experiments the growth temperature was close to the temperature of thermal disassociation of InN in a vacuum [22–24], we assume that the formation of nanotubes can be explained by the ascending diffusion of In inside nanostructures, which in turn can result in a local increase in the III/V ratio above the nanotubes [21, 25, 26]. The height of the nanowires was 2–2.5 µm. The average density of the nanowires was $1.1 \cdot 10^9$ cm^{-2} (Fig. 1b).

An analysis of the inner structure and the chemical composition of the samples demonstrated that the concentration of In as compared to Ga in the nanotubes was about 20%. The nanotubes had a Wurtzite crystal structure. At the same time, the concentration of In in the nanowires formed above the nanotubes varied from 40 to 60% (Fig. 2a-d). Besides, at the base and in the middle of the nanowires (Fig. 2a-c) a spontaneously formed core-shell structure was observed with x of 40–50% in the cores of the nanowires and 0–5% in the shells of the nanowires. At the same time, the ratio of In with regard to Ga was 60% at the top of the nanowires. The diameter of the cores increased from 60 to 120 nm along the nanowires, while the diameter of the shells decreased accordingly, which, apparently, is explained by an increased concentration of In in the nanowires.

The samples demonstrated photoluminescence at room temperature in the range from 450 to 1000 nm (Fig. 3). The maximum PL was registered close to 890 nm. As it was previously demonstrated, the concentration of In in InGaN in the range from 0 to 50% can be evaluated with good accuracy using photoluminescence spectra [13, 16, 27, 28] according to the modified Vegard's

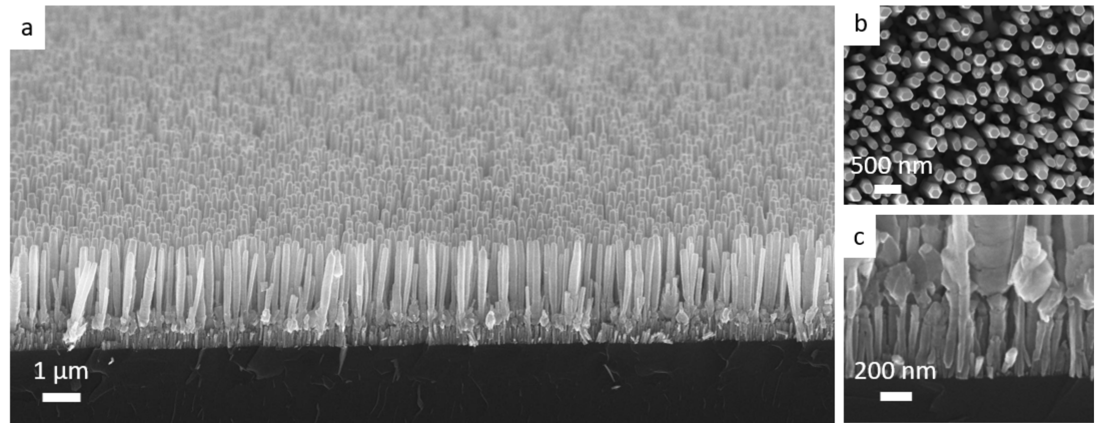

Fig. 1. Typical ISO (a) and plan-view (b) SEM images of the grown nanowires. Typical ISO SEM image of nanotubes (c)

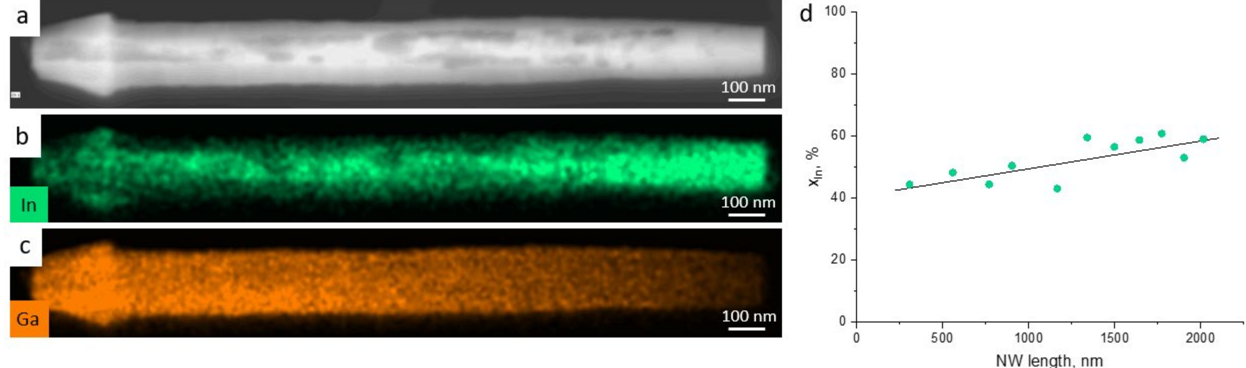

Fig. 2. A typical TEM image of InGaN nanowires (a); the distribution of Ga and In inside the nanowires (b,c); the distribution of In relative to Ga along the nanowires obtained using energy-dispersive microanalysis (d)

law with the bowing parameter b of 1.43 eV: $E_g = xE_g^{InN} + (1-x)E_g^{GaN} - bx(1-x)$, where E_g^{InN} and E_g^{GaN} are band gaps of InN and GaN (0.7 and 3.4 eV respectively), x is the concentration of In in InGaN, and b is the bowing parameter equal 1.43 eV. If we apply this law to the PL spectrum of the grown nanowires (Fig. 3), the maximum PL should correspond to InGaN with the concentration of In of 62%, which agrees well with the chemical composition at the top of the nanowires determined by means of transmission electron microscopy. Therefore, the observed maximum PL is connected with the radiation from the top of the nanowires. At the same time, the PL spectrum demonstrated regions of relatively low intensity in the range from 500 to 700 nm, which apparently can be explained by the radiation from the low-component regions of the nanowires.

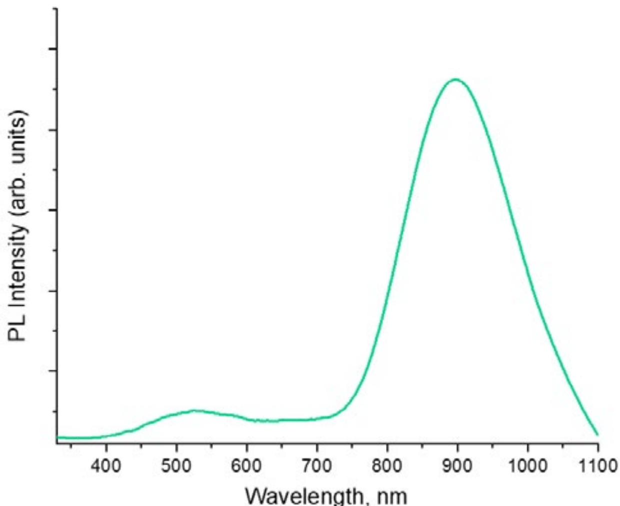

Fig. 3. A typical PL spectrum at room temperature from grown nanowires

4. Conclusions

In our study, we analyzed the structural and optical properties of composition gradient InGaN nanowires. The study demonstrated that at relatively high growth temperatures (the thermocouple temperature of 580 °C) the formation of nanowires can proceed in several stages, including the formation of nanotubes and the growth of nanowires above them. According to the TEM data, the concentration of In increases along the nanowires from 40 to 60%. The obtained nanowires demonstrated maximum photoluminescence close to 890 nm, which corresponds to the concentration of In of about 62% according to the modified Vegard's law with the bowing parameter b of 1.43 eV. The obtained results can be of practical interest for the development of devices for water splitting induced by sunlight or sources of near IR radiation.

Author contributions

V. O. Gridchin – growth of the samples, analysis of the results, text writing, conclusions. R. R. Reznik – growth of the samples. K. P. Kotlyar – analysis of the samples by means of scanning and transmission electron microscopy. D. A. Kirilenko – analysis of the samples by means of transmission electron microscopy. A. S. Dragunova – analysis of the samples by means of photoluminescence spectroscopy. N. V. Kryzhanovskaya – analysis of the samples by means of photoluminescence spectroscopy. G. E. Cirlin – problem statement, supervision.

Conflict of interests

The authors declare that they have no known competing financial interests or personal relationships that could have influenced the work reported in this paper.

References

1. Yang J., Liu Q., Zhao Z., Yuan Y., Redko R., Li S., Gao F. Hydrogen production strategy and research progress of photoelectro-chemical water splitting by InGaN nanorods. *International Journal of Hydrogen Energy*. 2023. https://doi.org/10.1016/j.ijhydene.2023.06.061

2. Tijent F. Z., Voss P., Faqir M. Recent advances in InGaN nanowires for hydrogen production using photoelectrochemical water splitting. *Materials Today Energy*. 2023;33: 101275. https://doi.org/10.1016/j.mtener.2023.101275

3. Vanka S., Zhou B., Awni R. A., … Mi Z. InGaN/Si double-junction photocathode for unassisted solar water splitting. *ACS Energy Letters*. 2020;5(12): 3741–3751. https://doi.org/10.1021/acsenergylett.0c01583

4. Lin J., Wang W., Li G. Modulating surface/interface structure of emerging InGaN nanowires for efficient photoelectrochemical water wplitting. *Advanced Functional Materials*. 2020;30(52): 2005677. https://doi.org/10.1002/adfm.202005677

5. Lin J., Zhang Z., Chai J., … Li. G. Highly efficient InGaN nanorods photoelectrode by constructing Z-scheme charge transfer system for unbiased water splitting. *Small*. 2021;17(3): 2006666. https://doi.org/10.1002/smll.202006666

6. Chen H., Wang P., Wang X., … Nötzel R. 3D InGaN nanowire arrays on oblique pyramid-textured Si (311) for light trapping and solar water splitting enhancement. *Nano Energy*. 2021;83:105768. https://doi.org/10.1016/j.nanoen.2021.105768

7. Morkoç H. *Handbook of nitride semiconductors and devices, Materials Properties, Physics and Growth*. Vol. 1. John Wiley & Sons; 2009. https://doi.org/10.1002/9783527628438

8. Hwang Y. J., Wu C. H., Hahn C., Jeong H. E., Yang P. Si/InGaN core/shell hierarchical nanowire arrays and their photoelectrochemical properties. *Nano Letters*. 2012;12(3): 1678–1682. https://doi.org/10.1021/nl3001138

9. Ho I., Stringfellow G. Solid phase immiscibility in GaInN. *Applied Physics Letters*. 1996;69(18): 2701–2703. https://doi.org/10.1063/1.117683

10. Karpov S. Strategies for creating efficient, beautiful whites. *Compound Semiconductor*. 2015; 44–47. Available at: https://compoundsemiconductor.net/article/96572/Strategies_For_Creating_Efficient_Beautiful_Whites/feature

11. Dubrovskii V. G. Liquid-solid and vapor-solid distributions of vapor-liquid-solid III-V ternary nanowires. *Physical Review Materials*. 2023;7(9): 096001. https://doi.org/10.1103/PhysRevMaterials.7.096001

12. Kuykendall T., Ulrich P., Aloni S., Yang P. Complete composition tunability of InGaN nanowires using a combinatorial approach. *Nature Materials*. 2007;6(12): 951–956. https://doi.org/10.1038/nmat2037

13. Roche E., Andre Y., Avit G., … Trassoudaine A.. Circumventing the miscibility gap in InGaN nanowires emitting from blue to red. *Nanotechnology*. 2018;29(46): 465602. https://doi.org/10.1088/1361-6528/aaddc1

14. Dubrovskii V., Cirlin G., Ustinov V. Semiconductor nanowhiskers: synthesis, properties, and applications. *Semiconductors*. 2009;43(12): 1539–1584. https://doi.org/10.1134/S106378260912001X

15. Consonni V. Self-induced growth of GaN nanowires by molecular beam epitaxy: A critical review of the formation mechanisms. *Physica Status Solidi (RRL)–Rapid Research Letters*. 2013;7(10): 699–712. https://doi.org/10.1002/pssr.201307237

16. Gridchin V. O., Kotlyar K. P., … Cirlin G. G. Multi-colour light emission from InGaN nanowires monolithically grown on Si substrate by MBE. *Nanotechnology*. 2021;32(33): 335604. https://doi.org/10.1088/1361-6528/ac0027

17. Chen H., Wang P., Ye H., … Nötzel R. Vertically aligned InGaN nanowire arrays on pyramid textured Si (1 0 0): A 3D arrayed light trapping structure for photoelectrocatalytic water splitting. *Chemical Engineering Journal*. 2021;406: 126757. https://doi.org/10.1016/j.cej.2020.126757

18. Pan X., Hong H., Deng R., Luo M., Nötzel R. In desorption in InGaN nanowire growth on Si generates a unique light emitter: from In-Rich InGaN to the intermediate core–shell InGaN to pure GaN. *Crystal Growth & Design*. 2023;23(8): 6130–6135. https://doi.org/10.1021/acs.cgd.3c00622

19. Gridchin V. O., Reznik R. R., Kotlyar K. P., … Cirlin G. E. MBE growth of InGaN nanowires on SiC/Si (111) and Si (111) substrates. *Technical Physics Letters*. 2022;48(14): 24–25. https://doi.org/10.21883/TPL.2022.14.52105.18894

20. Lu Y. J., Wang C. Y., Kim J., … Gwo S. All-color plasmonic nanolasers with ultralow thresholds: autotuning mechanism for single-mode lasing. *Nano Letters*. 2014;14(8): 4381–4388. https://doi.org/10.1021/nl501273u

21. Morassi M., Largeau L., Oehler F., … Gogneau N. Morphology tailoring and growth mechanism of Indium-rich InGaN/GaN axial nanowire heterostructures by plasma-assisted molecular beam epitaxy. *Crystal Growth & Design*. 2018;18(4): 2545–2554. https://doi.org/10.1021/acs.cgd.8b00150

22. Calleja E., Ristić J., Fernández-Garrido S., … Sánchez B. Growth, morphology, and structural properties of group-III-nitride nanocolumns and nanodisks. *Physica Status Solidi (b)*. 2007;244(8): 2816–2837. https://doi.org/10.1002/pssb.200675628

23. Koblmüller G., Gallinat C., Speck J. Surface kinetics and thermal instability of N-face InN grown by plasma-assisted molecular beam epitaxy. *Journal of Applied Physics*. 2007;101(8): 083516. https://doi.org/10.1063/1.2718884

24. Casallas-Moreno Y., Gallardo-Hernández S., Yee-Rendón C., … López-López M. Growth mechanism and properties of self-assembled inn nanocolumns on al covered si (111) substrates by pa-MBE. *Materials*. 2019;12(19): 3203. https://doi.org/10.3390/ma12193203

25. Gridchin V., Dragunova A., Kotlyar K., … Cirlin G. E. Morphology transformation of InGaN nanowires grown on Si substrate by PA-MBE. *Journal of Physics: Conference Series*. 2021;2086(1): 012013. https://doi.org/10.1088/1742-6596/2086/1/012013

26. Zhang X., Haas B., Rouvière J. L., Robin E., Daudin B. Growth mechanism of InGaN nano-umbrellas. *Nanotechnology*. 2016;27(45): 455603. https://doi.org/10.1088/0957-4484/27/45/455603

27. Orsal G., El Gmili Y., Fressengeas N., … Salvestrini J. P. Bandgap energy bowing parameter of strained and relaxed InGaN layers. *Optical Materials Express*. 2014;4(5): 1030–1041. https://doi.org/10.1364/OME.4.001030

28. Tourbot G., Bougerol C., Grenier A., … Daudin B. Structural and optical properties of InGaN/GaN nanowire heterostructures grown by PA-MBE. *Nanotechnology*. 2011;22(7): 075601. https://doi.org/10.1088/0957-4484/22/7/075601

Information about the authors

Vladislav O. Gridchin, Cand. Sci. (Phys.–Math.), Junior Researcher, St. Petersburg University; Alferov University; Institute for Analytical Instrumentation of the Russian Academy of Sciences (St. Petersburg, Russian Federation).

https://orcid.org/0000-0002-6522-3673
gridchinvo@gmail.com

Rodion R. Reznik, Cand. Sci. (Phys.–Math.), Head of Laboratory, St. Petersburg University; Alferov University; Institute for Analytical Instrumentation of the Russian Academy of Sciences (St. Petersburg, Russian Federation).

https://orcid.org/0000-0003-1420-7515
moment92@mail.ru

Konstantin P. Kotlyar, Cand. Sci. (Phys.–Math.), Junior Researcher, St. Petersburg University; Alferov University; Institute for Analytical Instrumentation of the Russian Academy of Sciences (St. Petersburg, Russian Federation).

https://orcid.org/0000-0002-0305-0156
konstantin21kt@gmail.com

Demid A. Kirilenko, Dr. Sci. (Phys.–Math.), Researcher, Ioffe Institute (St. Petersburg, Russian Federation). https://orcid.org/0000-0002-1571-209X
info.unifel@yandex.ru

Anna S. Dragunova, Junior Researcher, Higher School of Economics (St. Petersburg, Russian Federation).

https://orcid.org/0000-0002-0181-0262
olianndra@gmail.com

Natalia V. Kryzhanovskaya, Dr. Sci. (Phys.–Math.), Head of Laboratory, Higher School of Economics (St. Petersburg, Russian Federation).

https://orcid.org/0000-0002-4945-9803
nataliakryzh@gmail.com

George E. Cirlin, Dr. Sci. (Phys.–Math.), Head of Laboratory, St. Petersburg University; Alferov University, Institute for Analytical Instrumentation of the Russian Academy of Sciences; Ioffe Institute (St. Petersburg, Russian Federation).

https://orcid.org/0000-0003-0476-3630
cirlin.beam@mail.ioffe.ru

Received 20.09.2023; approved after reviewing 27.09.2023; accepted for publication 16.10.2023; published online 26.12.2023.

Translated by Yulia Dymant

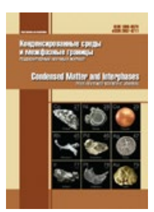

ISSN 1606-867X (Print)
ISSN 2687-0711 (Online)
Condensed Matter and Interphases
Kondensirovannye Sredy i Mezhfaznye Granitsy
https://journals.vsu.ru/kcmf/

Original articles

Research article
https://doi.org/10.17308/kcmf.2023.25/11474

Confirmation of spontaneous doping of GaN nanowires grown on vicinal SiC/Si substrate by electron beam induced current mapping

R. R. Reznik[1–3]✉, V. O. Gridchin[1–3], K. P. Kotlyar[1–3], V. V. Neplokh[2], A. V. Osipov[4], S. A. Kukushkin[4], O. Saket[5], M. Tchernycheva[5], G. E. Cirlin[1–3]

*[1]St. Petersburg State University,
7-9 Universitetskaya Embankment, St. Petersburg 199034, Russian Federation*

*[2]Alferov University,
8/3 Khlopina st., St. Petersburg 194021, Russian Federation*

*[3]Institute for Analytical Instrumentation of the Russian Academy of Sciences,
26 Rizhsky st., St. Petersburg 190103, Russian Federation*

*[4]Institute for Problems in Mechanical Engineering of the Russian Academy of Science,
61 Boljshoy prospekt V.O., St. Petersburg 199178, Russian Federation*

*[5]Centre de Nanosciences et de Nanotechnologies (C2N), University Paris-Saclay,
10 Boulevard Thomas, Gobert, Palaiseau 91120, France*

Abstract

This study is devoted to the confirmation of spontaneous doping of GaN nanowires grown on vicinal SiC/Si hybrid substrates by electron beam induced current mapping.

GaN nanowires (NWs) were grown on singular and vicinal SiC/Si substrates by molecular beam epitaxy with nitrogen plasma activation. The morphological properties of the NWs were studied by scanning electron microscopy. The electrophysical properties of the obtained nanostructures were studied by electron beam induced current mapping.

By electron beam induced current mapping, we confirmed the spontaneous doping of the GaN NWs grown on vicinal SiC/Si wafers. It was also shown that the GaN NWs grown on singular SiC/Si substrates did not exhibit an induced current signal, indicating that they were not doped.

Keywords: Semiconductors, GaN, Nanowires, Molecular beam epitaxy, Spontaneous doping, Silicon, Silicon carbide, Electron beam induced current method

Funding: The synthesis of the experimental samples was financially supported by the Russian Science Foundation, Grant No. 23-79-00012. The morphological studies of the obtained samples were financially supported by the Ministry of Science and Higher Education (FSRM 2023-0007). The electrophysical studies of the obtained samples were supported by PHC KOLMOGOROV project No. 43784UJ (2019).

For citation: Reznik R. R., Gridchin V. O., Kotlyar K. P., Neploh V. V., Osipov A. V., Kukushkin S. A., Saket O., Tchernycheva M., Cirlin G. E. Confirmation of spontaneous doping of GaN nanowires grown on vicinal SiC/Si substrate by electron beam induced current mapping. *Condensed Matter and Interphases*. 20223;25(4): 526–531. https://doi.org/10.17308/kcmf.2023.25/11474

Для цитирования: Резник Р. Р., Гридчин В. О., Котляр К. П., Неплох В. В., Осипов А. В., Кукушкин С. А., Saket O., Tchernycheva M., Цырлин Г. Э. Подтверждение методом картирования тока, наведенного электронным пучком, самопроизвольного легирования GaN нитевидных нанокристаллов из вицинальной подложки SiC/Si. *Конденсированные среды и межфазные границы*. 2023;25(4): 526–531. https://doi.org/10.17308/kcmf.2023.25/11474

✉ Rodion R. Reznik, e-mail: moment92@mail.ru

© Reznik R. R., Gridchin V. O., Kotlyar K. P., Neploh V. V., Osipov A. V., Kukushkin S. A., Saket O., Tchernycheva M., Cirlin G. E., 2023

The content is available under Creative Commons Attribution 4.0 License.

1. Introduction

Nowadays, wide-gap semiconductor nanostructures based on nitride compounds are of great interest to researchers due to their unique optical, electrophysical, transport, and other properties [1-3]. Nitride nanostructures are already used in a number of applications, such as LEDs, solar cells, transistors, single photon sources, and others [4–7]. Modern methods for the formation of semiconductor nanostructures make it possible to grow two-dimensional, one-dimensional, and zero-dimensional structures based on nitride compounds, as well as their combinations [8–11]. One of the most common methods for growing such nanostructures is molecular beam epitaxy (MBE). The advantages of this method include the ultrahigh vacuum level in the growth chamber, low growth rate, precise control over the growth processes, and, as a consequence, high crystallographic and optical quality of the resulting nanostructures [12–14]. It is important to note that nonplanar nitride nanostructures, such as nanowires (NWs), in some cases make it possible to increase the efficiency of devices or design a new generation of devices [15, 16]. Moreover, producing nanostructures in the form of nanowires allows us to solve the issue of integrating nitride compounds with mismatched substrates [17, 18]. Nevertheless, in most cases, to develop applications based on nitride nanowires, it is necessary to obtain nanostructure sites of P- and/or N-type conductivity to enable contact with the nanowires or the formation of the P-N junctions. To obtain efficient devices, it is necessary to consider all doping mechanisms of semiconductor nanostructures. As we demonstrated earlier, the substrate on which the nanostructures grow can also influence the type and level of doping of the nanowires [19]. In this study, we proved the fundamental possibility of growing GaN nanowires on singular and vicinal Si hybrid substrates with a thin SiC layer on the surface. Due to the optical studies, we observed the effect of spontaneous doping of the GaN nanowires grown on vicinal substrates with Si atoms. We also described the mechanism of doping of GaN nanowires with Si atoms from the SiC layer. It should be noted that the doping level of nanowires turned out to be higher than the solubility level of Si in GaN, which provides prospects for new applications based on this material.

The aim of the study was to confirm the spontaneous doping of the GaN nanowires grown on vicinal SiC/Si hybrid substrates by electron beam induced current mapping (induced current method).

2. Experimental

The GaN nanowires were grown using a Riber Compact 12 MBE unit equipped with a Ga effusion source and a plasma nitrogen source. Singular and vicinal Si(111) wafers with a thin SiC buffer layer were used as substrates. The technology for growing GaN nanowires on SiC/Si substrates is described in detail in [19]. All samples were grown under identical conditions. During the first stage, the substrate was placed in the growth chamber and heated to 950 °C in order to thermally clean the surface. After holding the substrate at a high temperature for 20 min, the substrate temperature was lowered to the growth temperature of 870 °C. During the next stage, nitrogen plasma was initiated at the source power of 520 W, with the N^+ flux rate of 1.5 sccm. Then, the Ga source was opened to grow GaN nanowires on the substrate surface. The total GaN nanowire growth time was 16 hours. The Ga flux from the source had a pressure of $1.6 \cdot 10^{-7}$ according to preliminary calibrations using the Bayard–Alpert gauge.

Changes in the surface morphology were recorded *in situ* by reflected high energy electron diffraction (RHEED), which indicated the wurtzite crystallographic phase of the growing nanostructures. The morphological properties of the grown nanostructures and the induced current maps were analyzed at room temperature using a Hitachi SU8000 scanning electron microscope (SEM) equipped with a Gatan DigiScan system for electron beam induced current mapping. Micromanipulators (probes) connected to a SR570 low-noise current preamplifier were used to contact the grown nanostructures. The methodology of the induced current measurements is described in detail in [20].

3. Results and discussion

The GaN nanowires were formed in the (111) direction on the singular SiC/Si substrate and on

the flat surface of the vicinal SiC/Si substrate. However, the nanowires grown on the slopes of the vicinal substrate also had another direction. The average height of the GaN NWs was 1.5 μm, and their average diameter was 300 nm.

The doping of the GaN NWs grown on vicinal SiC/Si substrates was confirmed by electron beam induced current mapping. In the induced current experiment, a tungsten probe contacted the top of the GaN nanowire, which generated a built-in electric field near the probe/nanowire contact due to the formation of a Schottky barrier at the tungsten/GaN interface. This built-in electric field effectively separated the electron-hole pairs generated by the electron beam. So, the induced current signal could be registered by an external measurement circuit connected to the probes. Moreover, the doping level of GaN nanowires could be estimated by the size of the space charge region (SCR), which is plotted as a plateau on the signal profile on the induced current maps [21]. The resistivity of undoped nanowires was high, the field magnitude of the Schottky barrier was low, and, consequently, the size of the SCR was large. So, electron-hole pairs could not be effectively separated by the built-in electric field. Together with the high resistivity of the NWs, it resulted in a very small measured value of the induced current signal.

A typical SEM image with a research probe and a characteristic induced current map for the GaN NWs grown on a vicinal SiC/Si substrate are shown in Figs. 1a and 1b, respectively. In Fig. 1a, it can be seen that the probe touches the apex of the GaN NWs. As can be seen from Fig. 1b, a GaN nanowire grown on vicinal SiC/Si substrate has a clearly distinguishable region of the induced current signal near the probe/nanowire interface, indicating an extremely high degree of NW doping.

The opposite pattern was observed for the GaN NWs grown on singular SiC/Si substrates. Figures 2a and 2b show a typical SEM image with a research probe and a characteristic map of the induced current for such a nanowire. As can be seen from the figures, a nanowire grown on singular GaN substrate does not manifest the induced current signal, which proves that it was not doped.

4. Conclusions

Thus, we confirmed the spontaneous doping of GaN nanowires grown on vicinal SiC/Si substrates by electron beam induced current mapping. It was also shown that the GaN NWs grown on singular SiC/Si substrates did not exhibit an induced current signal, indicating that they were not doped.

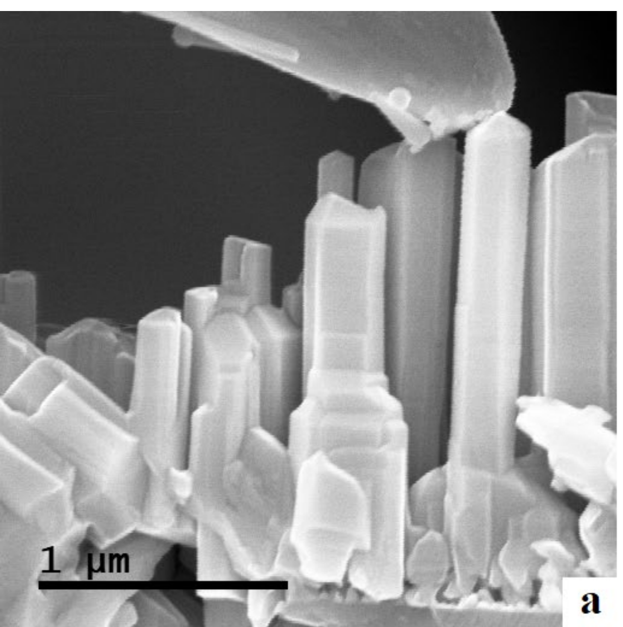

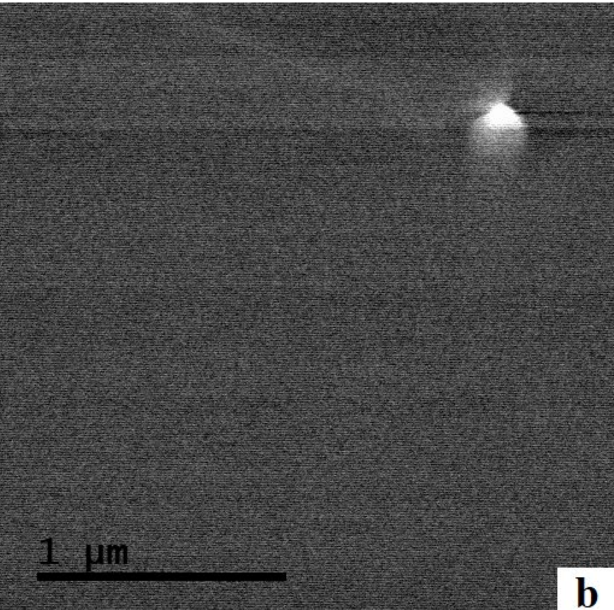

Fig. 1. Typical SEM image with a research probe (a) and a characteristic map of the induced current for a GaN NW grown on vicinal SiC/Si substrate (b)

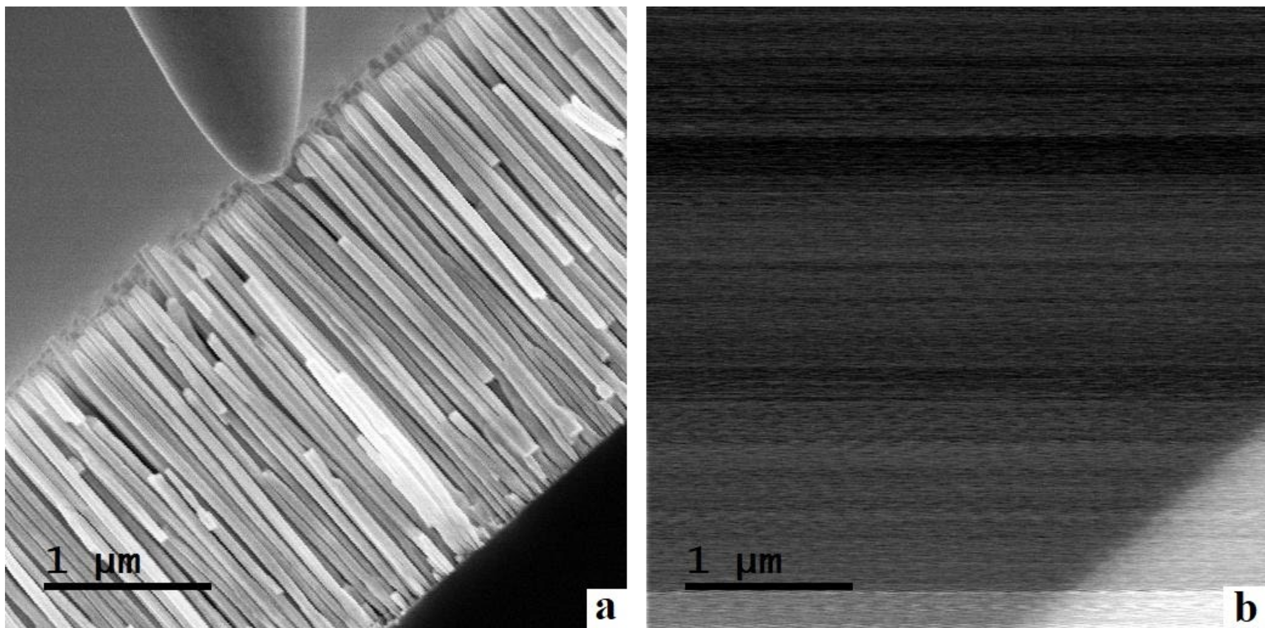

Fig. 2. Typical SEM image with a research probe (a) and a characteristic map of the induced current for a GaN NW grown on singular SiC/Si substrate (b)

Author contributions

R. R. Reznik – growing the samples, planning the experiment, text writing, and final conclusions. V. O. Gridchin – growing the samples. K. P. Kotlyar – SEM measurements of the samples. V. V. Neplokh – analysis of the results. A. V. Osipov – production of the substrates for growing the samples. S. A. Kukushkin – production of the substrates for growing the samples. O. Saket – study of the electrical properties of the samples. M. Tchernycheva – study of the electrophysical properties of the samples and analysis of the results. G. E. Cirlin – planning the experiments, analysis of the results.

Conflict of interests

The authors declare that they have no known competing financial interests or personal relationships that could have influenced the work reported in this paper.

References

1. Kente T., Mhlanga S. D. Gallium nitride nanostructures: Synthesis, characterization and applications. *Journal of Crystal Growth*. 2016;444: 55–72. https://doi.org/10.1016/j.jcrysgro.2016.03.033

2. Patra S. K., Schulz S. Electrostatic built-in fields in wurtzite III-N nanostructures: Impact of growth plane on second-order piezoelectricity. *Physical Review B*. 2017;96(15): 155307. http://dx.doi.org/10.1103/PhysRevB.96.155307

3. Gridchin V. O., Kotlyar K. P., Reznik R. R., Borodin B. R., Kudryashov D. A., Alekseev P. A., Cirlin G. E. Electrical properties of InGaN nanostructures with branched morphology synthesized via MBE on *p*-type Si (111). *Journal of Physics: Conference Series*. 2020;1695(1): 012030. https://doi.org/10.1088/1742-6596/1695/1/012030

4. Pearton S. J., Ren F. GaN electronics. *Advanced Materials*. 2000;12(21): 1571–1580. https://doi.org/10.1002/1521-4095(200011)12:21<1571::AID-ADMA1571>3.0.CO;2-T

5. Chen F., Ji X., Lau S. P. Recent progress in group III-nitride nanostructures: From materials to applications. *Materials Science and Engineering: R: Reports*. 2020;142: 100578. https://doi.org/10.1016/j.mser.2020.100578

6. Gridchin V. O., Kotlyar K. P., Reznik R. R., … Cirlin G. G. Multi-colour light emission from InGaN nanowires monolithically grown on Si substrate by MBE. *Nanotechnology*. 2021;32(33): 335604. https://doi.org/10.1088/1361-6528/ac0027

7. Tijent F. Z., Voss P., Faqir M. Recent advances in InGaN nanowires for hydrogen production using photoelectrochemical water splitting. *Materials Today Energy*. 2023;33: 101275. https://doi.org/10.1016/j.mtener.2023.101275

8. Mäntynen H., Anttu N., Sun Z., Lipsanen H. Single-photon sources with quantum dots in III–V nanowires. *Nanophotonics*. 2019;8(5): 747–769. https://doi.org/10.1515/nanoph-2019-0007

9. Leandro L., Gunnarsson C. P., Reznik R., … Akopian, N. Nanowire quantum dots tuned to atomic resonances. *Nano Letters*. 2018;18(11): 7217–7221. https://doi.org/10.1021/acs.nanolett.8b03363

10. Heiss M., Fontana Y., Gustafsson A., … Fontcuberta i Morral A. Self-assembled quantum dots in a nanowire system for quantum photonics. *Nature Materials*. 2013;12(5): 439–444. https://doi.org/10.1038/NMAT3557

11. Deshpande S., Frost T., Yan L., … Bhattacharya P. Formation and nature of InGaN quantum dots in GaN nanowires. *Nano Letters*. 2015;15(3): 1647–1653. https://doi.org/10.1021/nl5041989

12. Consonni V. Self-induced growth of GaN nanowires by molecular beam epitaxy: A critical review of the formation mechanisms. *Physica Status Solidi (RRL)–Rapid Research Letters*. 2013;7(10): 699–712. https://doi.org/10.1002/pssr.201307237

13. Arthur J. R. Molecular beam epitaxy. *Surface Science*. 2002;500(1-3): 189–217.

14. Dubrovskii V. G. Theory of diffusion-induced selective area growth of III-V nanostructures. *Physical Review Materials*. 2023;7(2): 026001. https://doi.org/10.1103/PhysRevMaterials.7.026001

15. Tribu A., Sallen G., Aichele T., … Kheng K. A high-temperature single-photon source from nanowire quantum dots. *Nano Letters*. 2008;8(12): 4326–4329. https://doi.org/10.1021/nl802160z

16. Alekseev P. A., Sharov V. A., … Lähderanta E. Piezoelectric current generation in wurtzite GaAs nanowires. *Physica Status Solidi (RRL) – Rapid Research Letters.* 2018;12(1): 1700358. https://doi.org/10.1002/pssr.201700358

17. Cirlin G. E., Reznik R. R., Shtrom I. V., … Akopian N. AlGaAs and AlGaAs/GaAs/AlGaAs nanowires grown by molecular beam epitaxy on silicon substrates. *Journal of Physics D: Applied Physics*. 2017;50(48): 484003. https://doi.org/10.1088/1361-6463/aa9169

18. Cirlin G. E., Dubrovskii V. G., Soshnikov I. P., … Glas F. Critical diameters and temperature domains for MBE growth of III–V nanowires on lattice mismatched substrates. *Physica Status Solidi (RRL) – Rapid Research Letters*. 2009:3(4): 112-114. https://doi.org/10.1002/pssr.200903057

19. Talalaev V. G., Tomm J. W., Kukushkin S. A., … Cirlin G. E. Ascending Si diffusion into growing GaN nanowires from the SiC/Si substrate: up to the solubility limit and beyond. *Nanotechnology*. 2020;31(29): 294003. https://doi.org/10.1088/1361-6528/ab83b6

20. Lavenus P., Messanvi A., Rigutti L. … Tchernycheva M. Experimental and theoretical analysis of transport properties of core–shell wire light emitting diodes probed by electron beam induced current microscopy. *Nanotechnology*. 2014;25(25): 255201. https://doi.org/10.1088/0957-4484/25/25/255201

21. Yakimov E. B., Borisov S. S., Zaitsev S. I. EBIC measurements of small diffusion length in semiconductor structures. *Semiconductors*. 2007;41: 411–413. https://doi.org/10.1134/s1063782607040094

Information about the authors

Rodion R. Reznik, Cand. Sci. (Phys.–Math.), Head of the Laboratory, St. Petersburg University; Alferov University; Institute for Analytical Instrumentation of the Russian Academy of Sciences (St. Petersburg, Russian Federation).

https://orcid.org/0000-0003-1420-7515
moment92@mail.ru

Vladislav O. Gridchin, Cand. Sci. (Phys.–Math.), Junior Researcher, St. Petersburg University; Alferov University; Institute for Analytical Instrumentation of the Russian Academy of Sciences (St. Petersburg, Russian Federation).

https://orcid.org/0000-0002-6522-3673
gridchinvo@gmail.com

Konstantin P. Kotlyar, Cand. Sci. (Phys.–Math.), Junior Researcher, St. Petersburg University; Alferov University; Institute for Analytical Instrumentation of the Russian Academy of Sciences (St. Petersburg, Russian Federation).

https://orcid.org/0000-0002-0305-0156
konstantin21kt@gmail.com

Vladimir V. Neploh, Cand. Sci. (Phys.–Math.), Senior Researcher, Alferov University (St. Petersburg, Russian Federation).

https://orcid.org/0000-0001-8158-0681
vneplox@gmail.com

Andrei V. Osipov, Dr. Sci. (Phys.–Math.), Main Researcher, Institute for Problems in Mechanical Engineering of the Russian Academy of Sciences (St. Petersburg, Russian Federation).

https://orcid.org/0000-0002-2911-7806
andrey.v.osipov@gmail.com

Sergey A. Kukushkin, Dr. Sci. (Phys.–Math.), Head of Laboratory, Institute for Problems in Mechanical Engineering of the Russian Academy of Sciences (St. Petersburg, Russian Federation).

https://orcid.org/0000-0002-2973-8645
sergey.a.kukushkin@gmail.com

Omar Saket, PhD, Researcher, Centre de Nanosciences et de Nanotechnologies (C2N), de l'université Paris-Saclay (Palaiseau, France).

https://orcid.org/0000-0002-9002-5871
omar.saket@c2n.upsaclay.fr

Maria Tchernycheva, Dr. Sci. (Phys.–Math.), Head of Laboratory, Centre de Nanosciences et de Nanotechnologies (C2N), de l'université Paris-Saclay (Palaiseau, France).

https://orcid.org/0000-0003-4144-0793

maria.tchernycheva@c2n.upsaclay.fr

George E. Cirlin, Dr. Sci. (Phys.–Math.), Head of Laboratory, St Petersburg University; Alferov University; Institute for Analytical Instrumentation of the Russian Academy of Sciences (St. Petersburg, Russian Federation).

https://orcid.org/0000-0003-0476-3630

cirlin.beam@mail.ioffe.ru

Received 20.09.2023; approved after reviewing 28.09.2023; accepted for publication 16.10.2023; published online 26.12.2023.

Translated by Anastasiia Ananeva

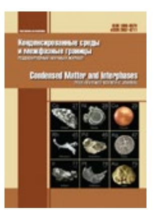

ISSN 1606-867X (Print)
ISSN 2687-0711 (Online)
Condensed Matter and Interphases
Kondensirovannye Sredy i Mezhfaznye Granitsy
https://journals.vsu.ru/kcmf/

Original articles

Research article
https://doi.org/10.17308/kcmf.2023.25/11482

GaN micro- and nanostructures selectively grown on profiled sapphire substrates using PA-MBE without lithography

A. N. Semenov[1]✉, D. M. Nechaev[1], S. I.Troshkov[1], D. S. Berezina[1], A. S. Abbas[2], V. N. Jmerik[1]

[1]*Ioffe Institute,*
26 Politekhnicheskaya st., St. Petersburg 194021, Russian Federation

[2]*King Abdulaziz City for Science and Technology (KACST),*
King Abdullah Rd, Al Raed, Riyadh 12354, Saudi Arabia

Abstract

Purpose: Development of technology for the formation of ordered arrays of nanocolumns (NCs) of GaN microcrystals using plasma-activated molecular beam epitaxy from nitrogen (PA-MBE) on profiled sapphire substrates (SPS) of large diameter with a micro-cone profile. The proposed method eliminates the use of low-performance and expensive nanolithography methods. The article is aimed at a deeper understanding of the processes that determine the growth kinetics of III-N nanocolumns using PA MBE on patterned sapphire substrates with multiple orientations of various non-polar and polar planes.

A new technological process for the fabrication of GaN NCs using PA-MPE is proposed, which ensures selectivity of their growth at the tops of PPS micro-cones and suppresses growth on the semipolar planes of these substrates. GaN NCs and microcrystals were grown using PA-MBE on commercially available PPS.

A technology has been developed for the formation of discharged arrays of GaN nanocolumns without the use of lithographic procedures. Modes have been established that allow the formation of microcrystals and NCs with different diameters: from 30 nm to several microns. A diagram of the growth of GaN by the PA MBE method on PPS has been constructed, demonstrating the boundaries of the technological regimes for the formation of GaN NCs and microcrystals with different surface topography.

Keywords: Selective area growth, Whiskers, Microcrystals, Nanocolumns, Plasma-activated molecular beam epitaxy, Wide-gap semiconductor compounds A^3N

Funding: The research was carried out with financial support from the Ministry of Science and Higher Education Higher Education of Russian Federation (agreement 075-15-2022-1224 “Bio-Light”).

For citation: Semenov A. N., Nechaev D. M., Troshkov S. I, Berezina D. S., Abbas A. S., Jmerik V. N. Micro- and nanostructures of GaN selectively grown on patterned sapphire substrates by PA-MBE without lithography techniques. *Condensed Matter and Interphases*. 2023;25(4): 532–541. https://doi.org/10.17308/kcmf.2023.25/11482

Для цитирования: Семенов А. Н, Нечаев Д. М., Трошков С. И., Березина Д. С., Аббас А. С., Жмерик В. Н. Микро- и наноструктуры GaN, селективно выращенные на паттернировванных сапфировых подложках методом ПА-МПЭ без использования литографии. *Конденсированные среды и межфазные границы*. 2023;25(4): 532–541. https://doi.org/10.17308/kcmf.2023.25/11482

✉ Alexey Semenov, e-mail: semenov@beam.ioffe.ru
© Semenov A. N., Nechaev D. M., Troshkov S. I., Berezina D. S., Abbas A. S., Jmerik V. N, 2023

The content is available under Creative Commons Attribution 4.0 License.

1. Introduction

Recently, three-dimensional (3D) nano- and microcrystals based on group III metal nitrides A^3N (BN, AlN, GaN, InN) with a predominant orientation along the *c* or –*c* axes, which are also commonly called nanocolumns (NCs) or nanowires, have been widely studied. Such structures are important both for fundamental studies of the properties of III-N compounds and for the creation of new electronic and optoelectronic devices based on them. In the latter case, nanocolumnar heterostructures can significantly improve the parameters of light-emitting and photo-receiving devices operating in various spectral ranges [1–4]. Highly efficient LEDs in the visible and ultraviolet (UV) ranges, respectively, have been successfully implemented based on InGaN/GaN and GaN/AlGaN "core-shell" heterostructures [5–10]. In particular, based on NC AlN structures, Zhao et al. [9] demonstrated the shortest wavelength UV LEDs emitting at a wavelength λ = 207 nm, which showed not only high structural perfection due to the absence of threading dislocations in them, but also high efficiency of TM-polarized radiation output through the upper c-plane individual NCs [11]. In addition, an increased efficiency of p-doping with Mg atoms was discovered for AlGaN NCs compared to planar layers of the same composition [12]. And finally, NCs in the A3N material system are promising for the development of new types of emitters, including sources of single photons in the visible and UV ranges [13–16].

One of the main requirements for the design of most device structures based on NCs is their regular arrangement on the surface of the substrate with varying distances between individual NCs - from a minimum ~1 μm (in LEDs) to several microns (in single photon sources). To solve this problem, methods for spatially selective epitaxial growth of A^3N-based NCs have been developed, in which the formation of preferred nucleation sites for group III adatoms is achieved using nano-lithographic operations on the surface of various dielectric masks. Most of these works use the processes of nanoimprinting [17] or electron beam lithography [18, 19]. The selectivity of NC growth is ensured due to its occurrence in open areas of nano-masks, i.e. on the surface of underlying substrates, with its complete absence on the surface of mask dielectrics. These methods provide spatial resolution from several hundred to tens of nanometers and are also characterized by relatively high spatial selectivity and uniformity of NC growth. However, these methods also have some disadvantages. For electron beam lithography, this is, first of all, the low productivity of the method, which precludes its use in the industrial production of devices on large-diameter substrates. The high cost of nanoimprinting matrices also hinders the widespread use of this method. Despite the success of nano-lithographic methods, the technological problems of ensuring high homogeneity of structures on large-area substrates and achieving sufficient growth selectivity with suppression of parasitic growth in the spaces between NCs have not yet been fully resolved [14]. In addition, all nano-lithographic methods are characterized by edge effects associated with excessive accumulation of adatoms near the edge of the dielectric mask. Finally, the resistive masks made of organic materials used in these methods can serve as a source of contamination of the NCs.

To solve the above problems, an active search is underway for methods for growing regularly distributed NCs without the use of nano-lithographic processes [20–25]. In our previous works [20–22], for the selective growth of A^3N NCs by plasma-activated molecular beam epitaxy (PA MBE), it was proposed to use patterned c-sapphire substrates (PPS) with individual micro-cones with characteristic values of base diameters, heights and distances between the peaks are several microns. Such substrates are relatively easy to fabricate using standard photolithographic methods and wet etching of commercial planar c-sapphire substrates [26]. Currently, PPS are used mainly for the manufacture of LED heterostructures, the efficiency of which increases due to the effects of reducing the concentrations of extended defects (dislocations) and improving the output of radiation through the semipolar planes of such substrates [27].

In our work [21], we demonstrated the possibility of selective growth of nitrogen-polar GaN(000-1) NCs using the PA MBE method in nitrogen-enriched conditions at the tops of PPS micro-cones and presented a qualitative model that describes such growth taking into

account the features of thermodynamics (surface energy) and surface mobility of adatoms on various polar and semipolar crystallographic planes. The influence of the PPS geometry, the roughness of the initial surface, the substrate temperature, and the ratio of the fluxes of group 3 atoms (Ga) to activated nitrogen Ga/N_2^* on the growth kinetics of single NCs was studied. These studies identified the important role of the initial growth stages in promoting selective growth of GaN NCs. In addition, the influence of the In flow as a surfactant on the growth of light-emitting NCs with InGaN/GaN quantum wells (QWs) was studied and the optimal ratios of the fluxes of all growth flows and substrate temperature were determined, ensuring maximum selectivity for the growth of GaN NCs, as well as the formation of InGaN/GaN QWs in them [22]. The use of PPS for selective growth of A^3N microcolumns has been demonstrated by other groups. In particular, recent work by Ahn et al. [25], this approach was used to obtain GaN NCs with a diameter of several microns on such substrates using metal-organic vapor phase epitaxy. In this work, varying the diameters of the microcone apexes was achieved using pre-epitaxial chemical-mechanical polishing of PPS, during which the flat apexes expanded.

This paper presents the results of a study of the characteristics of GaN growth by PA MBE on PPS with microcones in a wide range of varying growth temperatures and the ratio of gallium and plasma-activated nitrogen fluxes. Changing the growth parameters made it possible to vary the size of GaN NCs in a wide range from several tens of nm to 1 μm, and also to move from the growth of conventional cylindrical (hexagonal) NCs to the growth of microcrystals with a complex topology of polar and semi-polar crystallographic planes.

2. Experimental section

The samples were grown by PA-MBE on commercially available PPS with microcones with a base diameter of 2 μm, a height of 1.4 μm, and a distance between them of 2.1 μm, as shown in the images obtained using a scanning electron microscope (SEM) and shown in Fig. 1.

Before the start of growth of GaN NCs, the substrates were annealed at a temperature of 800 °C and nitrided at the same temperature in an active nitrogen flow of 0.5 Monolayers (ML)/sec (where thickness 1 ML = 0.25 nm), calibration of which was carried out by measuring the growth rate of AlN into metal -enriched conditions. Then, in all samples, GaN nucleation layers were grown under gallium-enriched conditions with a flux ratio of $Ga/N_2^* = 2.2$ ($N_2^* = 0.1$ML/s) at a substrate temperature of 760 – 770 °C. The thickness of this layer in the planar regions of the PPS was ~55 nm. Further growth of GaN NCs was carried out using two modes, differing primarily in the values of gallium (*Ga*) fluxes at the same active nitrogen flux ($N_2^* = 0.4$ ML/s). In the first mode, the growth of two samples was carried out under nitrogen-enriched conditions with the same Ga/N_2^* flux ratio ~ 0.25 and at different substrate temperatures (see below) for 4 hours in pulsed

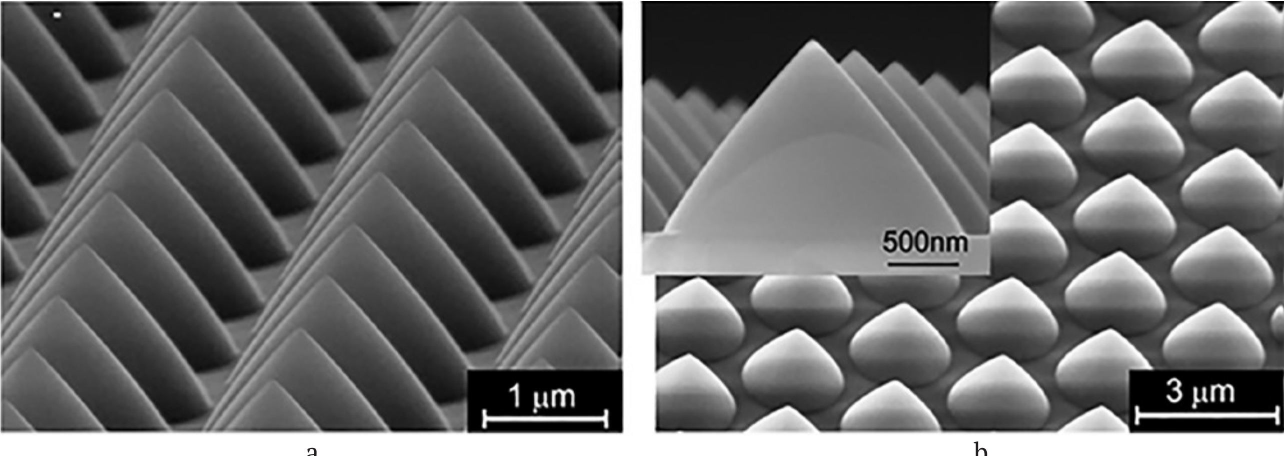

a b

Fig. 1. SEM images of the initial micro-cone-shaped patterned c-sapphire substrate (μ-CPSS) surface (a) cross section of the μ-CPSS with micro-cones and (b) general view of the μ-CPSS surface

mode with growth interruption every 30 seconds by the blocking of all growth fluxes using the main shutter. During this growth interruption for 30 s, an increase in the substrate temperature was observed almost linearly from the initial (growth) values of 760 °C and 780 up to 785°C and 805 °C, respectively. Temperature values were measured using an infrared pyrometer. After NC growth, some of the samples were etched in a KOH solution (10%) for 10 minutes at 20 °C. In the second mode, GaN NCs were grown on the same PPS for 5 hours under Ga-enriched growth conditions at Ga/N_2^* ~ 1.5 (without taking into account Ga desorption) and various substrate temperatures from 695 to 795°C. In all NC growth processes described above, an indium flux of In = 0.2–0.4 ML/sec was used as a surfactant.

The surface topographies of GaN NCs were studied using a CamScan 4-88-DV-100 SEM.

3. Results and discussion

3.1. Selective growth of GaN NCs on PPS under nitrogen-enriched conditions

In this work, compared with our previous work [21], to increase the selectivity of GaN NC growth (i.e., suppress the growth of parasitic NCs on the side faces of micro-cones) and reduce their diameter, relatively low Ga fluxes (Ga ~ 0.1 ML/s) and low flux ratios (Ga/N_2^* = 0.25). In addition, in our opinion, the increase in selectivity was facilitated by the transition from a constant to a pulsed growth mode with short-term annealing of the sample to stimulate the upward diffusion of Ga atoms to the top of the microcones. An increase in the substrate temperature by 20 °C allowed a larger number of adatoms to reach the tops of the PPS microcones. The high degree of spatial selectivity in the growth of GaN NCs with a height of 500 – 700 nm and a diameter of up to 35 nm was confirmed by their SEM images in Fig. 2a-c. Note that in previous work [21], the typical diameters of GaN NCs were 50–100 nm. However, NC growth was observed only at relatively low substrate temperatures of 760/785 °C during NC growth/annealing, respectively, and when temperature was increased to 780/805 °C, there was no growth of NCs on the tops of the PPS, as evidenced by the SEM images in Fig. 2d,e. We associate the lack of growth with increasing temperature with an increase in the desorption

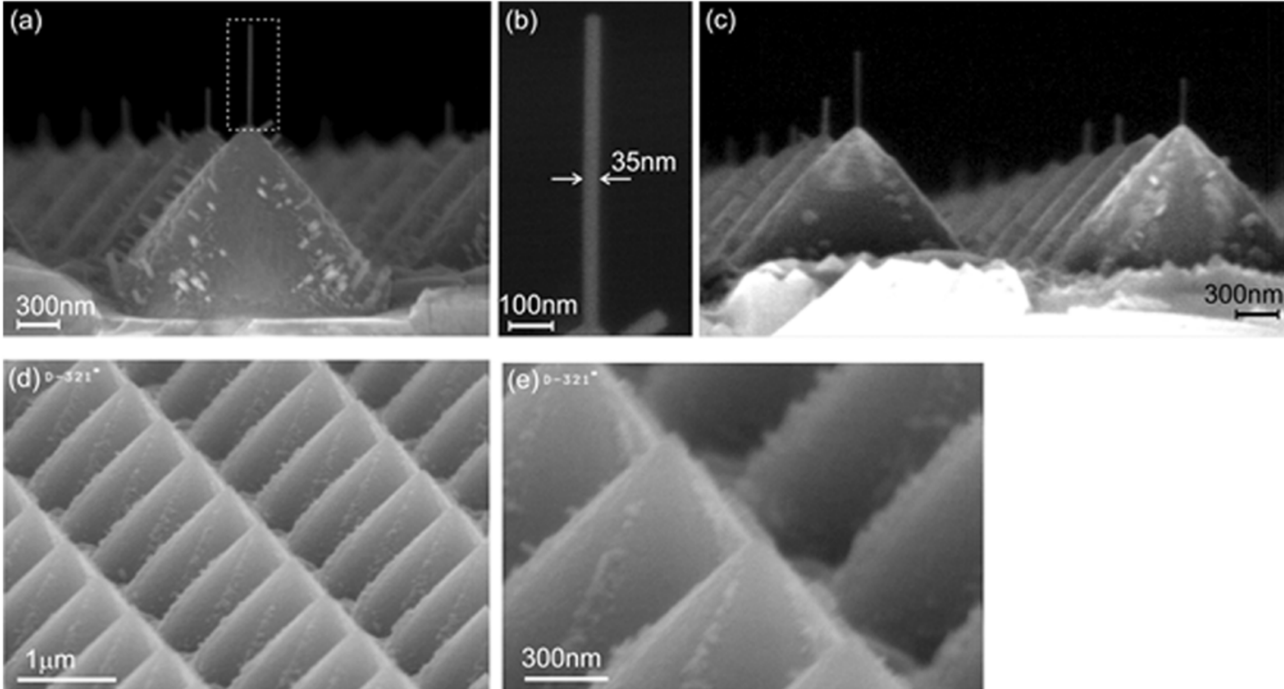

Fig. 2. SEM images of GaN NCs grown using nitrogen-enriched conditions (Ga/N_2^* = 0.25) and short-term growth interruptions with increasing temperature from 760 to 785°C (a-c) and from 780 to 805°C (d, e). (a) – general view of NC after growth; (b) – enlarged image of the NC, highlighted in (a) with a dotted line; (c) – General view of the NC after etching in KOH

of Ga atoms and the thermal decomposition of GaN NCs.

Unfortunately, the nucleation of GaN NCs at the tops of the PPS was of a probabilistic nature and the growth of NCs was not observed at every vertex even at relatively low substrate temperatures, as shown in Fig. 2a. This is most likely due to the scatter in the parameters of the substrates and the absence of flat nanoregions with a (0001) orientation on some vertices, on which NCs with nitrogen polarity [000-1] nucleate [21]. Note also that the formation of parasitic GaN NCs of smaller height, which were directed perpendicular to these planes, was also observed on the semipolar planes of the PPS.

The samples after etching in KOH did not reveal significant changes in the shape of the NCs at the tops of the PPS, but complete etching (i.e., disappearance) of the parasitic NCs on the semipolar planes was observed. This result demonstrates the relatively slow etching of polarly oriented GaN [000-1] on NC vertices and confirms the high chemical stability of non-polar {1-100} planes to etching in KOH solutions, as recently demonstrated by Tautz et al. [28].

2.2. Growth of GaN on PPS under metal-enriched conditions

Fig. 3 shows SEM images of microcrystals and NCs formed under the same Ga-enriched conditions ($Ga/N_2{}^*$ = 1.5) at a substrate temperature varying from 695 to 795 °C. In the images of all GaN micro- and nanocrystals, complete correspondence was observed between their density and the density of the original micro-cones on the surface of the PPS. Moreover, at low growth temperatures (695–707 °C), many (>50%) of the top parts of GaN microcrystals had

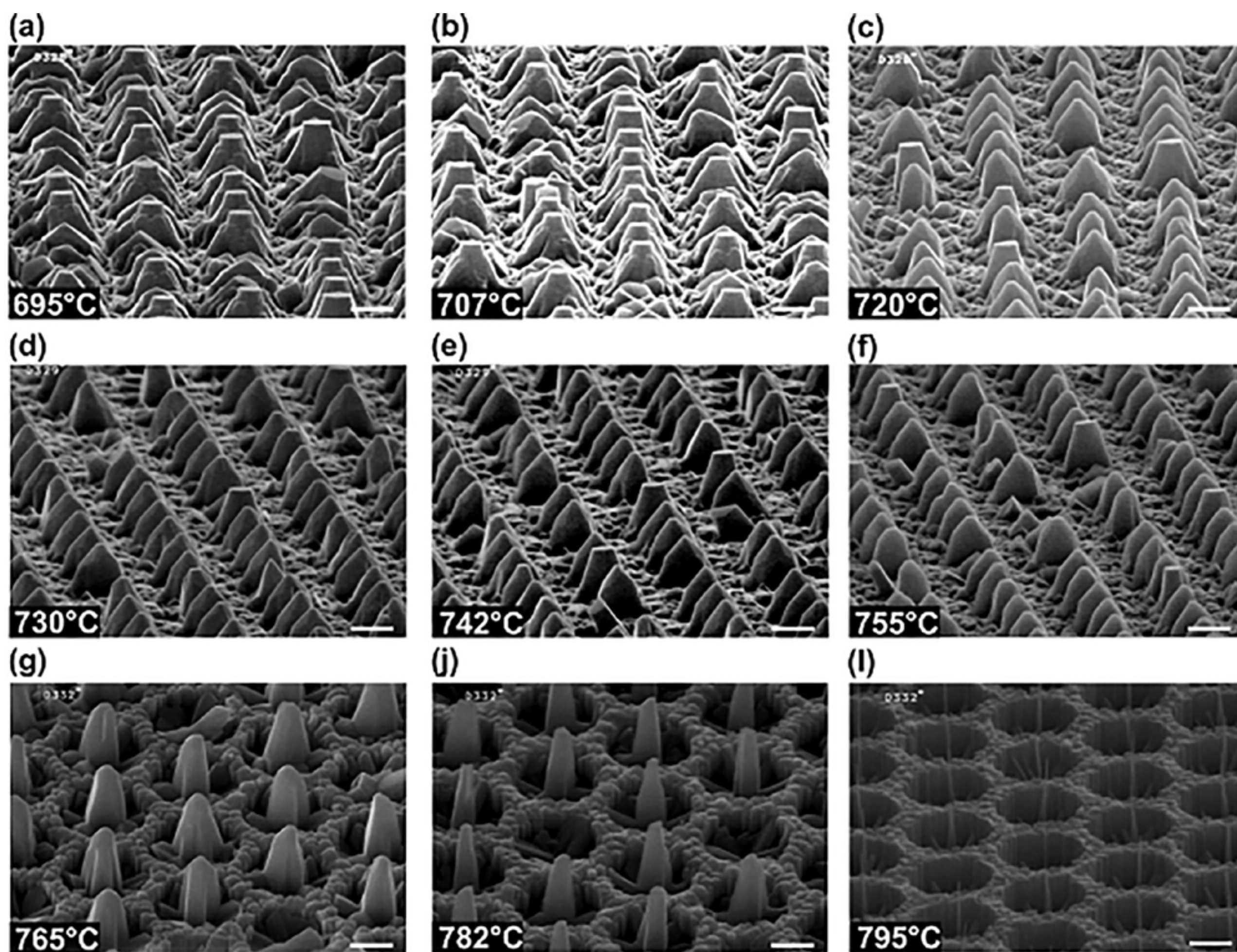

Fig. 3. SEM images of GaN micro- and nanocrystals grown in Me-(Ga) enriched conditions ($Ga/N_2{}^*$ = 1.5) at different substrate temperatures: (a) – 695 °C, (b) – 707 °C, (c) – 720 °C, (d) – 730 °C, (e) – 742 °C, (f) – 755 °C, (g) – 765 °C, (j) – 782 °C, (i) – 795 °C

the shape of hexagonal parallelepipeds with a height of ~300 nm and flat tops with a diameter of ~0.5 µm, as shown in Fig. 3a, b.

As the growth temperature increased up to 755 °C, a decrease in the number of such GaN microcrystals with flat tops was observed, the diameters of which also decreased and, moreover, a pencil-like cut of the tops was observed, as shown in Fig. 3b-f. A further increase in temperature to 795 °C led to a decrease in the diameter of GaN microcrystals until the transition to the growth of single nanocolumns with a diameter decreasing in the direction of the vertices down to a minimum diameter of <50 nm. Importantly, these single NCs were precisely located at the centers of regular micro-holes with a diameter of 2 µm (i.e., in full accordance with the topology of the PPS cones). GaN layers grown on flat areas of the PPS form a "honeycomb" flat surface morphology, as shown in Fig. 3g-i.

Fig. 4a-c show cross-sectional images of cleavages of several structures with GaN NCs grown at different substrate temperatures, the general appearance of which is shown in Fig. 3. Figure 4a shows that the growth of GaN at low temperatures (695 °C) begins at the top of the PPS in the form of an inverted pyramid (i.e., with the top oriented downward) similar to the hexagonal pyramids that we observed in a similar work on the growth of InN on PPS in metal-enriched conditions [20].

During the growth of this pyramid, when it reached a height of ~1 µm, its inclined (semi-polar) growth planes mirrored their orientation, and growth continued in the form of a normally oriented pyramid (i.e., with the apex at the top). However, when this pyramid reached a height of about 1 µm, the angle of the inclined planes changed again and further growth of GaN occurred in the form of a hexagonal flat-topped pyramid oriented in the vertical direction. Note that simultaneously with this growth from the tops of the PPS, growth of GaN was also observed on inclined (semi-polar) planes perpendicular to them, as shown in Fig. 4a. On flat areas of the PPS surface, continuous GaN layers with a relatively smooth surface topography grew in comparison with the rough topography of layers grown on the same flat areas of PPS under nitrogen-enriched conditions (see Fig. 2a).

With an increase in the growth temperature, first of all, a decrease in the diameters of the NCs and a transition to their more vertically oriented growth of the side walls was observed.

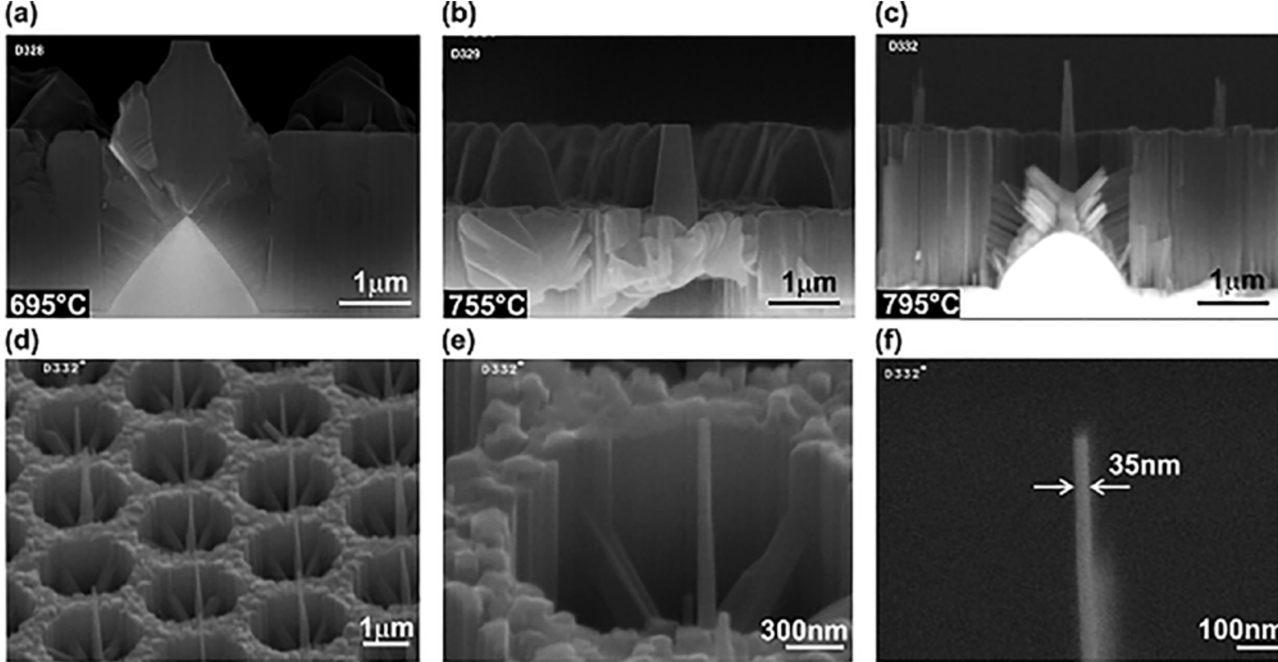

Fig. 4. SEM images of cross sections of GaN microcrystals and NCs grown in Ga-enriched conditions (Ga/N_2^* = 1.5) at different substrate temperatures: (a) – 695 °C, (b) – 755 °C, (c) – 795 °C. (d-f) – SEM images with different magnifications of the last NC (c), grown at a maximum substrate temperature of 795 °C

At the same time, in the region of average substrate temperatures (720-765 °C), the NCs demonstrated a change in the angle of inclination of the walls. However, in the sample grown at the maximum temperature in this work, 795 °C, the NC diameter varied from ~250 nm at the base to 35 nm at the top, with a NC height of more than 2 μm. It is important that the growth rate of the NCs significantly exceeded the growth rate of the bulk GaN layer above the flat PPS region, which over five hours of growth led to the heights of the NC tops exceeding the level of the continuous layer by approximately 1 μm. Thus, a series of experiments on the growth of GaN on PPS using PA MBE under significantly different growth conditions showed the possibility of significantly varying the shape of growing NCs and micro(nano) crystals.

According to Wulff's theorem, the equilibrium shape of any crystal is determined by the minimum surface energy of its faces—differently oriented crystallographic planes [29]. For the hexagonal semiconductor compound GaN, first-principles calculations show significantly lower surface energies of the non-polar [1-100] and [11-20] planes compared to the polar and semi-polar planes [0001], [000-1], [11-22], [1-101], [1-102], etc. [30]. Therefore, GaN NCs under equilibrium conditions should demonstrate preferential vertical growth in one of two polar directions - [0001] or [000-1]. The results of this work on the growth of N-polar GaN NCs on PPS under highly nitrogen-enriched PA MBE conditions generally confirm the above conclusion (see Fig. 2) and are fully consistent with the results of our previous work [21].

The growth of such NCs under metal-enriched conditions at high substrate temperatures (~800 °C) was discovered for the first time, and its important feature is the growth of NCs on almost all the tops of PPS micro-cones, in contrast to NCs that randomly form on the same vertices under nitrogen-enriched conditions. It should also be noted that it is possible to form GaN micro- and nanocrystals of complex shapes with multiple faces of semi-polar orientation through their growth in Ga-enriched conditions at low and medium substrate temperatures (695–720 °C and 720–765 °C, respectively).

The results on the growth of GaN NCs on PPS under Me-enriched conditions indicate a significant role of the kinetic factors of PA MPE in this growth regime. Indeed, with an increase in the substrate temperature during the growth of GaN under nominally metal-enriched conditions, one can first assume a significant increase in the rate of thermal desorption of Ga above a temperature of 700°C (Ga^{TD}), where its value for the [0001] plane exceeds 0.3 ML/s [31,32]. This leads to the disappearance of Ga adsorption layers on the GaN surface (a monolayer for (000-1)-GaN and a bilayer in the case of (0001) GaN growth), providing high mobility of all adatoms and, as a consequence, 2D growth modes with an atomically smooth surface morphology. As the substrate temperature increases (>750 °C), one should expect the onset of thermal congruent decomposition of GaN at a rate of (Ga^{CD}) [33, 34]. These processes lead to a significant change in the effective flux ratio $(Ga - Ga^{D} - Ga^{CD})/(N_2^* - N_2^{CD})$, which decreased as the temperature increased. Thus, the shape of a GaN NC is determined not only by the equilibrium values of the surface energies of differently oriented planes. Unfortunately, an accurate quantitative calculation of the growth processes of GaN NCs under nonequilibrium metal-enriched conditions is impossible because in the known literature there are no parameters of thermal desorption and congruent decomposition for various crystalline faces of GaN. Nevertheless, to qualitatively explain the transitions between complex forms of GaN micro- and nanocrystals on PPS, one can use the dependences of the theoretically calculated values of the relative surface energies of various planes on the chemical potential of nitrogen under varying stoichiometric conditions of PA MPE. Such dependencies were constructed in the work of Lee et al. [30] and according to them, only under nitrogen-rich conditions the (000-1)N plane is the most stable, i.e. has lower surface energy compared to the energies of other planes. However, upon transition to Me-enriched conditions (i.e., when the chemical potential of nitrogen decreases), a different relationship between the surface energies of the planes is observed and the semipolar planes {11-2-2}Ga have the lowest energy. This explains the initial growth of inverted pyramids we observed under highly Ga-enriched conditions. These studies of the crystallographic features of GaN growth on

PPS under various PA MBE conditions will be continued in the future. At the present stage of research, it is possible to construct a schematic diagram of various growth modes of GaN NCs on PPS depending on the substrate temperature and the nominal Ga/N_2* flux ratio, which is presented in Fig. 5.

4. Conclusion

The features of selective area growth of GaN nano- and microcrystals without the use of lithography methods have been studied. The possibilities of such growth using plasma-activated molecular beam epitaxy on profiled c-sapphire substrates with a microcone profile have been demonstrated. It has been shown that when using nitrogen-enriched growth conditions (with a flux ratio of Ga/N_2* = 0.25), an increase in the selectivity of the growth of GaN nanocolumns and a decrease in their diameter to 35 nm (at a height of several hundred nm) is achieved by carrying out the process in a pulsed mode at a temperature substrates 780 °C with short-term annealing, during which the substrate temperature increases by 25 °C. However, in this growth mode, the nucleation of NCs at the tops of microcones is characterized by a probability of no more than 50%.

In the opposite case of metal (Ga)-enriched GaN growth conditions with a flux ratio of Ga/N_2* = 1.5, the growth of nanocrystals is determined by the substrate temperature. At high values (~800 °C), the formation of GaN nanocolumns with a diameter in the upper part of ~30 nm is observed, which nucleate at almost every vertex of the patterned substrate. Importantly, the tops of individual regular GaN NCs are almost 1 micron higher than the level of the flat GaN layer grown between the microconuses. In the case of lower growth temperatures, the growth of complex micro- and nanocrystals with different surface topologies and orientations of semi-polar side walls is observed. At extremely low growth temperatures (~700 °C), the growth of complex GaN microcrystals is observed, which in the upper part have the regular shape of hexagonal parallelepipeds with flat tops.

Contribution of the authors

A. N. Semenov – concept of the study, text writing, final conclusions, carrying out epitaxial growth; D. V. Nechaev – carrying out epitaxial growths, results discussing and text editing; S. I. Troshkov – SEM measurements of the samples and results discussing; V. N. Zhmerik – ideas, development of methodology, scientific guidance and text editing.

Conflict of interests

The authors declare that they have no known competing financial interests or personal relationships that could have influenced the work reported in this paper.

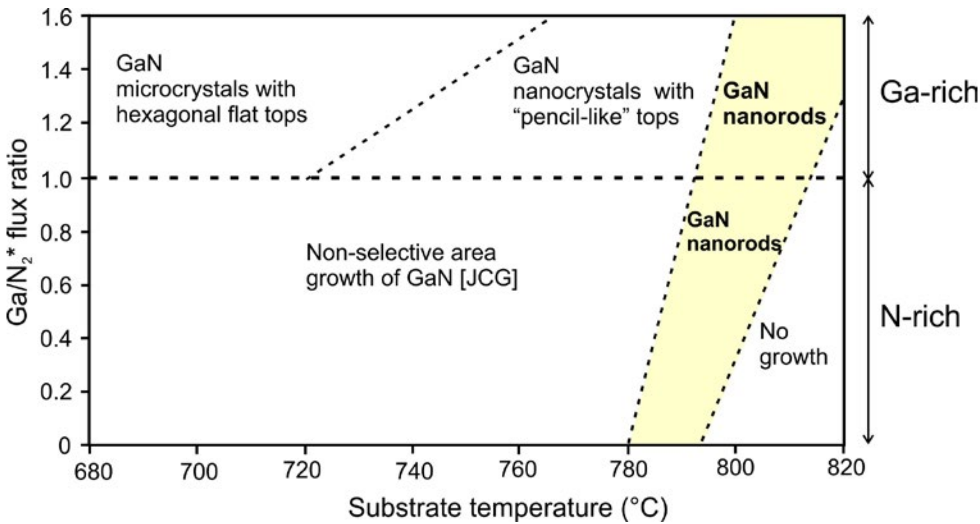

Fig. 5. Schematic diagram of different growth modes of micro-, nanocrystals and GaN nanorods grown by PA-MBE on PSS at different substrate temperatures and Ga/N_2^* flux ratios

References

1. Li S., Waag A. GaN based nanorods for solid state lighting. *Journal of Applied Physics*. 2012;111: 071101. https://doi.org/10.1063/1.3694674

2. Mandl M., Wang X., Schimpke T., … Strassburg M. Group III nitride core–shell nano- and microrods for optoelectronic applications. *Physica Status Solidi (RRL) – Rapid Research Letters*. 2013;7(10): 800–814. https://doi.org/10.1002/pssr.201307250

3. Zhao C.; Alfaraj N.; Subedi R. C., …Ooi B. S. III-nitride nanowires on unconventional substrates: From materials to optoelectronic device applications. *Progress in Quantum Electronics*. 2018;61: 1–31. https://doi.org/10.1016/j.pquantelec.2018.07.001

4. Chen F., Ji X., Lau S. P. Recent progress in group III-nitride nanostructures: from materials to applications. *Materials Science and Engineering: R: Reports*. 2020;142: 100578. https://doi.org/10.1016/j.mser.2020.100578

5. Schimpke T., Mandl M., Stoll I., … Strassburg M. Phosphor-converted white light fromblue-emitting InGaN microrod LEDs. *Physica Status Solidi A*. 2016;213(6): 1577–1584. https://doi.org/10.1002/pssa.201532904

6. Sun H., Li X. Recent advances on III-nitride nanowire light emitters on foreign substrates – toward flexible photonics. *Physica Status Solidi A*. 2019;216: 1800420. https://doi.org/10.1002/pssa.201800420

7. Meier J., Bacher G. Progress and challenges of InGaN/GaN-based core–shell microrod LEDs. *Materials*. 2022;15: 1626. https://doi.org/10.3390/ma15051626

8. Adhikari S., Kremer F., Lysevych M., Jagadishae C., Tan H. H. Core–shell GaN/AlGaN nanowires grown by selective area epitaxy. *Nanoscale Horizons*. 2023;8: 530. https://doi.org/10.1039/d2nh00500j

9. Zhao S., Djavid M., Mi Z. Surface emitting, high efficiency near-vacuum ultraviolet light source with aluminum nitride nanowires monolithically grown on silicon. *Nano Letters*. 2015;15: 7006–7009. https://doi.org/10.1021/acs.nanolett.5b03040

10. Mi Z., Zhao S., Woo S. Y., … Botton G. A. Molecular beam epitaxial growth and characterization of Al(Ga)N nanowire deep ultraviolet light emitting diodes and lasers. *Journal of Physics D: Applied Physics*. 2016;49: 364006. https://doi.org/10.1088/0022-3727/49/36/364006

11. Djavid M., Mi Z. Enhancing the light extraction efficiency of AlGaN deep ultraviolet light emitting diodes by using nanowire structures. *Applied Physics Letters*. 2016;108: 051102. https://doi.org/10.1063/1.4941239

12. Zhao C., Ebaid M., Zhang H., … Ooi B. S. Quantified hole concentration in AlGaN nanowires for high-performance ultraviolet emitters. *Nanoscale*. 2018;10: 15980–15988. https://doi.org/10.1039/C8NR02615G

13. Holmes M. J., Choi K., Kako S., Arita M., Arakawa Y. Room-temperature triggered single photon emission from a III-nitride site-controlled nanowire quantum dot. *Nano Letters*. 2014;14(2): 982–986. https://doi.org/10.1021/nl404400d

14. Yamamoto T., Maekawa M., Imanishi Y., Ishizawa S., Nakaoka T., Kishino K. Photon correlation study of background suppressed single InGaN nanocolumns. *Japanese Journal of Applied Physics*. 2016;55: 04EK03. https://doi.org/10.7567/JJAP.55.04EK03

15. Mäntynen H., Anttu N., Sun Z., Lipsanen H. Single-photon sources with quantum dots in III–V nanowires. *Nanophotonics*. 2019;8(5): 747–769. https://doi.org/10.1515/nanoph-2019-0007

16. Arakawa Y., Holmes M. J. Progress in quantum-dot single photon sources for quantum information technologies: A broad spectrum overview. *Applied Physics Reviews*. 2020;7: 021309. https://doi.org/10.1063/5.0010193

17. Dai J., Liu B., Zhuang Z., … Xie, Fabrication of AlGaN nanorods with different Al compositions for emission enhancement in UV range. *Nanotechnology*. 2017;28: 385205. https://doi.org/10.1088/1361-6528/aa7ba4

18. Nami M., Eller R. F., Okur S., Rishinaramangalam A. K., Liu S., Brener I., Feezell D. F. Tailoring the morphology and luminescence of GaN/InGaN core-shell nanowires using bottom-up selective-area epitaxy. *Nanotechnology*. 2017;28: 025202. https://doi.org/10.1088/0957-4484/28/2/025202

19. Hasan S. M. N., You W., Ghosh A., Sadaf S. Md., Arafin S. Selective area epitaxy of GaN nanostructures: MBE growth and morphological analysis. *Crystal Growth & Design*. 2023. https://doi.org/10.1021/acs.cgd.2c01506

20. Shubina T. V., Pozina G., Jmerik V. N., … Ivanov S. V. III-nitride tunable cup-cavities supporting quasi whispering gallery modes from ultraviolet to infrared. *Scientific Reports*. 2015;5: 17970. https://doi.org/10.1038/srep17970

21. Jmerik V. N., Kuznetsova N. V., Nechaev D. V., … Ivanov S. V. Selective area growth of N-polar GaN nanorods by plasma-assisted MBE on micro-cone-patterned c-sapphire substrates. *Journal of Crystal Growth*. 2017;477: 207–211. https://doi.org/10.1016/j.jcrysgro.2017.05.014

22. Semenov A. N., Nechaev D. V., Troshkov S. I., … Ivanov S. V. Features of the selective growth of GaN nanorods on patterned c-sapphire substrates of various configurations. *Semiconductors*. 2018;52(13): 1770–1774. https://doi.org/10.1134/S1063782618130158

23. Kim J., Choi U., Pyeon J., So B., Nam O. Deep-ultraviolet AlGaN/AlN core-shell multiple quantum wells on AlN nanorods via lithography-free method.

Scientific Reports. 2018;8: 935. https://doi.org/10.1038/s41598-017-19047-6

24. Shen J., Yu Y., Wang J., Zheng Y., Gan Y., Li G. Insight into the Ga/In flux ratio and crystallographic plane dependence for MBE self-assembled growth of InGaN nanorods on patterned sapphire substrates. *Nanoscale*. 2020;12(6): 4018–4029. https://doi.org/10.1039/c9nr09767h

25. Ahn M. J., Jeong W. S., Shim K. Y., … Byun D. Selective-area growth mechanism of GaN microrods on a plateau patterned substrate. *Materials*. 2023;16: 2462. https://doi.org/10.3390/ma16062462

26. Wang J., Guo L. W., Jia H. Q., … Zhou J. M. Fabrication of patterned sapphire substrate by wet chemical etching for maskless lateral overgrowth of GaN. *Journal of the Electrochemical Society*. 2006;153(3): C182. https://doi.org/10.1149/1.2163813

27. Takano T., Mino T., Sakai J., Noguchi N., Tsubaki K., Hirayama H. Deep-ultraviolet light-emitting diodes with external quantum efficiency higher than 20% at 275 nm achieved by improving light-extraction efficiency. *Applied Physics Express*. 2017;10: 031002. https://doi.org/10.7567/APEX.10.031002

28. Tautz M., Weimar A., Graßl C., Welzel M., Díaz D. D. Anisotropy and mechanistic elucidation of wet-chemical gallium nitride etching at the atomic level. *Physica Status Solidi A*. 2020;217(21): 2000221. https://doi.org/10.1002/pssa.202000221

29. Sun Q., Yerino C. D., Leung B., Han J., Coltrin M. E. Understanding and controlling heteroepitaxy with the kinetic Wulff plot: A case study with GaN. *Journal of Applied Physics*. 2011;110: 053517. https://doi.org/10.1063/1.3632073

30. Li H., Geelhaar L., Riechert H., Draxl C. Computing equilibrium shapes of wurtzite crystals: the example of GaN. *Physical Review Letters*. 2015;115: 085503. https://doi.org/10.1103/PhysRevLett.115.085503

31. Jmerik V. N., Nechaev D. V., Ivanov S. V. Kinetics of metal-rich PA molecular beam epitaxy of AlGaN heterostructures for mid-UV photonics. In: *Molecular beam epitaxy (second edition)*. M. Henini (ed.). Elsevier; 2018. pp. 135–179. https://doi.org/10.1016/B978-0-12-812136-8.00008-6

32. Koblmüller G., Averbeck R., Riechert H., Pongratz P. Direct observation of different equilibrium Ga adlayer coverages and their desorption kinetics on GaN (0001) and (000-1) surfaces. *Physical Review B*. 2004;69: 035325. https://doi.org/10.1103/PhysRevB.69.035325

33. VanMil B. L., Guo H., Holbert L. J., … Myers T. H. High temperature limitations for GaN growth by RF-plasma assisted molecular beam epitaxy: Effects of active nitrogen species, surface polarity, and excess Ga-overpressure. *Physica Status Solidi (c)*. 2005;2(7): 2174–2177. https://doi.org/10.1002/pssc.200461573

34. Fernández-Garrido S., Koblmüller G., Calleja E., Speck J. S. In situ GaN decomposition analysis by quadrupole mass spectrometry and reflection high-energy electron diffraction. *Journal of Applied Physics*. 2008;104: 033541. https://doi.org/10.1063/1.2968442

Information about the authors

Alexey N. Semenov, Cand. Sci. (Phys.–Math.), Senior Researcher, Ioffe Institute (St. Petersburg, Russian Federation).

https://orcid.org/0000-0002-0719-0236
semenov@beam.ioffe.ru

Dmitii V. Nechayev, Cand. Sci. (Phys.–Math.), Senior Researcher, Ioffe Institute (St. Petersburg, Russia).

https://orcid.org/0000-0003-4420-8420
nechayev@mail.ioffe.ru

Sergei I. Troshkov, Cand. Sci. (Phys.–Math.), Senior Researcher, Ioffe Institute (St. Petersburg, Russia).

https://orcid.org/0000-0002-3307-6226
S.Troshkov@mail.ioffe.ru

Darya S. Berezina, postgraduate student, Young Researcher, Ioffe Institute (St. Petersburg, Russia).

https://orcid.org/0000-0001-9190-1768
Dariya.Burenina@mail.ioffe.ru

Abbas Arwa Saud, Ph.D, Researcher, King Abdulaziz City for Science and Technology (Riyadh, Saudi Arabia).

arwasaudabdullah@gmail.com

Valentin Nikolaevich Jmerik, Dr. Sci. (Phys.–Math.), Professor, Chief Researcher, Ioffe Institute (St. Petersburg, Russia).

https://orcid.org/0000-0001-8759-7273
jmerik@pls.ioffe.ru

Received 10.10.2023; approved after reviewing 13.10.2023; accepted for publication 16.10.2023; published online 25.12.2023.

Translated by the author of the article

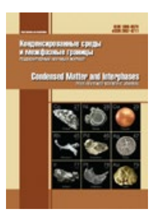

ISSN 1606-867X (Print)
ISSN 2687-0711 (Online)
Condensed Matter and Interphases
Kondensirovannye Sredy i Mezhfaznye Granitsy
https://journals.vsu.ru/kcmf/

Original articles

Research article
https://doi.org/10.17308/kcmf.2023.25/11476

Fabrication of α-Ga_2O_3:Sn/α-Cr_2O_3/α-Al_2O_3 heterostructure by mist CVD and HVPE

P. N. Butenko[1]✉, R. B. Timashov[1], A. I. Stepanov[1], A. I. Pechnikov[1,2], A. V. Chikiryaka[1], L. I. Guzilova[1], S. I. Stepanov[2], V. I. Nikolaev[1,2]

[1]*Ioffe Institute,*
26 Polytechnicheskaya st., St. Petersburg 194021, Russian Federation

[2]*Perfect Crystals LLC,*
38 Torez ave., St. Petersburg 194223, Russian Federation

Abstract

Corundum-structured chromium oxide (α-Cr_2O_3), exhibiting *p*-type conductivity, is a highly attractive candidate for forming high-quality *p-n* heterojunctions with α-Ga_2O_3. Two CVD growth techniques were employed in the fabrication of the heterostructure. A ~ 0.2-micron α-Cr_2O_3 layer was grown on a (0001) sapphire substrate using mist CVD at 800 °C. It possesses high morphological homogeneity and low roughness, which is acceptable for further epitaxial processes. Subsequently, Sn-doped α-Ga_2O_3 with a thickness of ~ 1.5 μm was grown on the α-Cr_2O_3 layer using HVPE at 500 °C. The feasibility of fabricating this heterostructure with the specified layer thickness and acceptable surface morphology using CVD techniques has been demonstrated.

Keywords: Gallium Oxide, Sapphire substrate, Heteroepitaxy, CVD, Mist-CVD, HVPE

Funding: P.N. Butenko, A.I Pechnikov, and L.I. Guzilova gratefully appreciate the Russian Science Foundation for financial support (grant No. 23-29-10196).

For citation: Butenko P. N., Timashov R. B., Stepanov A. I., Pechnikov A. I., Chikiryaka A. V., Guzilova L. I., Stepanov S. I., Nikolaev V. I. Fabrication of α-Ga_2O_3:Sn/α-Cr_2O_3/α-Al_2O_3 heterostructure by mist CVD and HVPE. *Condensed Matter and Interphases*. 2023;25(4): 542–547. https://doi.org/10.17308/kcmf.2023.25/11476

Для цитирования: Бутенко П. Н., Тимашов Р. Б., Степанов А. И., Печников А. И., Чикиряка А. В., Гузилова Л. И., Степанов С. И., Николаев В. И. Создание гетероструктуры α-Ga_2O_3:Sn/α-Cr_2O_3/α-Al_2O_3 методами газофазной эпитаксии. *Конденсированные среды и межфазные границы*. 2023;25(4): 542–547. https://doi.org/10.17308/kcmf.2023.25/11476

✉ Pavel N. Butenko, e-mail: pavel.butenko@mail.ioffe.ru

© Butenko P. N., Timashov R. B., Stepanov A. I., Pechnikov A. I., Chikiryaka A. V., Guzilova L. I., Stepanov S. I., Nikolaev V. I., 2023

The content is available under Creative Commons Attribution 4.0 License.

1. Introduction

Gallium oxide is a new-generation semiconductor that opens up horizons in applications in power and high-frequency electronics [1–3]. This promising material outperforms all known commercial semiconductors in terms of electrical, optoelectrical, chemical, and mechanical properties [4]. Its α-polymorph has a corundum-type structure (R3c symmetry). Among the five Ga_2O_3 modifications, it has the largest bandgap (E_g = 5.3 eV), along with a high breakdown field (E_c = 8.5 MV·cm^{-1}) and dielectric constant (ε = 10) [5–7]. By doping gallium oxide with Sn or Si, *n*-type conductivity can be achieved with an electron concentration of up to 10^{19} cm^{-3} [8]. However, a method to provide *p*-type conductivity has not yet been found, which is perhaps the biggest drawback of this material, limiting its potential applications.

It is, however, feasible to create a heterojunction of α-Ga_2O_3 with another material owing the same crystal structure while demonstrating *p*-type conductivity [9]. Among the promising candidates, α-Cr_2O_3 stands out as one of the best options. Both share the same rhombohedral structure and have a very low a-plane lattice mismatch (0.4 %). The latter parameter mismatch is slightly more attractive for α-Ir_2O_3 (0.3 %) [10]. Nonetheless, the high cost associated with iridium renders it impractical for practical consideration. Another inexpensive candidate is α-Fe_2O_3, but it has a 1.2 % lattice mismatch and a lower optical bandgap (2.3 eV vs. 3.0 eV for α-Cr_2O_3) [11]. To be fair it should be noted, that the lattice mismatch in α-Al_2O_3/α-Cr_2O_3 pair is high (3.74 % [12]), but the double pairing choice is limited.

In our previous work [13], we demonstrated a α-Ga_2O_3/α-Cr_2O_3/sapphire structure. Our aim was to create a buffer layer of α-Cr_2O_3 to enhance the crystal quality of gallium oxide. The deposition of a 150 nm chromium oxide layer using magnetron deposition, followed by annealing at 500–800 °C, contributed to the growth of corundum α-Ga_2O_3 in a single phase, resulting in a fourfold reduction in threading dislocation density. This experimental evidence confirms the isostructural nature of these oxides and their potential for further research.

Recently, mist-CVD and HVPE have emerged as two CVD techniques of particular interest for Ga_2O_3 growth [14–17]. Among all vapor-phase methods, only these two methods allow the production of thick layers of gallium oxide [18, 19]. Both techniques offer high growth rates (microns per hour) and simple doping schemes. When employed, they enable the achievement of high crystal perfection along with high-quality surface morphology. Moreover, these methods are cost-effective as long as vacuum setups are not required.

In this paper, we employ mist-CVD and HVPE techniques to fabricate a α-Ga_2O_3/α-Cr_2O_3/sapphire heterostructure. The primary goal of this work is to determine the fundamental feasibility of growing such a heterostructure using CVD, while achieving the specified layer thickness and maintaining acceptable surface morphology.

2. Experimental

Cr/Ga oxide heterostructures were grown on epi-ready sapphire c-plane (0001) substrates. In the first step, a Cr_2O_3 layer was deposited using the mist-CVD technique. We employed a homemade mist-CVD reactor equipped with a 2.4 MHz ultrasonic transducer, which produces droplets with a diameter in the range of 10-100 nm. The growth run lasted for 180 minutes, and the substrate temperature was maintained within a range of 700-850 °C. Detailed descriptions of the precursors and process parameters can be found in [20].

In the second step, a layer of Ga_2O_3 was deposited over the Cr_2O_3 layer using the HVPE method. We also utilized a homemade setup for this process. This reactor is built according to a hot-wall horisontal design and uses gallium chloride (GaCl) and oxygen (O_2) as precursors. The growth rate was approximately 2.4 μm/h, and the process temperature was set at 500 °C. Additional information regarding the process parameters can be found in [7].

The phase composition of the fabricated heterostructures was characterized by X-ray diffraction (XRD) technique. The Bourevestnik DRON 7 diffractometer with Cu$K_{\alpha1}$ = 1.5406 Å radiation was used. The surface roughness of the Cr_2O_3 layer was measured by Mahr MarSurf PS10 profilometer. The surface morphology of the Ga_2O_3 layer was analyzed using a Phenom ProX scanning electron microscope (SEM) operating in

secondary electron mode. To visualize the cross-section of the heterostructure and ascertain the thickness of the layers, samples were sectioned and examined by SEM.

3. Results and Discussion

The surface morphology of the first layer, which underwent the subsequent epitaxy process, should ideally be as smooth as possible. The visualization of the α-Cr_2O_3 layer's morphology is presented in Fig. 1. It is evident that the surface exhibits a homogeneous relief with no distinct features, except for some spots related to layer defects.

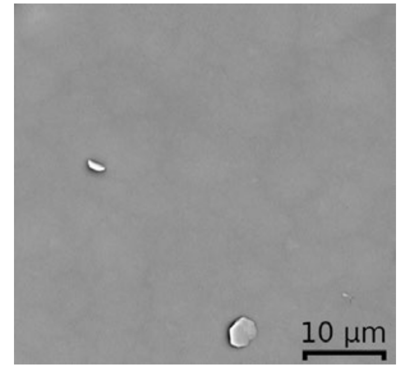

Fig. 1. SEM plan-view image of α-Cr_2O_3 layer grown by mist-CVD

The roughness (r_a) of the α-Cr_2O_3 layer was measured by the profilometer in both directions threefold. The r_a values appeared to be close and the average value ($\bar{r}_a$ = 24 nm) and is happened to be low enough for a consequent epitaxy process. The selected profiles of chromium oxide layer surface are shown in Fig. 2.

In the next step, the α-Ga_2O_3 layer was grown using the HVPE method. The surface morphology of this layer is depicted in Fig. 3, where distinct surface features can be observed.

The cross-sectional SEM image of the α-Ga_2O_3/α-Cr_2O_3/sapphire heterostructure is shown in Fig. 4. The thickness of the α-Ga_2O_3 layer is almost uniform along its lateral direction, measuring approximately 1.5 μm. Similarly, the α-Cr_2O_3 layer exhibits consistent thickness, albeit at a lower value of about 0.2 μm.

Analysis of the XRD θ-2θ curve of α-Ga_2O_3/α-Cr_2O_3/sapphire heterostructure revealed (000*l*) plane reflections for all three phases, plotted in logarithmical scale (see Fig. 5). Namely: for α-Al_2O_3 (0 0 0 6) is at 41.69 deg, (0 0 0 12) is at 90.69 deg; for α-Cr_2O_3 (0 0 0 6) is at 39.8 deg, (0 0 0 12) is at 85.9 deg; for α-Ga_2O_3 (0 0 0 6) is at 40.25 deg, (0 0 0 12) is at 86.96 deg. The angle values for sapphire and gallium oxide both coincide the tabulated ones very well. However, in the case of chromium oxide the experimental values differ significantly from the tabulated values ((0 0 0 6) is at 38.96 deg, (0 0 0 12) is at 83.66 deg). Since both values are shifted towards larger angles, this indicates decrease in lattice parameter of this phase relative tabulated one. One can conclude that the Cr_2O_3 layer, being a buffer one is stressed due to lattice mismatch of the neighbors.

Finally, employing the chromium oxide buffer layer, it was possible to grow homogeneous

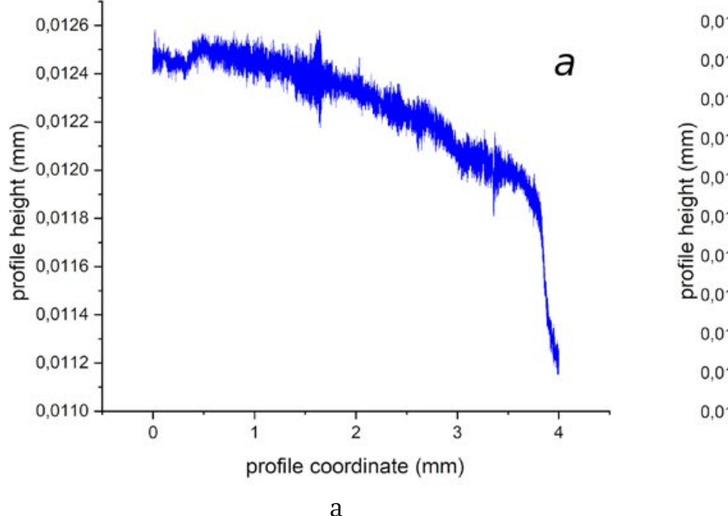

a

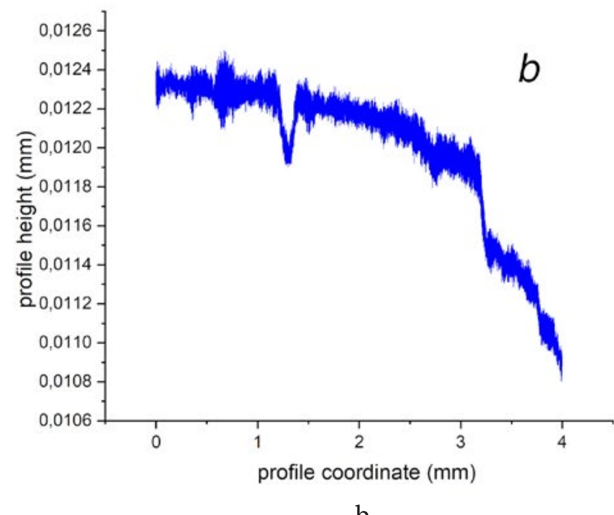

b

Fig. 2. The α-Cr_2O_3 layer surface relief in both lateral directions (a) OX direction scan, (b) OY direction scan

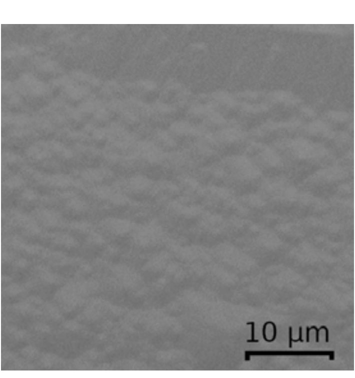

Fig. 3. SEM plan-view image of α-Ga_2O_3 layer grown by HVPE

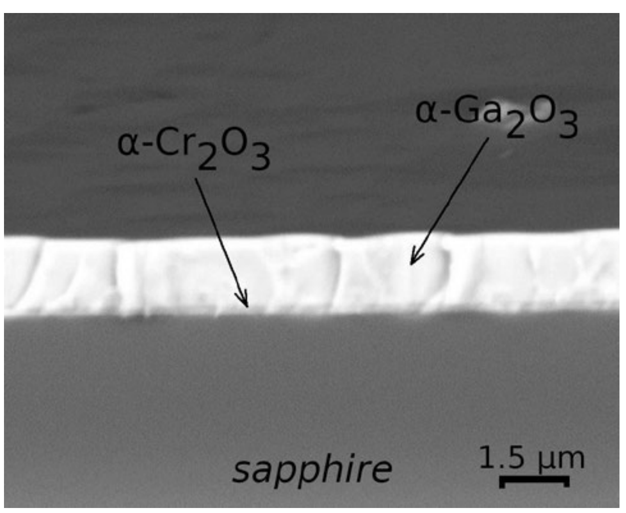

Fig. 4. SEM bird`s eye view image of the α-Ga_2O_3/α-Cr_2O_3/sapphire heterostructure

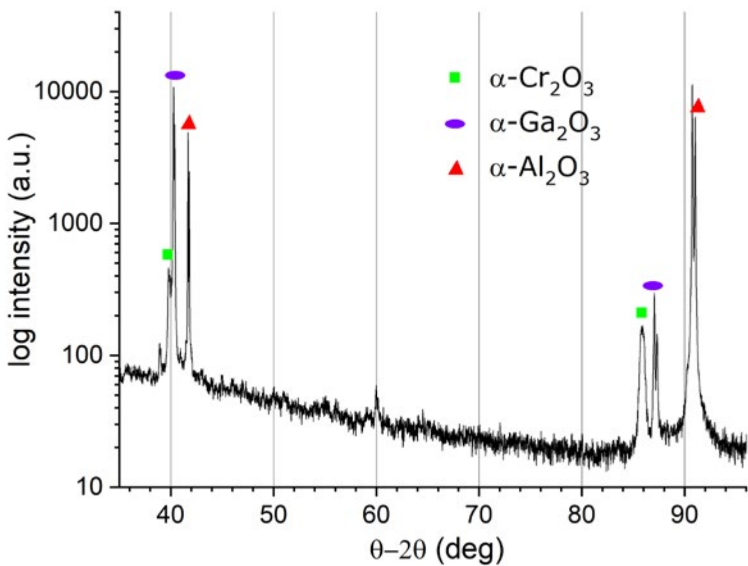

Fig. 5. XRD pattern of α-Ga_2O_3 / α-Cr_2O_3 / sapphire heterostructure

1.5 µm-thick gallium oxide layer with a constant thickness and relatively smooth surface. It is characterized by single-phase structure of relatively high perfection.

4. Conclusions

Thus, we have demonstrated the feasibility of fabricating α-Ga_2O_3/α-Cr_2O_3/sapphire heterostructures with the specified thicknesses and excellent morphology using CVD techniques. Both mist CVD and HVPE exhibit high growth rates. XRD patterns reveal the absence of any phases other than corundum-like.

Further studies are planned to focus on measuring the electrical parameters of the heterostructure and thinning the sapphire layer. This will allow the creation of a substrate with high thermal conductivity. It is also planned to investigate the possibility of separating the Ga_2O_3 layer from the sapphire substrate to obtain free-standing layers. This will allow the growth of high-quality gallium oxide layers on Cr_2O_3 buffer layer for device applications.

Contribution of the authors

The authors contributed equally to this article.

Conflict of interests

The authors declare that they have no known competing financial interests or personal relationships that could have influenced the work reported in this paper.

References

1. Hasan M. N., Swinnich E., Seo J. H. Recent progress in gallium oxide and diamond based high power and high-frequency electronics. *International Journal of High Speed Electronics and Systems*. 2019;28(01n02): 1940004. https://doi.org/10.1142/S0129156419400044

2. Yadava N., Chauhan R. K. Review—recent advances in designing gallium oxide MOSFET for RF application. *ECS Journal of Solid State Science and Technology*. 2020;9(6): 065010. https://doi.org/10.1149/2162-8777/aba729

3. Qiao R., Zhang H., Zhao S., Yuan L., Jia R., Peng B., Zhang Y. A state-of-art review on gallium oxide field-effect transistors. *Journal of Physics D: Applied Physics*. 2022;55(38): 383003. https://doi.org/10.1088/1361-6463/ac7c44

4. Stepanov S. I., Nikolaev V., Bougrov V. E., Romanov A. Gallium oxide: properties and applications - a review. *Review. Advanced Materials Science*. 2016;44: 63–86. Режим доступа: https://www.elibrary.ru/item.asp?edn=wsoxph

5. Pearton S. J., Aitkaliyeva A., Xian M., … Kim J. Review — radiation damage in wide and ultra-wide bandgap semiconductors. *ECS Journal of Solid State Science and Technology.* 2021;10: 055008. https://doi.org/10.1149/2162-8777/abfc23

6. Oshima Y., Ahmadi E. Progress and challenges in the development of ultra-wide bandgap semiconductor α-Ga_2O_3 toward realizing power device applications. *Applied Physics Letters.* 2022;121(26): 260501. https://doi.org/10.1063/5.0126698

7. Ping L. K., Berhanuddin D. D., Mondal A. K., Menon P. S., Mohamed M. A. Properties and perspectives of ultrawide bandgap Ga_2O_3 in optoelectronic applications. *Chinese Journal of Physics.* 2021;73: 195–212. https://doi.org/10.1016/j.cjph.2021.06.015

8. Jiao T., Li Z., Chen W., Dong X., Li Z., Diao Z., Zhang Y., Zhang B. Stable electron concentration Si-doped β-Ga_2O_3 films homoepitaxial growth by MOCVD. *Coatings*. 2021;11: 589. https://doi.org/10.3390/coatings11050589

9. Kaneko K., Fujita S., Shinohe T., Tanaka K. Progress in α-Ga_2O_3 for practical device applications. *Japanese Journal of Applied Physics.* 2023;62: SF0803. https://doi.org/10.35848/1347-4065/acd125

10. Kan S., Takemoto S., Kaneko K., Takahashi I., Sugimoto M., Shinohe T., Fujita S. Electrical properties of α-Ir_2O_3/α-Ga_2O_3 *pn* heterojunction diode and band alignment of the heterostructure. *Applied Physics Letters*. 2018;113: 212104. https://doi.org/10.1063/1.5054054

11. Kaneko K., Nomura T., Fujita S. Corundum-structured α-phase Ga_2O_3-Cr_2O_3-Fe_2O_3 alloy system for novel functions. *Physica Status Solidi C.* 2010;7(10): 2467–2470. https://doi.org/10.1002/pssc.200983896

12 Abdullah M. M., Rajab Fahd M., Al-Abbas Saleh M. Structural and optical characterization of Cr_2O_3 nanostructures: Evaluation of its dielectric properties. *AIP Advances*. 2014;4(2): 027121. https://doi.org/10.1063/1.4867012

13 Stepanov S., Nikolaev V., Almaev A., … Polyakov A. HVPE growth of corundum-structured α-Ga_2O_3 on sapphire substrates with α-Cr_2O_3 buffer layer. *Materials Physics and Mechanics*. 2021;47: 577–581. https://doi.org/10.18149/MPM.4742021_4

14. Yang D., Kim B., Eom T. H., Park Y., Jang H. W. Epitaxial growth of alpha gallium oxide thin films on sapphire substrates for electronic and optoelectronic devices: Progress and perspective. *Electronic Materials Letters*. 2022;18: 113–128. https://doi.org/10.1007/s13391-021-00333-5

15. Nikolaev V. I., Polyakov A. Y., Stepanov S. I., Pechnikov A. I., Guzilova L. I., Scheglov M. P., Chikiryaka A. V. Epitaxial stabilization of α-Ga_2O_3 layers grown on r-plane sapphire. *Materials Physics and Mechanics*. 2023;51(1): 1–9. https://doi.org/10.18149/MPM.5112023_1

16. Oda M., Kaneko K., Fujita S., Hitora T. Crack-free thick (~5 μm) α-Ga_2O_3 films on sapphire substrates with α-$(Al,Ga)_2O_3$ buffer layers. *Japanese Journal of Applied Physics*. 2016;55(12): 1202B4. https://doi.org/10.7567/JJAP.55.1202B4

17. Kim K.-H., Ha M.-T., Kwon Y.-J., Lee H, Jeong S.-M., Bae S.-Y. Growth of 2-inch α-Ga_2O_3 epilayers via rear-flow-controlled mist chemical vapor deposition. *ECS Journal of Solid State Science and Technology*. 2019;8(7): Q3165. https://doi.org/10.1149/2.0301907jss

18. Cheng Y., Xu Y., Li Z., Zhang J., … Zhang C. Heteroepitaxial growth of α-Ga_2O_3 thin films on a-, c- and r-plane sapphire substrates by low-cost mist-CVD method. *Journal of Alloys and Compounds*. 2020;831(5): 154776. https://doi.org/10.1016/j.jallcom.2020.154776

19. Cha A. N., Bang S., Rho H., … Ha J. S. Effects of nanoepitaxial lateral overgrowth on growth of α-Ga_2O_3 by halide vapor phase epitaxy. *Applied Physics Letters*. 2019;115(9): 091605. https://doi.org/10.1063/1.5100246

20. Nikolaev V. I., Timashov R. B., Stepanov A. I., … Polyakov A. Y. Synthesis of thin single-crystalline α-Cr_2O_3 layers on sapphire substrates by ultrasonic-assisted chemical vapor deposition. *Technical Physics Letters*. 2023;49(5): 81-84. http://dx.doi.org/10.21883/TPL.2023.05.56036.19549

Information about the authors

Pavel N. Butenko, Cand. Sci. (Tech.), Senior Researcher, Ioffe Institute of the Russian Academy of Sciences (St. Petersburg, Russian Federation).

https://orcid.org/0000-0003-1364-3016
pavel.butenko@mail.ioffe.ru

Roman B. Timashov, Researcher, Ioffe Institute of the Russian Academy of Sciences (St. Petersburg, Russian Federation).

https://orcid.org/0000-0001-9103-545X
timashov@inbox.ru

Andrey I. Stepanov, Dr. Sci. (Phys.–Math.), Researcher, Ioffe Institute of the Russian Academy of Sciences (St. Petersburg, Russian Federation).

https://orcid.org/0000-0003-2908-0385
stepanoffai@yandex.ru

Alexey I. Pechnikov, Researcher, Ioffe Institute of the Russian Academy of Sciences (St. Petersburg, Russian Federation).

https://orcid.org/0000-0003-4604-1935
alpechn@yahoo.com

Andrey V. Chikiryaka, Researcher, Ioffe Institute of the Russian Academy of Sciences (St. Petersburg, Russian Federation).

https://orcid.org/0000-0002-2087-8086
chikiryaka@mail.ru

Liubov I. Guzilova, Researcher, Ioffe Institute of the Russian Academy of Sciences (St. Petersburg, Russian Federation).

https://orcid.org/0000-0003-4205-3226

Sergey I. Stepanov, Cand. Sci. (Phys.–Math.), Researcher, Perfect Crystal LLC (St. Petersburg, Russian Federation).

s.i.stepanov@gmail.com

Vladimir I. Nikolaev, Cand. Sci. (Phys.–Math.), Leading Researcher, Ioffe Institute of the Russian Academy of Sciences (St. Petersburg, Russian Federation).

https://orcid.org/0000-0002-5630-0833
nikolaev.v@mail.ioffe.ru

Received 20.09.2023; approved after reviewing 25.09.2023; accepted for publication 16.10.2023; published online 25.12.2023.

Translated by the author of the article

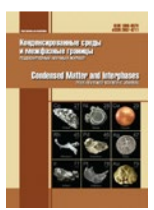

ISSN 1606-867X (Print)
ISSN 2687-0711 (Online)
Condensed Matter and Interphases
Kondensirovannye Sredy i Mezhfaznye Granitsy
https://journals.vsu.ru/kcmf/

Original articles

Research article
https://doi.org/10.17308/kcmf.2023.25/11484

A study of gallium oxide by using the piezoelectric composite oscillator technique at a frequency of 100 kHz

V. V. Kaminskii✉, D. A. Kalganov, D. I. Panov, V. A. Spiridonov, A. Yu. Ivanov, M. V. Rozaeva, D. A. Bauman, A. E. Romanov

ITMO University,
49 Kronverksky pr., St. Petersburg 197101, Russian Federation

Abstract

The article presents the results of the study of the mechanical properties and defect structure of gallium oxide (Ga_2O_3) by using the piezoelectric composite oscillator technique. Bulk samples of the Ga_2O_3 beta phase in the form of single crystals and their intergrowths were obtained by growth from a melt with a shaper (Stepanov technique). The research involved studying the dependences of the longitudinal elastic modulus and the damping of elastic vibrations at a frequency of 100 kHz on the strain amplitude. Changes in the elastic and microplastic properties of the samples at different temperatures were attributed to possible relaxation phenomena in the structure of the material.

Studying the defect structure in samples of pure and doped Ga_2O_3 is necessary to improve the technology for the production of large single crystals. The fundamental questions in this area are the influence of defects on the anisotropy of electrical conductivity, band structure, and other functional properties of the resulting semiconductor material. The purpose of this article is to establish the features of sample preparation, research, and interpretation of the results obtained by the piezoelectric composite oscillator technique for gallium oxide samples.

In the studied samples, the first longitudinal vibration mode was excited, which corresponded to a length of about 27 mm and a small cross-section of the sample. The temperature dependences in the region of low and high strain amplitudes were determined separately. The crystalline quality of the prepared samples was assessed by X-ray diffraction with the analysis of the rocking curve.

The value of Young's modulus obtained along the growth axis (crystalline orientation <010>) in Ga_2O_3 crystals $E \approx 260$ GPa is in line with the results of previous studies. Relaxation peaks corresponding to various dislocation interactions were found on the temperature dependences of internal friction at a temperature of 280 K.

Keywords: Gallium oxide, Single crystal, Defect structure, Real structure, Semiconductor, Piezoelectric composite oscillator technique

Funding: This work was supported by the grant of Russian Science Foundation No. 19-19-00617.

For citation: Kaminskii V. V., Kalganov D. A., Panov D. I., Spiridonov V. A., Ivanov A. I., Rozaeva M. V., Bauman D. A., Romanov A. E. A study of gallium oxide by using the piezoelectric composite oscillator technique at a frequency of 100 kHz. *Condensed Matter and Interphases*. 20223;25(4): 548–556. https://doi.org/10.17308/kcmf.2023.25/11484

Для цитирования: Каминский В. В., Калганов Д. А., Панов Д. Ю., Спиридонов В. А., Иванов А. Ю., Розаева М. В., Бауман Д. А., Романов А. Е. Исследование оксида галлия методом составного пьезоэлектрического осциллятора на частоте 100 кГц. *Конденсированные среды и межфазные границы*. 2023;25(4): 548–556. https://doi.org/10.17308/kcmf.2023.25/11484

✉ Vladimir V. Kaminskii, e-mail: vvkaminskii@itmo.ru
© Kaminskii V. V., Kalganov D. A., Panov D. I., Spiridonov V. A., Ivanov A. I., Rozaeva M. V., Bauman D. A., Romanov A. E., 2023

The content is available under Creative Commons Attribution 4.0 License.

1. Introduction

The search for new techniques for the manufacture and study of large-sized single crystals of β-Ga_2O_3 is associated with the possibility to use them to create substrates and functional parts for semiconductor devices [1]. Due to the unique properties of various forms of gallium oxide, it can be used to miniaturize existing power electronics components and to develop new ones [2, 3]. In this case, β-Ga_2O_3 substrates will allow using the advantages of homoepitaxy, simplifying the production technology, and ensuring the durability of the finished devices [4]. Applications of Ga_2O_3 for the creation of ultraviolet [5, 6] and X-ray detectors [7], gas sensors [8, 9], and other devices [10] have also been described. Currently, the largest linear dimensions of produced single crystals of β-Ga_2O_3 are up to 11 cm [11]. Intrinsic defects (oxygen vacancies [12]) and unintentional alloying which occur in the process of growth, as a rule, have a negative impact on their functional properties [13, 14]. However, the control of the density and distribution of defects of various types can allow the thermal conductivity, electrical conductivity, band structure, and many other properties of crystals to be purposefully changed [15, 16].

The defect-impurity structure of semiconductors has been widely studied by methods based on their optical and electronic radiofrequency properties [13, 17]. The band structure of Ga_2O_3 and its other properties which are important for solving applied problems have been studied analytically [18], numerically, and comprehensively [19]. However, one of the most universal techniques of structure analysis is based on the interaction of defects with the field of elastic waves [20, 21]. The piezoelectric composite oscillator (PCO) technique has been widely used to excite elastic vibrations [22]. Depending on the temperature, crystal orientation, and vibration frequency and amplitude, such interactions will have different values of energy loss due to internal friction [21, 23]. The maximum sensitivity of the PCO technique to the interaction of dislocations with point defects of various kinds is achieved at strain amplitudes from 10^{-7} to 10^{-4} in the frequency range of $10^3 \div 10^6$ Hz [24, 25]. The amplitude-independent part of the damping of elastic vibrations makes it possible to construct so-called indicative surfaces of the internal friction background [23] and to determine the orientation and activity of the dislocation slip systems. The damping of high-amplitude vibrations characterizes various processes of dislocation reproduction and motion in the elastic fields of other defects [26].

Despite the large amount of data on the structural properties of β-Ga_2O_3 [27], scientists continue to research the activation of various dislocation slip systems [28, 29]. The mechanical properties of bulk crystals of β-Ga_2O_3 necessary for the effective manufacture of wafer substrates have also been poorly studied. The study of these properties appears to be challenging due to the strict requirements to the preparation of samples of the specified shape and size and due to the need for additional research by other techniques. In this regard, so far, studies of the mechanical properties of Ga_2O_3 have only been carried out by those techniques that could be adapted for measurements on thin films and small-sized crystals.

The purpose of this work is to study bulk Ga_2O_3 crystals by the piezoelectric composite oscillator technique at a frequency of 100 kHz and to obtain data on the elastic and plastic features of the mechanical characteristics of Ga_2O_3.

2. Experimental

Bulk crystals of β-Ga_2O_3 were produced by the liquid-phase growth technique from a melt with a shaper (Stepanov technique) [11, 12] (Fig. 1a).

In this paper, the piezoelectric composite oscillator (PCO) technique with a measurement frequency of about 100 kHz was used as the main method for studying mechanical properties [25, 26]. The experiments were carried out at strain amplitudes from 10^{-7} to 10^{-4} in a wide temperature range from 120 to 320 K.

A piezoelectric composite oscillator was two soldered quartz single crystals. The studied material was attached to the oscillator with

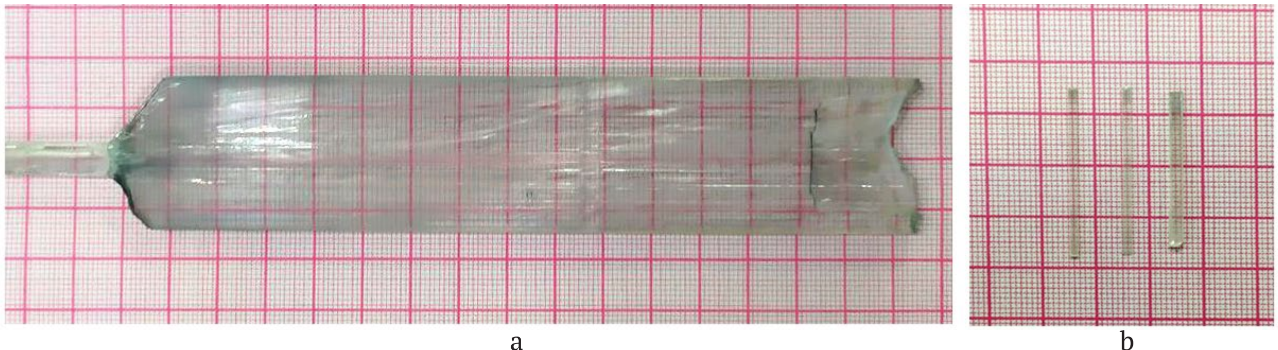

Fig. 1. The appearance of the β-Ga_2O_3 bulk samples obtained by Stepanov edge-defined film-fed growth method (a) and samples prepared for investigation by composite oscillator technique (b)

various adhesive substances. When an alternating voltage was applied to the electrodes of one of the crystals, it started to oscillate and transmit elastic vibrations to the sample. The value of the damping coefficient was obtained from the ratio of the signal on the electrodes of the second measuring crystal to the first one. The oscillation frequencies of the entire system were also measured. The values of internal friction and elastic moduli were found by the measured values with due account of the characteristics of the quartz oscillator and the coupling coefficient. In this research, measurements were taken at a resonance frequency of about 100 kHz for the first longitudinal oscillation mode. In this case, the change in frequency corresponded to the value of the Young's modulus. The Young's modulus and internal friction determined by this technique provided cumulative information about the dynamic properties of the microstructure and their changes under the influence of deformations in the studied material:

$$m_{osc}\delta_{osc} = m_{qu}\delta_{qu} + m_{sam}\delta_{sam},$$
$$m_{osc}f_{osc} = m_{qu}f_{qu} + m_{sam}f_{sam},$$

where m_{osc} is the mass of the entire oscillator; m_{qu} is the mass of quartz; m_{sam} is the mass of the sample; δ_{osc} is the damping of vibrations on the entire oscillator; δ_{qu} is the damping the vibrations on quartz; δ_{sam} is the damping of vibrations on the sample; f_{osc} is the frequency of vibrations on the entire oscillator; f_{qu} is the frequency of vibrations on quartz; and f_{sam} is the frequency of vibrations on the sample.

The Young's modulus for the sample material is defined as:

$$E = 4\rho l^2 f_{sam}^2,$$

ρ is the density of the studied material; and l is the length of the sample.

The relative change in elastic properties associated with the heating of the sample and its reversible dislocational deformation is characterized by the Young's modulus defect. In the case of longitudinal oscillations, this value is determined from the ratio:

$$\Delta E = \frac{(E_i - E(\varepsilon))}{E_i},$$

where E_i is the elastic modulus at the amplitude-independent stage, $E(\varepsilon)$ is the elastic modulus at the amplitude-dependent stage, and ε is the strain amplitude of the sample.

For PCO measurements, a diamond-coated circular saw was used to prepare samples in the form of parallelepipeds with dimensions of about 27×2×1 mm^3. The long side of the samples coincided with the growth axis <010> and the propagation direction of elastic vibrations from the piezoelectric oscillator to the sample. To ensure reliable results, measurements were taken on three samples of the same type (Fig. 1b).

The density of the samples was determined by hydrodensitometry using GH-252 accuracy class III balances (A&D Company) and a V7-78/1 temperature meter (AKIP). For the studied material, the average density value was ρ = 5915±12 kg/m^3.

In this experiment, in addition to the PCO technique, an X-ray diffraction analysis (a DRON-8 diffractometer, CuK_α-radiation, slit configuration, BSV-29 tube, NaI-Tl detector) was used to assess the crystalline perfection of the studied samples. The crystals prepared

for the PCO were studied in continuous and discrete modes in a wide range of angles. Rocking curves for reflection maxima (12 0 0) were also studied. Since the maximum deforming stress during the first longitudinal mode is localized in the center of the sample, we studied this area. The size of the X-ray beam on the surface was approximately equal to the width of the sample of ~ 2 mm.

2. Results and discussion

The obtained diffraction data are shown in Fig. 2. The overall diffraction pattern (Fig. 2A) has clear plane diffraction peaks (1 0 0) of different diffraction orders. The profile and diffraction angles correspond to the PDF 01-087-1901 data. The sample was examined and positioned by reflection (12 0 0). Fig. 2b shows the reflection diffractograms in a discrete mode to determine $2\Theta K_{\alpha1}$ = 102.24°. The rocking curve for the reflection maxima (12 0 0) was obtained with a narrow slit configuration in a discrete mode at two step values (Fig. 2c). The rocking curve profile has an asymmetric shape with a "tail" at smaller ω, the full width at half maximum intensity is approximately 0.011°.

The amplitude dependences of internal friction and Young's modulus were obtained by the PCO technique at room temperature (Fig. 3).

In all samples, both amplitude hysteresis due to internal friction (IT) and the Young's modulus (YM) are present, in other words, the dependences measured sequentially during increasing or decreasing amplitudes do not coincide with each other. The dependence measured during a decreasing amplitude is located above the dependence measured with an increasing amplitude. This behavior is characteristic of various types of single crystals and polycrystals [30, 31]. From the theoretical perspective, the amplitude hysteresis indicates the oscillatory motion of dislocations in the force fields of stops that secure dislocations of point defects [32, 33]. The hysteresis depends on the maximum strain amplitude at which the dependences were taken. For example, hysteresis was not observed at an amplitude of less than 10^{-5} (blue curves). A further slight increase

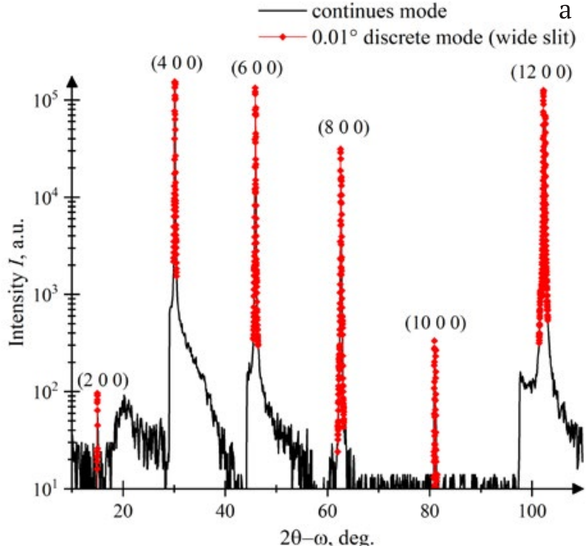

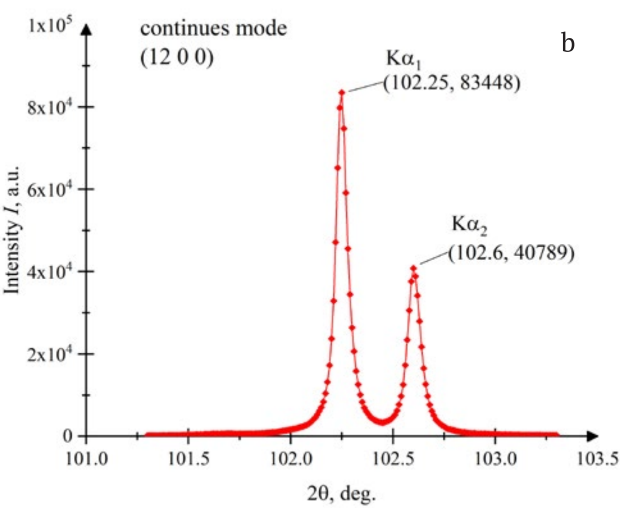

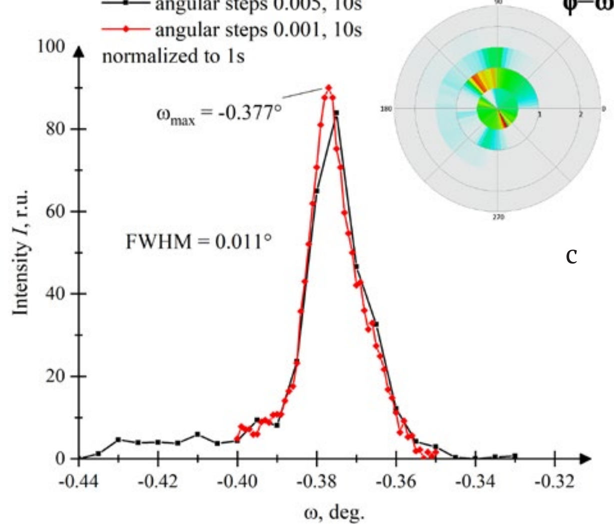

Fig. 2. The X-ray diffraction of the central region of the β-Ga_2O_3 sample over a wide range of angles (a), profile and rocking curve of the maximum (12 0 0) (b) and (c) respectively

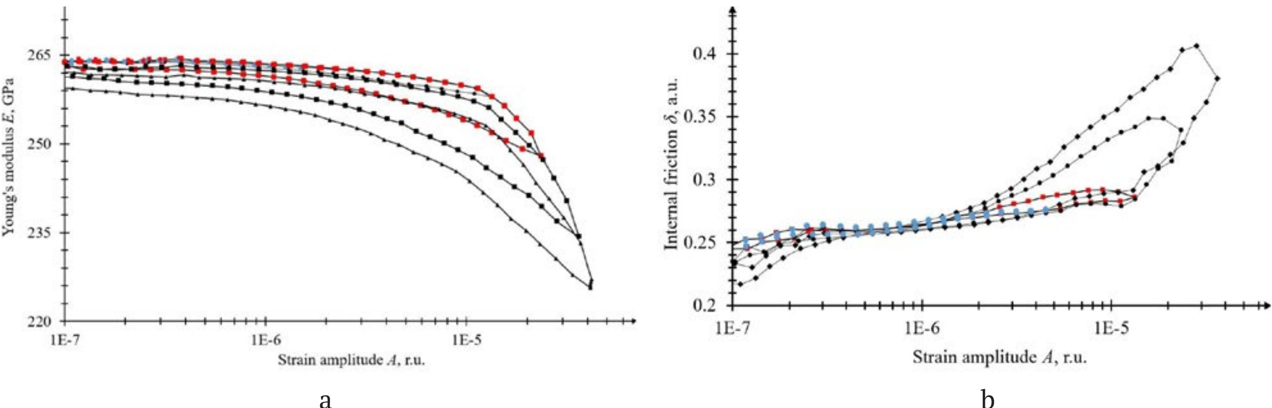

Fig. 3. Dependences of Young's modulus (a) and internal friction (b) on strain amplitude at room temperature

in amplitude (red curves) resulted in the appearance of a small reversible hysteresis. At amplitudes considerably higher than 10^{-5} (black curves), there were large reversible and irreversible hystereses.

These curves can be divided into two stages: (i) low-amplitude, characterized by a moderate increase in IF and a fall in the YM; (ii) high-amplitude with a significant increase in IF and a fall in the YM. During the first stage, there were vibrations of dislocations trapped at point defects (pinning centers) in the form of impurity atoms and vacancies and during the second stage, vibrations of dislocations appeared after the detachment [30]. The transition from the first stage to the second occurred at a strain amplitude of about 10^{-5}.

Fig. 4 shows the Young's modulus defect caused by the deformation of Ga_2O_3 samples. The curves were taken at three temperatures: 300, 225, and 118 K. In this case, the amplitude dependences of the Young's modulus defect are associated with the two stages of the sample microdeformation described above. Despite the fact that the YM defect is determined primarily by the density of defect structures and their distribution over the section and length of the studied sample, the temperature also has a significant impact on this characteristic [30]. When the temperature rose, the growth of the YM defect was due to unlocking dislocations [34]. It should be noted that the graph was built from the dependences $E(\varepsilon)$ taken at the very

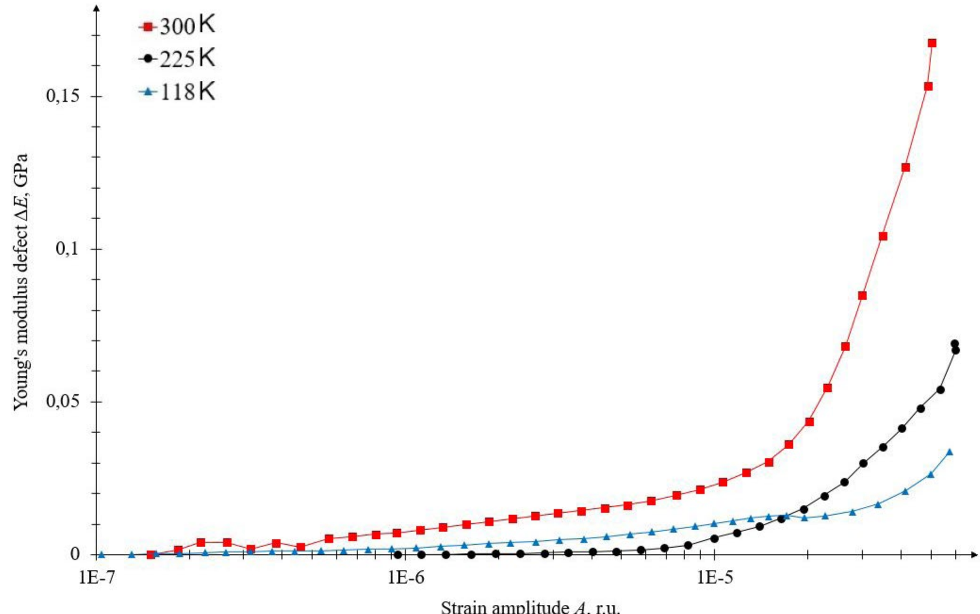

Fig. 4. Amplitude dependence of the Young's modulus defect

first increase in amplitude on samples that had never been exposed to high amplitudes.

Fig. 5 shows the temperature dependences of the YM and IF. On the whole, when the temperature decreased, the Young's modulus increased, while the IF decreased. This behavior of dependences of mechanical characteristics is conventional. There was also a slight gap in the dependences around 273 K, apparently due to the presence of residual moisture in the measuring cell. It should be noted that the YM was in the range of 261–272 GPa (Fig. 5a) and at room temperature it fully correlated with the data presented in other papers [35, 36]. For example, the authors of [35] studied nanomechanical resonators based on β-Ga_2O_3 nano flakes grown by low pressure chemical vapor deposition (LPCVD). The measurements taken in this paper revealed the Young's modulus E = 261 GPa and anisotropic biaxial inline tension of 37.5 and 107.5 MPa. At a temperature of about 280 K, there was an IF peak (Fig. 5b), while on the YM temperature dependence there was an inflection. This peak and inflection are associated with dislocation interactions, apparently with Hasiguti relaxation or Snoek–Koster relaxation [37]. Hasiguti relaxation is associated with the interaction of dislocations (inflections) with their intrinsic defects: interstitial defects, vacancies, and their complexes. In our case, Snoek–Koster relaxation can be due to the "dragging" or "separation" of impurity atmospheres during the motion of dislocations. The obtained results can be associated with the technology of obtaining monocrystalline intergrowths. At growth temperatures, the melt is unstable and subject to decomposition into gas components: divalent gallium oxide, monovalent oxide, metallic gallium, and oxygen: (Ga_2O_3 → GaO → Ga_2O → Ga, and O). This process cannot be fully compensated for by an excess of oxygen in the growth atmosphere, which, as a rule, leads to the emergence of oxygen vacancies in the growing bulk crystal [38]. Hence, it can be assumed that the Hasiguti relaxation is the main mechanism responsible for the formation of the IF peak and the inflection on the YM dependence. However, further research is required to reliably prove the determined nature of the peaks. When comparing equivalent samples of the same initial material, the Hasiguti relaxation peaks in some of them can be annealed during the reverse stage [37].

3. Conclusion

The obtained diffraction curve profile (Fig. 2a) and the value of the parameter a of the crystal lattice of the synthesized monoclinic phase correspond to the reference data in the PDF database and the data presented in other scientific publications [39], which may indicate a high degree of structural perfection of the obtained β-Ga_2O_3 samples and a small value of residual stresses in the crystal. The small value (for the used slit configuration) of the half-width of the rocking curve indicates a high degree of crystalline perfection of the studied region within the sample. An inconsiderable asymmetry of this curve in the

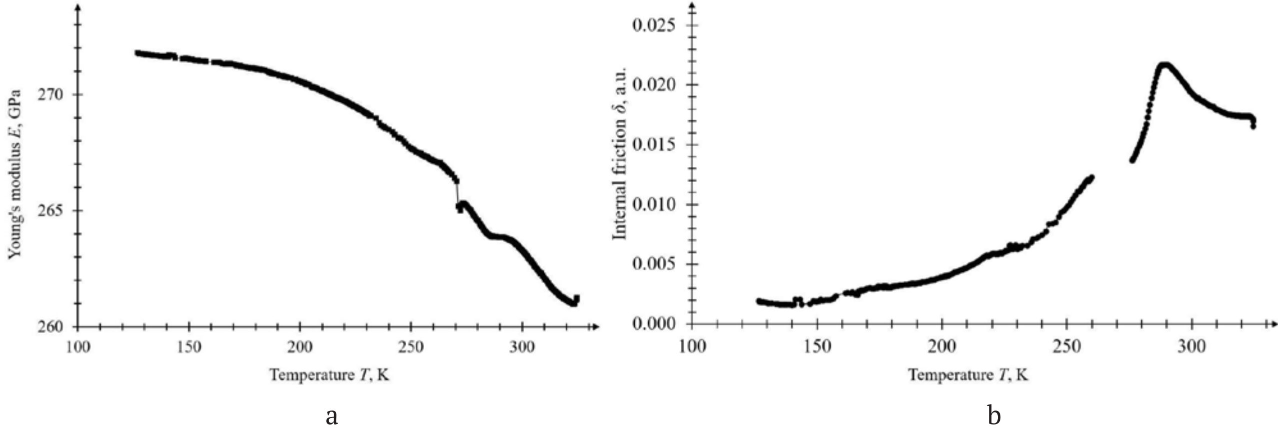

Fig. 5. Temperature dependences of Young's modulus (a) and internal friction (b) of Ga_2O_3

area of small angles can be due to various factors, such as the small-angle disorientation of blocks (grains) or the presence of twins. The crystal structure of the studied samples corresponds to the initial material [11, 12].

The PCO technique was used to obtain the mechanical characteristics of the samples at a frequency of 100 kHz. During the experiments, the amplitude dependences of the YM and IF were obtained and interpreted. The amplitude dependences can be divided into two stages: (i) low-amplitude, in which vibrations of dislocations occur within impurity atmospheres; (ii) high-amplitude, in which vibrations of dislocations occur outside impurity atmospheres. The value of strain amplitude was found at which there is the transition from the first stage to the second. As a result, the temperature dependences of the YM and IF at a frequency of about 100 kHz were obtained for β-Ga_2O_3. Those dependences are in line with the results of other experiments. Further research is required to interpret the nature of the IF relaxation peak at 285 K associated with dislocation interactions.

Contribution of the authors

The authors contributed equally to this article.

Conflict of interests

The authors declare that they have no known competing financial interests or personal relationships that could have influenced the work reported in this paper.

References

1. Kitsay A. A., Nosov YU. G., CHikiryaka A. V., Nikolaev V. I. Growth of β-Ga_2O_3 single crystals by the solution-melt method. *Technical Physics Letters*. 2023;49(14): 16–18. https://doi.org/10.21883/PJTF.2023.14.55819.19589

2. Kalygina V. M., Nikolaev V. I., Almaev A. V., Tsymbalov A. V., Petrova Y. S., Pechnikov I. A., Butenko P. N. Properties of resistive structures based on gallium oxide polymorphic phases. *Technical Physics Letters*. 2020;46: 867–870. https://doi.org/10.1134/S1063785020090060

3. Green A. J., Speck J., Xing G., ... Higashiwaki M. β-gallium oxide power electronics. *Apl Materials*. 2022;10(2): 029201. https://doi.org/10.1063/5.0060327

4. Kalygina V. M., Lygdenova T. Z., Petrova Y. S., Chernikov E. V. Influence of the substrate material on the properties of gallium-oxide films and gallium-oxide-based structures. *Semiconductors.* 2019;53(4): 452–457. https://doi.org/10.1134/S1063782619040122

5. Kaur D., Kumar M. A strategic review on gallium oxide based deep-ultraviolet photodetectors: recent progress and future prospects. *Advanced Optical Materials*. 2021;9(9): 2002160. https://doi.org/10.1002/adom.202002160

6. Kalygina V. M., Kiselyeva O. S., Kushnarev B. O., Oleinik V. L., Petrova Y. S., Tsymbalov A. V. Self-powered photo diodes based on Ga_2O_3/n-GaAs structures. *Semiconductors.* 2022;56(9): 707–711. https://doi.org/10.21883/SC.2022.09.54139.9868

7. Lu X., Zhou L., Chen L., Ouyang X., Liu B., Xu J., Tang H. Schottky X-ray detectors based on a bulk β-Ga_2O_3 substrate. *Applied Physics Letters*. 2018;112(10): 103502 https://doi.org/10.1063/1.5020178

8. Zhu J., Xu Z., Ha S., Li D., Zhang K., Zhang H., Feng J. Gallium oxide for gas sensor applications: A comprehensive review. *Materials*. 2022:15(20): 7339. https://doi.org/10.3390/ma15207339

9. Nikolaev V. I., Almaev A. V., Kushnarev B. O., ... Chernikov E. V. Gas-sensing properties of In_2O_3-Ga_2O_3 alloy films. *Technical Physics Letters.* 2022;48(7): 76–79. https://doi.org/10.21883/TPL.2022.07.54046.19211

10. Petrenko A. A., Kovach Ya. N., Bauman D. A., Odnoblyudov M. A., Bougrov V. E., Romanov A. E. Current state of Ga_2O_3-based electronic and optoelectronic devices. Brief review. *Reviews on Advanced Materials and Technologies.* 2021;3(2): 1–26. https://doi.org/10.17586/2687-0568-2021-3-2-1-26

11. Bauman D. A., Panov D. Iu., Spiridonov V. A... Romanov A. E. High quality β-Ga_2O_3 bulk crystals, grown by edge-defined film-fed growth method: growth features, structural and thermal properties. *Journal of Vacuum Science and Technology A.* 2023;41: 053203. https://doi.org/10.1116/6.0002644

12. Bauman D. A., Panov D. I., Spiridonov V. A., Kremleva A. V., Romanov A. E. On the successful growth of bulk gallium oxide crystals by the EFG (Stepanov) method. *Functional Materials Letters*. 2023: 2340026. https://doi.org/10.1142/S179360472340026X

13. Son N. T., Goto K., Nomura K., ... Janzén E. Electronic properties of the residual donor in unintentionally doped β-Ga_2O_3. *Journal of Applied Physics*. 2016;120(23): 235703. https://doi.org/10.1063/1.4972040

14. Ivanova E. V., Dementev P. A., Zamoryanskaya M. V., ... Bougrov V. E. Study of charge carrier traps in bulk crystal gallium oxide β-Ga_2O_3. *Physics of the Solid State.* 2021;63(4): 544–549. https://doi.org/10.1134/S1063783421040089

15. Wang Z., Chen X., Ren F. F., Gu S., Ye J. Deep-level defects in gallium oxide. *Journal of Physics D: Applied Physics.* 2020;54(4): 043002. https://doi.org/10.1088/1361-6463/abbeb1

16. Manikanthababu N., Sheoran H., Siddham P., Singh R. Review of radiation-induced effects on

β-Ga_2O_3 materials and devices. *Crystals*. 2022;12(7): 1009. https://doi.org/10.3390/cryst12071009

17. Seyidov P., Ramsteiner M., Galazka Z., Irmscher K. Resonant electronic Raman scattering from Ir^{4+} ions in β-Ga_2O_3. *Journal of Applied Physics*. 2022;131(3): 035707. https://doi.org/10.1063/5.0080248

18. Abdrakhmanov V. L., Zav'yalov D. V., Konchenkov V. I., Kryuchkov S. V. Effect of a strong electromagnetic wave on the conductivity of β-Ga_2O_3. *Bulletin of the Russian Academy of Sciences: Physics*. 2020;84(1): 53-57. https://doi.org/10.3103/S1062873820010037

19. Guzilova L. I., Grashchenko A. S., Pechnikov A. I., ... Nikolaev V. I. *Materials Physics and Mechanics*. 2016;29(2): 166–171. (In Russ., abstract in Eng.). Available at: https://www.ipme.ru/e-journals/MPM/no_22916/MPM229_09_guzilova.pdf

20. Quimby S. L. On the experimental determination of the viscosity of vibrating solids. *Physical Review*. 1925;25(4): 558. https://doi.org/10.1103/PhysRev.25.558

21. Kimball A. L., Lovell D. E. Internal friction in solids. *Physical Review*. 1927;30(6): 948. https://doi.org/10.1103/PhysRev.30.948

22. Marx J. Use of the piezoelectric gauge for internal friction measurements. *Review of Scientific Instruments*. 1951;22(7): 503–509. https://doi.org/10.1063/1.1745981

23. Naimi E. K. Internal-friction anisotropy in a real crystal and construction of characteristic internal-friction surfaces. *Soviet Physics Journal*. 1975;18: 371–375. https://doi.org/10.1007/BF00889303

24. Granato A. V., Lücke K. Application of dislocation theory to internal friction phenomena at high frequencies. *Journal of Applied Physics*. 1956;27(7): 789–805. https://doi.org/10.1063/1.1722485

25. Robinson W. H., Edgar A. The piezoelectric method of determining mechanical damping at frequencies of 30 to 200 KHz. *IEEE Transactions on Sonics and Ultrasonics*. 1974;21(2): 98–105. https://doi.org/10.1109/T-SU.1974.29798

26. Tyapunina N. A., Zinenkova G. M., Shtrom E. V. Dislocation multiplication in alkali halide crystals exposed to ultrasonic waves. The original stage. *Physica Status Solidi (a)*. 1978;46(1): 327–336. https://doi.org/10.1002/pssa.2210460143

27. Nikolaev V. I., Stepanov S. I., Romanov A. E., Bougrov V. E. Gallium oxide. In: *Single Crystals of Electronic Materials*. R. Fornari (ed.). Woodhead Publishing; 2019. 487–521. https://doi.org/10.1016/B978-0-08-102096-8.00014-8

28. Yamaguchi H., Kuramata A., Masui T. Slip system analysis and X-ray topographic study on β-Ga_2O_3. *Superlattices and Microstructures*. 2016;99: 99–103. https://doi.org/10.1016/j.spmi.2016.04.030

29. Wu Y., Rao Q., Best J. P., Mu D., Xu X., Huang H. Superior room temperature compressive plasticity of submicron beta-phase gallium oxide single crystals. *Advanced Functional Materials*. 2022;32(48): 2207960. https://doi.org/10.1002/adfm.202207960

30. Kaminskii V. V., Kalganov D. A., Podlesnov E., Romanov A. E. Influence of dislocation and twin structures on the mechanical characteristics of Ni-Mn-Ga alloys at ultrasonic frequencies. *Frontier Materials and Technologies*. 2022;2: 28–36. https://doi.org/10.18323/2782-4039-2022-2-28-36

31. Kaminskii V. V., Lyubimova Y. V., Romanov A. E. Probing of polycrystalline magnesium at ultrasonic frequencies by mechanical spectroscopy. *Materials Physics and Mechanicals*. 2020;44(1): 19–25. https://doi.org/10.18720/MPM.4412020_3

32. Guzilova L. I., Kardashev B. K., Pechnikov A. I., Nikolaev V. I. Elasticity and Inelasticity of bulk GaN crystals. *Technical Physics*. 2020;90(1): 138–142. https://doi.org/10.1134/s1063784220010089

33. Sapozhnikov K. V., Golyandin S. N., Kustov S. B. Amplitude dependence of the internal friction and young's modulus defect of polycrystalline indium. *Physics of the Solid State*. 2010;52(1): 43–48. https://doi.org/10.1134/S1063783410010087

34. Lebedev A. B., Kustov S. V., Kardashov B. K. On internal friction and the Young's modulus defect in the crystal deformation process*. *Solid State Physics*. 1992;34(9): 2915. (In Russ.). Available at: https://journals.ioffe.ru/articles/viewPDF/22631

35. Zheng X. Q., Lee J., Rafique S., Han L., Zorman C. A. Zhao H., Feng P. X. L. Ultrawide band gap β-Ga_2O_3 nanomechanical resonators with spatially visualized multimode motion. *ACS Applied Materials and Interfaces* 2017;9(49): 43090–43097. https://doi.org/10.1021/acsami.7b13930

36. Zheng X. Q., Zhao H., Feng P. X. L. A perspective on β-Ga_2O_3 micro/nanoelectromechanical systems. *Applied Physics Letters*. 2022;120(4). https://doi.org/10.1063/5.0073005

37. Golovin I. S. Internal friction and mechanical spectroscopy of metals and alloys. *Metal Science and Heat Treatment*. 2012;54(5-6): 207–208. https://doi.org/10.1007/s11041-012-9482-7

38. Zakgeim D. A., Panov D. I., Spiridonov V. A., ... Bougrov V. E. Volume gallium oxide crystals grown from melt by the Czochralski method in an oxygen-containing atmosphere. *Technical Physics Letters*. 2020;46: 1144–1146. https://doi.org/10.1134/S1063785020110292

39. Samoylov A. M., Kopytin S. S., Oreshkin K. V., Shevchenko E. A. Synthesis of chemically pure β-phase powders of gallium(III) oxide. *Condensed Matter and Interphases*. 2022;24(3): 345–355. https://doi.org/10.17308/kcmf.2022.24/9857

Translated by author of the article.

Information about the authors

Vladimir V. Kaminskii, Cand. Sci. (Phys.–Math.), Head of the Laboratory, ITMO University (Saint Petersburg, Russian Federation).

https://orcid.org/0000-0002-4388-2459
vvkaminskii@itmo.ru

Dmitrii A. Kalganov, Junior Researcher at the Advanced Data Transfer System Institute, ITMO University (Saint Petersburg, Russian Federation).

https://orcid.org/0000-0003-1986-3693
kalganov@itmo.ru

Dmitrii I. Panov, Cand. Sci. (Phys.–Math.), Head of the Laboratory, ITMO University (Saint Petersburg, Russian Federation).

https://orcid.org/0000-0001-8715-9505
dmitriipnv@itmo.ru

Vladislav A. Spiridonov, Engineer at the Advanced Data Transfer System Institute, ITMO University (Saint Petersburg, Russian Federation).

https://orcid.org/0000-0001-5751-8597
vladspiridonov@itmo.ru

Andrey I. Ivanov, Engineer at the Advanced Data Transfer System Institute, ITMO University (Saint Petersburg, Russian Federation).

https://orcid.org/0000-0003-0737-9079
aiivanov@itmo.ru

Margarita V. Rozaeva, master student, Engineer at the Advanced Data Transfer System Institute, ITMO University (Saint Petersburg, Russian Federation).

https://orcid.org/0009-0000-2978-5380
412189@niuitmo.ru

Dmitrii A. Bauman, Cand. Sci. (Phys.–Math.), Associate Professor at the Advanced Data Transfer System Institute, ITMO University (Saint Petersburg, Russian Federation).

https://orcid.org/0000-0002-5762-5920
dabauman@itmo.ru

Alexey E. Romanov, Dr. Sci. (Chem.), Professor, Head of the Advanced Data Transfer System Institute, ITMO University (Saint Petersburg, Russian Federation).

https://orcid.org/0000-0003-3738-408X
aeromanov@itmo.ru

Received 20.09.2023; approved after reviewing 13.10.2023; accepted for publication 16.10.2023; published online 26.12.2023.

Translated by Irina Charychanskaya

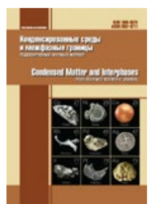

ISSN 1606-867X (Print)
ISSN 2687-0711 (Online)
Condensed Matter and Interphases
Kondensirovannye Sredy i Mezhfaznye Granitsy
https://journals.vsu.ru/kcmf/

Original articles

Research article
https://doi.org/10.17308/kcmf.2023.25/11479

Phase transformations during the annealing of Ga_2O_3 films

A. V. Osipov[1]✉, Sh. Sh. Sharofidinov[2], A. V. Kremleva[3], A. M. Smirnov[3], E. V. Osipova[1], A. V. Kandakov[1], S. A. Kukushkin[1]

[1]*Institute for Problems in Mechanical Engineering of the Russian Academy of Science, 61 Boljshoy prospekt V.O., St. Petersburg 199178, Russian Federation*

[2]*Ioffe Institute, 26 Polytechnicheskaya st., St. Petersburg 194021, Russian Federation*

[3]*ITMO University, 49 Kronverksky pr., bldg. A, St. Petersburg 197101, Russian Federation*

Abstract

A growth technique has been developed to obtain the three main crystalline phases of Ga_2O_3, namely: α-phases, ε-phases, and β-phases using hybrid vapour phase epitaxy (HVPE). The substrate temperatures and precursor fluxes were determined at which only the α-phase, only the ε-phase, or only the β-phase were deposited. It was found that the annealing of the metastable α- and ε-phases led to completely different results. The ε-phase quickly transforms into the stable β-phase as a result of annealing, while the α-phase, upon annealing, transforms into an intermediate amorphous phase, after which it peels off and is destroyed. The obtained result is explained by the fact that the reconstructive phase transition from the α-phase into the β-phase is accompanied by too large an increase in density (~10%), leading to enormous elastic stresses and, consequently, an increase in the height of the phase transition barrier.

Keywords: Reconstructive phase transitions, Gallium oxide, Polymorphs, X-ray diffraction, Spectroscopic ellipsometry, Raman spectrum

Funding: A. V. Kremleva carried out her part of the study with financial support Russian Science Foundation (grant No. 21-79-00211).

For citation: Osipov A. V., Sharofidinov Sh. Sh., Kremleva A. V., Smirnov A. M., Osipova E. V., Kandakov A. V., Kukushkin S. A. Phase transformations during the annealing of Ga_2O_3 films. *Condensed Matter and Interphases*. 20223;25(4): 557–563. https://doi.org/10.17308/kcmf.2023.25/11479

Для цитирования: Осипов А. В., Шарофидинов Ш. Ш., Кремлева А. В., Смирнов А. М., Осипова Е. В., Кандаков А. В., Кукушкин С. А. Превращения фаз в процессе отжига пленок Ga_2O_3. *Конденсированные среды и межфазные границы*. 2023;25(4): 557–563. https://doi.org/10.17308/kcmf.2023.25/11479

✉ Andrei V. Osipov, e-mail: andrey.v.osipov@gmail.com
© Osipov A. V., Sharofidinov Sh. Sh., Kremleva A. V., Smirnov A. M., Osipova E. V., Kandakov A. V., Kukushkin S. A., 2023

The content is available under Creative Commons Attribution 4.0 License.

1. Introduction

In recent years, there has been enormous interest in the growth of so-called transparent conductors, which are often metal oxides such as zinc oxide ZnO, magnesium oxide MgO, gallium oxide Ga_2O_3 and some other oxides [1]. Among these materials, gallium oxide Ga_2O_3 [2–4], which is a semiconductor with a large band gap ~ 5 eV, characterized by very high breakdown voltage ~ 8 $Mvcm^{-1}$ is distinguished. It is easily doped, which makes it very promising for micro- and optoelectronics applications. In addition, it is easy to mix with the magnetic material Cr_2O_3, which makes it promising for spintronics. Another important feature of Ga_2O_3 is its existence in several crystalline modifications. Reviews [2–4] indicate 5 phases as the main ones, namely, the stable β-phase with monoclinic structure C2/m and metastable the ε-phase with orthorhombic structure $Pna2_1$, the α-phase with a rhombohedral structure $R\bar{3}c$ (corundum structure), the δ-phase with a body-centred cubic structure $la\bar{3}$, and the γ-phase with a cubic structure $Fd\bar{3}m$. Despite the fairly large number of metastable phases, it is extremely difficult to obtain them, since mainly only the stable β-phase grows. Currently, a fairly large number of Ga_2O_3 growth methods have been developed. These are various technologies for the volumetric growth of Ga_2O_3, and methods of molecular beam epitaxy, and chemical vapour deposition, as well as methods of chloride-hydride vapour epitaxy [5–7]. Usually, Al_2O_3 sapphire crystals with different orientations, silicon carbide [8], as well as silicon are used as substrates for the growth of Ga_2O_3 layers. Silicon, which is used quite often, is not a very good choice for Ga_2O_3 growth, since it can conduct electric current and Ga_2O_3 grows much worse on it. Firstly, silicon poorly orients growing Ga_2O_3 layers, secondly, oxygen O_2 and water H_2O when used as reagents for the production of Ga_2O_3, react with silicon to form amorphous silicon dioxide SiO_2, which further worsens the epitaxy of Ga_2O_3. Therefore, in this study, Al_2O_3sapphire (0001) was used as the substrate.

The purpose of this study was the investigation of solid-phase transformations between various polymorphs of Ga_2O_3. In the study [7] a method for obtaining the three main phases of Ga_2O_3 was developed, namely, the stable β-phase, the metastable α-phase and the metastable ε-phase by chloride-hydride epitaxy on SiC-3C/Si hybrid substrates at different temperatures. In this study, these three phases were obtained by a similar method, but in this case using sapphire Al_2O_3, which is especially important for α-phases, since it has the same corundum structure as sapphire. As a result, the quality of the resulting phases was significantly higher, which made it possible to study the various optical properties of Ga_2O_3 phases by ellipsometry and Raman spectroscopy methods. Next, the metastable α-phase and the ε-phase were annealed at different temperatures in order to transform them into a stable β-phase. All phases were studied in detail by X-ray diffraction, Raman spectroscopy, and spectral ellipsometry.

2. Experimental

Standard sapphire substrates with the orientation <0001> were used for the growth of Ga_2O_3 layers. Ga_2O_3 layers were grown using hydride vapour phase epitaxy (HVPE) due to the following chemical reaction [7]:

$$2GaCl + 3/2O_2 = Ga_2O_3 + Cl_2. \qquad (1)$$

Gallium chloride was synthesized directly in the source zone of the reactor by passing hydrogen chloride gas (HCl 99.999%) over gallium metal (Ga 99.9999%). The yield of the GaCl synthesis reaction was approximately 85%. The oxygen necessary for the formation of gallium oxide was supplied in a mixture with argon (20% oxygen, 80% argon). The synthesis of gallium oxide was carried out under conditions of excessive oxygen flow. The ratio of components of groups VI/III was in the range of 3–5. The rate of Ga_2O_3 deposition was determined by the HCl flow through the gallium source and depended on the deposition temperature, which varied over a wide range of 500–1000 °C. With total gas flow ~ 5 000 cm^3/min Ga_2O_3 deposition rate started from approximately 0.4–0.5 μm/min at 500 °C and ended at 0.8–1.0 μm/min at 1000 °C [7]. The deposition time was chosen to be approximately 2–4 min in order to obtain a Ga_2O_3 layer approximately ~2 μm thick. After growth was completed, the substrate was cooled in an argon flow to room temperature. The results of the analysis showed that different phases of Ga_2O_3 were synthesised

at different temperatures. At 800–1000 °C, Ga_2O_3 precipitated in the stable β-phase, as in the vast majority of other experiments [3,4,9]. At a synthesis temperature of 550–600 °C, Ga_2O_3 precipitated only in the metastable ε-phase. At synthesis temperature of 500–520 °C, Ga_2O_3 deposited only in the metastable α-phase. X-ray diffraction patterns of three Ga_2O_3 samples, grown on Al_2O_3 (0001) at temperatures of 510, 575, and 900 °C respectively are shown in Fig. 1. It is clearly seen that in the first case Ga_2O_3 was deposited in the most symmetrical α-phase with a rhombohedral structure $R\bar{3}c$, in the second case Ga_2O_3 deposited in the least symmetrical ε-phase with the orthorhombic structure $Pna2_1$, and in the third case Ga_2O_3 deposits in a stable β-phase with a monoclinic structure C2/m.

3. Results and discussion

The dependence of permittivity on photon energy plays an important role in the optical properties of materials [7], therefore it was measured for all three Ga_2O_3samples using a M-2000D J.A. Woollam ellipsometer with a rotating compensator operating in the range of 0.75–6.45 eV. The measured dependence is presented in Fig. 2. Based on the imaginary part of the dielectric permittivity ε_2 associated with light absorption, we can conclude that the β-phase absorbs light most strongly and has the lowest band gap. The most symmetrical α-phase, on the contrary, was the most transparent and had the largest band gap. The least symmetric ε-phase occupied an intermediate position in terms of transparency and band width (in all three cases, the band gap was indirect). The result obtained is in full agreement with the results of calculations by the quasi-particle method (GW) [10].

The Raman spectrum of all three phases measured using a WiTec Alpha300R confocal Raman microscope is shown in Fig. 3. The main basic lines are signed. In addition to the lines corresponding to the Ga_2O_3 phases, there are sapphire lines, since at the laser wavelength of 532 nm all phases of Ga_2O_3 are transparent. The measured spectra are in very good agreement with the theoretical spectra computed by the density functional theory (DFT) [7].

Next, samples of the metastable α- and ε-phases were kept in a vacuum at various

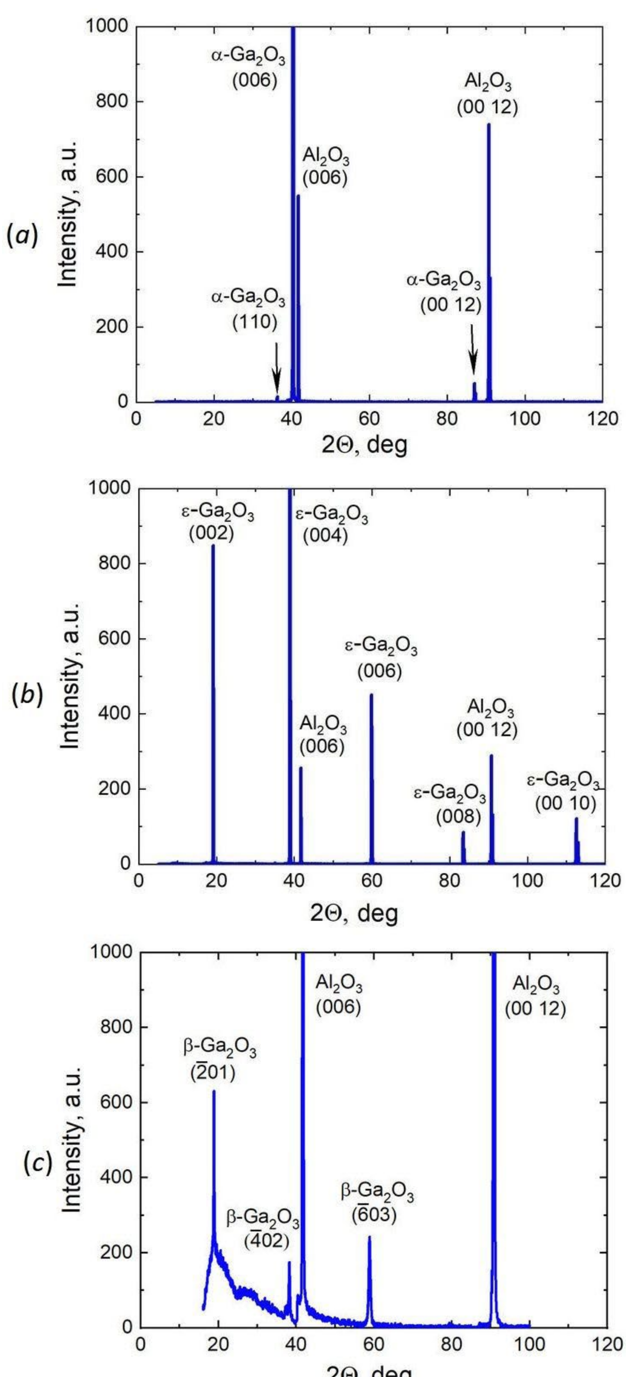

Fig. 1. X-ray diffractograms of three Ga_2O_3 samples grown on Al_2O_3(0001) sapphire at temperatures of 510 (a), 575 (b), 900 °C (c)

temperatures from 650 to 950 °C. The annealing time varied from 10 to 30 min. The resulting samples were again studied by X-ray diffraction, Raman spectroscopy, and spectroscopic ellipsometry. The research results were as follows. The metastable ε-phase transforms into a stable

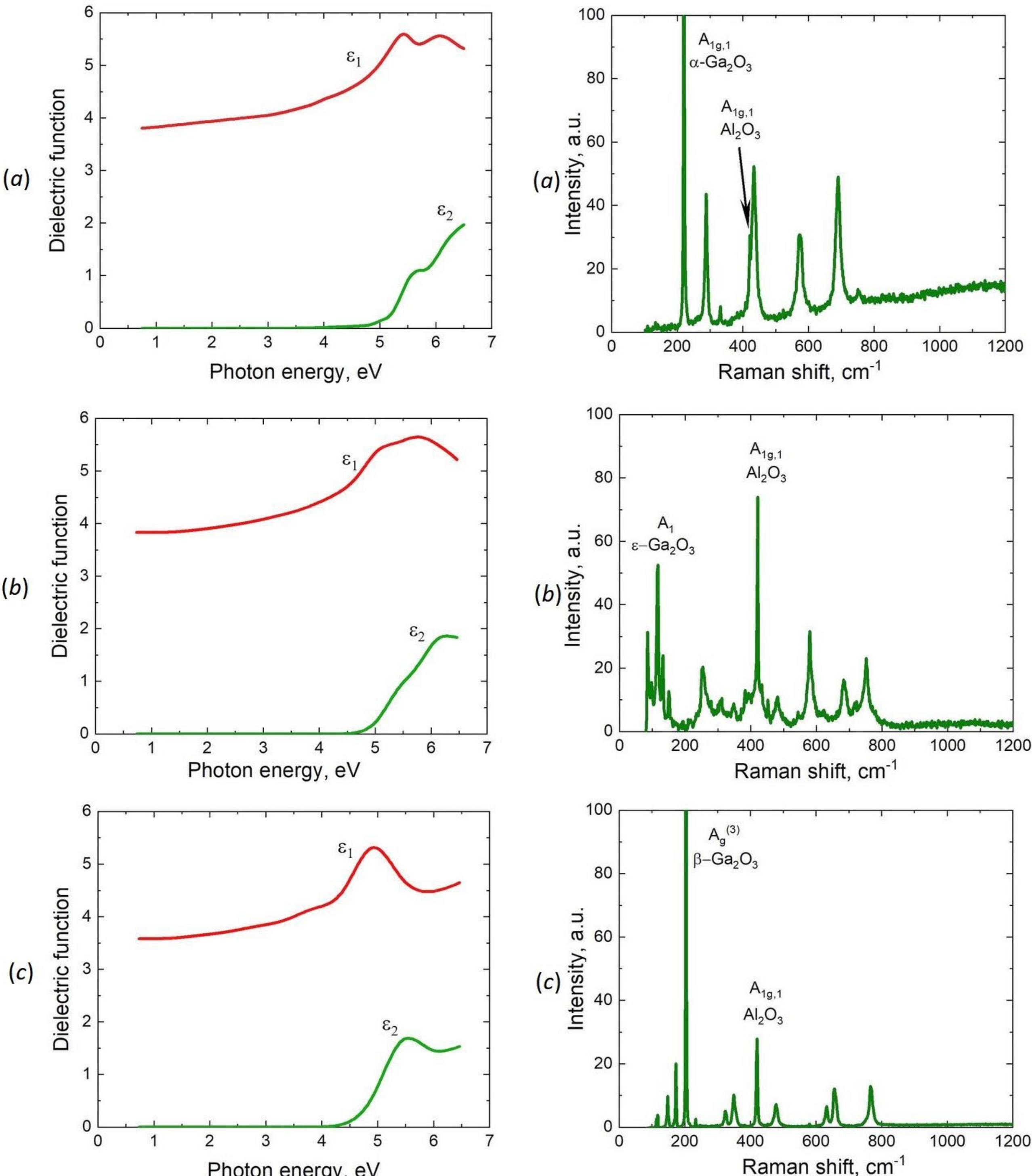

Fig. 2. Dependence of the dielectric constant of three Ga_2O_3 samples grown on Al_2O_3(0001) sapphire at temperatures of 510 (a), 575 (b), 900 °C (c) on the photon energy. ε_1 is the real part of the dielectric constant, ε_2 is the imaginary part of the dielectric constant

Fig. 3. Raman spectra of three Ga_2O_3 samples grown on Al_2O_3(0001) sapphire at temperatures of 510 (a), 575 (b), 900 °C (c). The main lines of each phase and sapphire are signed

β-phase within 10 min during annealing, starting at a temperature of 650 °C. The X-ray diffraction pattern of the ε-phase sample after annealing for 10 min at 650 °C is shown in Fig. 4. With high temperatures and high annealing times, the result did not change. It is interesting to note that after annealing ε-phase was converted into the β-phase with orientation <$\bar{3}$10> (Fig. 4), whereas during direct growth by the HVPE method, a β-phase was formed with the orientation <$\bar{2}$01> (Fig. 1c). The annealing of the metastable α-phase proceeds completely differently. The α-phase film becomes rough and cracks. Transitions into a stable β-phase did not occur. Complete cracking followed by shedding of the film at a temperature of 750 °C occurred in approximately 25 min, and at a temperature of 850 °C within 10 min. Annealing at a temperature of 650 °C for 30 min also did not lead to the appearance of the β-phase. The X-ray diffraction pattern and Raman spectrum of the sample of α-phases after annealing at a temperature of 750 °C for 15 min, i.e. immediately before cracking and shedding of the film is shown in Fig. 5. It can be seen that of any crystalline phases, only sapphire, i.e., the substrate material is present. High-energy electron diffraction of this sample also revealed only the amorphous phase on the surface. It was impossible to carry out ellipsometric analysis of this sample due to the enormous surface roughness. Thus, we can conclude that instead of the non-crystalline β-phase, the intermediate amorphous Ga_2O_3 phase was formed as a result of annealing of the α-phase and transition of this phase into the β-phase never occurs.

The results obtained can be explained by the difference in phase density. Simulations carried out using the density functional theory [7], allows to determine the density values of each phase with high accuracy. The least dense is the stable β-phase, its density is equal to

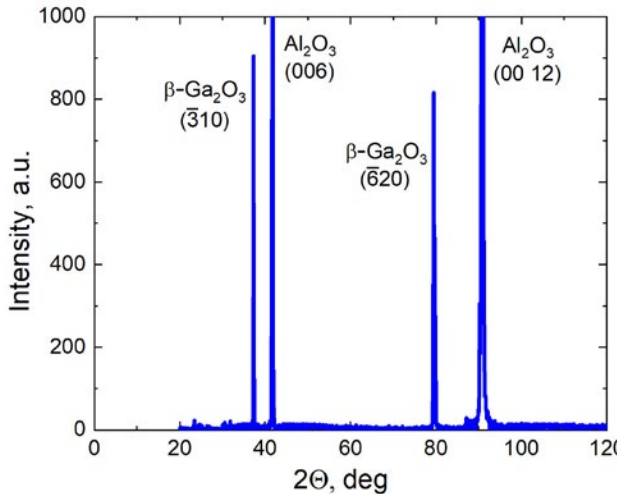

Fig. 4. X-ray diffractogram of ε-Ga_2O_3 sample after annealing for 10 min at 650 °C. It can be seen that the annealing resulted in the formation of β-phase with <$\bar{3}$10> orientation

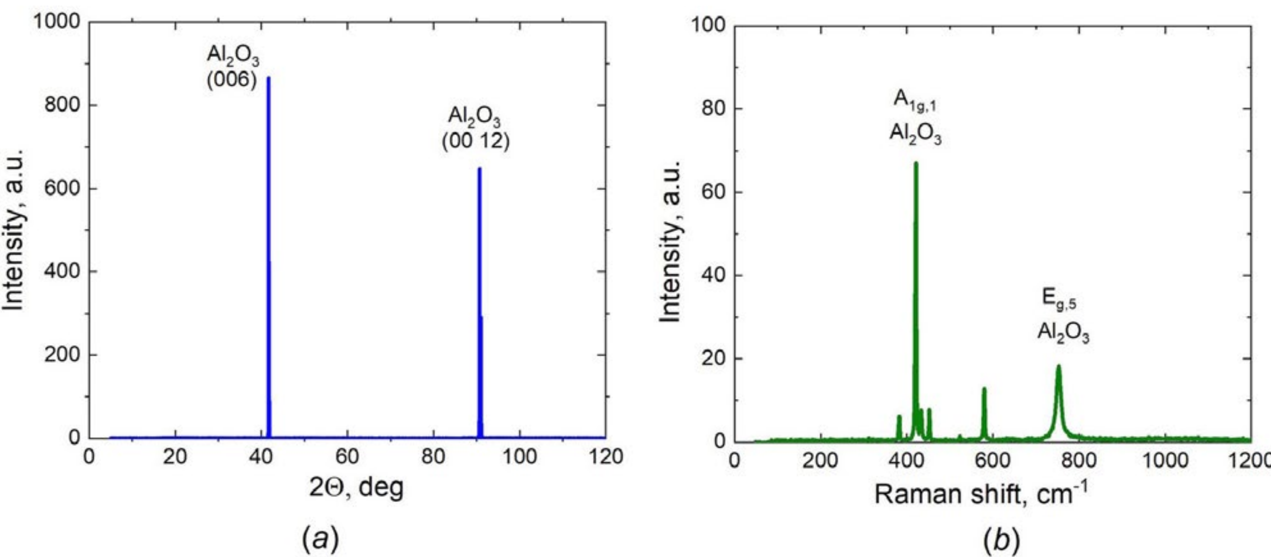

Fig. 5. X-ray diffractogram (a) and Raman spectrum (b) of α-Ga_2O_3 sample after annealing at 750 °C for 15 min. It can be seen that only Al_2O_3 sapphire is present among the crystalline phases

ρ_β = 5.9 g/cm^3, the densest is the most symmetric α-phase, its density is ρ_α = 6.5 g/cm^3, ε the phase is characterized by an intermediate density value ρ_ε = 6.05 g/cm^3. Thus, the reconstructive phase transition from the α into the β-phase was accompanied by a slight increase in volume of about 2.5%. Therefore, it led only to weak, almost imperceptible cracking of the film, which accompanies the phase change. Reconstructive phase transition from the ε into the β-phase was already accompanied by a significant increase in volume of about 10%. Such an increase cannot occur, since the emerging elastic stresses sharply increase the value of the phase transition barrier. As a result, an intermediate amorphous phase is formed, obviously with an intermediate density value, after which the film is destroyed.

4. Conclusions

It is shown that reconstructive phase transitions in Ga_2O_3 into a stable and least dense β-phases proceed in completely different ways. Transition from ε-phases into the β-phase with a decrease in density by 2.5% occurred quite easily and quickly already at a temperature of 650 °C. Transition from α-phases into the β-phase with a decrease in density by 10% proceeded more difficultly. Under the action of huge elastic stresses, the transition only into an intermediate amorphous phase occurred, after which the sample was destroyed without passing into a stable β-phase. Thus, in this study, we concluded that elastic stresses play a decisive role in reconstructive phase transitions by increasing the height of the nucleation barrier. With the significant increase in volume, the transformation may not occur at all.

Contribution of the authors

The authors contributed equally to this article.

Conflict of interests

The authors declare that they have no known competing financial interests or personal relationships that could have influenced the work reported in this paper.

References

1. Tsao J. Y., Chowdhury S., Hollis M. A., … Simmons J. A. Ultrawide-bandgap semiconductors: research opportunities and challenges. *Advanced Electronic Materials*. 2018;4(1): 1600501. https://doi.org/10.1002/aelm.201600501

2. Jamwal N. S., Kiani A. Gallium oxide nanostructures: A review of synthesis, properties and applications. *Nanomaterials (Basel)*. 2022;12: 2061. https://doi.org/10.3390/nano12122061

3. Pearton S. J., Yang J., Cary P. H., Ren F., Kim, J., Tadjer M. J., Mastro M. A. A review of Ga_2O_3 materials, processing, and devices. *Applied Physics Reviews* 2018;5(1): 011301, https://doi.org/10.1063/1.5006941

4. Stepanov S. I.; Nikolaev V.; Bougrov V. E.; Romanov A. Gallium oxide: properties and applications – A review. *Revviews on Advanced Materials Science*. 2016;44: 63–86. Режим доступа: https://www.elibrary.ru/item.asp?id=26987785

5. Nomura K., Goto K., Togashi R., … Koukitu A. Thermodynamic study of β-Ga_2O_3 growth by halide vapor phase epitaxy. *Journal of Crystal Growth*. 2014;405: 19–22. https://doi.org/10.1016/j.jcrysgro.2014.06.051

6. Osipov A. V., Grashchenko A. S., Kukushkin S. A., Nikolaev V. I., Osipova E. V., Pechnikov A. I., Soshnikov I. P. Structural and elastoplastic properties of β-Ga_2O_3 films grown on hybrid SiC/Si substrates. *Continuum Mechanics and Thermodynamics*. 2018;30(5): 1059-68. https://doi.org/10.1007/s00161-018-0662-6

7. Osipov A. V., Sharofidinov, S. S., Osipova E. V., Kandakov A. V., Ivanov A. Y., Kukushkin S. A. Growth and optical properties of Ga_2O_3 layers of different crystalline modifications. *Coatings*. 2022;12(12): 1802. https://doi.org/10.3390/coatings12121802

8. Kukushkin S. A., Osipov A. V. Theory and practice of SiC growth on Si and its applications to wide-gap semiconductor films. *Journal of Physics D: Applied Physics*. 2014;47(31): 313001 https://doi.org/10.1088/0022-3727/47/31/313001

9. Fiedler A., Schewski R., Galazka Z., Irmscher K. Static dielectric constant of β-Ga_2O_3 perpendicular to the principal planes (100), (010), and (001). *ECS Journal of Solid State Science and Technology*. 2019;8(7): Q3083. https://doi.org/10.1149/2.0201907jss

10. Furthmüller J., Bechstedt F. Quasiparticle bands and spectra of Ga_2O_3 polymorphs. *Physical Review B*. 2016;93(11): 115204. https://doi.org/10.1103/PhysRevB.93.115204

Information about the authors

Andrei V. Osipov, Dr. Sci. (Phys.–Math.), Head of the Laboratory of Structural and Phase Transformations of the Institute for Problems of Mechanical Engineering of the Russian Academy of Sciences (St. Petersburg, Russian Federation).

https://orcid.org/0000-0002-2911-7806
andrey.v.osipov@gmail.com

Shukrillo Sh. Sharofidinov, Cand. Sci. (Phys.–Math.), Senior Researcher of the Laboratory of Semiconductor Devices Physics, Ioffe Institute of the Russian Academy of Sciences (St. Petersburg, Russian Federation).

https://orcid.org/0000-0003-0354-5981
shukrillo71@mail.ru

Arina V. Kremleva, Cand. Sci. (Phys.–Math.), Associate Professor, National Research University ITMO (St. Petersburg, Russian Federation).

https://orcid.org/0000-0002-7045-0918
avkremleva@itmo.ru

Andrey M. Smirnov, Cand. Sci. (Phys.–Math.), Associate Professor, National Research University, ITMO (Saint-Petersburg, Russian Federation).

https://orcid.org/0000-0002-7962-6481
smirnov.mech@gmail.com

Elena V. Osipova, Cand. Sci. (Phys.–Math.), Senior Researcher of the Laboratory of Wave Process Modeling, Institute for Problems of Mechanical Engineering of the Russian Academy of Sciences (St. Petersburg, Russian Federation).

https://orcid.org/0000-0003-1292-5871
elena.vl.osipova@gmail.com

Andrei V. Kandakov, Research Associate, Laboratory of Structural and Phase Transformations, Institute for Problems of Mechanical Engineering, Russian Academy of Sciences (St. Petersburg, Russian Federation).

https://orcid.org/0000-0003-4335-3378
andrey.v.kandakov@gmail.com

Sergey A. Kukushkin, Dr. Sci. (Phys.–Math.), Professor, Chief Researcher, Head of the Laboratory of Structural and Phase Transformations in Condensed Media, Institute for Problems in Mechanical Engineering of the Russian Academy of Sciences (St. Petersburg, Russian Federation).

https://orcid.org/0000-0002-2973-8645
sergey.a.kukushkin@gmail.com

Received 28.04.2023; approved after reviewing 02.05.2023; accepted for publication 15.09.2023; published online 26.12.2023.

Translated by Valentina Mittova

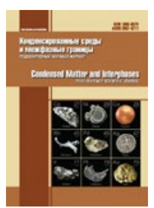

ISSN 1606-867X (Print)
ISSN 2687-0711 (Online)
Condensed Matter and Interphases
Kondensirovannye Sredy i Mezhfaznye Granitsy
https://journals.vsu.ru/kcmf/

Original articles

Research article
https://doi.org/10.17308/kcmf.2023.25/11483

Crystallization features and physical properties of the thin-film heterostructure of lead zirconate titanate – lead oxide

I. P. Pronin[1]✉, E. Yu. Kaptelov[1], E. V. Gushchina[1], S. V. Senkevich[1,2], V. P. Pronin[2], I. V. Ryzhov[2], V. L. Ugolkov[3], O. N. Sergeeva[4]

*[1]Ioffe Institute,
26 Polytechnicheskaya, St. Petersburg 194021, Russian Federation*

*[2]The Herzen State Pedagogical University of Russia,
48 Moika Emb., St. Petersburg 191186, Russian Federation*

*[3]Institute of Silicate Chemistry of Russian Academy of Sciences,
2 Makarov Emb., St. Petersburg 199034, Russian Federation*

*[4]Tver State University,
33 Zhelyabova, Tver 170100, Russian Federation*

Abstract

Various diagnostic techniques aimed at studying the structure and physical properties (synchronous thermal analysis, atomic force microscopy operating in the current measurement mode, electron-probe X-ray spectral microanalysis, dynamic method for determining the pyroelectric response) were used to study the crystallization features and physical properties of the thin-film heterostructure PZT – PbO_{1+x} formed by a two-stage technique of RF magnetron sputtering of a ceramic target.

During the first stage, amorphous films were deposited on a “cold” platinized silicon substrate, while the second stage involved high-temperature annealing in air. It was shown that annealing of amorphous films and crystallization of the intermediate pyrochlore phase are accompanied by additional oxidation of the structure resulting in the formation of lead orthoplumbate and lead dioxide and additional oxidation of organic inclusions. The presence of a liquid phase of lead oxide contributes to the formation of the pyrochlore phase.

It was found that lead oxide layers have significantly higher through conductivity than perovskite blocks. It was assumed that the increased conductivity of lead oxide layers is associated with lead dioxide, which has high conductive properties. Self-polarized thin films were detected to have an abnormal electrical response to the strobing thermal exposure, including the typical pyroelectric response, local photoconductivity shunted by layers of the perovskite phase, and through photoconductivity. The presence of photoconductivity is also associated with the conductive properties of lead dioxide.

Keywords: Thin film heterostructure of lead zirconate titanate and lead oxide, Crystallization of pyrochlore and perovskite phases, Differential scanning calorimetry, Thermal analysis, Atomic force microscopy, Pyroelectricity

Funding: The study was supported by Herzen State Pedagogical University of Russia (internal grant No. 25 VN).

For citation: Pronin I. P., Kaptelov E. Yu., Gushchina E. V., Senkevich S. V., Pronin V. P., Pyzhov I. V., Ugolkov V. L., Sergeeva O. N. Crystallization features and physical properties of the thin-film heterostructure of lead zirconate titanate – lead oxide. *Condensed Matter and Interphases*. 2023;25(4): 564–571. https://doi.org/10.17308/kcmf.2023.25/11483

Для цитирования: Пронин И. П., Каптелов Е. Ю., Гущина Е. В., Сенкевич С. В., Пронин В. П., Рыжов И. В., Уголков В. Л., Сергеева О. Н. Особенности кристаллизации и физических свойств тонкопленочной гетероструктуры цирконат-титанат свинца – оксид свинца. Конденсированные среды и межфазные границы. 2023;25(4): 564–571. https://doi.org/10.17308/kcmf.2023.25/11483

✉ Igor P. Pronin, e-mail: Petrovich@mail.ioffe.ru
© Pronin I. P., Kaptelov E. Yu., Gushchina E. V., Senkevich S. V., Pronin V. P., Pyzhov I. V., Ugolkov V. L., Sergeeva O. N., 2023

The content is available under Creative Commons Attribution 4.0 License.

1. Introduction

Thin films of lead zirconate titanate (($Pb(Zr,Ti)O_3$ or PZT), the composition of which corresponds to the morphotropic phase boundary region, are characterized by abnormally high electromechanical and piezoelectric coefficients and are currently the most common materials used in microelectronics [1–3], electro-optics [4], and microelectromechanics (MEMS) [5–7]. Optimization of the film structure and properties is largely associated with the control of their composition. Their formation is characterized by lead loss due to the high volatility of lead oxide vapors at high temperatures [8–9] especially during phase transformations and crystallization and recrystallization of the perovskite phase [10–11]. Experiments have shown that when the lead content is below the stoichiometric content the perovskite phase does not form [11]. To compensate for lead loss, during physical (vacuum) film deposition techniques, excess lead oxide (PbO) is added to the sputtered target. When using chemical methods, excess lead is added to the chemical solution. As a rule, as a result of the formation of the perovskite structure of the films, traces of excess lead oxide remain in the form of separate microinclusions or microlayers depending on its amount. The presence of excess lead in large quantities (over 5–10 mol. %) leads to the appearance of properties different from the single-phase perovskite structure [12–16], and, in particular, to the effect of spontaneous (macroscopic) polarization (self-polarization), the presence of which increases the efficiency and competitiveness of thin PZT films when used in microelectromechanical devices [17–19]. In most studies, lead oxide is identified by its divalent modification, PbO.

The presence of excess lead in thin PZT films indicated the heterostructure (or composite) PZT – PbO_{1+x}, where $x = 1÷2$, which differs in the arrangement of the lead oxide inclusions PbO_{1+x} in the volume of the thin film, Fig. 1. Despite the increased use of such thin-film composites in practical applications, the configuration of the location of lead oxide inclusions along the thickness has been poorly studied. Another problem is related to understanding which of the three oxides, lead oxide (PbO), lead dioxide (PbO_2), or lead orthoplumbate (Pb_3O_4), is actually present as a component of the heterostructure, since their chemical parameters and electronic properties differ significantly. This makes it impossible to purposefully optimize the production technology and the physical properties of such structures. In this regard, the purpose of this work was to obtain additional data on the peculiarities of the formation process and physical properties of the heterostructure PZT – PbO_{1+x}, and to analyze the data obtained both during this and previous research.

2. Sample preparation and research methods

The heterostructure was formed using a two-stage technique. During the first stage, RF magnetron sputtering of a ceramic target was used to deposit amorphous films at the temperature of the substrate determined by the heating temperature of the argon-oxygen plasma which

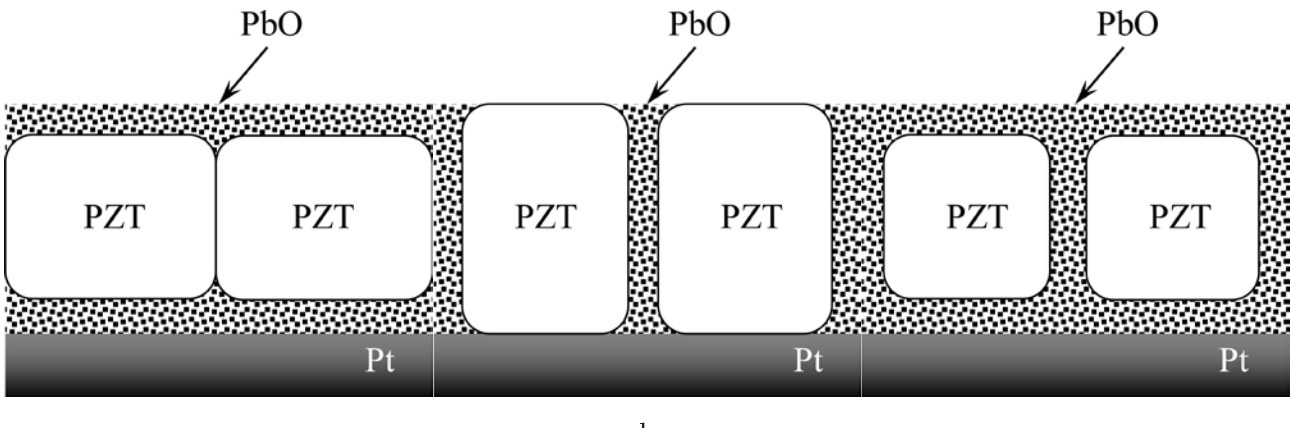

Fig. 1. Different arrangement of lead oxide layers (a-c) in the PZT–PbO_{1+x} heterostructure

was 130–140 °C at a gas mixture pressure of 8 Pa. Platinized silicon wafers were used as a substrate. The composition of the sputtering target corresponded to the region of the morphotropic phase boundary ($PbZr_{0.54}Ti_{0.46}O_3$). To compensate for lead loss, 10 mol % of PbO was added to the target. The thickness of the formed films was 200–500 nm. To take electrophysical measurements, a 200×200 µm platinum electrode array was formed on the surface of the samples.

The phase state of the films was studied by X-ray diffraction phase analysis (DRON-7) and optical microscopy. Phase transformations were monitored by synchronous thermal analysis using a STA 429 CD unit. Heating was carried out in the temperature range from 20 to 560 °C at a rate of 10 °C/min in an air and in an argon atmosphere. When taking the measurements, the mass of the sample and the change in enthalpy were evaluated.

The perovskite structure was formed by annealing amorphous films in air at 550–600 °C for 1 hour. The state of the microstructure was monitored by scanning electron microscopy (EVO-40) and atomic force microscopy in the contact mode of current measurement (Solver P47, NT-MDT). The composition of the thin films was determined by electron probe X-ray microanalysis using an INCA analyzer. Dielectric properties were studied using an E7-20 immitance meter. The pyroelectric properties of the films were studied by the dynamic technique using a strobing heat flow of laser radiation at a wavelength of 632.8 nm [14].

3. Results and discussion

Synchronous thermal analysis (DSC curves) of films with a thickness of 500 nm in an air atmosphere showed that in the range of temperatures from 430 to 480 °C there was a change in the system enthalpy due to the chemical transformation and crystallization of the intermediate pyrochlore phase. The results are represented by curve 1 for an empty crucible, curve 2 for a sample placed in the system, and the DDSC differential curve is represented by curve 3 (Fig. 2). There were no other changes in the system enthalpy up to a temperature of 600 °C, however, microstructural studies showed that low concentrations of individual islets of the perovskite phase appeared in the film. The linear size of such islets did not exceed 1–2 µm.

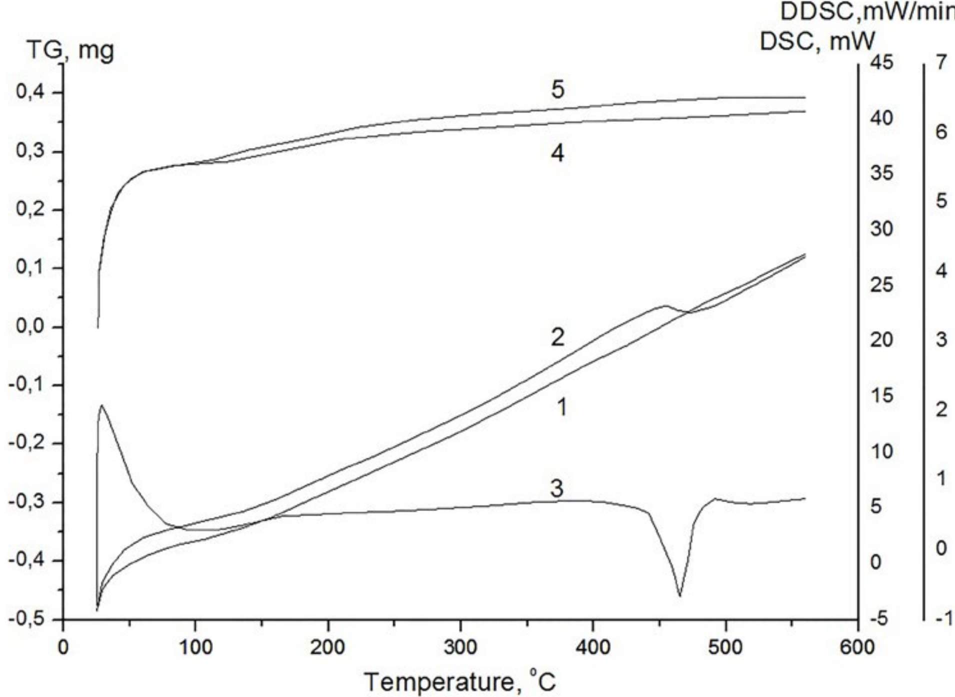

Fig. 2. Results of synchronous thermal analysis. DSC analysis corresponds to curve *1* (for an empty crucible), and *2* (for a crucible with a sample). Curve *3* represents the derivative of the DSC – DDSC curve. Curves *4* and *5* reflect the change in the mass of the empty crucible and the crucible with the sample, respectively

When similar measurements were taken in an argon atmosphere, there were no changes in the system enthalpy. An analysis of the change in mass (TG curves 4 and 5) showed that in air there was additional oxidation of thin films and the change in the total mass was ~ 3 μg (microgram) with a total film mass of ~ 50 μg. This meant that the amount of oxygen in the film increased by approximately ~ 40% and the mass by ~ 6%.

The additional oxidation of the film observed in the experiment (and the increase in the mass of the sample) against the background of the formation of the pyrochlore phase seem to be illogical. Indeed, according to previously obtained results, during the crystallization of the pyrochlore phase from the amorphous phase in samples similar to the studied, the estimated lead losses were 5–7% [16]. These losses are due to the pushing of excess lead in the form of oxide to the interphase regions (between the amorphous and pyrochlore phases), the diffusion rate in the interphase regions near the surface of the film due to their porosity is significantly higher than in the amorphous or pyrochlore phases. Similar processes occur during the crystallization and recrystallization of the perovskite phase at high annealing temperatures and are also accompanied by the removal of excess lead oxide [16]. No decrease in mass in the studied samples at high temperatures may indicate that under the conditions of a rapidly rising temperature and a low rate of diffusion of lead (oxide) to the surface of the thin film, lead depletion will only occur in its near-surface part. This should have practically no effect on the total mass of the sample.

The data of elemental analysis of samples of amorphous films showed that the relative oxygen content in them was excessive and 1.3 times higher than necessary for the synthesis of the pyrochlore phase with the chemical formula $A_2B_2O_6$ or the perovskite phase with the formula ABO_3, where lead atoms were located in position A, whereas titanium or zirconium atoms were located in position B. What is more, the excess of lead was ~ 25% relative to the stoichiometric composition. In addition, it was found that the films contained carbon, which indicated the presence of organic matter in the vacuum system, which was largely responsible for the presence of excess oxygen. In this regard, we associate the additional oxidation of samples not only with the chemical reactions of lead oxide (PbO) with oxygen and the formation of either lead orthoplumbate Pb_3O_4 or lead dioxide PbO_2 [20]:

$$2PbO + O_2 = 2PbO_2; \quad (1)$$

$$6PbO + O_2 = 2Pb_3O_4; \quad (2)$$

$$Pb_3O_4 + O_2 = 3PbO_2, \quad (3)$$

but also carbon oxidation. Calculations showed that when lead is additionally oxidized to the tetravalent state, an increase in the film mass due to this will be 75% while 25% of increase will be due to carbon oxidation. However, it is difficult to say now what is the real distribution of lead oxide modifications in the heterostructure. The temperature range for lead dioxide stability can be used as an argument against its presence: at 290 °C it changes into a liquid state, while the melting points of lead orthoplumbate and lead oxide are 830 and 890 °C, respectively. The argument in favor of the possible presence of lead dioxide is that the melting point of lead dioxide in a thin film is likely to be significantly higher than in its bulk analog. In addition, the crystallization of both the intermediate pyrochlore phase and the perovskite phase will be significantly simpler in the presence of mobile layers of the liquid phase. Further experiments made it possible to evaluate qualitatively if certain modifications of lead oxide were present in the studied heterostructure.

The formation of the perovskite structure was accompanied by the removal of organic inclusions, a diffusion to the surface, and subsequent evaporation of a significant part of excess lead. What is more, the oxygen content practically corresponded to the chemical formula of the heterostructure PZT – PbO_{1+x}.

Fig. 3 shows an image of a film with a thickness of 200 nm obtained by atomic force microscopy in the conductivity mode. A constant voltage of 10 V was applied to the conducting probe. It was obvious that the conductivity differed significantly (by several times) in polycrystalline

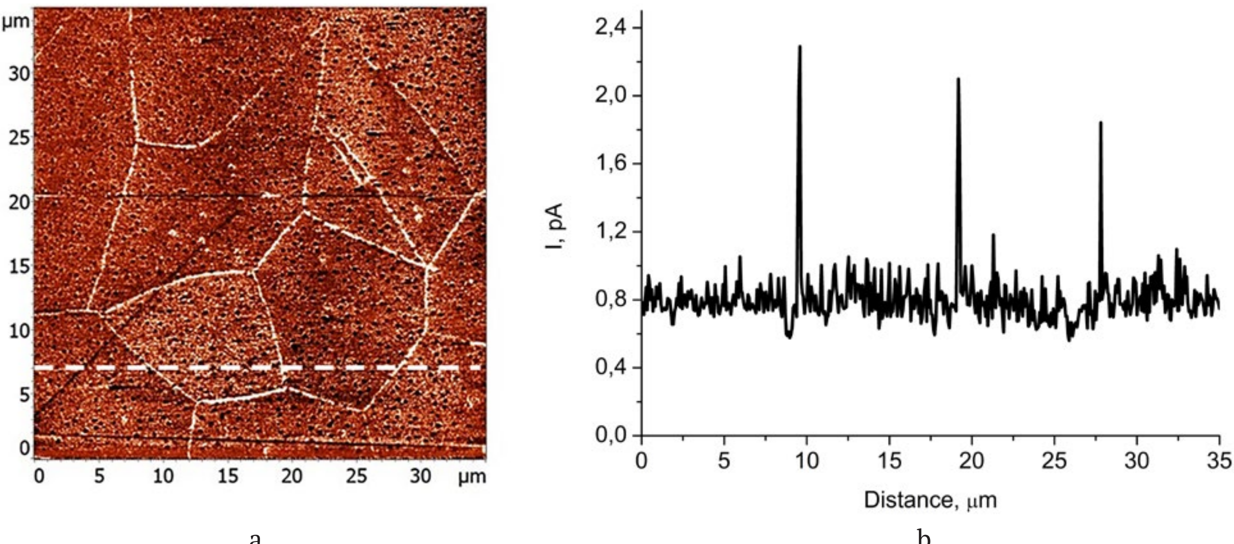

Fig. 3. AFM map of a thin PZT perovskite film, obtained in conduction mode (a) and current distribution profile through the sample along the horizontal dotted line (b)

(spherulitic) blocks and interblock boundaries. The interblock boundaries are inclusions of excess lead in the form of oxide. A comparative analysis of the conductive layers of lead oxides (PbO, PbO_2, Pb_3O_4) indicated that it was lead dioxide that had the conductive (semiconductor) properties, whose impurity zone was located below the conductivity zone by ~ 0.2 eV [21]. For comparison, the band gap width of PbO was 2.59 eV and at room temperature it exhibited dielectric properties with a dielectric constant of ~ 10. A fairly wide gap width was also characteristic of lead orthoplumbate (2.14 eV).

Another confirmation of the highly conductive properties of lead dioxide is the results of the study of the electrical response of self-polarized PZT films under the influence of a strobing heat flow produced by laser radiation at a wavelength of 632.8 nm. Fig. 4a shows the pyroelectric response of the film (narrow peaks on the leading and trailing edges of the thermal pulse), in which the inclusions of lead oxide did not exceed 7–8%, and were mainly located near the lower and upper interface of the structure (Fig. 1a). An increase in the content of lead oxide (up to 10–11%) led to the appearance of a significant amplitude of opposite polarity on the edges of pulses, which indicates a local (non-through) photocurrent (Fig. 4b). A similar effect can be achieved by increasing the content of lead oxide and the formation of discontinuous (separate) fragments located along the boundaries of perovskite grains or blocks. Finally, a further increase in the content of lead oxide (over 15%) in the heterostructure led to the formation of inclusions of lead oxide which formed conductive channels (Fig. 1b) and to the emergence of through photoconductivity in the form of a shelf on the electrical response signal, Fig. 4c. Such conductive properties, similar to the case of the conductivity of interblock boundaries, are characteristic of lead dioxide.

Dielectric measurements showed that an increase in the content of lead oxide in the composite led to a sharp decrease (three times or more, from 900 to 250) in the effective value of dielectric constant and an increase in dielectric losses. This was due to the formation of thin dielectric layers of PbO_{1+x} located along the thickness consecutive to the perovskite layers.

4. Conclusions

We studied the crystallization features and physical properties of the thin-film heterostructure PZT – PbO_{1+x} formed by the two-stage technique of RF magnetron sputtering. It was shown that the annealing of amorphous films is accompanied by their additional oxidation which is absolutely necessary for the

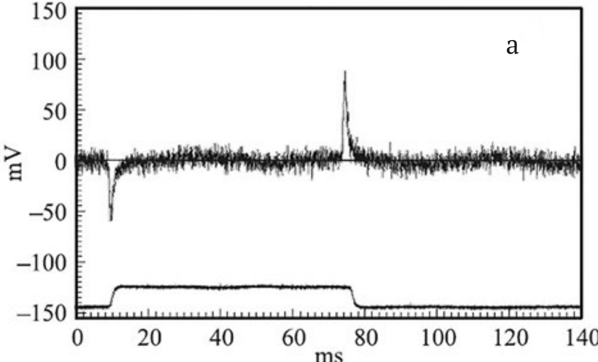

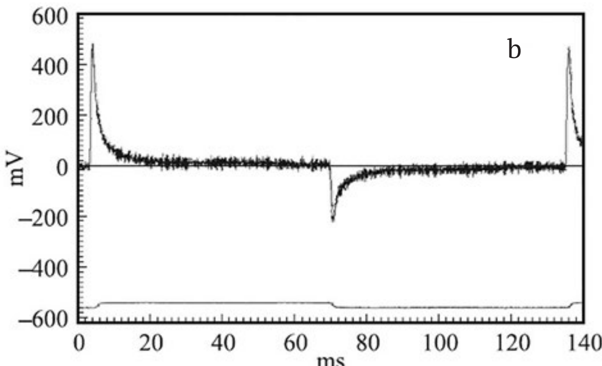

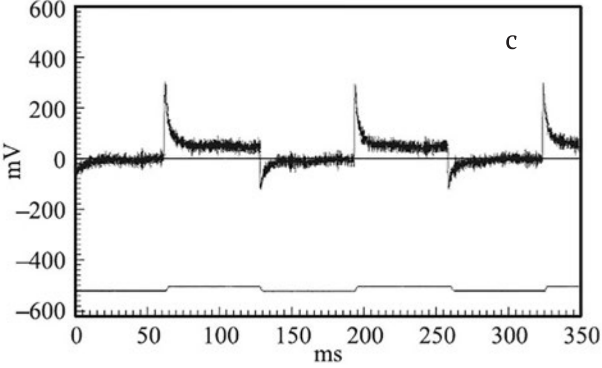

Fig. 4. Changes in the shape and magnitude of the electrical response under rectangularly modulated thermal radiation in self-polarized PZT films with increasing content of lead oxide inclusions PbO_{1+x}: a) 7-8%, b) 11-12%, c) over 15%

crystallization of the intermediate pyrochlorine phase and the subsequent transformation into the perovskite phase. The obtained results indicate that the second component of the heterostructure in the form of lead oxide should in reality be a mixture of oxides (PbO, PbO_2, Pb_3O_4) with different lead valencies. The difference between the conductive and dielectric properties of lead oxides leads to the appearance of unusual properties uncharacteristic of a single-phase perovskite structure.

Contribution of the authors

The authors contributed equally to this article.

Conflict of interests

The authors declare that they have no known competing financial interests or personal relationships that could have influenced the work reported in this paper.

References

1. Ma Y.-C., Song J., Zhao Y.-Y., ... Liu Y. Excellent uniformity and properties of micro-meter thick lead zirconate titanate coatings with rapid thermal annealing. *Materials*. 2023;16(8): 3185. https://doi.org/10.3390/ma16083185

2. JoJi Y.-Y., Lee Y., Park E.-P., ... Song H.-C. Epitaxial PZT film-based ferroelectric field-effect transistors for artificial synapse. *ACS Applied Electronic Materials*. 2023; 5(8):4549–4555. https://doi.org/10.1021/acsaelm.3c00691

3. Ma Y., Son J., Wang X., Liu Y., Zhou J. Synthesis, microstructure and properties of magnetron sputtered lead zirconate titanate (PZT) thin film coatings. *Coatings*. 2021;11(8): 944. https://doi.org/10.3390/coatings11080944

4. Singh S., Selvaraja S. K. Sputter-deposited PZT on patterned silicon optimization for C-band electro-optic modulation. *Journal of the Optical Society of America B*. 2023;40(9): 2321-2329. https://doi.org/10.1364/josab.497538

5. Teuschel M., Heyes P., Horvath S., Novotny C., Cleric A. R. Temperature stable piezoelectric imprint of epitaxial grown PZT for zero-bias driving MEMS actuator operation. *Micromachines*. 2022;13(10): 1705. https://doi.org/10.3390/mi13101705

6. Song L, Glinsek S., Defay E. Toward low-temperature processing of lead zirconate titanate thin films: Advances, strategies, and applications. *Applied Physical Review*. 2021;8: 041315. https://doi.org/10.1063/5.0054004

7. Picco A., Ferrarini P., Ferrarini P., ... Lazzari M. Piezoelectric Materials for MEMS. In: Vigna B., Ferrari P., Villa F.F ., Lasalandra E., Zerbini S. (eds). *Silicon Sensors and Actuators*. Springer, Cham; 2022. pp. 293–344. https://doi.org/10.1007/978-3-030-80135-9_10

8. Krupanidhi S. B., Roy D., Maffei N., Peng C. J. Pulsed excimer laser deposition of ferroelectric thin films. *Integrated Ferroelectrics*. 1992;1: 253–268. https://doi.org/10.1080/10584589208215716

9. Izyumskaya N., Alivov Y.-I., Cho S.-J., Morkoç H.,

Lee H., Kang Y.-S. Processing, structure, properties, and applications of PZT thin films. *Critical Reviews in Solid State and Materials Sciences*. 2007;32: 111–202. https://doi.org/10.1080/10408430701707347

10. Pronin V. P., Senkevich S. V., Kaptelov E. Yu., Pronin I. P. Anomalous losses of lead in crystallization of the perovskite phase in thin PZT films. *Physics of the Solid State*. 2013;55: 105–108. https://doi.org/10.1134/s1063783413010277

11. Dolgintsev D. M., Pronin V. P., Kaptelov E. Yu., Senkevich S. V., Pronin I. P. Studying the composition and phase state of thin PZT films obtained by high-frequency magnetron sputtering under variation of working gas pressure. *Technical Physics Letters*. 2019;45(3): 245–248. https://doi.org/10.1134/s1063785019030258

12. Song Z.-T., Gao J.-X., Zhu X.-R., Wang L.-W., Fu X.-R., Lin C.-G. Effect of excess Pb on structural and electrical properties of $Pb(Zr_{0.48}Ti_{0.52})O_3$ thin films using MOD process. *Journal of Materials Science*. 2001;36: 4285–4289. https://doi.org/10.1023/A:1017999223329

13. Park C.-S., Lee J.-W., Lee S.-M., Jun S.-H., Kim H.-E. Effect of excess PbO on microstructure and orientation of PZT (60/40) films. *Journal of Electroceramics*. 2010;25: 20–25. https://doi.org/10.1007/s10832-009-9584-9

14. Senkevich S. V., Pronin I. P., Kaptelov E. Yu., Sergeeva O. N., Il'in N. A., Pronin V. P. Effect of lead oxide on the dielectric characteristics of heterogeneous $Pb(Zr,Ti)O_3$ + PbO films obtained by a two-stage method. *Technical Physics Letters* 2013;39: 400–403. https://doi.org/10.1134/s1063785013040238

15. Mukhin N., Chigirev D., Bakhchova L., Tumarkin A. Microstructure and properties of PZT films with different PbO content. Ionic mechanism of built-in fields formation. *Materials*. 2019;12(18): 2926. https://doi.org/10.3390/ma12182926

16. Osipov V. V., Kiselev D. A., Kaptelov E. Yu., Senkevich S. V., Pronin I. P. Internal field and self-polarization in lead zirconate titanate thin films. *Physics of the Solid State*. 2015;57: 1793-1799. https://doi.org/10.1134/s1063783415090267

17. Balke N., Bdikin I., Kalinin S. V., Kholkin A. L. Electromechanical imaging and spectroscopy of ferroelectric and piezoelectric materials: state of the art and prospects for the future. *Journal of American Ceramic Society*. 2009;92(8): 1629–1647. https://doi.org/10.1111/j.1551-2916.2009.03240.x

18. Mtebwa M., Setter N. Control of self-polarization in doped single crystalline $Pb(Zr_{0.5}Ti_{0.5})O_3$ thin films. *Integrated Ferroelectrics*. 2022;230(1): 148–155. https://doi.org/10.1080/10584587.2022.2102807

19. Zhang T., Yin C., Zhang C., … Fei W.-D. Self-polarization and energy storage performance in antiferroelectric-insulator multilayer thin films. *Composites Part B Engineering*. 2021;221: 109027l. https://doi.org/10.1016/j.compositesb.2021.109027

20. Tentilova I. Yu., Kaptelov E. Yu., Pronin I. P., Ugolkov V. L. Micropore formation in lead zirconate titanate films. *Inorganic Materials*. 2012;48(11): 1136–1140. https://doi.org/10.1134/s0020168512110155

21. Scanlon D. O., Kehoe A. B., Watson G. W., … Walsh A. Nature of the band gap and origin of the conductivity of PbO_2 revealed by theory and experiment. *Physical Review Letters*. 2011;107(24): 246402. https://doi.org/10.1103/physrevlett.107.246402

Информация об авторах.

Igor P. Pronin, Dr. Sci. (Phys.–Math.), Leading Researcher, Department of Physics of Dielectrics and Semiconductors, Ioffe Institute (St. Petersburg, Russian Federation).

https://orcid.org/0000-0003-3749-8706
Petrovich@mail.ioffe.ru

Evgeny Yu. Kaptelov, Cand. Sci. (Phys.–Math.), Senior Researcher, Department of Physics of Dielectrics and Semiconductors, Ioffe Institute (St. Petersburg, Russian Federation).

https://orcid.org/0000-0002-7423-6943
Kaptelov@mail.ioffe.ru

Ekaterina V. Gushchina, Cand. Sci. (Phys.–Math.), Researcher, Department of Solid State, Ioffe Institute (St. Petersburg, Russian Federation).

https://orcid.org/0000-0001-7097-7691
Ekaterina.Gushchina@mail.ioffe.ru

Stanislav V. Senkevich, Cand. Sci. (Phys.–Math.), Senior Researcher, Department of Physics of Dielectrics and Semiconductors, Ioffe Institute (St. Petersburg, Russian Federation).

https://orcid.org/0000-0002-4503-1412
SenkevichSV@mail.ioffe.ru

Vladimir P. Pronin, Dr. Sci. (Phys.–Math.), Professor of Physics Department, Herzen State Pedagogical University of Russia (St. Petersburg, Russian Federation).

https://orcid.org/0000-0003-0997-1113
Pronin.v.p@yandex.ru

Igor I. Ryzhov, Cand. Sci. (Phys.–Math.), Assistant Professor of Physics Department, Herzen State Pedagogical University of Russia (St. Petersburg, Russian Federation).

https://orcid.org/0000-0002-9878-4338
igoryzhov@yandex.ru

Valerii L. Ugolkov, Cand. Sci. (Tech.), Leading Researcher, Laboratory of Physical-Chemical Design and Synthesis of Functional Materials, Institute of Silicate Chemistry of Russian Academy of Sciences (St. Petersburg, Russian Federation).

https://orcid.org/0000-0003-2895-0625
ugolkov.52@mail.ru

Olga N. Sergeeva, Cand. Sci. (Phys.–Math.), Leading Engineer of Physics Department Tver State University, (Tver, Russian Federation).

https://orcid.org/0000-0001-9469-4063
o_n_sergeeva@mail.ru

Received 20.09.2023; approved after reviewing 27.09.2023; accepted for publication 16.10.2023; published online 25.12.2023.

Translated by Irina Charychanskaya

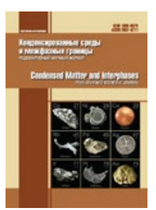

ISSN 1606-867X (Print)
ISSN 2687-0711 (Online)
Condensed Matter and Interphases
Kondensirovannye Sredy i Mezhfaznye Granitsy
https://journals.vsu.ru/kcmf/

Original articles

Research article
https://doi.org/10.17308/kcmf.2023.25/11481

Anomalous electron channeling in PZT thin films

M. V. Staritsyn[1]✉

[1]National Research Center "Kurchatov Institute"- Central Research Institute of Structural Materials "Prometey", 49 Shpalernaya st., St. Petersburg 191015, Russian Federation

Abstract

The study of the surface of lead zirconate-titanate (PZT) thin films using a scanning electron microscope (SEM) identified the patterns of electron channeling on the surface of the perovskite phase crystals. However, the observation conditions were completely uncommon and contradicted model representations. Thus, there was enough evidence to believe that the observed patterns of electron channeling were an anomaly. It was necessary to conduct an additional detailed study of the perovskite crystal in a PZT thin film in order to clarify which conditions could cause this anomaly.

In particular, the method of electron backscatter diffraction (EBSD) in SEM was used to study the crystallographic specific features of the crystal. The method is based on the collection and automatic processing of electron diffraction patterns which calculate a corresponding crystallographic orientation for each point on the scanned crystal surface.

As a result, the study revealed the unusual features of the crystallographic structure of perovskite in a PZT thin film that provided an opportunity for the manifestation of anomalous electron channeling. The research showed that the crystal lattice of perovskite experienced an axially symmetric monotone bend, which determined the round shape of the crystal. The study demonstrated the possibility of producing ferroelectric crystals with a curved crystallographic surface. In order to describe the growth of round perovskite crystals from the amorphous phase in PZT thin films, the author provided a dislocation model where the continuous bending of the perovskite crystal lattice could be explained by the accommodation of mechanical stresses with a decrease in the phase volume of the film material. In addition, it was shown that the bands observed in the electron channeling patterns corresponded to crystallographic planes, while any distortions of the pattern indicated a local deformation of the lattice in a highly symmetrical uniformly curved perovskite crystal in a PZT thin film.

Keywords: Anomalous electron channeling, Channeling, Thin films, Lead zirconate-titanate, PZT, Perovskite, Deformed crystals, EBSD

Acknowledgements: Experimental studies were performed using the equipment of the Center for the Collective Use of Scientific Equipment "Composition, structure, and properties of structural and functional materials" of the National Research Center Kurchatov Institute – Central Research Institute of Structural Materials "Prometey".

For citation: Staritsyn M. V. Anomalous electron channeling in thin films of PZT. *Condensed Matter and Interphases*. 2023;25(4): 572–580. https://doi.org/10.17308/kcmf.2023.25/11481

Для цитирования: Старицын М. В. Аномальное электронное каналирование в тонких пленках ЦТС. *Конденсированные среды и межфазные границы*. 2023;25(4): 572–580. https://doi.org/10.17308/kcmf.2023.25/11481

✉ Mikhail V. Staritsyn, e-mail: ms_145@mail.ru
© Staritsyn M. V., 2023

The content is available under Creative Commons Attribution 4.0 License.

1. Introduction

The solid solutions of lead zirconate titanate (PZT) are among the main ferroelectric materials with properties suitable for IR detectors, microwave electronics, micro-electromechanical devices, and static and dynamic memory elements [1–6].

Electronic devices are being constantly improved, which also involves the development of radioelectronic components towards energy efficiency and smaller sizes. Thus, miniature, film, and thin-film versions of ferroelectrics are becoming increasingly widespread. However, it is known that with the decrease of film thickness, it becomes difficult to control the electrical characteristics of PZT films [7]. This trend is usually associated with the introduction of additional factors with an increasing impact of the surface. The final properties of the ferroelectric film are also more and more influenced by the characteristics of the substrate, such as the linear expansion coefficient, oxidation resistance, and barrier properties. Therefore, the task of studying thin-film ferroelectrics based on PZT appears to be highly relevant.

As for the research regarding PZT thin films, continuous perovskite films and films with an island structure are both essential. The term «island» here describes the round-shaped crystals that are formed during the annealing of PZT thin films. With a small concentration of crystallization centers, single islands of the perovskite phase in the amorphous matrix grow in the form of flat round-shaped crystals. As the number of the island crystallization centers increases, perovskite phases merge and form together a continuous surface [8–10].

The radiant patterns observed on the surface of the islands (Fig. 1) were also described in a number of works that present some assumptions about their nature [9–13].

This study analyses the structure of perovskite islands of PZT thin films grown on a Pt-TiO_2-sitall substrate. And the results of the study are presented in this article. Even at the stage of obtaining electron images (Fig. 2) from a scanning electron microscope (SEM), the islands looked different from what was observed in PZT films on Pt-TiO_2-SiO_2-Si substrates (Fig. 1). Thus, a pattern in the form of intersecting bands, similar to the Kikuchi diffraction pattern, could be seen in the electron image of a PZT film island on a sitall substrate (Fig. 2), instead of radially divergent radiant patterns. Electron images in Figs. 1 and 2 were obtained with normal incidence of an electron beam with an energy of 12 keV.

Similar patterns in SEM were observed in the case of bulk single crystals with significantly different angles of incidence of the scanning electron beam on the sample due to the manifestation of the electron channeling effect [14]. An example of the electron channeling pattern on a large-sized ingot of alpha-titanium alloy is presented in Fig. 3. The pattern was obtained from the most available field and was limited by the circle of the lens aperture. The

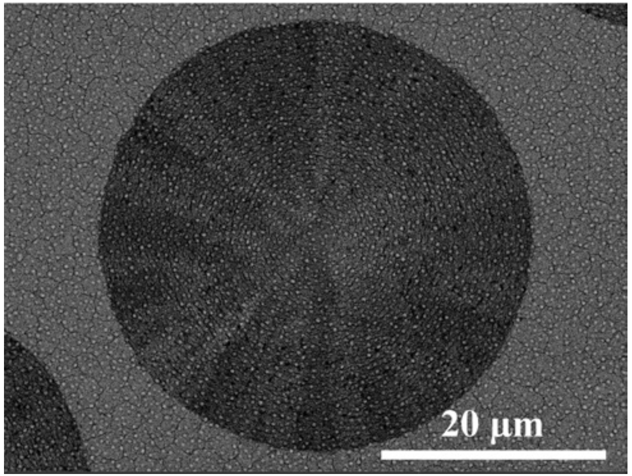

Fig. 1. The electron image of an island of perovskite in a thin film of PZT on a substrate Pt-TiO_2-SiO_2-Si

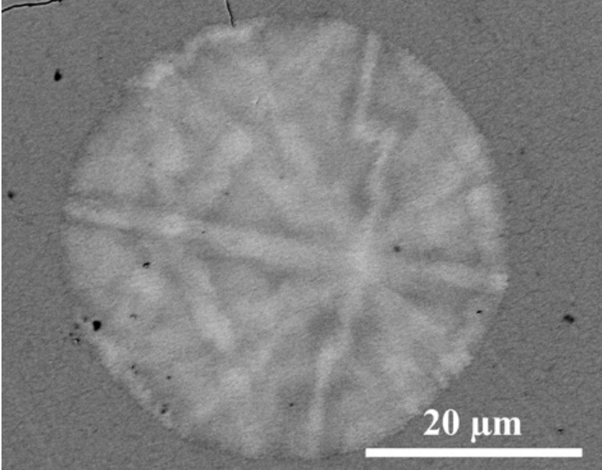

Fig. 2. The electron image of an perovskite island in a thin film of PZT on a substrate Pt-TiO_2-sitall

difference in the angles of incidence of the electron beam on the crystal surface aimed at obtaining the pattern shown in Fig. 3 was 30°.

The channeling of charged particles in crystals could be explained by the movement of particles along the “channels” formed by parallel rows of atoms (Fig. 4a). In this case, the particles experience sliding collisions (the momentum did not change significantly) with rows of atoms that hold them in these “channels.” If the particle path is between two atomic planes, this can be called planar channeling [15, 16]. During beam incidence on a crystal lattice at significantly different angles (Fig. 4b), it encounters planes with low atomic density on its way, along which electrons channel before scattering [16, 17].

As you can see, if the scale markers in Figs. 2 and 3 are compared, the observing conditions for electron channeling patterns on perovskite islands differ from those described above. The perovskite island is small and is scanned with a very small discrepancy by almost parallel electron beams (the angle of the electron beam deflection did not exceed 0.15° while scanning the island along its diameter). The effect upon which the channeling pattern was observed when irradiated by parallel beams was an anomaly that contradicted model representations. Thus, the electron channeling effect observed on perovskite islands in PZT thin films prepared on a Pt-TiO_2-sitall substrate was an anomaly.

The goal of this work was to study the structural features of perovskite islands that formed the conditions for observing anomalous electron channeling in a thin layer of PZT films.

2. Experimental

A PZT thin film in which the effect of anomalous electron channeling was observed, was deposited on a layered substrate. The layered substrate was a system of textured platinum (with the crystallographic plane (111) egressing to the surface) with a thickness of about 0.2 μm which was deposited on a titanium dioxide sublayer (about 20 nm) located on a thick (approximately 0.5 mm) ST-50 sitall substrate. The films were deposited using high-frequency magnetron sputtering of a PZT ceramic target with a composition corresponding to the morphotropic phase boundary. Upon deposition, the amorphous films were annealed in an oven in order to crystallize the perovskite phase in them. Heated at a rate of 300 °C/hour up to 570 °C and kept for 1 hour, the films as well as the oven were cooled to room temperature.

Such widespread research techniques as optical, scanning electron, and atomic force microscopy do not provide information about the crystallographic specific features of the material when they are used to analyze film structures [18]. However, electron backscatter diffraction (EBSD), which combines the possibility to analyze

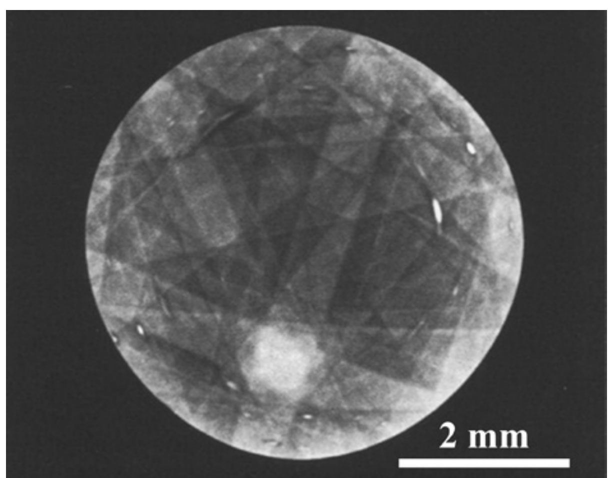

Fig. 3. An example of an electron channeling pattern obtained on a large-sized alpha-titanium alloy ingot. The observation of the picture is limited by the objective aperture of the SEM. The scale marker makes it possible to evaluate the characteristic conditions for observing the pattern of electron channeling

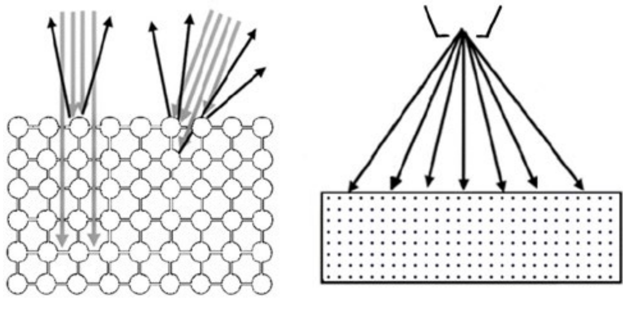

Fig. 4. A schematic diagram showing the origin of the channeling effect as the penetration of beam electrons along the crystal planes (a). Scanning at low magnification of the SEM is associated with a significant change in the incidence angeles of electrons on the crystal surface (b)

local crystal orientations and SEM high spatial resolution, is a suitable method for studying the features of crystalline phases in thin films.

Thus, the PZT films annealed in the oven were studied using a Tescan Lyra 3 scanning electron microscope (SEM) equipped with a system for recording EBSD patterns. The EBSD method involves point scanning of a sample and also registering and processing the resulting electron diffraction patterns. The lack of accuracy while determining crystal orientations regarding the macroscopic SEM-related coordinate system using EBSD (error 1–2°) did not affect the angular resolution when analyzing relative orientations between two close points [19]. Crystallographic orientation maps accumulated using the EBSD method can clarify the origin and nature of the structural features of crystals and help to explain the mechanisms of their growth.

During the study, it was experimentally confirmed that a change in the electron beam parameters while scanning the studied surface did not result in physical degradation or phase transformations on the surface of a PZT thin film. Therefore, the accelerating voltage and the beam current were selected in accordance with the achievement of a suitable mapping speed with sufficient resolution of the Kikuchi diffraction patterns and their exposure. The scanning step and digital resolution of the accumulated map were determined using the representativeness of the display of the relevant structural features at a certain SEM magnification. The obtained diffraction patterns were indexed taking into account the relative position of 10–12 Kikuchi bands in order to avoid the "pseudosymmetry" issues, which led to incorrect conclusions in [20]. In a series of trial studies, similar to [20], data on tetragonal, monoclinic, and rhombohedral crystal lattices typical for PZT were entered into a computer program so as to analyze the diffraction patterns. However, as the results showed, the lattice parameters and angles (with a deviation of no more than 0.4°) were so similar that it was impossible to distinguish them using this method. Therefore, in order to describe a real crystallographic system, it was decided to use deformed pseudocubic lattice approximation.

3. Results and discussion

The map of crystallographic orientations of a perovskite island accumulated using EBSD in a PZT thin film on a Pt(111)-TiO_2-sitall substrate is shown in Fig. 5 on the left. The lattice orientation in each map point is encoded using a standard inverse pole figure (IPF) color distribution built for the macroscopic direction that coincides with the surface normal to the sample surface plane. The color coding IPF for a pseudocubic perovskite

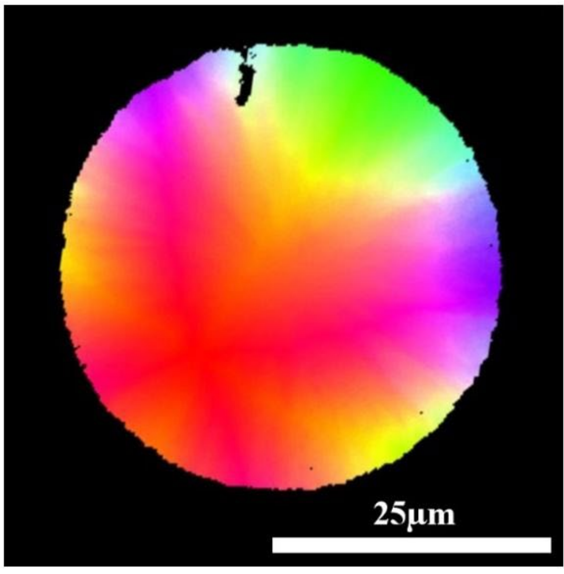

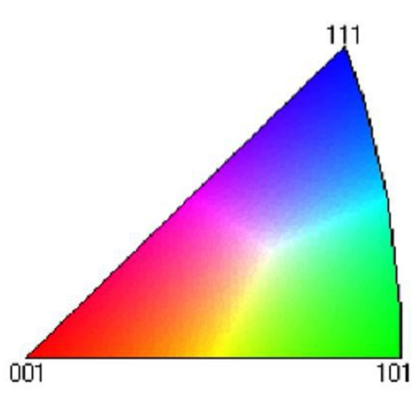

Fig. 5. A map of the crystallographic orientations of the perovskite crystal and a color coding triangle for it

lattice is presented in Fig. 5 on the right. The areas marked in black on the map of crystallographic orientations are those where scanning obtained Kikuchi diffraction patterns that were not suitable for processing.

As it can be seen, the island structure is encoded with smoothly spread color gradients, with no expressed crushing into radially divergent "rays" that are typical for perovskite islands in PZT thin films on Pt(111)-TiO_2-SiO_2-Si [9].

The software for processing orientation maps allowed information to be obtained about the crystallographic disorientations achieved within the studied island. Therefore, based on the orientation map (Fig. 5), maps of grain reference orientation deviation (GROD) from a certain average orientation calculated for a specific island (Fig. 6) were plotted. The deviation angles of the crystal lattice orientations in each point on the GROD map are encoded in the colors of the map key.

The resulting GROD map (Fig. 6) indicates the presence of a homogeneous axially symmetric deformation of the crystal lattice of the perovskite phase island. It can be clearly seen that the crystal lattice of the island was evenly deformed in all radial directions in relation to the center of the island, the orientation of which obviously

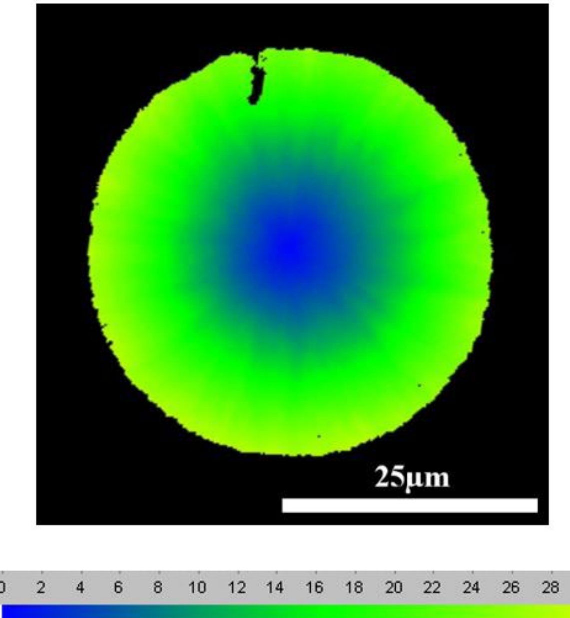

Fig. 6. GROD – a map of the perovskite island and the colour legend for it

coincided with the growth nucleus. The profile of changes in crystallographic orientation angles calculated along the radial directions (Fig. 7) indicates the linear and monotonously continuous nature of the lattice rotation from the starting to the ending point. The lattice rotation gradient calculated from the profile was 1.4 °/μm.

Taking into account the identified homogeneity of the crystal lattice rotation in all possible radial directions (Figs. 5–7), it is reasonable to interpret the effect observed in Fig. 2 as an electron-optical anomaly associated with the specific features of the crystallographic structure of perovskite islands in a PZT thin film grown on a platinized sitall substrate. The anomalous effect of electron channeling appeared due to a homogeneous axially symmetric distortion of the crystal lattice of the island. Due to the monotonous and continuous bending of crystallographic planes represented by the model in Fig. 8 [21], the angles of electron entry into the crystal lattice also changed, and it was possible to observe the pattern of electron channeling in parallel electron beams.

What is more, the author noted that if the slope of the sample in the SEM chamber changed (for instance 10°) while observing the surface of the perovskite phase islands (Figs. 2, 9a) then the system of mutually intersecting lines on the island shifted (Fig. 9b). This shift could be explained by a change in the position of the crystallographic planes relative to the electron beam falling on them, i.e., the angle of electron entry into the crystal lattice.

It can be easily shown that the lines observed in the electron channeling patterns corresponded to crystallographic planes [14–17]. Therefore, the position of the crystallographic planes could be directly observed in Figs. 2 and 9. Any additional stresses applied to the film were expressed as a distortion of the electron channeling pattern. In particular, the "break" of the vertical line in Fig. 2 can indicate local deformations of the crystal lattice in a highly symmetric and homogenously curved perovskite crystal.

A dislocation model can be suggested to describe the growth of perovskite islands from the amorphous phase in a thin layer of a PZT film. The lattice rotation in this model occurs as a result of the accommodation of mechanical stresses

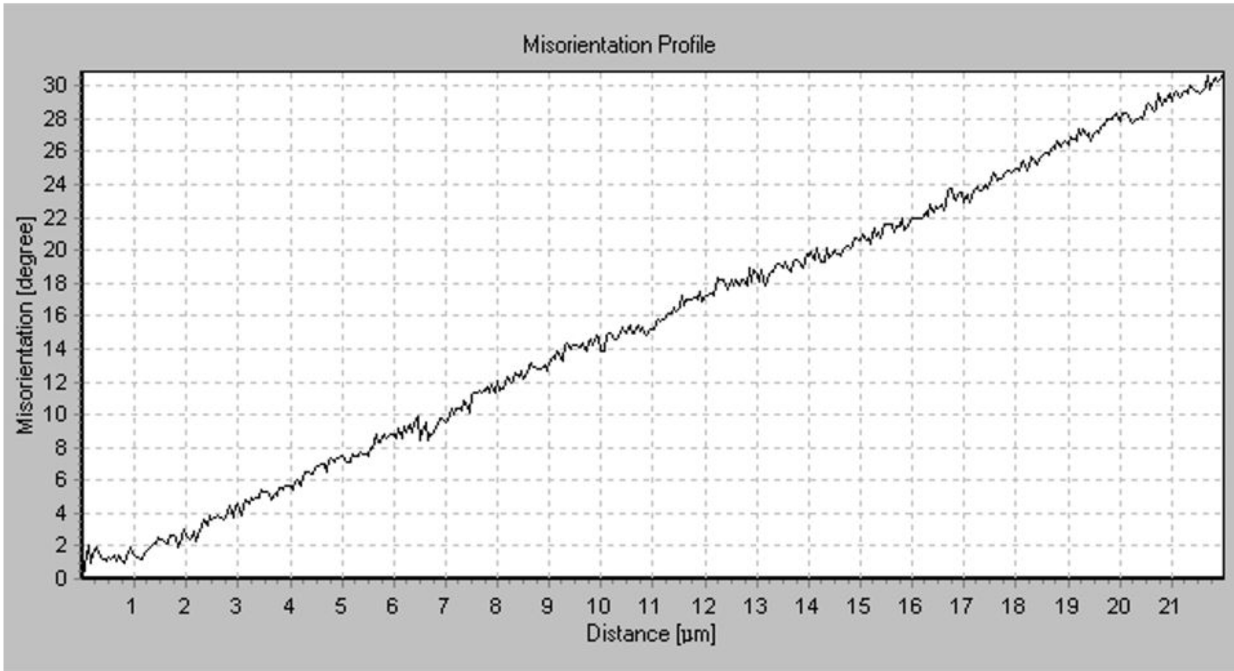

Fig. 7. The profile showing the change in the orientation angle of the crystal lattice of the perovskite island measured radially

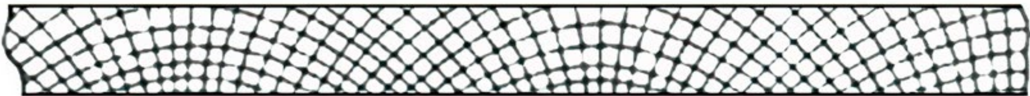

Fig. 8. An exaggerated model showing the bending of the crystal lattice planes

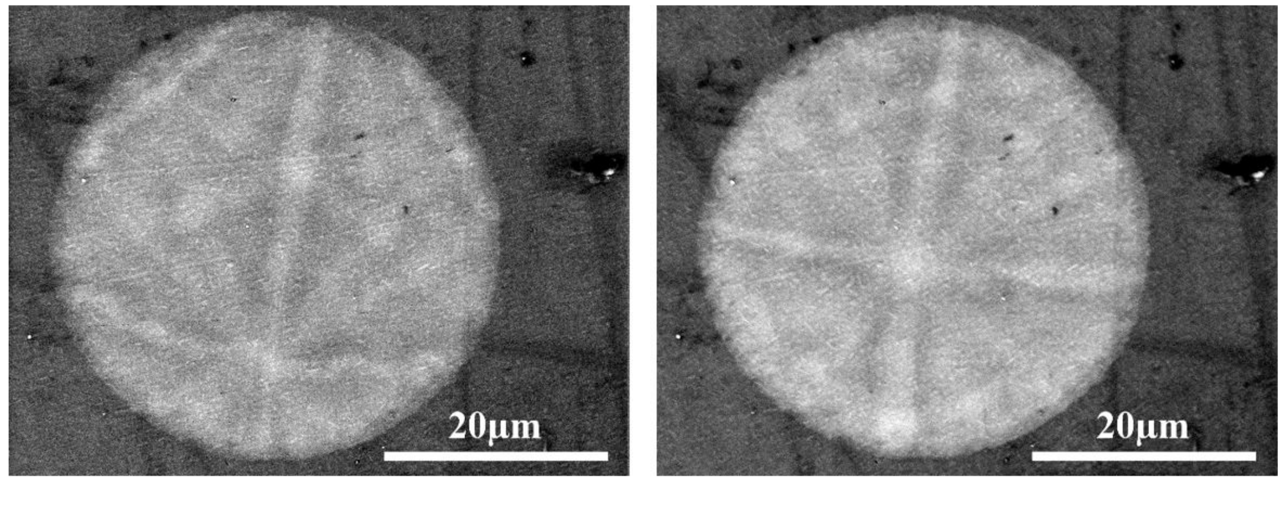

a b

Fig. 9. Electron images of the perovskite island showing a combination of intersecting stripes. In the image a) the incidence angle of the scanning electron beam in the center of the frame is close to normal. Image b) was received after physically rotating the sample around the horizontal axis by 10 degrees

upon a change in the phase volume. This model is adapted for PZT thin films of the model presented in [18, 22, 23]. The model contains assumptions that the crystallization front near the surface was ahead of the front near the substrate and that on the whole this front was propagating in a direction parallel to the film-substrate interface.

Thus, in the course of the crystallization, the material was considerably densified due to shrinkage along the pyrochlore-perovskite interface. For a thin film, in particular, the density increased perpendicular to the free surface, as only in this direction the change in shape was unlimited [22]. An additional half-plane appeared on the crystal side due to the smaller distance between atoms (of higher density) of the crystalline state. These unpaired dislocations, which initially appeared at the perovskite-pyrochlore interface, remained in the bulk of the growing crystal and formed a cloud of geometrically necessary dislocations responsible for the “bending” of the entire crystal lattice inside the crystal. This model is illustrated in Fig. 10 using a set of curved lattice planes that were initially parallel to the surface (left side of Fig. 10) and gradually bended towards the substrate with the growth of the crystal. According to the model, during island growth the lattice rotation axis should lie in the plane of the film, perpendicular to the direction of movement of the crystallization front. This position of the rotation axis with the constant rotation angle is a condition for the formation of the observed round-shaped crystals.

The suggested dislocation model can be experimentally verified by accessing the predicted density of dislocations. A relatively simple formula can be used for a theoretical evaluation of the local plane of dislocations in case of their homogenous distribution [24,25]:

$$\rho_{\text{hom}} = \frac{\theta_{\text{tot}}}{|b|\Delta X},$$

where θ_{tot} is the lattice bending angle at the distance ΔX implemented using dislocations with Burgers’ b vector.

Provided that $\theta_{\text{tot}} = 28^{\circ}$, $\Delta X = 20$ μm, and $|b|$, which equals to a pseudocubic lattice period ($a = 4.05$ Å), the average density of dislocations inside the perovskite island must take on a value of $3.5 \cdot 10^{15}$ m^{-2}.

4. Conclusions

A new phenomenon, an anomalous electron channeling, was discovered in PZT thin films on a sitall substrate. It was possible to observe the channeling patterns on the surface of perovskite islands upon radiation with parallel electron beams due to their unusual crystallographic structure. Based on the example of an individual

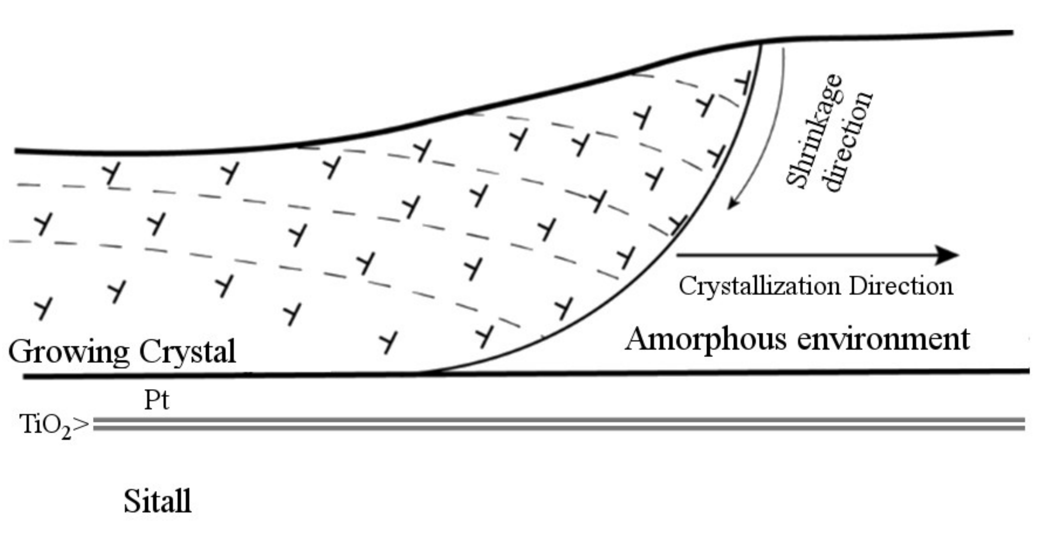

Fig. 10. An illustration of the dislocation model showing the bending of a perovskite island crystal lattice while growing from a quasi-amorphous environment

island, it was established that the crystallographic lattice of the islands had an axially symmetric bend increasing with the distance from the center according to the linear law. Therefore, it was shown that crystals with a symmetrically curved crystallographic surface could be obtained in thin films. A verifiable dislocation growth model was suggested for perovskite islands with a curved crystallographic surface from a quasi-amorphous surrounding in thin PZT thin films.

Contribution of the authors

The authors contributed equally to this article.

Conflict of interests

The authors declare that they have no actual or potential competing financial interests or personal relationships that could have influenced the work reported in this paper.

References

1. Wang Y., Yan J., Ouyang J., Cheng H., Chen N., Yan P. Microstructure evolution with rapid thermal annealing time in (001)-oriented piezoelectric PZT films integrated on (111) Si. *Materials.* 2023;16(5): 2068. https://doi.org/10.3390/ma16052068

2. Bukharaev A. A., Zvezdin A. K., Pyatakov A P., Fetisov Y. K. Straintronics: a new trend in micro- and nanoelectronics and materials science. *Physics-Uspekhi*. 2018;61(12): 1175–1212. https://doi.org/10.3367/UFNe.2018.01.038279

3. Ma Y., Son J., Wang X., Liu Y., Zhou J. Synthesis, microstructure and properties of magnetron sputtered lead zirconate titanate (PZT) thin film coatings. *Coatings*. 2021;11(8): 944 https://doi.org/10.3390/coatings11080944

4. Song L, Glinsek S., Defay E. Toward low-temperature processing of lead zirconate titanate thin films: Advances, strategies, and applications. *Applied Physical Review*. 2021;8: 041315. https://doi.org/10.1063/5.0054004

5. Picco A., Ferrarini P., Ferrarini P., … Lazzari M. Piezoelectric materials for MEMS. In: Vigna B., Ferrari P., Villa F. F., Lasalandra E., Zerbini S. (eds). *Silicon Sensors and Actuators*. Springer, Cham.; 2022. https://doi.org/10.1007/978-3-030-80135-9_10

6. Teuschel M., Heyes P., Horvath S., Novotny C., Cleric A. R. Temperature stable piezoelectric imprint of epitaxial grown PZT for zero-bias driving MEMS actuator operation. *Micromachines*. 2022;13(10): 1705. https://doi.org/10.3390/mi13101705

7. Scott J. F. Future issues in ferroelectric miniaturization. *Ferroelectrics*. 1998;206(1): 365-379. https://doi.org/10.1080/00150199808009170

8. Valeeva A. R., Pronin I. P., Senkevich S. V., … Nemov S. A. Microstructure and dielectric properties of thin polycrystalline PZT films with inhomogeneous distribution of the composition over thickness. *Journal of Surface Investigation: X-Ray, Synchrotron and Neutron Techniques*. 2021;15(1): 12–17. https://doi.org/10.1134/S1027451022010189

9. Staritsyn M. V., Fedoseev M. L., Kaptelov E. Yu., Senkevich S. V., Pronin I. P. Structure changing of submicron PZT films with a fine variation of the composition corresponding to morphotropic phase boundary. *Physical and Chemical Aspects of the Study of Clusters, Nanostructures and Nanomaterials*. 2021;13: 400–410. https://doi.org/10.26456/pcascnn/2021.13.400

10. Elshin A. S., Staritsyn M. V., Pronin I. P., Senkevich S. V., Mishina E. D. Nonlinear optics for crystallographic analysis in lead zirconate titanate. *Coatings*. 2023;13(2): 247. https://doi.org/10.3390/coatings13020247

11. Staritsyn M. V, Fedoseev M. L., Kiselev D. A., Kaptelov E. Yu., Pronin I. P., Senkevich S. V., Pronin V. P. Ferroelectric properties of lead zirconate titanate thin films obtained by RF magnetron sputtering near the morphotropic phase boundary. *Physics of the Solid State*. 2023;65(2): 290. https://doi.org/10.21883/PSS.2023.02.55414.531

12. Pronin V. P., Dolgintsev D. M., Osipov V. V., Pronin I. P., Senkevich S. V., Kaptelov E. Yu. The change in the phase state of thin PZT layers in the region of the morphotropic phase boundary obtained by the RF magnetron sputtering with varying target-substrate distance. *IOP Conference Series: Materials Science and Engineering*. 2018;387: 012063. https://doi.org/10.1088/1757-899X/387/1/012063

13. Elshin A. S., Pronin I. P., Senkevich S. V., Mishina E. D. Nonlinear optical diagnostics of thin polycrystalline lead zirconate titanate films. *Technical Physics Letters*. 2020;46: 385–388. https://doi.org/10.1134/S1063785020040215

14. Goldstein J. I., Newbury D. E., Echlin P., … Michael J. R. Special topics in scanning electron microscopy. In: *Scanning electron microscopy and X-ray microanalysis*. Springer, Boston, MA; 2003. pp. 247–256. https://doi.org/10.1007/978-1-4615-0215-9_5

15. Tulinov A. F. Influence of the crystal lattice on some atomic and nuclear processes. *Sov. Phys. Usp*. 1966;8: 864–872. https://doi.org/10.1070/PU1966v008n06ABEH003001

16. Lindhard J. Influence of crystal lattice on motion of energetic charged particles. *Uspekhi Fizicheskih Nauk.* 1969;99(10): 249–296. https://doi.org/10.3367/UFNr.0099.196910c.0249

17. Thompson M. W. The channelling of particles in crystals. *Contemporary Physics.* 1968;9(4): 375–398. https://doi.org/10.1080/00107516808220091

18. Lutjes N. R.; Zhou S.; Antoja-Lleonart J.; Noheda B., Ocelík V. Spherulitic and rotational crystal growth of quartz thin films. *Scientific Reports*. 2021;11(1): 14888. https://doi.org/10.1038/s41598-021-94147-y

19. Wright S. I., Nowell M. M., De Kloe R., Chan L. Orientation precision of electron backscatter diffraction measurements near grain boundaries. *Microscopy and Microanalysis*. 2014;20(3): 852–863. https://doi.org/10.1017/S143192761400035X

20. Pronin V. P., Kanareikin A. G., Dolgintsev D. M., Kaptelov E. Y., Senkevich S. V., Pronin I. P. Microstructure, phase analysis and dielectric response of thin $Pb(Zr,Ti)O_3$ films at the morphotropic phase boundary. *Journal of Surface Investigation: X-Ray, Synchrotron and Neutron Techniques*. 2017;11(1): 216–222. https://doi.org/10.1134/S1027451017010323

21. Kolosov V. Y., Thölén A. R. Transmission electron microscopy studies of the specific structure of crystals formed by phase transition in iron oxide amorphous films. *Acta Materialia*. 2000;48(8): 1829–1840. https://doi.org/10.1016/S1359-6454(99)00471-1

22. Kooi B. J., De Hosson J. Th. M. On the crystallization of thin films composed of Sb3.6Te with Ge for rewritable data storage. *Journal of Applied Physics*. 2004;95(9): 4714–4721. https://doi.org/10.1063/1.1690112

23. Savytskii D., Jain H., Tamura N., Dierolf V. Rotating lattice single crystal architecture on the surface of glass. *Scientific Reports*. 2016;6: 36449. https://doi.org/10.1038/srep36449

24. Konijnenberg P. J., Zaefferer S. Raabe D. Assessment of geometrically necessary dislocation levels derived by 3D EBSD. *Acta Materialia*. 2015;99: 402–414. https://doi.org/10.1016/j.actamat.2015.06.051

25. Pantleon W. Resolving the geometrically necessary dislocation content by conventional electron backscattering diffraction. *Scripta Materialia*. 2008;58(11): 994–997. https://doi.org/10.1016/j.scriptamat.2008.01.050

Information about the author

Mikhail V. Staritsyn, Engineer, National Research Centre Kurchatov Institute - Central Research Institute of Structural Materials "Prometey" (St. Petersburg, Russian Federation).

https://orcid.org/0000-0002-0088-4577

ms_145@mail.ru

Received 09.10.2023; approved after reviewing 12.10.2023; accepted for publication 16.10.2023; published online 26.12.2023.

Translated by Marina Strepetova

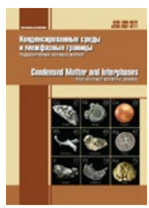

ISSN 1606-867X (Print)
ISSN 2687-0711 (Online)
Condensed Matter and Interphases
Kondensirovannye Sredy i Mezhfaznye Granitsy
https://journals.vsu.ru/kcmf/

Original articles

Brief review
https://doi.org/10.17308/kcmf.2023.25/11472

Natural ferromagnetic resonance in microwires and its applications. Brief review

S. A. Baranov[1,2]✉

[1]*Moldova State University, Institute of Applied Physics,*
5 Academiei st., Chisinau MD-2028, Republic of Moldova

[2]*Shevchenko Pridnestrov'e State University,*
128 25- Oktyabrya st., Tiraspol 33000, Pridnestrov'e, Republic of Moldova

Abstract

The paper analyzes technological aspects of the Taylor–Ulitovsky method used to produce microwires of various structures.

Natural ferromagnetic resonance (NFMR) in cast glass-coated amorphous magnetic micro- and nanowires was theoretically and experimentally studied. The NFMR phenomenon is due to the large residual stresses appearing in the core of the microwire during the casting process. These stresses, along with magnetostriction, determine magnetoelastic anisotropy. Besides residual stresses, the NFMR frequency is influenced by externally applied stresses on the microwire or the composite containing the so-called stress effect (SE).

The dependence of the NFMR frequency on the deformation of microwires and the external stresses on them is proposed to be used for remote diagnostics in medicine.

Keywords: Cast glass-coated amorphous magnetic micro- and nanowire, Magnetostriction, Natural ferromagnetic resonance

Funding: The study was supported by the Moldovan National Project and the project of Shevchenko Transnistria State University.

For citation: Baranov S. A. Natural ferromagnetic resonance in microwire and its application. Brief review. *Condensed Matter and Interphases*. 2023;25(4): 581–586. https://doi.org/10.17308/kcmf.2023.25/11472

Для цитирования: Баранов С. А. Естественный ферромагнитный резонанс в микропроводе и его применения. Краткий обзор. *Конденсированные среды и межфазные границы*. 2023;25(4): 581–586. https://doi.org/10.17308/kcmf.2023.25/11472

✉ Serghei A. Baranov, e-mail: sabaranov07@mail.ru
© Baranov S. A., 2023

The content is available under Creative Commons Attribution 4.0 License.

1. Introduction

The purpose of this work is to draw attention to the possibility of solving a number of technological problems associated with the application of micro- and nanowires.

One such problem may be related to increasing the mechanical toughness of windows in industrial and residential buildings. Another problem is associated with electromagnetic shielding. Both problems are related to protection against terrorist attacks, since terrorists use concentrated electromagnetic pulses to destroy computers or other electronic equipment.

These problems can be solved by manufacturing window glasses reinforced with cast glass-coated amorphous micro- and nanowires (GCAMNW) with a special composition and structure, which, on the one hand, increase their tensile strength during mechanical destruction, and on the other hand, are responsible for properties shielding them against electromagnetic radiation.

The proposed ideas are related to the technology of production of cast glass-coated amorphous micro- and nanowires. The technology for the production of cast glass-coated amorphous micro- and nanowires (GCAMNW) by the Taylor-Ulitovsky method is presented, for example, in [1–4] (see below). The phenomenon of natural ferromagnetic resonance (NFMR) for cast glass-coated micro- and nanowires with a magnetic core (GCAMNW) has been studied by many teams of researchers (the main results are presented in [3–7]).

Recently, the NFMR has attracted some interest in terms of using them for the remote contactless diagnostics of deformations [7]. This is possible due to the stress effect (SE) in the NFMR. SE leads to a change in the NFMR frequency during the deformation of the controlled object and, accordingly, the mechanically connected magnetic core in GCAMNW. The change in the NFMR frequency can be detected with a radar at frequencies near the NFMR which detects the reflected high-frequency signal and its deviations from the original value [7]. The remote testing proposed in this paper will allow monitoring these deformations and stresses.

In [7], we assumed that the controlled objects can include infrastructure facilities, namely: bridges, dams, levees, wind generator towers, high-rise buildings, pipes of thermal power stations, embankments, etc. The diagnostics can also be applied to moving objects: automobiles, airplanes, drones, missiles, etc., which can be at risk of destruction caused by natural, man-made, or technological disasters (including repeated or long-term effects of stresses and deformations). We have conducted a number of detailed studies dedicated to this topic, namely, the possibility of implementing the proposed control method. For example, SEs have been analyzed in terms of their practical application (according to [7]) in medicine. The changes in the frequency of natural ferromagnetic resonance (NFMR) have also been studied. They were detected with a radar by changes in the absorption of an electromagnetic wave by an object with GCAMNW. These effects were due to applied external mechanical stresses. The absorption of composite materials in the form of screens with built-in segments of GCAMNW have been experimentally investigated. Theoretical studies have also been carried out, which have shown that a significant proportion of the absorption can also be due to geometric resonance [3, 4, 7–10]. The greatest effect is expected for nanowires with a core radius comparable with the thickness of the skin layer.

Scientific literature presents the results of simultaneous research of the use of giant magnetic impedance (GMI) to measure such SEs (see, for example [8]). However, the use of the GMI effect does not seem to be technological (this issue has already been covered in [7]) and will not be considered in this paper. It should be noted that the influence of SEs on GMI has also been studied in [9].

The method proposed in this article is valuable due to its simplicity (see below). The microwire, if used to diagnose stresses within the skeletal system, must be placed inside the tested object. Microwave scanning and signal analysis of the receiving device (radar) will allow detecting the stresses and deformations of a skeletal object. To avoid exposing the entire body to microwave radiation, GCAMNW can be used in radio-absorbing materials which shield the rest of the body.

2. Technology of microwave production

It is known that GCAMNW is produced by a modified Taylor–Ulitovsky method (see [1–4]). In other words, to manufacture GCAMNW, a metal alloy (in the form of a thin bar) is placed in a glass tube. Due to the fact that it is heated in a high-frequency inductor to the glass melting and then metal melting temperatures (see Fig. 1), the part of the glass tube adjacent to the molten metal softens and envelops the metal droplet. The capillary, which is filled with a liquid alloy metal, is drawn out of the droplet. The metal forms the core of the microwire, and the walls of the capillary, made of silicate glass, form its glass coating (which often serves as insulation). Depending on the composition of the metal droplet (which is in the molten state and is located in a silicate glass microbath) and on the GCAMNW casting speed, the structure of the micro- and nanowire core can be mono- or polycrystalline, amorphous, or nanocrystalline (importantly, these structures can be combined in the core).

In [3], a formula was derived for the radius of the microwire, R_s (the outer radius of the glass coating), which was determined by the formula:

$$R_c \sim A\eta^{2-k}V_d^k\sigma_s^{1-k}, \quad (1)$$

where k is a parameter which depends on the casting speed ($0 < k < 1$); $A \sim 1/\rho$, ρ is the average density of the microwire; V_d is the casting speed; σ_s is the surface tension; and η is the dynamic viscosity of the glass:

$$\eta \sim \eta_0 \exp\{\Delta H/RT + c[\exp(\varepsilon/RT) - 1]\},$$

where $\varepsilon \sim 2$–10 kJ/mol, $\Delta H \sim 10^2$ kJ/mol, R is the universal gas constant, η_0 is the initial glass viscosity, and c ($c \sim 0.4$–0.9) is material constants.

Formula (1) is characterized by the following asymptotic behavior.

1. If the value of the speed of pulling the microwire is extremely small, the value R_c is large, therefore, the formula:

$$R_c \sim \eta^{5/3}V_d^{1/3}\sigma_s^{2/3}, \quad (1a)$$

where $k = 1/3$.

2. If the casting speed is high enough, R_c is:

$$R_c \sim \eta V_d \quad (1c)$$

where $k = 2/3$.

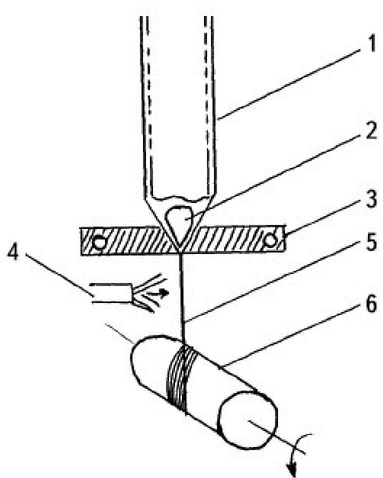

Fig. 1. The process of microwire casting: *1* – glass tube; *2* – metal droplet; *3* – inductor; *4* – water; *5* – glass-coated microwire; *6* – rotating receiver coil

2. Within limits of extremely high casting speed, at $k \to 1$, we obtain:

$$R_c \sim \eta V_d \quad (1c)$$

These formulas have been confirmed by experiment.

Here is the simplest solution to the problem of calculating residual stresses (on the surface between silicate glass and metal) for GCAMNW, which has already been considered, for example, in [3]. The formulas for the radial $\sigma_{r(0)}$, tangential $\sigma_{\varphi(0)}$, and axial $\sigma_{z(0)}$ stress components have the form of [3]:

$$\sigma_{r(0)} = \sigma_{\varphi(0)} = P = \sigma_m \frac{kx}{\left(\frac{k}{3}+1\right)x + \frac{4}{3}},$$

$$\sigma_{z(0)} = P\frac{(k+1)x+2}{kx+1}, \quad (2)$$

$$x = \left(\frac{RA}{Rm}\right)^2 - 1,$$

$\sigma_m = \varepsilon E_1$, $\varepsilon = (\alpha_1 - \alpha_2)(T^* - T) \approx 5 \cdot 10^{-3}$, α_i is thermal expansion coefficients (TEC) of metal ($i = 1$) and glass ($i = 2$); T^* is the solidification temperature of the composite in the metal/glass contact region ($T^* \sim 800$–1000 K); T is temperature at which the experiment is carried out; R_m is radius of the metal core of the microwire ($d_m = 2R_m$); and R_c is the outer radius of the glass coating of the microwire ($D_c = 2R_c$):

$$k = \frac{E_2}{E_1} \sim (0.3 \div 0.5),$$

E_i is Young's moduli (metal (i = 1) and glass (i = 2)).

To simplify the above formulas, Poisson's ratios for glass and metal are taken ~ 1/3. According to (1), the highest stress is the longitudinal stress:

$\sigma_{z(0)} \sim (2 \div 3)P$,

i.e.:

$\sigma_{z(0)} > \sigma_{r,\varphi(0)}$,

and the maximum value of P is defined as:

$P \to 0.5\sigma_m \sim 10^9$ Pa.

With additional longitudinal strain, that occurs when the microwire is embedded in a solid matrix, which also deforms under external influence, the following term is added to the expression for residual axial tension in the metal core:

$$\sigma_{ez} = \frac{P_0}{S_m(k\,x\,+1)}, \quad (2,a)$$

where P_0 is the force applied to the composite and, accordingly, to the core of the microwire; $S_m = \pi R_m^2$ is the cross-sectional area of the core of the microwire; k is the ratio of the Young's modulus of the coating to the Young's modulus of the microwire; and x is the ratio of the area of the coating to the area of the microwire (see (1).

We also give the formulas for stresses inside the metal (they are presented in [3]):

$$\sigma_r \approx P_1'\left(1 - \frac{b_1^2}{r^2}\right), \qquad \sigma_\varphi \approx P_1'\left(1 + \frac{b_1^2}{r^2}\right), \quad (2b)$$

where $P_1' \approx \dfrac{P_1}{1-(b_1/R_m)^2} \approx P_1 \approx P$.

These formulas have been confirmed experimentally.

3. Prerequisites to using high-frequency properties of the microwire

The theory of NFMR is presented in [3–7]. For a ferromagnetic metal cylinder (with a small radius R_m) located in GCAMNW, the depth of the skin layer is determined by:

$$\delta \sim [\omega(\mu\mu_0)_e\Sigma_2]^{-1/2} \sim \delta_0(\mu)_e^{-1/2}, \quad (3)$$

where $(\mu\mu_0)_e$ is the effective high-frequency magnetic permeability, and Σ_2 is the electrical conductivity of the microwire, and ω is microwave frequency.

In the case of GCAMNW, the relative high-frequency magnetic permeability can reach a value of ~ 10^3 in the frequency range of ~ 9–10 GHz; in this case, the depth of the skin layer decreases to 1–2 μm.

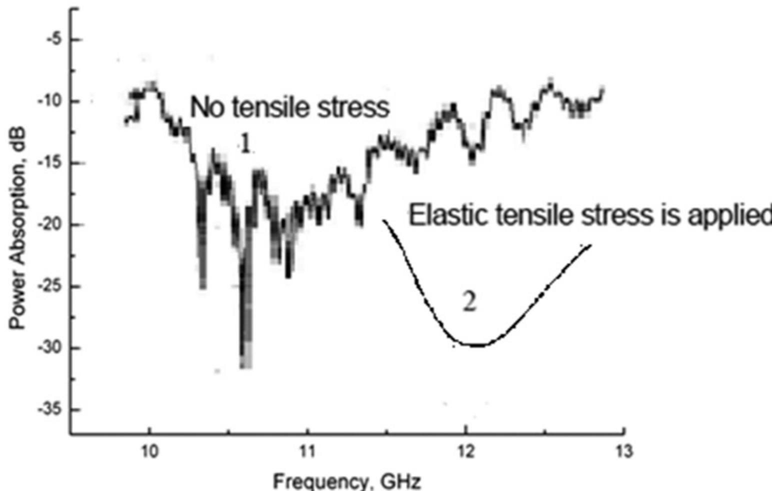

Fig. 2. *1* – average absorption characteristics of a shielding containing a microwire exhibiting NFMR at microwave frequencies ranging from 10–12 GHz for $Fe_{68}C_4B_{16}Si_{10}Mn_2$ (R_m ~ 5 μm, x ~ 5) microwires; *2* – hypothetical absorption curve in case of external pressure

It is known (see [3–5]) that if $R_m > \delta$, the general expression for the frequency of ferromagnetic resonance (FMR or NFMR) ω is:

$$(\omega/\gamma)^2 = (Hk + 4\pi M_s)\cdot Hk, \quad (3a)$$

where M_s is the saturation magnetization and γ is the gyromagnetic ratio [3, 7]. The value of anisotropy is determined as $Hk \sim 3\,\lambda\sigma/M_s$, where λ is the magnetostriction constant and σ is the effective mechanical stress in the GCAMNW metal core.

For the FMR and NFMR frequencies, the following can be obtained:

$$\omega(\text{GHz}) \approx \omega_0 \left(\frac{0.4x}{0.4x+1} + \frac{\sigma_{ez}}{\sigma_0} \right)^{1/2}, \quad (4)$$

where $\omega_0(\text{GHz}) \approx 1.5(10^6\,\lambda)^{1/2}$.

Therefore, a change in the geometric parameters of GCAMNW, the applied external stress and, most importantly, due to magnetostriction, makes it possible to overlap the frequency range from 1 to 12 GHz, which creates prerequisites for using GCAMNW for the purposes proposed above.

4. Conclusions

The article presents the main results of the theory and the experiment related to the production of cast glass-coated microwires. The method of continuous casting of glass-coated microwires (Taylor–Ulitovsky method) has some limitations determined by the physical properties of metal and glass. The range of casting operating temperatures is specific for a given metal alloy composition and a certain type of glass, i.e. for each pair, metal alloy – glass.

We presented simple analytical expressions for residual stresses in the metal core of the microwire, which clearly show their dependence on the ratio of the radius of the microwire to the radius of the metal core and on the ratio of Young's moduli of glass and metal (see formulas (1) and (2)). Theoretical modeling based on the theory of thermoelastic relaxation shows that the residual stresses increase from the axis of the microwire to the surface of its metal core, which is in accordance with the previously obtained experimental data. Therefore, when cast microwires are manufactured by the Taylor–Ulitovsky method, the residual stresses reach the maximum values on the surface of the metal core.

These cast microwires are characterized by the presence of residual stresses which appear because of the difference in the thermal expansion coefficients of the metal alloy and the glass coating. This feature is the main factor determining the physical properties of such microwires, in particular, their magnetic properties.

For GCAMNW, the NFMR frequency depends on residual stresses and applied external mechanical stresses. The NFMR phenomenon, which we discovered in GCAMNW [3, 7], allows creating new materials that work in the microwave region with a wide frequency range. NFMR in GCAMNW is characterized by an important property, stress effect (SE). This SE can be used for the remote contactless diagnostics of deformations in objects. These objects can be periodically scanned with a floating-frequency radar to determine the deviation of the initial NFMR frequency. In this way, it is possible to track potentially dangerous deformations and stresses in any studied object.

We also considered the application of microwires in composites to improve their absorption characteristics of shielding.

Conflict of interests

The author declares that they has no known competing financial interests or personal relationships that could have influenced the work reported in this paper.

References

1. Taylor G. F. A method of drawing metallic filaments and a discussion of their properties and uses. *Physical Review*. 1924;23(5): 655–660. https://doi.org/10.1103/physrev.23.655

2. Vazquez M. Soft magnetic wires. *Physica B: Condensed Matter*. 2001;299(3-4): 302–313. https://doi.org/10.1016/S0921-4526(01)00482-3

3. Baranov S. A., Larin V. S., Torcunov A. V. Technology, preparation and properties of the cast glass-coated magnetic microwires. *Crystals*. 2017;7(6): 1–12. https://doi.org/10.3390/cryst7060136

4. Peng H. X., Qin F. X., Phan M. H. *Ferromagnetic microwires composites: from sensors to microwave applications*. Springler: 2016. 245 p. https://10.1007/978-3-319-29276-2

5. Starostenko S. N., Rozanov K. N., Osipov A. V. Microwave properties of composites with glass coated

amorphous magnetic microwires. *Journal of Magnetism and Magnetic Materials.*2006; 298 (1): 56–64. https://doi.org/10.1016/j.jmmm.2005.03.004

6. Yıldız F., Rameev B. Z., Tarapov S. I., Tagirov L. R.,Aktaş B. High-frequency magnetoresonance absorption in amorphous magnetic microwires. *Journal of Magnetism and Magnetic Materials*. 2002;247(2): 222–229. https://doi.org/10.1016/s0304-8853(02)00187-7

7. Adar E., Yosher A. M., Baranov S. A. Natural ferromagnetic resonance in cast microwires and its application to the safety control of infrastructures. *International Journal of Physics Research and Applications*. 2020;3(1): 118–122. https://doi.org/10.29328/journal.ijpra.1001028

8. Nematov M. G., Adam A. M., Panina L.V., … Qin F.X. Magnetic anisotropy and stress-magnetoimpedance (S-MI) in current-annealed Co-rich glass-coated microwires with positive magnetostriction. *Journal of Magnetism and Magnetic Materials*. 2019;474: 296–302. https://doi.org/10.1016/j.jmmm.2018.11.042

9. Buznikov N. A., Kim C. O. Modeling of torsion stress giant magnetoimpedance in amorphous wires with negative magnetostriction. *Journal of Magnetism and Magnetic Materials*. 2007;315(2): 89–94. https://doi.org/10.1016/j.jmmm.2007.03.186

Information about the authors

Serghei A. Baranov, Dr. Sci. (Phys.-Math.), Senior Researcher of the Moldova State University, Institute of Applied Physics, Laboratory of Electrical and Electrochemical Treatment of Materials (Chisinau, Republic of Moldova); Associate Professor of the Shevchenko Pridnestrov’e State University (Tiraspol, Pridnestrov’e, Republic of Moldova).

sabaranov07@mail.ru

Received 28.09.2023; approved after reviewing 10.10.2023; accepted for publication 16.10.2023; published online 25.12.2023.

Translated by Irina Charychanskaya

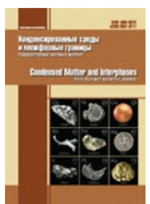

ISSN 1606-867X (Print)
ISSN 2687-0711 (Online)
Condensed Matter and Interphases
Kondensirovannye Sredy i Mezhfaznye Granitsy
https://journals.vsu.ru/kcmf/

Original articles

Research article
https://doi.org/10.17308/kcmf.2023.25/11478

Electronic structure of germanium dioxide with rutile structure according to ab initio computer simulation data

M. D. Manyakin✉**, S. I. Kurganskii**

Voronezh State University,
1 Universitetskaya pl., Voronezh 394018, Russian Federation

Abstract

The article focuses on the electronic structure of the tetragonal crystalline modification of germanium dioxide. The electronic structure was theoretically studied by means of the full-potential linearized augmented plane wave method using the Wien2k software.

Total and partial densities of electronic states were calculated. The spectra of the X-ray absorption near edge structure were simulated for various absorption edges of germanium and oxygen atoms. The Z+1 approximation method was used to calculate Ge K-, Ge L_3- and O K absorption edges for the tetragonal modification of GeO_2. The result obtained for the Ge K absorption edge is in good agreement with the experimental data.

The Ge L_3 spectrum was calculated for the first time, and the result is of predictive nature. In order to obtain a better agreement with the experimental calculations of the oxygen K absorption edge, besides the Z+1 approximation method, we also used the core hole method, including the simulation of a partial core hole. The study demonstrated that the use of a core hole with an electron charge of 0.7 results in a better agreement between the calculations and the experiment.

Keywords: Computer simulation, Germanium dioxide, Electronic structure, Density of states, XANES, Core hole, Rutile

Funding: The study was supported by the Russian Science Foundation, project No. 22-72-00145.

For citation: Manyakin M. D., Kurganskii S. I. Electronic structure of germanium dioxide with rutile structure according to ab initio computer simulation data. *Condensed Matter and Interphases*. 2023;25(4): 587–593. https://doi.org/10.17308/kcmf.2023.25/11478

Для цитирования: Манякин М. Д., Курганский С. И. Электронное строение диоксида германия со структурой рутила по данным ab initio компьютерного моделирования. *Конденсированные среды и межфазные границы*. 2023;25(4): 587–593. https://doi.org/10.17308/kcmf.2023.25/11478

✉ Maxim D. Manyakin, e-mail: manyakin@phys.vsu.ru
© Manyakin M. D., Kurganskii S. I., 2023

The content is available under Creative Commons Attribution 4.0 License.

1. Introduction

Germanium dioxide is a wide bandgap semiconductor [1] used in optoelectronics, solar energy, and catalysis [2–5]. Normally, germanium dioxide exists in two stable crystalline modifications: a hexagonal *q*-GeO_2 (quartz structure) and a tetragonal *r*-GeO_2 (rutile structure) [6].

Due to several reasons, the electronic structure of the tetragonal phase of germanium dioxide is of great scientific interest. Firstly, there are a lot of studies focusing on the synthesis and analysis of nanomaterials based on GeO_x compounds [3, 4, 7, 8]. Secondly, *r*-GeO_2 is one of oxide materials that have a rutile-type spatial structure [9]. These materials have similar parameters of their crystal lattices and can therefore be used to synthesise new functional materials in the form of interfaces and heterostructures based on them [10]. In both cases, an accurate analysis and interpretation of the experimentally determined properties of such materials requires understanding of the specifics of the electronic structure of *r*-GeO_2.

X-ray absorption near edge structure (XANES) is one of the methods commonly used in experimental studies of the atomic and electronic structure of materials [11]. XANES spectra provide researchers with information about the distribution of the density of the unoccupied electronic states in the conduction band of solids. They are also highly sensitive to the thin layers on the material's surface and to the short-range order in the spatial distribution of atoms of the studied material.

Analyses of the experimental spectra of the studied samples usually involve their comparison with the spectra of well-studied materials considered as reference materials. For the materials of the Ge – O system, one of such reference materials is *r*-GeO_2. There have been a number of studies obtaining experimental XANES spectra of the *r*-GeO_2 phase. Several works [12–14] demonstrate the K edge X-ray absorption spectra of germanium and [15, 16] demonstrate the K edge X-ray absorption spectra of oxygen. Some studies use the Ge K edge as a reference when analysing the spatial structure of the studied samples of the Ge – O system [13, 14, 17]. However, the existing literature provides no theoretical, neither experimental information about the L_3 edge absorption spectra of germanium in *r*-GeO_2.

At the same time, the results of computer simulation, as well as the results of experiments, can be used as reference spectra [18]. Although there are quite a number of works focusing on the tetragonal GeO_2 electronic structure modelling [5, 16, 19, 20–23], they do not contain the Ge K edge and Ge L_3 edge XANES spectra calculations results. Apparently, up to now there have been no publications providing such information. There has only been a study focusing on the calculation of the K edge absorption spectrum of oxygen in *r*-GeO_2 [15]. The results of this study are in good agreement with the experimental results. However, they demonstrated some significant differences in the intensity ratios of the structural features of the spectrum.

Therefore, it is important to perform first-principles calculations of the tetragonal phase of GeO_2 and calculate the XANES spectra, which was the purpose of our study.

2. Calculation methodology

The tetragonal phase of germanium dioxide has a rutile-type spatial structure with the space group $P4_2/mnm$ [19]. In our study, we used the experimental values of unit cell parameters presented in [24] analogous to the calculations performed in [5, 23]. The appearance of the *r*-GeO_2 unit cell is given in Fig. 1. The parameters of the crystal structure are given in Table 1.

The electronic structure was calculated using a Wien2k program package [25] based on a full-potential linearized augmented plane wave method (LAPW). Within the framework of the density functional theory, generalized gradient

Table 1. Parameters of the *r*-GeO_2 crystal lattice

Space group	$P4_2/mnm$		
Unit cell parameters a, b, Å	4.40656		
Unit cell parameter c, Å	2.86186		
Atomic position	*x/a*	*y/b*	*z/c*
Ge_1	0.5	0.5	0.5
Ge_2	0.0	0.0	0.0
O_1	0.806	0.806	0.5
O_2	0.194	0.194	0.5
O_3	0.694	0.306	0.0
O_4	0.306	0.694	0.0

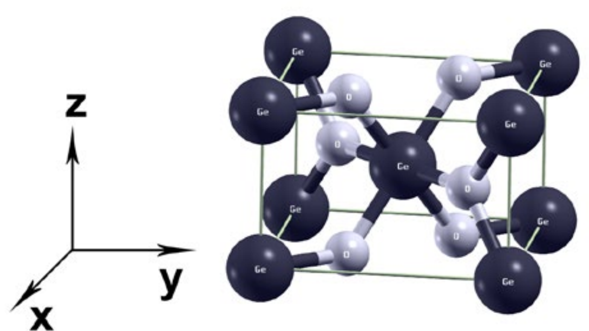

Fig. 1. *r*-GeO_2 unit cell. The Ge atom is dark-grey, the O atom is light-grey

approximation (GGA) was used for the exchange-correlation energy. The muffin-tin radii of Ge were 1.85 a.u., and the muffin-tin radii of O were 1.67 a.u.

The XANES spectra were simulated using the core hole method and the Z+1 approximation method. The formalism of each of these methods is slightly different. Both methods are based on the idea that it is necessary to perform the calculation of excited state when simulating the electronic structure of the conduction band in order to compare the result with experimental XANES spectra [26, 27]. The experimental studies of the conduction band were performed using the XANES method, with high-energy X-ray photon beam aimed at a sample whose core electrons absorb energy and pass to the conduction band. This means that it is necessary to calculate the band structure of the material in this particular electronic configuration: with a +1*e* positive charge on the atomic core and a −1*e* negative charge in the conduction band. For this, the core hole method can be used [26-28]. It involves removing a core electron from a previously selected atom A, whose spectrum needs to be calculated. This electron passes to the conduction band to maintain electroneutrality. The core hole is simulated on the same energy level, where the electron vacancy occurs during the experiment. When the Z+1 approximation method is used [28], atom A is replaced with an atom of the next chemical element with the charge number Z+1. We should note that for both methods atom A is a part of a supercell, whose volume is several times larger than the unit cell volume. All the other atoms in the supercell are in a ground energy state. At the same time, the supercell volume should be large enough to prevent the interaction between neighbouring atoms with core holes or the charge number Z+1 [26, 27]. In our study, we used 2×2×3 supercells analogous to the calculations performed in [15, 29]. With these parameters the shape of the supercell is close to cubic, and the minimum distance between two excited atoms is ~ 8.585 Å. When the spectra of germanium were calculated using the *Z*+1 approximation method, one of the germanium atoms in the supercell was replaced with an arsenic atom. Similarly, when the oxide spectra were calculated, one of oxygen atoms was replaced with a fluorine atom. Thus, we performed theoretical calculations of the absorption spectra of Ge K, Ge L_3, and O K.

3. Results and discussion

3.1. The density of electronic states of r-GeO_2

The calculated total $N(E)$ and partial $n(E)$ densities of electronic states (DOS) of *r*-GeO_2 in the ground state are given in Fig. 2. The beginning of the energy scale was the valence band top. The bandwidth of the valence band was 10.4 eV. The curve of the total DOS of the valence band has a three-peak structure characteristic of the other oxides of elements in group 14 of the periodic table that have a rutile-type spatial structure [29, 30]. The intensity of peaks of the DOS grows from the bottom to the top of the valence band. The peak at −9.65 eV is equally contributed to by the 4*s* states of germanium and the 2*p* states of oxygen. The peak in the middle of the valence band at −5.4 eV is mainly formed by the 2*p* states of oxygen with a small part by the 4*p* states of germanium. The most intensive peak at a distance of −1.2 eV from the top of the valence band is almost completely formed by the 2*p* states of oxygen atoms. The dominance of the occupied electronic states of oxygen in the valence band can be explained by a greater electronegativity of oxygen atoms as compared to germanium atoms.

Below the valence band there are two narrow subvalent groups: Ge 3*d* in the energy range from −24.8 to – 23.8 eV and O 2*s* in the energy range from −21.3 to −16.7 eV (they are not shown in the figure). The valence band is divided from the conduction band by a band gap, whose width is 1.996 eV, which is lower than the experimental value 4.680 eV [1]

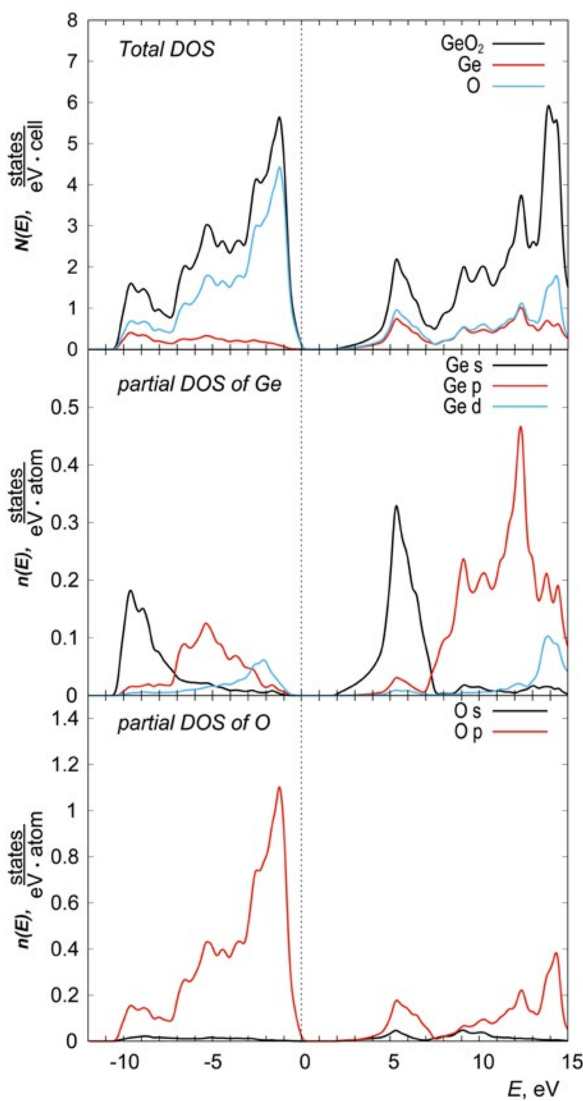

Fig. 2. Total $N(E)$ and partial $n(E)$ densities of electronic states of r-GeO_2.

due to the fact that it was calculated using GGA, which tends to underestimate the bandwidth of the band gap in semiconductors and dielectrics [31]. An analysis of the conduction band demonstrated that the contribution of germanium and oxygen states are practically the same in a wide energy range up to 15 eV.

We should also note that the results of our calculation of the DOS of r-GeO_2 are in good agreement with the calculations presented in [5, 16, 20–22].

3.2. XANES spectra of r-GeO₂

Fig. 3 demonstrated a Ge K edge XANES spectrum calculated using the Z+1 approximation. The Ge K spectrum shows the density of unoccupied Ge *p* states in the conduction band. We compared the model spectrum to the experimental spectrum described in [14]. The spectra were compared using a single energy scale based on the position of the main peak at E ~ 11110 eV. The comparison showed that the shape and position of the main energy features, including several low-intensity peaks in the range of 50 eV from the absorption edge, correspond well to the experimental ones. This confirms the accuracy of the calculations and the validity of the Z+1 approximation method and makes it possible to use this method when modelling other absorption edges of r-GeO_2.

Fig. 4 demonstrates the results of calculations of a Ge L_3 edge XANES spectrum by means of the Z+1 approximation. The Ge L_3 spectrum shows the density of unoccupied Ge *s*- and *d*- states in the conduction band. The existing literature does not provide any data regarding the experimental calculations of the Ge L_3 absorption edge in r-GeO_2. Therefore, we compared the calculated spectrum to the theoretical and experimental Sn L_3 spectra in rutile-type SnO_2 described in [32]. The spectra were aligned along the position of the peak at ~ 11 eV using the energy scale corresponding to the model Ge L_3 spectrum. The germanium spectrum is quite similar to the tin spectrum with regard to the shape and the location of the main structural features. The main difference is that the germanium spectrum has a single main peak, while in the tin spectrum the main peak is bifurcated. This is explained by the difference in the energy distribution of Ge 4*d* and Sn 5*d* states that form the considered spectra. The result obtained for the Ge L_3 absorption edge is of predictive nature and can be used to analyse

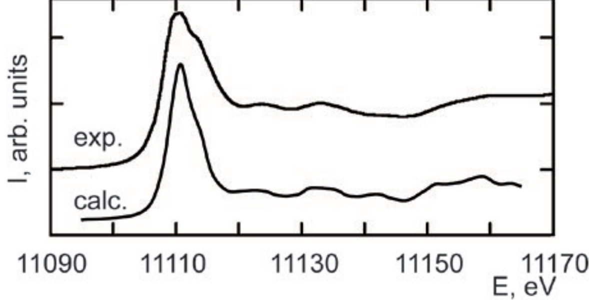

Fig. 3. Calculated (calc.) Ge K absorption spectrum in comparison with the experimental (exp.) spectrum presented in [14]

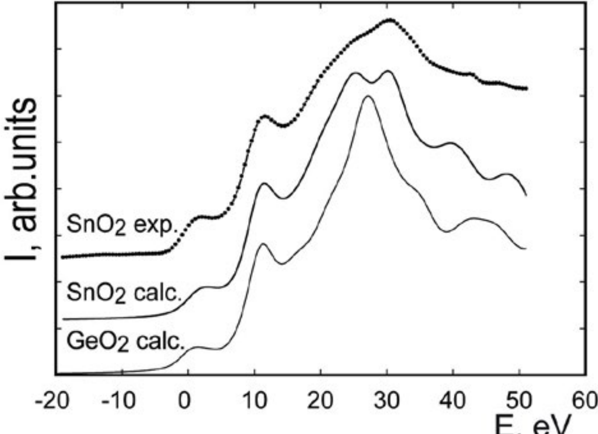

Fig. 4. Calculated (GeO_2 calc.) Ge L_3 absorption spectrum in comparison with the calculated (SnO_2 calc.) and experimental (SnO_2 exp.) Sn L_3 spectra in SnO_2 [32]

experimentally studied samples of the Ge – O system.

Then we calculated the O K absorption edge. Fig. 5 demonstrates the calculated spectra in comparison with the experimental and model spectra presented in [15]. We compared the calculated spectra to the experimental ones based on the position of the main peak at 535 eV on the energy scale. In general, the results of our calculations performed by means of the Z+1 approximation method agree well with the experiment [15]. However, similar to the theoretical calculations [15], the obtained spectrum demonstrated a redistribution of the intensity of the spectrum's thin structure in the range of 540–545 eV as compared to the experimental intensity. In [15], this is explained by the too attractive potential of the core hole. This is why we also calculated the O K XANES spectrum using the core hole method, including by introducing a partial core hole. A similar approach was used to calculate the XANES spectra in [28] and helped to enhance the agreement between the calculated and experimental results. Fig. 5 demonstrates the spectra calculated for the full core hole and core holes with charges 0.8*e* and 0.7*e* (1.0 ch, 0.8 ch, and 0.7 ch respectively). The result obtained for the full core hole is practically the same as the result obtained using the Z+1 approximation method. A decrease in the charge of the core hole results in changes in the intensity ratio of the structural features of the calculated absorption spectrum in the region of 540–545 eV.

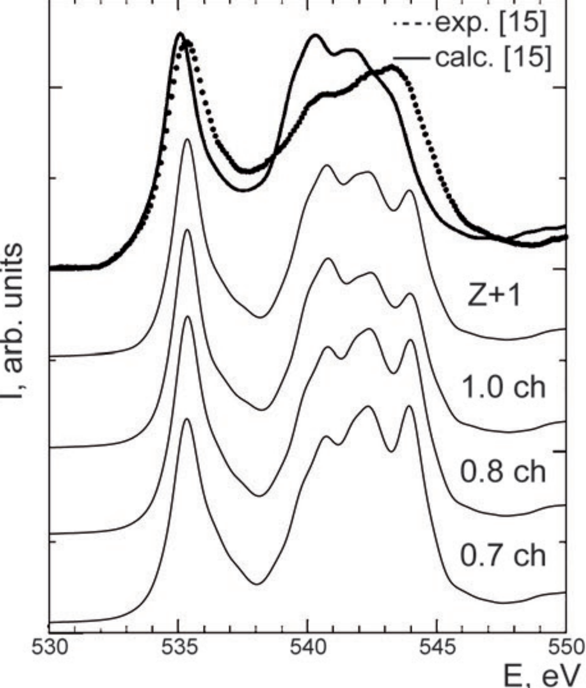

Fig. 5. O K XANES absorption spectra calculated using various methods in comparison to the results presented in [15]

The theoretical spectrum obtained using the core hole with the 0.7*e* charge demonstrated a better agreement with the experiment.

4. Conclusions

A linearised augmented plane wave method was used to study the electronic structure of the tetragonal crystalline modification of germanium dioxide.

Ge K and Ge L_3 XANES absorption spectra were calculated for the first time using the Z+1 approximation method.

O K XANES spectrum was for the first time calculated using the partial core hole method. The model spectrum obtained using the core hole with the 0.7*e* charge demonstrated a better agreement with the experiment.

The obtained results can be used to analyse experimentally studied specimens of the Ge – O system.

Contribution of the authors

The authors contributed equally to this article.

Conflict of interests

The authors declare that they have no known competing financial interests or personal

relationships that could have influenced the work reported in this paper.

References

1. Stapelbroek M., Evans B. D. Exciton structure in the u.v.-absorption edge of tetragonal GeO_2. *Solid State Communications*. 1978;25: 959–962. https://doi.org/10.1016/0038-1098(78)90311-3

2. Nikisihina E. E., Lebedeva E. N., Piletsky A. V., Drobot D. V. Hydroxide and oxide of germanium(IV): synthesis and chemical-physical properties. *Fine Chemical Technologies*. 2015;10(5):19–26. (In Russ.). Available at: https://www.finechem-mirea.ru/jour/article/view/254?locale=ru_RU

3. Peng M., Li Y., Gao J., Zhang D., Jiang Z., Sun X. Electronic structure and photoluminescence origin of single-crystalline germanium oxide nanowires with green light emission. *The Journal of Physical Chemistry C*. 2011;115: 11420–11426. https://doi.org/10.1021/jp201884y

4. Armelao L., Heigl F., Kim P.-S. G., Rosenberg R. A., Regier T. Z., Sham T.-K. Visible emission from GeO_2 nanowires: site-specific insights via X-ray excited optical luminescence. *The Journal of Physical Chemistry C*. 2012;116(26): 14163–14169. https://doi.org/10.1021/jp3040743

5. Samanta A., Jain M., Singh A. K. Ultra-sensitive pressure dependence of bandgap of rutile-GeO_2 revealed by many body perturbation theory. *The Journal of Chemical Physics*. 2015;143: 064703. https://doi.org/10.1063/1.4928526

6. Dinsdale A. T., Akhmetova A., Khvan A. V., Aristova N. A critical assessment of thermodynamic and phase diagram data for the Ge-O system. *Journal of Phase Equilibria and Diffusion*. 2015;36: 254–261. https://doi.org/10.1007/s11669-015-0379-1

7. Torrey J. D., Vasko S. E., Kapetanovic A., Rolandi M. Scanning probe direct-write of germanium nanostructures. *Advanced Materials*. 2010;22: 4639–4642. https://doi.org/10.1002/adma.201001987

8. Wysokowski M., Motylenko M., Beyer J., ... Ehrlich H. Extreme biomimetic approach for developing novel chitin-GeO_2 nanocomposites with photoluminescent properties. *Nano Research*. 2015;8: 2288–2301. https://doi.org/10.1007/s12274-015-0739-5

9. Baur W. H. The rutile type and its derivatives. *Crystallography Reviews*. 2007;13(1): 65–113. http://dx.doi.org/10.1080/08893110701433435

10. Lim H. Y., Park S. O., Kim S. H., Jung G. Y., Kwak S. K. First-principles design of rutile oxide heterostructures for oxygen evolution reactions. *Frontiers in Energy Research*. 2021;9: 606313. https://doi.org/10.3389/fenrg.2021.606313

11. Stohr J. *NEXAFS spectroscopy*. Springer-Verlag Berlin Heidelberg; 1992. 404 p. https://doi.org/10.1007/978-3-662-02853-7

12. Okuno M., Yin C. D., Morikawa H., Marumo F., Oyanagi H. A high resolution exafs and near edge study of GeO_2 glass. *Journal of Non-Crystalline Solids*. 1986;87: 312–320. https://doi.org/10.1016/S0022-3093(86)80005-9

13. Itie J. P., Polian A., Calas G., Petiau J., Fontaine A., Tolentino H. Pressure-induced coordination changes in crystalline and vitreous GeO_2. *Physical Review Letters*. 1989;63: 398–401. https://doi.org/10.1103/PhysRevLett.63.398

14. Majérus O., Cormier L., Itié J.-P., Galoisy L., Neuville D. R., Calas G. Pressure-induced Ge coordination change and polyamorphism in SiO_2–GeO_2 glasses. *Journal of Non-Crystalline Solids*. 2004;345-346: 34–38. https://doi.org/10.1016/j.jnoncrysol.2004.07.039

15. Cabaret D., Mauri F., Henderson G. S. Oxygen K-edge XANES of germanates investigated using first-principles calculations. *Physical Review B*. 2007;75: 184205. https://doi.org/10.1103/PhysRevB.75.184205

16. Wang H. M., Henderson G. S. Investigation of coordination number in silicate and germanate glasses using O K-edge X-ray absorption spectroscopy. *Chemical Geology*. 2004;213: 17–30. https://doi.org/10.1016/j.chemgeo.2004.08.029

17. Ohtaka O., Yoshiasa A., Fukui H., ... Nishihata Y. Structural changes of quartz-type crystalline and vitreous GeO_2 under pressure. *Journal of Synchrotron Radiation*. 2001;8: 791–793. https://doi.org/10.1107/S0909049500018306

18. Manyakin M. D., Kurganskii S. I., Dubrovskii O. I., ... Turishchev S. Yu. Electronic and atomic structure studies of tin oxide layers using X-ray absorption near edge structure spectroscopy data modelling. *Materials Science in Semiconductor Processing*. 2019;99: 28–33. https://doi.org/10.1016/j.mssp.2019.04.006

19. Svane A., Antoncik E. Electronic structure of rutile SnO_2, GeO_2 and TeO_2. *Journal of Physics and Chemistry of Solids*. 1987;48(2): 171–180. https://doi.org/10.1016/0022-3697(87)90081-3

20. Christie D. M., Chelikowsky J. R. Electronic and structural properties of germania polymorphs. *Physical Review B*. 2000;62: 14703. https://doi.org/10.1103/PhysRevB.62.14703

21. Liu Q.-J., Liu Z.-T., Feng L.-P., Tian H. First-principles study of structural, elastic, electronic and optical properties of rutile GeO_2 and α-quartz GeO_2. *Solid State Sciences*. 2010;12(10): 1748–1755. https://doi.org/10.1016/j.solidstatesciences.2010.07.025

22. Sevik C., Bulutay C. Theoretical study of the insulating oxides and nitrides: SiO_2, GeO_2, Al_2O_3, Si_3N_4, and Ge_3N_4. *Journal of Materials Science*. 2007;42: 6555–6565. https://doi.org/10.1007/s10853-007-1526-9

23. Mengle K. A., Chae S., Kioupakis E. Quasiparticle band structure and optical properties of rutile GeO_2, an ultra-wide-band-gap semiconductor. *Journal of*

Applied Physics. 2019;126: 085703. https://doi.org/10.1063/1.5111318

24. Bolzan A. A., Fong C., Kennedy B. J., Howard C. J. Structural studies of rutile-type metal Ddioxides. *Acta Crystallographica Section B Structural Science*. 1997;B53: 373–380. https://doi.org/10.1107/S0108768197001468

25. Blaha P., Schwarz K., Tran F., Laskowski R., Madsen G. K. H., Marks L. D. WIEN2k: An APW+lo program for calculating the properties of solids. *The Journal of Chemical Physics*. 2020;152: 074101. https://doi.org/10.1063/1.5143061

26. Hebert C., Luitz J., Schattschneider P. Improvement of energy loss near edge structure calculation using Wien2k. *Micron*. 2003;34: 219–225. https://doi.org/10.1016/S0968-4328(03)00030-1

27. Duscher G., Buczkoa R., Pennycooka S. J., Pantelides S. T. Core-hole effects on energy-loss near-edge structure. *Ultramicroscopy*. 2001;86: 355–362. https://doi.org/10.1016/S0304-3991(00)00126-1

28. Luitz J., Maier M., Hebert C., Schattschneider P., Blaha P., Schwarz K., Jouffrey B. Partial core hole screening in the Cu L_3 edge. *The European Physical Journal B*. 2001;21: 363–367. https://doi.org/10.1007/s100510170179

29. Kurganskii S. I., Manyakin M. D., Dubrovskii O. I., Chuvenkova O. A., Turishchev S. Yu., Domashevskaya E. P. Theoretical and experimental study of the electronic structure of tin dioxide. *Physics of the Solid State*. 2014;56: 1748–1753. https://doi.org/10.1134/S1063783414090170

30. Scanlon D. O., Kehoe A. B., Watson G. W., ... Walsh A. Nature of the band gap and origin of the conductivity of PbO_2 revealed by theory and experiment. *Physical Review Letters*. 2011;107: 246402. https://doi.org/10.1103/PhysRevLett.107.246402

31. Koller D., Tran F., Blaha P. Merits and limits of the modified Becke-Johnson exchange potential. *Physical Review B*. 2011;83: 195134. https://doi.org/10.1103/PhysRevB.83.195134

32. Manyakin M. D., Kurganskii S. I., Dubrovskii O. I., Chuvenkova O. A., Domashevskaya E. P., Turishchev S. Yu. Ab initio calculation and synchrotron X-ray spectroscopy investigations of tin oxides near the Sn L_3 absorption edges. *Physics of the Solid State*. 2016;58: 2379–2384. https://doi.org/10.1134/S1063783416120192

Information about the authors

Maxim D. Manyakin, Cand. Sci. (Phys.–Math.), Researcher, Joint Scientific and Educational Laboratory “Atomic and Electronic Structure of Functional Materials” of Voronezh State University and the National Research Center «Kurchatov institute», Voronezh State University, (Voronezh, Russian Federation).

https://orcid.org/0000-0003-2260-6233
manyakin@phys.vsu.ru

Sergey I. Kurganskii, Dr. Sci. (Phys.-Math.), Professor of the Solid State Physics and Nanostructure Department, Voronezh State University (Voronezh, Russian Federation).

https://orcid.org/0000-0002-4202-0953
kurganskii@phys.vsu.ru

Received 22.02.2023; approved after reviewing 06.03.2023; accepted for publication 17.04.2023; published online 25.12.2023.

Translated by Yulia Dymant

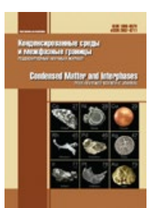

ISSN 1606-867X (Print)
ISSN 2687-0711 (Online)
Condensed Matter and Interphases
Kondensirovannye Sredy i Mezhfaznye Granitsy
https://journals.vsu.ru/kcmf/

Original articles

Brief review
https://doi.org/10.17308/kcmf.2023.25/11471

Solid wetting layer, interphase formation, and thin-film nanomaterials. Brief review

N. I. Plyusnin✉

Military Academy of Communications named after Marshal of the Soviet Union S.M. Budyonny Ministry of Defense of the Russian Federation,
3 Tikhoretsky pr., K-64, St. Petersburg, 194064, Russian Federation

Abstract

A review of the results on the formation of the interface between 3*d* metals and silicon silicides under identical conditions for various parameters of the deposited vapor, crystallographic orientation and substrate temperature is presented. A generalization of the results has been carried out, which consists of the fact that during the process of deposition of hot vapor on a colder substrate, the transition from the surface phase to the bulk phase occurs through a solid wetting layer (SWL). A classification of substrate-stabilized phases, including SWL, is proposed. It has been shown that SWL has an electronic density different from bulk phases, a smooth or nanostructured morphology, optical, electrical, and magnetic properties, and plays an important role in the formation of interfaces between bulk phases, their epitaxial films and multilayer nanostructures. These studies suggest the promise of SWL as a new nanotechnology object for the creation of thin-film nanomaterials.

The studied problem is the formation of interfaces in thin-film nanomaterials. The purpose of the article is to substantiate the discovery of nonequilibrium solid wetting layers, their uniqueness and their role in the formation of the above-mentioned interfaces. This is important research for nanomaterial technologies.

A review and generalization of the results of the study of the metal–silicon interface obtained under identical conditions was carried out. The review shows the detection a new type of transition state of the film under nonequilibrium conditions, a solid wetting layer, and the generalization justifies its role in the formation of the interface. Solid wetting layers are important as a new concept for the development of the theory of thin film growth, as well as a new object of nanotechnology for the production of thin-film nanomaterials.

Keywords: Solid wetting layers, Growth, Electronic and atomic structure, Nanomaterials, metal, Silicon

Funding: The research was carried out as part of a scientific project and with financial support from the Military Academy of Communications of the Ministry of Defense of the Russian Federation.

Acknowledgements: The experiments and basic research were carried out at the Institute of Automation and Control Processes, Far Eastern Branch of the Russian Academy of Sciences.

For citation: Plyusnin N. I. Solid wetting layer, interphase formation, and thin-film nanomaterials. Brief review. *Condensed Matter and Interphases*. 2023;25(4): 594–604. https://doi.org/10.17308/kcmf.2023.25/11471

Для цитирования: Плюснин Н. И. Твердый смачивающий слой, формирование межфазной границы и тонкопленочные наноматериалы. Краткий обзор. *Конденсированные среды и межфазные границы*. 2023;25(4): 594–604. https://doi.org/10.17308/kcmf.2023.25/11471

✉ Plyusnin Nikolay Nnokenievich, e-mail: nikolayplusnin@gmail.com
© Plyusnin N. I., 2023

The content is available under Creative Commons Attribution 4.0 License.

1. Introduction

It is known that the capillary theory of the nucleation and growth of a thin film is based on the relationship between the energy of surface tension and the "tension" energies of the interface and the bulk of the wetting layer as the parent phase. In this case, if the wetting layer is frozen to a sufficiently low temperature, then a solid-phase wetting layer (SWL) is formed, in which mass transfer is absent. In this case, the start of nucleation is provided only by the deposition of atoms on the SWL.

Moreover, since the temperature of the SWL is significantly lower than the temperature of atomic vapor, the deposition of atoms on it is accompanied by a short-term release of thermal energy, its dissipation over the surface and into the bulk, and at a certain thickness, when the stability of the SWL decreases to a critical level, activation of the transition of the SWL to a more non-bulk or bulk equilibrium state, when its electronic structure approaches the electronic structure of the bulk phase of the adsorbate [1, 2].

In this work, TSL is understood as a layer with a thickness ranging from a monolayer (MLs) to several MLs of adsorbate (equivalent by the number of atoms of MLs substrate), in which the density of atoms, their position and the type of their packaging is determined by its adaptation to the substrate under the influence of minimization of the free energy of the adsorbate-substrate system [3]. In this case, SWL is formed by spreading over the surface of the substrate or by diffusion of a layer of adsorbate atoms deposited from hot vapor and its freezing to a solid aggregate state under the influence of a colder substrate.

In the case of an adsorbate–substrate system, foreign in structure and density, such as metal–silicon, the SWL is weakly subject to the orienting influence of the substrate. The availability of the SWL for the emergence of a solid bulk phase (BP) in it when a small amount of heat appears from the outside is limited by a critical thickness d^*, determined by the interatomic interaction forces ("tension") in the film, on its surface and at the interface between the film and the substrate. In this case, the d^* value is determined by the minimum free energy of the system. The near thickness d^* atoms in the SWL acquire a three-dimensional environment, and the forces of collective interaction of their outer electrons begin to dominate. These forces destabilize the SWL, and it becomes ready for the transition into BP depending on the amount of heat released during the deposition of the adsorbate on the surface. With a small amount of heat d^* may be more than 3 MLs. At the same time, when there is conjugation of the adsorbate and substrate lattices, the SWL can be ordered, which further stabilizes the SWL and delays its transition into BP. For example, at the Cr-Si(111) interface, where mixing occurs at moderate deposition or annealing temperatures, an epitaxially oriented and ordered silicide SWL is formed. This occurs due to the fact that in this system the silicides have a small mismatch with the silicon lattice and grow epitaxially on it [4, 5].

In the literature, there is no concept of SWL as a frozen wetting layer formed at the vapor-substrate interface, especially in such a non-isostructural solid-state adsorbate-substrate system as metal-silicon. Only recently information on the SWL of water (ice) on a nanotube, in which freezing occurs at room temperature due to interaction forces with a solid substrate appeared [6]. However, there is a lot of information on pseudomorphic solid layers on a crystal. In particular, we can mention the foreign study of Ge on silicon [7] and the work of domestic authors on Ge on Si(111) and Si(001) [8–10].

The SWL was actually mentioned as an atomic-like [1, 2], surface [11], thin-film [12–14] phase (nanophase) and as a nanophase wetting layer [15–17] for the transitional 3*d* metal – silicon system (see also [18–24]). At the same time, the concept of SWL as a frozen layer formed from hot vapor introduced here most accurately reflects the nature of this layer and the method of its production.

This article substantiates and carries out a classification of solid phases stabilized by a substrate, including SWL as a phase distinct from submonolayer surface phases. The analysis of the results on SWL in the Cr, Co, Fe, Cu-Si(111), and Si(001) systems is provided. For these systems, the similarity of the obtained SWL according to features of their atomic and electronic structure, morphology and the mechanism of their transition to bulk phases is shown.

2. Classification of phases stabilized by a substrate

An important role in the development of the physics of interphases belongs to the concept of

solid surface phases (SP) as "two-dimensional layers in thermodynamic equilibrium with the bulk of the substrate" [11] or phases that have come into thermal equilibrium at the vapor-solid interface with the volume of the substrate heated to a certain temperature. SP usually considered as pseudo-equilibrium surface (with the thickness less than MLs) layers, formed during the deposition of the adsorbate and its diffusion over the surface of the substrate at a temperature below the threshold of desorption and melting of the adsorbate. Moreover, "surface phase transitions involve changes in the arrangement of atoms in the outermost layers of the solid, but not in the atoms inside the bulk of the material" [26]. Taking this into account, SP diagrams are plotted in the coordinates "temperature – thickness or surface concentration" (see, for example, [27, 28]). However, in nature there are other solid phases stabilized by a substrate. They are less stable and form at lower temperatures, but they usually reach a higher thickness. These phases were not considered, since the problem of structural identification of such phases as non-bulk phases had not previously been solved. Usually they were considered as bulk-like phases or some kind of "interface" compounds of small thickness. At the same time, there was essentially no classification of them, which made it difficult to understand the nature of these phases and their identification.

Let us consider the classification of solid phases stabilized by a substrate (films of massive or bulk phases, including metastable bulk phases, are not considered). Let us first turn to the surface phases.

The phases of "something" as separate parts of the entire system, are a thermodynamic concept, and their appearance is determined by the state in which this "something", together with the entire system, is characterized by minimum of free energy. It is generally accepted that surface phases are two-dimensional layers with a number of atoms per unit area of less than one ML, stabilized by the substrate, i.e., adapted to it in accordance with the minimum free energy.

It is known, that interatomic interaction at the thin film–substrate interface depends on the distance between the atoms on it and the type of their electronic shells. Therefore, if we do not consider the degree of hybridization of their electronic shells (associated with chemical interaction with the substrate), then the phases (non-bulk) stabilized by the substrate can be arranged according to the strength of interatomic interaction (from weak to strong), or according to the degree of their proximity to surfaces, or according to the depth of their immersion into the surface.

From this point of view, we can distinguish (Fig. 1) types of solid phases stabilized by a substrate with a thickness less than MLs or electron screening lengths – surface phases, and phases with a thickness higher than MLs – wetting layers. Among the surface phases the following phases can be distinguished: 1) phases with weak interaction – the surface phase, 2) phases with physical interaction – physisorbed phase, 3) phases with chemical interaction – chemadsorbed phase, 4) phases

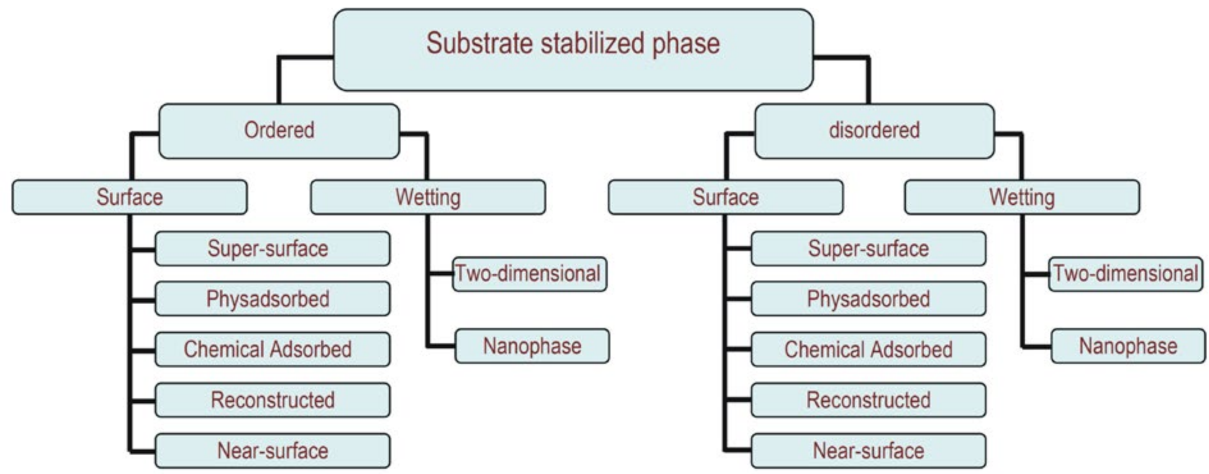

Fig. 1. Classification of phases stabilized by substrate

with rearrangement of the substrate surface – reconstructed phase and 5) phases with its own non-bulk structure – near-surface phase (compound). Moreover, with an increase in the strength of interatomic interaction with the substrate in these surface phases, the temperature of their existence increases.

Phases stabilized by the substrate, related to SWL with a number of atoms equal to or greater than MLs (up to several MLs) can be divided into two classes: 1) SWL in which there is no three-dimensional environment of atoms – two-dimensional (2D-SWL) and 2) SWL in which there is three-dimensional environment of atoms (3D-SWL). The 3D environment appears within a certain two-dimensional ensemble of clusters (domains). We will also call the second type of SWL nanophase SWL (using a similar name for BP, consisting of nanograins).

In addition, the division of all phases stabilized by the substrate into types reflects their degree of order: 1) disordered (or frozen) and 2) ordered (pseudo-equilibrium). The corresponding classification scheme is shown in Fig. 1.

3. Analysis and generalization of results

The discovery of metal SWL started in 1984 with the discovery of non-bulk ("atomically-like") electron density in thin (with the thickness of ~4–6 Å) Cr films deposited almost simultaneously and equally on Si(111) and SiO_X at room temperature. In this case, the composition and thickness of the films were determined using Auger electron spectroscopy - AES, and their electron density was determined using characteristic electron energy loss spectroscopy – EELS [1, 2]. Later, attention was drawn to the fact that the composition of the films in these studies was close to pure Cr due to the very fast (high deposition rate) spraying of Cr.

The review provided in [2] showed that the transition from the SWL ("atomic-like" phase) of pure metal (Cr and Pd) to bulk metal silicide occurs at approximately the same thickness as the transition of this SWL to the bulk metal on a non-reactive substrate (SiO_x, – in the case of Cr, and ZnO, – in the case of Pd). This indicated that a possible reason for readiness of SWL to transition into BP silicide is the appearance of a collective valence band in the metal film.

By that time, it was believed that the transition metal «mixed» with the silicon substrate («mixed» in this case indicated diffusion activated by a chemical reaction at the interface) and formed a silicide. The vapor deposition rate and other vapor parameters (temperature, kinetic energy) were not taken into account. Thus, in an earlier study, during annealing of Cr film on Si(111), obtained with a low deposition rate, a transition to the $\sqrt{3}\times\sqrt{3}$ surface structure and the transition of this structure to epitaxial $CrSi_2$ was discovered [11]. The composition and atomic density of the $\sqrt{3}\times\sqrt{3}$ structure were not known at that time, but the incorrect assumption that the nucleation of $CrSi_2$ occurs from bulk CrSi formed as a result of "mixing" was made.

The recognition of the discovery of SWL required that the detected phase: 1) did not have the properties of a bulk phase (at least according to electron density), 2) had simultaneously identified composition and density, 3) was structurally adapted to the substrate (at least in terms of atomic density), 4) behave as a nonequilibrium phase (frozen layer) and had a composition dependence on the kinetics (deposition rate) and energy (temperature and kinetic energy of vapor) of deposition.

Therefore, in order to obtain evidence of the existence of SWL, studies in the Cr–Si(111) system were continued, but these studies were conducted under stable and identical deposition conditions in one chamber at low rate (an original effusion cell was manufactured for this purpose – see [29]), as well as at different substrate temperatures and vapor parameters.

Unfortunately, the choice of a low deposition rate at high vapor temperatures led to silicide formation and then complicated the task of identification of phases as SWL based on electron density. However, Cr layers mixed with Si were discovered both at room temperature (frozen – amorphously like) and during annealing (ordered into various structures), and the influence of these mixed phases on the growth of silicides and their type was discovered [29 , 30, 31]. In addition, using the results of [11, 29-31], an ordered 2D phase $\sqrt{3}\times\sqrt{3}$ was grown, and conductivity and its temperature dependence were measured [32]. The specific conductivity of this phase increased exponentially with temperature and at 300 K it was

more than 4 times higher than that of bulk CrSi. Although this finding was not discussed in [32], in [33] it was noted that this fact cannot be explained within the framework of existing theories of the metal-insulator transition and localization.

Subsequently, systematic studies showed the role of the SWL of the metal and silicide in the formation of Cr and $CrSi_2$ on Si(111) [34], as well as the role of various types of SWL silicide in the epitaxy of the $CrSi_2$ seed layer-template of different orientations [29, 35]. In subsequent studies [13, 36], the analysis of the 2D-SWL 1×1-Cr and α-√3×√3-Cr crystal structure and 3D-SWL β-√3×√3-Cr_XSi(X = 0.6-1), as well as their thickness using the dependences of EELS on the energy of the primary beam was made. The absence of the Si(111) framework in the 3D-SWL β-√3×√3-Cr_xSi was proven and its thickness, which reached 9 MLs was determined. It was proven that its electron density is significantly lower than in epitaxial CrSi, to which this phase was unprovenly assigned [37], and even lower than in $CrSi_2$ (see Fig. 2c). All this showed the non-bulk structure of the studied SWL and their difference from bulk

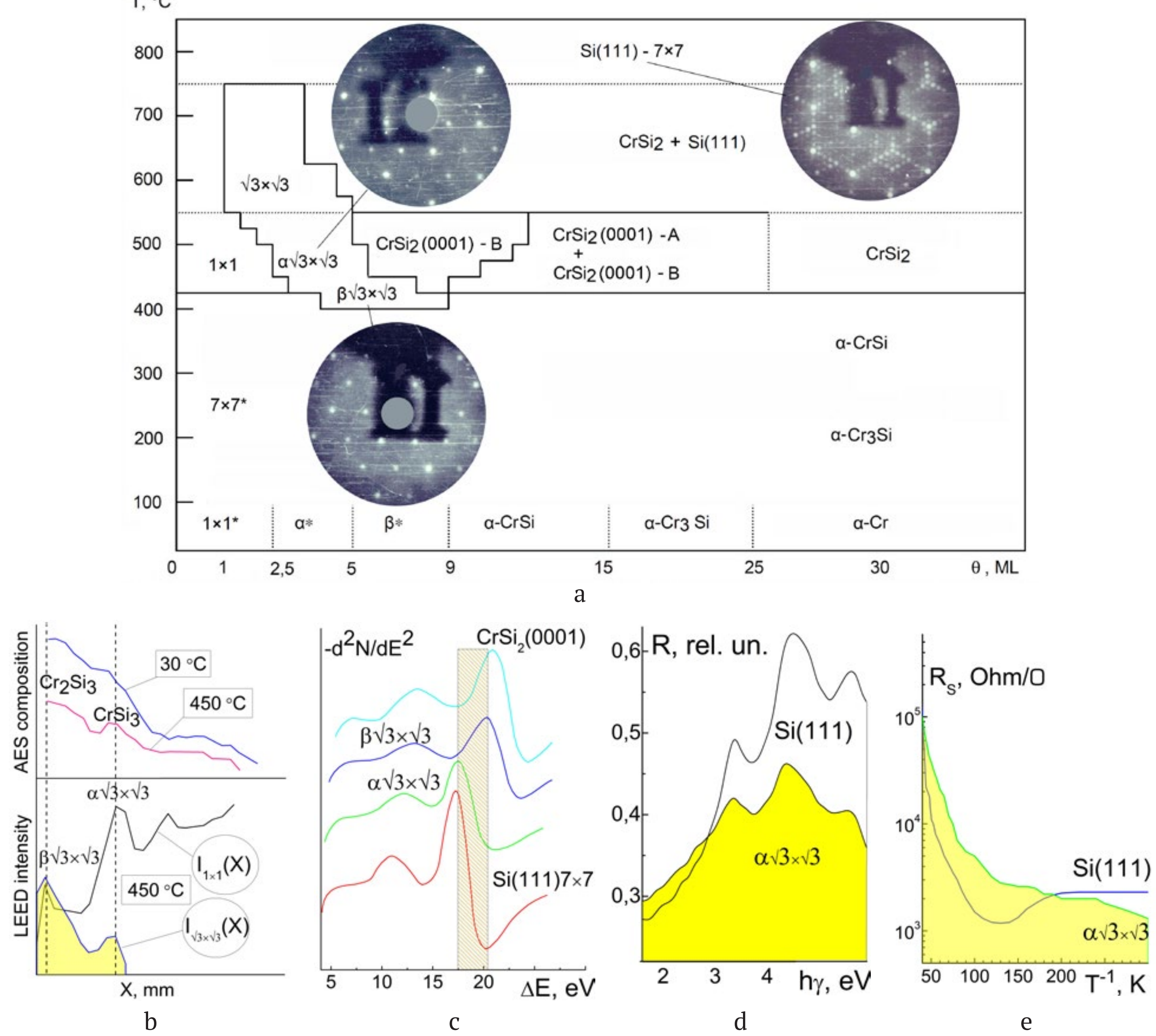

Fig. 2. Data on ordered TCC α-√3×√3 and β-√3×√3 in the Cr - Si(111) system: (a) regions of their formation on the phase diagram with LEED pictures; (b) AES Cr concentration (top) and LEED reflex intensity (bottom); (c) loss intensity in EELS; (d) reflection coefficient and (e) layer resistance, respectively, depending on: thickness and temperature (a), coordinates of the film with a monotonically decreasing thickness (b), electron loss energy (c), energy of light quanta (d) and temperature (d)

phases, as well as the fact that the thickness of the 3D-SWL can reach 9 MLs.

The final discovery of the ordered SWL β-√3×√3–Cr_xSi was comprehensively substantiated in studies [13, 29–31, 35, 36]. An entire paragraph was dedicated to it in the study [13] (pp. 244–248 – "5.2. Thin-film phase β-√3×√3–Cr on Si(111) and its transition to CrSi during layered growth and annealing"). Data from AES, EELS, low energy electron diffraction (LEED), transmission microscopy (TEM) and microdiffraction (TMD) showed that before and during the transition to the bulk phase, at d = 9 Å, non-monotone-stepped changes of following parameters occur with increasing film thickness: 1) width, intensity, and energy position of AES, EELS peaks, 2) width and intensity of LEED reflections, and 3) morphology on TEM images. This is illustrated by the diagram in Fig. 2a [35].

As can be seen from Fig. 2a–c, SWL differ from each other and from bulk phases by structure (a, b), composition (b), electronic and, accordingly, atomic density (c). In addition, 2D-SWL with the α-√3×√3 structure has anomalously high IR reflectance (Fig. 2d) and conductivity at room temperature (Fig. 2e).

Subsequently, the kinetic mechanisms (taking into account the deposition rate) of Si growth on $CrSi_2$(0001) as well as Cr and Co growth on Si(111) were studied experimentally and theoretically [13]. The concepts of SWL developed for metal on silicon were extended to silicon on silicide. Results obtained on 2D-SWL of silicon on single-crystal $CrSi_2$ are still unique and open up new possible prospects for nanoelectronics.

Under other growth conditions and in other systems, Cr, Co, and Si SWL new at that time were discovered [13, 14, 34, 37, 38]. In the Co – Si(111) system [38], where Co deposition was carried out at room temperature of the substrate with a high vapor temperature and low deposition rate, mixing of Co with Si(111), depending on the deposition rate, and two types of Co_xSi SWL were discovered: at 1–2 MLs (2D-SWL) and 3 (3D-SWL) MLs. In addition, a transition from 3D-SWL to $CoSi_2$ was discovered at a thickness of 4 MLs, and from it, to CoSi and from CoSi to Co_2Si at thicknesses of: 6–11 MLs and 13–30 MLs respectively. It was found that a high heating temperature of the W-helix of the Co source leads to agglomeration of the first phase after 3D-SWL ($CoSi_2$).

In the Cr – Si(111) system at room temperature of the substrate, the growth of Cr was studied at different deposition rates and Cr vapor temperatures [37]. For the first time, the formation of 3D-SWL of pure Cr at a thickness of 3 Å and then the transition to Cr islands with a layer of 3D-SWL of Cr between them was discovered and proven. In this Cr SWL, a very low resistivity was found – 9–18 μΩ cm at concentration of a metallic carrier of p-type – $(0.9–1.8)\cdot10^{22}$ cm^{-3} and high mobility for metal – 38 $V/cm^2\cdot sec$. In addition, epitaxial growth of ultra-thin (Cr thickness of 6 Å) and continuous $CrSi_2$ films of A-type during pulsed deposition of Cr with simultaneous pulsed heating of the substrate was performed [14].

The resulting $CrSi_2$ films of A-type had high conductivity – 180–360 μOhm·cm with high carrier concentration and mobility, respectively $(0.5\text{-}1.0)\cdot10^{20}$ cm^{-3} and 480 $V/cm^2\cdot sec$. This shows that such films, in terms of their parameters, are of interest as a silicide channel of a silicon spin transistor, regardless of whether these parameters relate to the $CrSi_2$ film or to the Si substrate layer adjacent to it.

Moreover, by lowering the temperature of Cr and Co vapor and the time of its pulsed deposition, their pseudo layered growth on Si(111) was carried out, and it was found that Cr 3D-SWL with a thickness of 3.3 A has a conductivity significantly higher than conductivity of bulk Cr [14]. In addition, it was shown that all the films obtained are characterized by conductivity anisotropy, which is most likely associated with equally-directed steps on the surface of the substrates.

As a result, a technology for growing SWL of metal on silicon was developed: with a low vapor temperature, a high deposition rate in one small portion, and a low average deposition rate during repeated deposition in small portions. Subsequently, this technology was protected by a number of patents according to methods for producing thin films, nanomaterials, metamaterials, and dispersed particles - see [39]. Using the developed technology, a pseudo layer-by-layer growth of super smooth Co layers on silicon was obtained up to a thickness of 28 Å [34]. In Co 2D-SWL with a thickness of 1–2 Å, a resistance minimum was discovered, which correlates with a

change in the concentration of valence electrons in the Si boundary layer. The reliability of the results of this experiment is beyond doubt, since in it, as in the experiments [14, 37], a joint AES-EELS analysis at the same probing depth comparable to the SWL thickness of 3 MLs was used [13]. Subsequently, similar properties of SWL as non-bulk 2D and 3D phases and their transition to the bulk phase were found in other systems: Fe and Cu – Si(111)/Si(001) [12, 40, 41]. Experimental evidence of the nature of SWL for other metals, under other conditions and on different orientations of the substrate makes the discovery of SWL in 3*d* metal-silicon system complete.

The morphology (a–d) and properties (e–g) of a smooth (relief height 0.2–0.3 nm) SWL Fe (1.2–6 nm) and fairly smooth (relief height 1.2 nm) Fe nanofilm (thickness 12 nm) is shown in Fig. 3: IR transmittance (e), reflectance spectra (f) and magnetization curves - MOKE (g). Anomalous properties of Fe 2D-SWL were discovered: high IR reflectance (Figs. 3e and 3f), strong quenching (due to absorption and reflection) of UV reflection (Fig. 3e) and a high degree of superparamagnetism (Fig. 3g). Obviously, these properties are mainly due to the nanostructured silicon interfacial layer under the 2D-SWL. They characterize the structure of the 2D-SWL Fe – Si(001) substrate system.

Overall, the results obtained clarify the role of deposition kinetics and energetics in the formation of SWL. In addition, they allow to develop phenomenological models of both the growth process and the structure of the SWL [23, 24]. Further research will reveal the possible applications of SWL more completely. Dendritic, a currently relevant application is the formation of epitaxial nanofilms of iron and its silicides from SWL Fe. The possibilities of such application are discussed in [17]. It demonstrates the formation of an intermediate $FeSi_2$ layer from annealed SWL and subsequent growth of a layered (stratified) film of $Fe/Fe_3Si/FeSi_2$ composition. It was noted that the results obtained can be used for the development of epitaxy methods of ultrathin $FeSi_2$, FeSi, and Fe films on Si(001).

In accordance with established ideas, freezing of the wetting layer occurs at room temperature of the substrate, which is significantly lower than the melting point of the adsorbate and the temperature (for the metals under consideration 1100 K and higher) of its vapor phase from which it is deposited. In this case, the SWL has a thickness from one to several MLs and stable

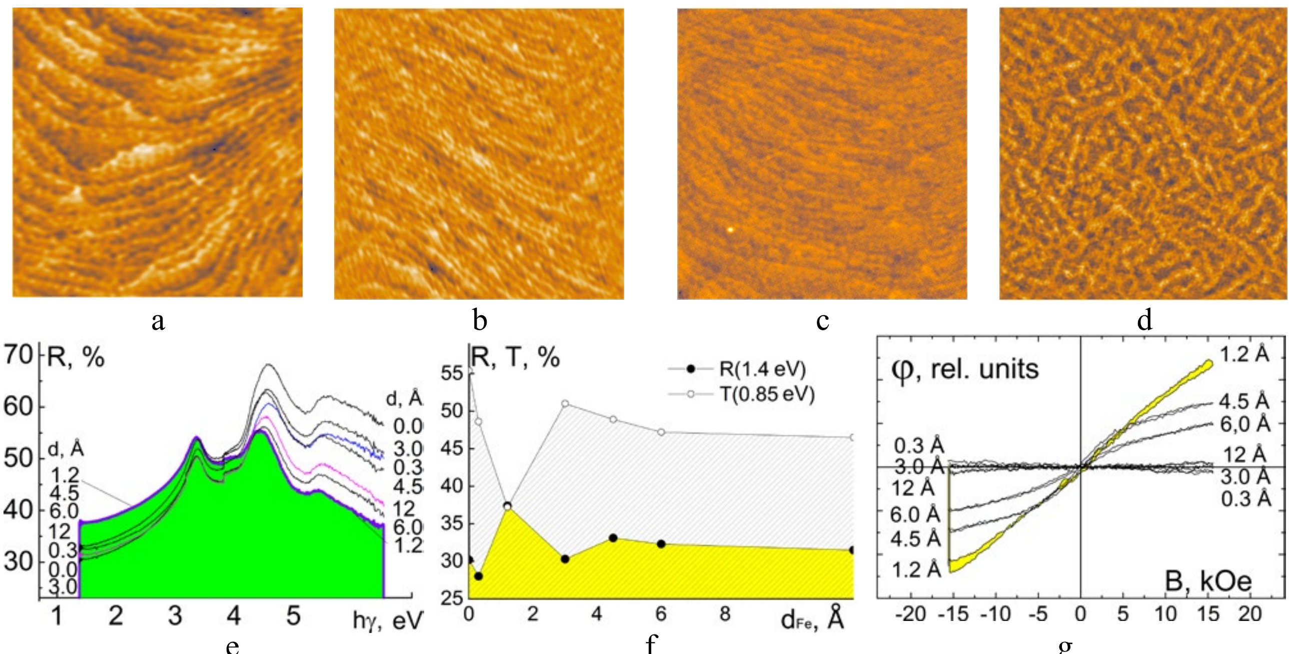

Fig. 3. Surface morphology on AFM images – 2×2 μm (a – Si(100); b – 2D-TCC Fe 1.5 ML; c – 3D-TCC Fe_3Si 7.5 ML; d – Fe 15 ML) and properties of TCC Fe 3–7.5 ML and Fe nanofilms 12 ML after annealing at 250 °C (e – IR transmission, f – reflection spectra and g – magnetization curves according to MOKE)

up to critical thickness d^*, the value of which is determined by the force of the influence of the substrate on the SWL, as well as the temperatures of its formation and freezing.

At $d > d^*$ in 3D-SWL there is an LD-3D transition from a low-dimensional (LD) state to a volumetric (3D) state [31]. Moreover, with severe freezing (in the limit at a temperature of – 0 K), the LD-3D transition begins when the first atom (or layer of atoms) appears in the 3D-SWL, which has a 3D environment and is shielded by neighboring atoms from influence of both the substrate and vacuum. It is known that d^* = 3 MLs for close-packed atoms is close to 3 Fermi screening radii [31] and is confirmed theoretically and experimentally [10]. However, with weak freezing, the SWL can also have a higher thickness due to the possibility of epitaxial ordering, which increases its interaction with the substrate and stability.

Subsequently, the discovery of SWL in various systems was supported by phenomenological models [23, 24]. According to these models, the methods of mutual adaptation of SWL structure and the substrate can be different. The SWL and the substrate can be adapted to each other not only due to elastic stresses and lattice deformations, but also due to the presence of interstitial atoms, defects and/or vacancies. In addition, with sufficiently strong freezing and proximity to the critical thickness (3D-SWL), this adaptation can be carried out by dividing the SWL into clusters (domains), and the boundary layer of the substrate into antiphase domains, resulting in the formation of SWL with a nanophase (two-dimensional-cluster) structure. It is also possible to adapt the SWL structure to the substrate due to the segregation of substrate atoms on the SWL surface.

The metal in SWL, despite the absolute mismatch of its lattice parameter with the lattice of the semiconductor (which can differ by more than 1.5 times), is well adapted in structure to the substrate both due to its nanophase structure and due to the structural-phase rearrangement of the boundary layer of the substrate [24, 25]. In contrast, the known pseudomorphic adsorbate layer on a substrate, which has a small (<5%) mismatch of crystal lattice parameters with the substrate, is adapted to the substrate only due to elastic deformations and mismatch dislocations. At the same time, it does not rebuild the substrate and retains its properties. Therefore, the nanophase 3D-SWL of a metal on a semiconductor with structural rearrangement of the boundary layer of the substrate is an exclusively new object in the physics of thin films.

At the same time, the adaptation of 3D-SWL to the substrate weakens with increasing its thickness, and after a critical thickness an LD-3D transition occurs, during which certain metastable and stable 3D phases are formed in it in the form of film grains or its islands consisting of 3D phases.

Thus, SWL plays an important role in the processes of growth of thin films from gas, vapor, or liquid phases. Its presence or absence, its tense state, as well as the release of latent energy in it changes the film growth mechanism according to one out of three options: 1) layer-by-layer (Frank Van Der Merwe growth), 2) layer-island (Stranski-Krastanov growth) and 3) island (Vollmer–Weber growth). In the case of Stranski–Krastanov growth, the released energy from the SWL can determine the size, density, composition and structure of the islands. In this case, at the interface between the film and the substrate, reactive-activated diffusion (activated by the release of latent energy) is possible, followed by the freezing of the diffusion layer (the so-called “mixing”).

SWL is characterized by a significant amount of latent stress energy. The use of this energy during the LD-3D transition to a film of subnanoscale or nanoscale thickness allows to control the structure of this film, its morphology, topography, and physical properties [42]. Due to this, continuous and relatively smooth films of metals and silicides of extremely small thickness with record conductive and other properties can be obtained on a semiconductor or dielectric substrate.

Thus, SWL Fe, as well as nanofilms of Fe, Cu, and Co silicide with a thickness (respectively 1.2 MLs, 12 MLs; 14 MLs and 28 MLs.) and average relief height (respectively 0.2, 0.5, 0.9 and 0.7 nm) were obtained [42, 23]. In the Fe film on Si(001), Fe 2D and 3D-SWL with different properties at different thicknesses were discovered [12, 40]: at 2 MLs – with a smooth 2D structure and at 3 MLs – with a nanophase structure. The unique

properties of the listed films were revealed. Thus, Fe 2D-SWL on Si(001) with a thickness of 2 MLs had anomalously high IR reflection and UV light scattering, associated with the restructuring of the boundary layer of the silicon substrate, as well as a high degree of superparamagnetism with almost zero coercivity [42]. The same 2D-SWL turned out to be stable to oxidation at room temperature in air and stable up to a temperature of 500 °C in vacuum.

Atomic-force microscope imaging studies have shown that Fe 2D-SWL follows the relief of the substrate surface steps [12]. The presence of these steps, which appear in the image as a set of parallel curved stripes, indicates the adaptation of Fe 2D-SWL to the substrate in structure and relief. With a higher thickness of Fe, when the height of the Fe film relief reaches 0.5–0.9 nm, a Fe 3D-SWL is formed, which in structure and relief does not adapt to the substrate and therefore hides its stepped relief. With a further increase in thickness, segregation of Si, nanograins of Fe film, and its roughness form a completely new film surface relief.

For the production of SWL of metals on silicon, a special belt source of metal with oversputtering was developed [13, 38]. This source due to the higher area and small distance to the substrate, expanded the range of deposition rates towards its increase, as well as the range of temperature and kinetic energy of the vapor towards it decrease. At the Advanced Institute for Materials Research of Tohoku University (Japan), this source was used for the epitaxy of single-crystal Ir and Pt films as substrates for diamond films (see joint articles with Professor S. Kono for 2005–2007 [43]).

The use of a similar source for Cu deposition at low temperature and kinetic energy of vapor allowed obtaining record-breaking thin continuous SWL Cu_2Si [41]. Moreover, in these SWL, using an atomic-force microscope, a nanosquare was drawn as a product of a probe pressure-activated chemical reaction of mixing the SWL with air and the lower layers of silicon [15]. This effect demonstrated the feasibility of using SWL for direct maskless nanolithography.

In recent years, during deposition from a developed source, SWL and multilayer nanostructures with nanofilms of ferromagnetic (Fe, Co) metal and two-dimensional layers (1–5 MLs) of non-magnetic metal (Cu) on silicon have been grown [16]. These nanostructures showed unique magnetic properties and their applicability as the drain and source of a silicon spin-field transistor. Indeed, an important stage in the creation of spin transistors is the formation of electrical and spin contacts based on ultrathin conducting and ferromagnetic layers, as well as multilayer nanofilms of ferromagnetic and non-magnetic metals. The lateral size of these contacts can reach 22 nm or less, and their nanolithography will require a proportional reduction in their thickness to nanometers and their interface to subnanometers. The use of SWL metal as a mother phase with latent energy for the formation of these silicide contacts, as well as nanolithography, will solve this problem.

4. Conclusions

A review and generalization of the results of studying the metal–silicon interface obtained under identical conditions was performed. The discovery of a new, general type of transition state of the coating - a solid wetting layer, which is formed under nonequilibrium conditions and which plays a key role in the formation of the interface was substantiated. Solid wetting layers are important as a new concept for the development of thin film growth theory, as well as a new nanotechnology object for the production of thin film nanomaterials.

Conflict of interests

The author declares that they has no known competing financial interests or personal relationships that could have influenced the work reported in this paper.

References

1. Lifshits V. G., Plyusnin N. I. Electronic interaction and silicide formation in the Cr-Si(111) system at the initial stage of growth*. *Physics, Chemistry and Mechanics of Surfaces*. 1984;9: 78–85. (In Russ.)

2. Lifshits V. G., Plyusnin N. I. Electronic structure and silicide formation in thin films of transition metals on silicon. *Preprint of IAPU FESC AS USSR*. 1984;18(127): 1–35. (In Russ.)

3. Plyusnin N. I. Solid-phase wetting layer. Great Russian Encyclopedia*. (Ed. Kostyuk A.V.). 2023. (In Russ.)

4. Fathauer R. W., Grunthaner P. J., Lin T. L., Chang K. T., Mazur J. H., Jamieson D. N. Molecular-

beam epitaxy of $CrSi_2$ on Si (111). *Journal of Vacuum Science & Technology B: Microelectronics Processing and Phenomena*. 1988;6(2): 708–712. https://doi.org/10.1116/1.584352

5. Wetzel P., Pirri C., Peruchetti J. C., Bolmont D., Gewinner G. Epitaxial growth of CrSi and $CrSi_2$ on Si (111). *Physical Review B*. 1988;65,10: 1217–1220. https://doi.org/10.1103/physrevb.35.5880

6. Feibelman P. J. The first wetting layer on a solid. *Physics Today*. 2010;63(2): 34. https://doi.org/10.1063/1.3326987

7. Voigtländer B. Fundamental processes in Si/Si and Ge/Si epitaxy studied by scanning tunneling microscopy during growth. *Surface Science Reports*. 2001;43(5-8): 127–254. https://doi.org/10.1016/s0167-5729(01)00012-7

8. Osipov A. V., Kukushkin S. A., Schmitt F., Hess P. Kinetic model of coherent island formation in the case of self-limiting growth. *Physical Review B*. 2001;64(20): 205421. https://doi.org/10.1103/physrevb.64.205421

9. Osipov, A. V., Kukushkin, S. A., Schmitt, F., Hess, P. Stress-driven nucleation of coherent islands: theory and experiment. *Applied Surface Science*. 2002;188(1-2): 156–162. https://doi.org/10.1016/s0169-4332(01)00727-9

10. Kukushkin S. A., Osipov A. V., Schmitt F., Hess P. The nucleation of coherent semiconductor islands during the Stranski–Krastanov growth induced by elastic strains. *Semiconductors*. 2002;36(10): 1097–1105. https://doi.org/10.1134/1.1513851

11. Lifshits V. G., Akilov V. B., Churusov B. K., Gavriljuk Y. L. The role of surface phases in processes on silicon surfaces. *Surface Science*. 1999;222(1): 21–30. https://doi.org/10.1016/0039-6028(89)90331-2

12. Plusnin N. I. Metal thin-film nanophases and their interface with silicon. *Journal of Physics: Conference Series*. 2008;100(5): 052094. https://doi.org/10.1088/1742-6596/100/5/052094

13. Plyusnin, N. I. *Substrate-stabilized phases and processes of interface formation in heterostructures based on transition 3d metal (Cr, Co) and silicon*. Dissertation for the degree of Doctor of Physical and Mathematical Sciences. Vladivostok: 2000. 376 p. (In Russ.) Available at: https://www.dissercat.com/content/fazy-stabilizirovannye-podlozhkoi-i-protsessy-formirovaniya-granitsy-razdela-v-geterostruktu

14. Plusnin N. I., Il'yashenko V. M., Milenin A. P. The growth and conductivity of transition metal nanolayers on silicon. *Physics of Low-Dimensional Structures*. 2002;11: 39–48. Режим доступа: https://elibrary.ru/item.asp?id=13410873

15. Plusnin N. I., Il'yashenko V. M., Milenin A. P. Atomic-force microscopy probe-activated morphological transformations in a nanophase copper wetting layer on silicon. *Technical Physics Letters*. 2018;44: 187–190. https://doi.org/10.1134/S1063785018030094

16. Plyusnin N. I., Usachev P. A., Pavlov, V. V. Effect of thickness and annealing of the Si (001) 2×1-Cu wetting layer on the morphology of layered nanofilms based on Fe, Co, and Cu and their ferromagnetic properties. *St. Petersburg Polytechnic University Journal. Physics and Mathematics*, 2022;15(3.1): 131–136. https://doi.org/10.18721/JPM.153.122

17. Plyusnin N. I. Stratification of the Fe/Si(001)2×1 interface by heat treatment of the wetting layer. *Technical Physics*. 2023;68(1): 146–150. https://doi.org/10.21883/TP.2023.01.55449.191-22

18. Pliusnin N. Subnanophase coatings as new type low-dimensional nanomaterials: Ultra-high-vacuum synthesis, properties and application. *Characterization and Application of Nanomaterials*. 2020;3(2): 81–86. https://doi.org/10.24294/can.v3i2.1069

19. Plusnin N. I. Atomic-scale AES-EELS analysis of structure-phase state and growth mechanism of layered nanostructures. *Advances in Materials Physics and Chemistry*. 2016;6(7): 195–210. https://doi.org/10.4236/ampc.2016.67020

20. Plusnin N. I. Atomic-scale control of molecular-beam growth of nanolayers. In: *Comprehensive guide for nanocoatings technology volume 2. Characterization and reliability*. New York: Nova Publisher; 2015. pp. 87–102. Available at: https://www.researchgate.net/publication/285582252

21. Plyusnin N. I. Atomic-scale control of molecular-beam growth of thin-film nanohetero structures. *Vestnik of Far Eastern Branch of Russian Academy of Sciences*. 2010(5): 26–34. (In Russ, abstract in Eng.). Available at: https://elibrary.ru/item.asp?id=17667265

22. Plusnin, N. From atomic-scale interfaces – To new nanomaterials. *Characterization and Application of Nanomaterials*. 2019;.2(2): 54–59. https://doi.org/10.24294/can.v2i2.835

23. Plyusnin, N. I. Formation of a Nanophase Wetting Layer and Metal Growth on a Semiconductor. *Technical Physics Letters*. 2018;44: 980–983. https://doi.org/10.1134/S1063785018110123

24. Plyusnin, N. I. Phenomenological models of nucleation and growth of metal on a semiconductor. *Physics of the Solid State*. 2019;61: 2431–2433. https://doi.org/10.1134/S1063783419120394

25. Maslov A. M., Plusnin N. I. Evolution of optical spectra at the initial stages of Fe growth on Si (001). *Defect and Diffusion Forum. Trans Tech Publications*. 2018;386: 15–20. https://doi.org/10.4028/www.scientific.net/ddf.386.15

26. Hannon J. B., Hibino H., Bartelt N. C., Swartzentruber B. S., Ogino T., Kellogg G. L. Dynamics of the silicon (111) surface phase transition. *Nature*. 2000;405(6786): 552–554. https://doi.org/10.1038/35014569

27. Lifshits V. G., Saranin A. A., Zotov A. V. *Surface phases on silicon: preparation, structures and properties*.

Chichester – New York-Brisbane – Toronto – Singapore: John Wiley & Sons. 1994. 448 p. Режим доступа: https://ci.nii.ac.jp/ncid/BA24106371

28. Lifshits V. G., Churusov B. K., Gavrilyuk Y. L., ... Tsukanov D. A. Surface phases and nanostructures on silicon surface. *Journal of Structural Chemistry*. 2004;45: S36–S59. https://doi.org/10.1007/s10947-006-0094-1

29. Plyusnin N. I. *Surface phases and the formation of the interface between Cr and $CrSi_2$ with single-crystalline silicon*. Dissertation for the degree of candidate of physical and mathematical sciences*. Vladivostok: 1986. 199 p. (In Russ.) Available at: https://search.rsl.ru/ru/record/01008595279

30. Plyusnin N. I. Growth and mixing processes activated by the reaction at the interface in the transition metal-silicon system. In: *Processes of heat and mass transfer and growth of single crystals and thin-film structures**: Proceedings of the Second Russian Symposium HT&CG'97 (22–24 September 1997), ed. V. P. Ginkina. Obninsk: 1998. pp. 303-309. (In Russ.). Available at: https://search.rsl.ru/ru/record/01000599767

31. Plyusnin N. I. Low-dimensional phases and the formation of nanoheterostructures in the transition 3D-metal-silicon system. *Surface. X-ray, synchrotron and neutron studies**. 2005;1: 17–27. (In Russ.) Available at: https://elibrary.ru/item.asp?id=9139519.

32. Grazhulis, V. A., Bondarev, V. V., ...Plusnin N. I. Electron transport in the Si (111)-Cr (√3×√3) °-αSi surface phase and in epitaxial films of CrSi, $CrSi_2$ on Si (111). *Surface Science*. 1993;292(3): 298–304. https://doi.org/10.1016/0039-6028(93)90335-H

33. Bondarev V. V. *Study of electronic transport properties of surface phases of In and Cr on Si(111)*. Abstract of the dissertation for the scientific degree of candidate of physical and mathematical sciences*. Chernogolovka: 1993. 17 p. (In Russ.) Available at: https://search.rsl.ru/ru/record/01000244435

34. Plusnin N. I., Il'yashenko V. M., Kitan S. A., Krylov S. V. Formation of Co ultrathin films on Si(111): Growth mechanisms, electronic structure and transport. *Applied Surface Science*. 2007;253(17): 7225–7229. https://doi.org/10.1016/j.apsusc.2007.03.001

35. Plusnin N. I., Galkin N. G., Lifshits V. G., Lobachev S. A. Formation of interfaces and templates in the Si (111)-Cr system. *Surface Review and Letters*. 1995;2(04): 439–449. https://doi.org/10.1142/s0218625x9500039x

36. Plusnin N. I., Soldatov V. Y., Milenin A. P. EELS peak intensity dependence on primary electron energy for the Si (111) 7×7 and Si (111)-Cr surface structures. *Surface Science*. 1999;426(1): 38–47. https://doi.org/10.1016/S0039-6028(99)00182-X

37. Plusnin N. I. Milenin A. P., Iliyashenko B. M., Lifshits V. G. Elevated rate growth of nanolayers of Cr and $CrSi_2$ on Si(111). *Physics of Low-Dimensional Structures*. 2002;9: 129–146. Режим доступа: https://elibrary.ru/item.asp?id=13398089

38. Plusnin N. I. Milenin A. P., Prihod'ko D. P. Formation of the Co/Si (111) 7×7 interface: AES-and EELS-study. *Applied Surface Science*. 2000;166(1-4): 125–129. https://doi.org/10.1016/s0169-4332(00)00393-7

39. Plyusnin N. I. *Method for formation an ultra thin film*. Patent RF No. 2011146799A. Publ. 27.05.2013, bull. No. 15. Available at: https://patents.google.com/patent/RU2011146799A/en?inventor=Николай+Иннокентьевич+Плюснин

40. Plyusnin N. I., Il'yashchenko V. M., Kitan' S. A., Krylov, S. V. Formation, electronic structure, and stability of film nanophases of transition metals on silicon. *Journal of Surface Investigation. X-Ray, Synchrotron and Neutron Techniques*. 2009;3: 734–746. https://doi.org/10.1134/S1027451009050139

41. Plyusnin N. I. and others. Structural and phase transformations during initial stages of copper condensation on Si(001). *Journal of Surface Investigation. X-ray, Synchrotron and Neutron Techniques*. 2011. https://doi.org/10.1134/s1027451011060140

42. Plusnin N. I. Metallic nanofilms on single crystal silicon: Growth, properties and applications. *Modern Electronic Materials*. 2017;3(2): 57–65. https://doi.org/10.1016/j.moem.2017.09.005

43. Profile: Nikolai Inokentievich Plyusnin. GOOGLE Academy. (In Russ.) https://scholar.google.ru/citations?hl=ru&user=EuZUhCEAAAAJ&pagesize=80&view_op=list_works

**Translated by author of the article.*

Information about the authors

Nikolay I. Plyusnin, Dr. Sci. (Phys.–Math.), Associate Professor, Senior Researcher at the Federal State Treasury Military Educational Institution of Higher Education "Military Order of Zhukov and Lenin Red Banner Academy of Communications named after Marshal of the Soviet Union S.M. Budyonny» (Military Academy of Communications) of the Ministry of Defense of the Russian Federation (St. Petersburg, Russian Federation).

https://orcid.org/0000-0001-9691-9721
nikolayplusnin@gmail.com

Received 11.07.2023; approved after reviewing 25.09.2023; accepted for publication 16.10.2023; published online 25.12.2023.

Translated by Valentina Mittova